Modélisation / Contrôle de la chaîne d'air des moteurs HCCI pour euro 7.

Felipe Castillo Buenaventura

UNIVERSITÉ DE GRENOBLE

THÈSE

Pour obtenir le grade de

DOCTEUR DE L'UNIVERSITÉ DE GRENOBLE

Spécialité : **Automatique-Productique**

Arrêté ministériel :

Présentée par

Felipe Castillo Buenaventura

Thèse dirigée par **MM. Luc Dugard, Emmanuel Witrant et Vincent Talon**

préparée au sein **du Gipsa Lab, de la DCMAP-Renault SAS**
et de **l'Ecole Doctorale Électronique, Électrotechnique, Automatique, Traitement du Signal**

Modélisation et Contrôle de la Boucle d'Air des Moteurs Diesel pour Euro 7

Thèse soutenue publiquement le **24 octobre 2013**,
devant le jury composé de :

M. Pierre Rouchon
Professeur, Mines ParisTech, Président
M. Joseph Winkin
Professeur, Université de Namur, Rapporteur
M. Sorin Olaru
Professeur, Ecole Supérieure d'Electricité, Rapporteur
M. Emmanuel Witrant
Maître de Conférences UJF Grenoble, Co-Directeur de thèse
M. Luc Dugard
Directeur de Recherche CNRS Gipsa-lab Grenoble, Directeur de thèse
M. Vincent Talon
Ingénieur de recherche Renault, Encadrant

Acknowledgments

I would like to express my deep gratitude to Luc Dugard and Emmanuel Witrant, my research supervisors, for their patient guidance, enthusiastic encouragement and the very useful advises that were essential for the development of this research work. I would also like to thank my industrial advisor Vincent Talon for his unconditional support, patience and assistance during the progress of my research project. My grateful thanks are also extended to Christophe Prieur for his substantial guidance, help and support during the development of the theoretical contributions of this thesis, to David Chalet and Pascal Chesse, who made the experimental validation of some of our results possible and the jury of this thesis Pierre Rouchon, Joseph Winkin and Sorin Olaru.

I also wish to thank GIPSA-Lab for its support and encouragement throughout my study and Renault for helping me carry out my doctoral research and their financial support. I would like to offer my special thanks to all the members of the Automatic Control Department for the good moments spent together.

Finally, I would like to thank my wife and family for their unconditional support.

Table of contents

1 Contexte et enjeux de la thèse **9**

1.1 Contexte de l'Étude: Développement de la Modélisation, de l'Observation et du Contrôle du moteur Diesel . . . 9

1.2 Objectifs de l'Étude . . . 12

1.3 Chapitre 3: Modélisation 0D de la boucle d'air orientée contrôle . . . 13

1.4 Chapitre 4: Contrôle de la Boucle d'Air en Utilisant des Formulations 0D . 16

1.5 Chapitre 5: Modélisation 1D de la Boucle d'Air . . . 18

1.6 Chapitre 6: Contrôle et Observation Frontière de Systèmes Hyperboliques du Premier Ordre . . . 20

1.7 Chapitre 7: Conclusions et perspectives . . . 22

2 Context and stakes of the study **23**

2.1 Context of the study: modeling, observation and control development of the Diesel Engine . . . 23

2.2 Objective of the study . . . 26

2.3 Manuscript outline . . . 27

2.3.1 Chapter 3: Control-Oriented 0-D Engine Air-Path Modeling . . . 27

2.3.2 Chapter 4: 0D Model-Based Air-Path Control . . . 27

2.3.3 Chapter 5: 1D Engine Air-Path Modeling . . . 28

2.3.4 Chapter 6: Boundary Control and Observation of First-Order Hyperbolic Systems . . . 29

2.3.5 Chapter 7: Conclusions and Perspectives . . . 29

2.4 Publications and Patents . . . 29

2.5 Nomenclature . . . 31

3 Control-Oriented 0D Engine Air-Path Modeling **35**

3.1 Dual Loop EGR Diesel Engine Air-Path . . . 37

3.2 Development of 0D Basic Equations . . . 40

3.3 Dual-EGR Engine Air Path Model . . . 42

3.3.1 Dynamics of the Engine Air-Path Model . . . 45

3.3.2 Statics of the Engine Air-Path Model . . . 50

3.4 Model Benchmark Validation . . . 55
3.4.1 Model and Simulation Parameters . . . 56
3.4.2 Steady State Validation . . . 56
3.4.3 Transient Validation . . . 58
3.5 Chapter Summary . . . 60

4 0D Model-Based Air-Path Control **61**
4.1 Background on Diesel Engine Air-Path Control . . . 64
4.1.1 Hybrid Robust Control for Diesel Engines Operated in Low Temperature and Conventional Combustion Modes (Junmin Wang) . . . 65
4.1.2 Control of a Turbocharged Diesel Engine Fitted with High Pressure and Low Pressure Exhaust Gas Recirculation Systems (Olivier Grondin, Philippe Moulin, Jonathan Chauvin) . . . 66
4.1.3 Nonlinear Input Transformation for EGR and VGT Control in Diesel Engines (Johan Wahlström and Lars Eriksson) . . . 68
4.2 Simultaneous Air Fraction and Low-Pressure EGR Mass Flow Rate Estimation for Diesel Engines . . . 70
4.2.1 Model Reduction for the Air Fraction and LP EGR Mass Flow Rate Estimation . . . 71
4.2.2 Low Pressure EGR Flow Rate Observer Design . . . 72
4.2.3 Air Fraction Observer . . . 74
4.2.4 Estimation Results . . . 77
4.3 Air Fraction and EGR Proportion Control for Dual Loop EGR Diesel Engines 80
4.3.1 Air-Path Air Fraction Control Model . . . 81
4.3.2 Air Fraction Control . . . 82
4.3.3 Air Fraction Controller Results . . . 87
4.4 Exhaust Manifold Pressure Estimation Diesel Equipped with a VGT Turbocharger . . . 91
4.4.1 Problem Formulation . . . 92
4.4.2 Exhaust Pressure Estimation . . . 93
4.4.3 Exhaust Manifold Pressure Estimation Results . . . 97
4.5 Boost Pressure Control Using a Novel VGT Positioning Algorithm . . . 100
4.5.1 Towards a Turbine Power Set-Point . . . 101
4.5.2 Optimal VGT Positioning . . . 104
4.5.3 Boost Pressure Control Simulation Results . . . 109
4.6 Chapter Summary . . . 112

5 1D Engine Air-Path Modeling **115**
5.1 Literature Review . . . 117
5.1.1 Pipe Flow Governing Equations and Discretization Schemes . . . 117
5.1.2 Engine Air-Path Boundary Conditions . . . 120

5.1.3 Boundary Resolution Methods Review . . . 130
5.2 Quasi-Steady Boundary Models and Data-map Generation . . . 133
5.2.1 Quasi-Steady Boundary Outflow Models . . . 134
5.2.2 Quasi-Steady Intra-Pipe Restriction Models . . . 139
5.3 Outflow and Intra-pipe Boundary Resolution Methods . . . 143
5.3.1 Outflow Boundary Resolution Methods . . . 144
5.3.2 Intra-Pipe Restriction Boundary Problem Resolution . . . 151
5.4 Experimental Evaluation of the Proposed Boundary Resolution Methods . 153
5.4.1 Experimental Setup . . . 154
5.4.2 Outflow Boundary Resolution Method Evaluation . . . 155
5.5 Chapter Summary . . . 162

6 Boundary Control and Observation of First-Order Hyperbolic Systems 165
6.1 Linear and Quasi-Linear Hyperbolic Systems: Boundary Control Review . 167
6.1.1 Backstepping boundary control for first-order hyperbolic PDEs (M. Krstic, A. Smyshlyaev, F. Di Meglio and R. Vazquez.) . . . 169
6.1.2 Dissisative boundary conditions for one-dimensional hyperbolic systems (J-M. Coron, G. Bastin, B. d'Andréa-Novel, C. Prieur, V. Dos Santos.) . . . 171
6.2 Dynamic Boundary Stabilization of Hyperbolic Systems . . . 172
6.2.1 Stability of Linear Hyperbolic Systems with Dynamic Boundary Conditions . . . 172
6.2.2 Stability of Parameter-Varying Linear Hyperbolic Systems with Dynamic Boundary Conditions . . . 176
6.2.3 Stability of Quasi-Linear Hyperbolic Systems with Dynamic Boundary Conditions . . . 180
6.3 Boundary Observers for Hyperbolic Systems . . . 181
6.3.1 Boundary Observer for Linear Hyperbolic Systems . . . 182
6.3.2 Boundary Observer for Quasi-Linear Hyperbolic Systems . . . 186
6.4 Fresh Air Mass Fraction Control . . . 189
6.4.1 Simulation Results . . . 194
6.5 Chapter Summary . . . 198

7 Conclusions and Perspectives 199

Bibliography 203

A Appendix 211
A.1 Motivation for 1D modeling for control purposes . . . 211
A.2 Effect of the variation of the heat ratio on the intra-pipe restriction models 212
A.3 Conservative Discretizations . . . 213

A.4 Air Fraction Estimation Taking into Account the Mass Transport Time for Diesel Engines 216

Chapter 1

Contexte et enjeux de la thèse

Cette thèse a été effectuée dans le cadre d'une *Convention Industrielle de Formation par la Recherche* (CIFRE), accord qui entre dans les programmes de l'*Association Nationale de la Recherche et de la Technologie*(ANRT). Le programme CIFRE est destiné aux entreprises françaises qui engagent un doctorant pour mener un projet de recherche de l'entreprise au sein d'un laboratoire de recherche public. Pour cette thèse, une convention CIFRE a été signée entre l'entreprise d'automobiles Renault France et le laboratoire de recherche universitaire GIPSA-Lab UMR CNRS de Grenoble.

1.1 Contexte de l'Étude: Développement de la Modélisation, de l'Observation et du Contrôle du moteur Diesel

Le transport propulsé par des moteurs à combustion interne joue un rôle fondamental dans les sociétés et les individus modernes car le développement de la mobilité est étroitement lié à la façon dont les gens interagissent, organisent la production et ont accès aux biens et aux services. En effet, tout indique que les véhicules vont devenir de plus en plus accessibles (au plus grand nombre), plus sûrs, plus performants et utilisés encore plus fréquemment. Cependant, comme le transport privé a augmenté de façon spectaculaire au cours des dernières décennies, de nombreuses conséquences indésirables sont apparues telles que l'augmentation de consommation de carburant, des émissions de polluants et une plus grande exposition des personnes à des substances dangereuses associées à de graves problèmes de santé [64]. Par exemple, en Europe, de nombreuses études ont présenté des données montrant le lien direct entre les émissions polluantes et l'utilisation des véhicules [2] [54].

La persistance de la dégradation de la qualité de l'air et les problèmes de santé liés au transport ont déclenché plusieurs réponses politiques, qui visent à réduire les émissions provenant des véhicules des particuliers [100]. Ces politiques deviennent de plus en plus strictes dans le monde entier avec:

- l'introduction de limites plus contraignantes pour les véhicules légers avec les normes Euro 5b en 2011 et Euro 6 en 2014 [87],
- le remplacement de l'actuel nouveau cycle européen de conduite (New European Driving Cycle (NEDC)) par un cycle de conduite harmonisé au niveau mondial pour 2014 [100],
- et potentiellement, la mise en œuvre de mesures supplémentaires pour vérifier les émissions des véhicules en dehors d'un seul cycle de conduite standardisé en 2014.

Le Tableau 1.1 présente un résumé des principales réglementations et de l'évolution de la législation sur les émissions polluantes pour la Communauté Européenne depuis sa première apparition. La Figure 1.1 illustre son évolution.

Stage	Date	CO	HC+NOx	NOx	PM
Euro 1*	1992.07	2.72 (3.16)	0.97 (1.13)	-	0.14 (0.18)
Euro 2	1996.01	1	0.7	-	0.08
Euro 3	2000.01	0.64	0.56	0.5	0.05
Euro 4	2005.01	0.5	0.3	0.25	0.025
Euro 5	2011.09	0.5	0.23	0.18	0.005
Euro 6	2014.09	0.5	0.17	0.08	0.005
* Les valeurs entre parenthèses sont la conformité des limites de production					

Table 1.1: Norme européenne pour les voitures des passagers (Catégorie M1*), g/km.

En dépit des limites strictes d'émissions, le transport routier reste la source la plus importante de pollution de l'air urbain en Europe à l'égard des NOx (oxydes d'azote) et de CO (monoxyde de carbone) [100]. Un autre facteur contraignant pour le développement du véhicule est la limitation des combustibles fossiles. Étant donné que la consommation de pétrole représente 35% de la consommation mondiale d'énergie primaire, avec le gaz naturel et le charbon qui composent 24% et 28%, respectivement, c'est un euphémisme de dire que l'économie mondiale dépend de manière critique de ces ressources non renouvelables. Comme le pétrole, le gaz naturel et le charbon sont des ressources naturelles limitées, il est clair qu'à un moment donné, la production atteindra un maximum et commencera à décliner [13].

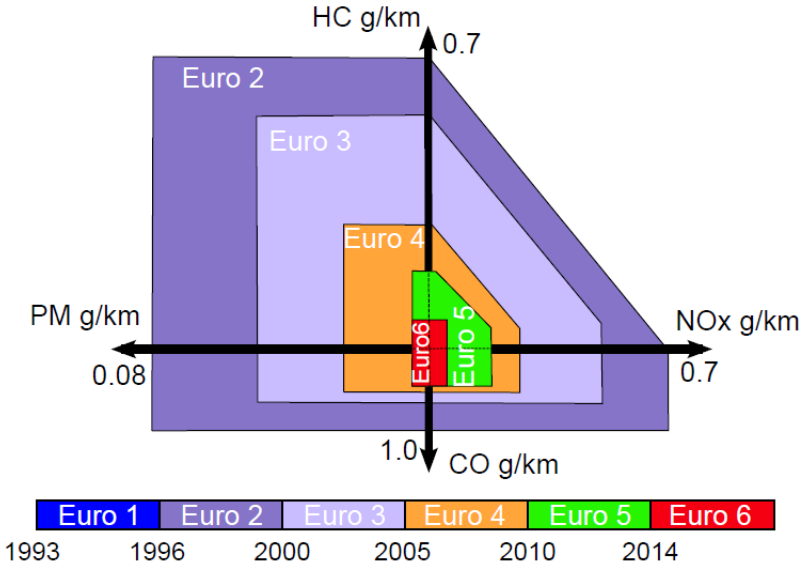

Figure 1.1: Limites européennes d'émission de la législation pour les moteurs Diesel [69]

La problématique énergétique, la limitation du carburant, les problèmes de santé et de l'environnement, ainsi que le cadre normatif des émissions de polluants sont quelques-uns des principaux problèmes à traiter au niveau international et en particulier dans le secteur du transport et de l'automobile. Ces aspects forcent les constructeurs automobiles à développer de nouvelles technologies pour économiser le carburant et réduire les émissions polluantes, tout en maintenant ou même en améliorant la performance du moteur. Plusieurs nouvelles technologies et des architectures de moteurs alternatifs ont permis d'atténuer certains aspects négatifs inhérents à la combustion interne des moteurs, montrant que l'augmentation de la complexité du moteur contribue à en améliorer l'efficacité.

En raison de la complexité des nouveaux équipements et des technologies développées dans les véhicules pour satisfaire les exigences actuelles au niveau des émissions polluantes, il y a une forte demande pour explorer de nouveaux modèles et concepts de contrôle capables de satisfaire les normes d'émissions. L'une des stratégies adoptées pour surmonter ces aspects est le contrôle moteur basé sur le modélisation mathématique du système. Avec cette approche, les modèles physiques des différents éléments constituant le véhicule sont conçus de manière à représenter, aussi bien que possible, leur comportement physique. Cette méthode permet d'évaluer et de mettre en oeuvre, d'une manière très efficiente, des nouveaux concepts et des stratégies qui permettent d'améliorer potentiellement les performances du moteur.

Actuellement, la majeure partie de la recherche et du développement du contrôle moteur est faite dans un cadre zéro-dimensionnel (0D). Cependant, les approches unidimensionnelles (1D) commencent à émerger puisque les limitations intrinsèques de la modélisation 0D commencent à limiter la performance des stratégies modernes du contrôle moteur.

La modélisation moteur 0D ne considère que l'évolution des variables dynamiques par rapport au temps tandis que les systèmes 1D permettent de décrire l'évolution d'une variable dans le temps et dans l'espace. Évidemment, les modèles 0D sont nettement moins complexes que les modèles 1D et pour cette raison (entre autres), les modèles 0D sont généralement utilisés pour concevoir et évaluer les stratégies de contrôle du moteur.

L'utilisation de stratégies de contrôle basées sur des modèles 0D-1D a de nombreux avantages par rapport aux stratégies de contrôle moteurs basées sur des cartographies (algorithmes statiques basés sur des tables de consultation). En effet, les seconds ne sont valables que sur les points de fonctionnement du moteur à partir desquels ils ont été calibrés. En outre, comme la commande du moteur basée sur des cartographies est une approche complètement statique, elle introduit des erreurs importantes pendant les conditions transitoires du moteur. En plus d'une meilleure description du système, l'utilisation des modèles physiques dynamiques pour contrôler le moteur offre d'autres avantages, comme la réduction du temps de développement et l'utilisation des bancs moteurs, ce qui réduit considérablement les coûts de conception du moteur.

1.2 Objectifs de l'Étude

La chaîne d'air du moteur est devenue un élément essentiel dans le développement des moteurs modernes. Le contrôle du système d'air a un impact direct sur les performances du moteur ainsi que sur son niveau d'émission de polluants. En effet, les stratégies qui agissent sur le système d'air permettent de contrôler les composants introduits dans le cylindre, ce qui est un moyen efficace et rentable de réduire les émissions polluantes. En conséquence, les chaînes d'air des moteurs modernes sont devenues de plus en plus complexes afin d'atteindre les stratégies de réduction de pollution et de permettre des réductions de consommation de carburant.

Dans ce contexte, cette thèse se focalise sur la modélisation et le contrôle de la chaîne d'air des moteurs Diesel. Nous avons divisé ce travail en développements à court terme et en développements à moyen et long termes.

Dans les développements à court terme (Chapitres 3 et 4), nous abordons plusieurs problématiques au niveau du contrôle de la chaîne d'air qui intéressent actuellement Renault. Nous fournissons des solutions orientées vers l'industrie, appropriées pour la mise en œuvre, avec les ressources disponibles sur les moteurs actuellement produits. Plus précisément, nous abordons les problèmes de:

- la conception d'une architecture de contrôle de la chaîne d'air qui utilise le taux de Recirculation de Gaz d'Échappement (RGE) comme variable de performance;
- l'estimation simultanée en boucle fermée du débit massique de RGE à basse pression

et la fraction d'air dans le collecteur d'admission;

- la commande de la fraction massique de l'air frais dans le collecteur d'admission, tout en satisfaisant une proportion de RGE souhaitée (entre RGE à basse pression et RGE à haute pression);
- l'estimation de la pression du collecteur d'échappement en prenant en compte l'effet de la vitesse de la turbine;
- l'amélioration de l'algorithme de positionnement de la Turbine à Géométrie Variable (TGV).

Dans les développements à moyen et long termes (Chapitres 5 et 6), nous nous focalisons sur certains défis qui doivent être abordés afin de répondre aux législations sur les émissions futures. Plus précisément, nous nous concentrons sur la modélisation, l'estimation et le contrôle du phénomène de transport de masse dans la chaîne d'air des moteurs Diesel. Nous contribuons au développement de méthodes de résolution de conditions limites axées sur les plateformes de simulation 1D orientées contrôle et nous construisons une partie du cadre théorique (approche de dimension infinie) qui permet de contrôler et d'estimer la fraction d'air frais dans le collecteur d'admission en prenant en compte le temps de transport de masse. En particulier, nous abordons les questions suivantes:

- des méthodes complètement non-isentropiques pour la résolution des conditions limites des restrictions de sortie et du tube pour la modélisation 1D en transitoire de l'écoulement compressible;
- le contrôle et l'observation frontière dynamique des systèmes hyperboliques du premier ordre linéaires, LPV et quasi-linéaires;
- la commande et l'observation de la fraction massique de l'air frais dans le collecteur d'admission, en tenant compte du phénomène de transport de masse.

Outre les traditionnels chapitres d'introduction, de conclusion et de perspectives, le manuscrit est organisé en 4 chapitres de la façon suivante :

1.3 Chapitre 3: Modélisation 0D de la boucle d'air orientée contrôle

La modélisation du moteur est un sujet pluridisciplinaire qui comprend la thermodynamique, la mécanique des fluides, les réactions chimiques, l'analyse mathématique de

la turbulence, du transfert de chaleur, de la combustion et des méthodes numériques. Différents niveaux de modélisation ont été utilisés pour représenter le comportement du moteur. Ces modèles peuvent être très basiques comme dans le cas des modèles du système d'air standard, jusqu'à des modèles à trois dimensions (3D) qui peuvent décrire divers phénomènes comme la turbulence, les réactions chimiques, la dynamique de pulvérisation, les retards associés au transport de masse, la géométrie du moteur, etc. La modélisation du moteur est généralement classée en trois catégories : modèles "zéro-dimensionnels" (0D), "mono-dimensionnels" (1D) et des modèles "multi-dimensionnels" (2D et 3D).

Dans les modèles 0D, le moteur est habituellement représenté par un réseau de volumes de contrôle (par exemple, les collecteurs d'admission et d'échappement) qui sont reliés entre eux en utilisant des équipements divers tels que des vannes, des turbines, des filtres, etc. Ces modèles ont une efficacité de calcul élevée et un bon degré de prévisibilité par rapport à la performance du moteur. Pour les applications de contrôle, la modélisation 0D est la technique la plus répandue pour représenter la boucle d'air en raison de sa relative simplicité, sa polyvalence et sa faible demande en terme de calcul. En outre, ces modèles sont représentés par des ensembles d'Équations Différentielles Ordinaires (EDO), ce qui est directement compatible avec la plupart des stratégies de synthèse de contrôleurs et d'observateurs.

Les modèles 1D donnent de meilleures caractéristiques sur les transitoires du moteur, permettant de vérifier la configuration de la boucle d'air du moteur et d'étudier la dynamique de la puissance de sortie du moteur sous de fortes conditions transitoires. Avec des modèles 1D, il est possible d'étudier l'économie de carburant, le fonctionnement du turbocompresseur et le rendement du moteur pour différentes conditions de fonctionnement du moteur. Dans le domaine du contrôle moteur, il y a très peu de travaux réalisés avec des modèles 1D en raison de la complexité des Équations aux Dérivées Partielles (EDP) qui décrivent le régime transitoire, ainsi que la difficulté à faire face aux conditions frontières. Toutefois, le contrôle des systèmes décrits par des EDP est un sujet très actif dans la communauté de l'automatique et de nombreux efforts sont déployés pour élaborer des lois de contrôle pour cette catégorie de systèmes.

D'autre part, la représentation 2D et 3D de la dynamique des fluides est très utile pour explorer et mieux comprendre les processus physiques qui se produisent à l'intérieur du moteur. Par conséquent, ces techniques de modélisation sont largement utilisées dans l'élaboration de nouveaux concepts de moteurs. Le principal objectif de la modélisation 2D et 3D est de décrire localement une grande variété de variables telles que les pressions, températures, les vitesses des gaz et la composition des gaz. En outre, ce type de représentation physique aide à relier les paramètres géométriques du moteur à diverses données du moteur. Ce schéma de modélisation fine aide à améliorer l'apprentissage des processus physiques du moteur, qui fournit une meilleure description des phénomènes physiques et permet de construire des systèmes de modélisation plus simples pour une

large gamme d'applications. Les ressources de calcul nécessaires à la modélisation 2D-3D sont évidemment beaucoup plus élevées et par conséquent, ces modèles ne sont pas, pour le moment, adaptés pour le contrôle moteur en temps réel.

En évaluant les caractéristiques des trois stratégies de modélisation du moteur précédemment décrites, nous avons choisi, dans cette thèse, de travailler avec la modélisation 0D pour le développement de la commande et l'observation de la boucle d'air car elle est la plus adaptée au secteur industriel. Cette stratégie de modélisation semble être la mieux adaptée à des fins de contrôle (au moins dans un scénario à court terme) en raison de sa polyvalence et sa faible charge de calcul. Pour obtenir un modèle efficace orienté vers le contrôle-commande, il est essentiel de proposer un modèle qui soit représentatif du moteur sur un large intervalle de conditions d'opération. Cependant, un modèle très précis implique typiquement une grande charge au niveau du calcul. En conséquence, il est crucial d'établir un bon compromis entre la charge de calcul et la précision du modèle.

Pour les moteurs à combustion interne des voitures de tourisme, il y a au moins deux aspects principaux de leur fonctionnement, modélisés par des approches de modélisation 0D [49]:

- le processus de combustion lui-même qui est fortement transitoire (cycle avec des rapides variations de température et de pression);
- la thermodynamique de la boucle d'air du moteur qui a une étroite influence sur le processus de combustion (pression et température d'admission, composition du gaz, etc.).

Les aspects thermodynamiques et cinétiques dans le processus de combustion sont très rapides et ne sont généralement pas accessibles à des fins de contrôle. En effet, les modèles nécessaires pour décrire ces phénomènes sont plutôt complexes et rarement utiles pour la conception de contrôleurs en temps réel. Par conséquent, ces types de phénomènes ne sont pas considérés dans les modèles développés dans cette thèse. Nous simplifions les propriétés rapides de la combustion en utilisant des expressions statiques, ce qui implique que la combustion elle-même évolue d'une manière identique à chaque fois. De toute évidence, ces modèles ne seront pas capables de représenter tous les phénomènes se produisant dans le moteur (par exemple, les pressions aléatoires de la combustion). Cependant, pour des applications de contrôle-commande, les méthodes utilisées pour représenter la combustion avec de formulations statiques ont montré leur efficacité.

Dans ce chapitre, nous nous concentrons sur les processus impliqués dans la boucle d'air; ceux-ci sont généralement modélisés en utilisant deux stratégies:

- Modèles à Valeur Moyenne (MVM): modèles continus qui négligent les cycles discrets

du moteur et supposent que tous les processus et les effets du moteur sont répartis sur le cycle du moteur;

- Modèles à Événements Discrets (MED): modèles qui tiennent compte de façon explicite du comportement du moteur à pistons.

Dans le MVM, la variable indépendante est le temps, tandis que dans le MED, l'angle du vilebrequin est la variable indépendante. Le bon choix de la classe du modèle dépend du problème à résoudre. Par example, les MVMs sont relativement bien adaptés pour les processus lents dans la périphérie du moteur, tels que la boucle d'air. Les MEDs sont utiles pour le contrôle de la richesse et la détection des allumages ratés.

Dans ce chapitre, un modèle 0D à valeur moyenne de la chaîne d'air d'un moteur Diesel est développé pour des applications de contrôle et d'observation. Ce modèle est destiné à servir de plate-forme pour la synthèse et l'évaluation de lois de commande et d'observation. L'objectif est d'illustrer le développement d'un modèle 0D de la chaîne d'air pour les applications de contrôle et de fournir les bases et la notation nécessaires pour les stratégies de contrôle proposées dans les chapitres suivants. A la fin de ce chapitre, nous présentons une validation basée sur des mesures obtenues sur banc moteur en régime stationnaire et en régime transitoire afin de démontrer que notre modèle est représentatif du moteur. Ce modèle est partiellement inspiré par les travaux de [5], [43], [55] et [94] parmi d'autres, où la modélisation 0D de la chaîne d'air a été utilisée avec succès pour des applications de contrôle-commande.

1.4 Chapitre 4: Contrôle de la Boucle d'Air en Utilisant des Formulations 0D

La réglementation des émissions des moteurs Diesel est devenue de plus en plus stricte; répondre simultanément aux législations des émissions et à la performance du moteur est un objectif particulièrement difficile. Bien que des améliorations importantes aient été apportées au cours des dernières années, il y a encore de nombreuses questions techniques qui doivent être abordées pour répondre aux futures lois de réglementation des émissions. L'introduction de modes de combustion sophistiqués tels que la combustion homogène par allumage de la charge de compression (HCCI : Homogeneous Charge Compression Ignition), la combustion à basse température (LTC : Low temperature Combustion) et l'allumage par compression contrôlée pré-mélangée (PCCI : Premixed Charge Combustion Ignition) offre un grand potentiel pour réduire le niveau des émissions des moteurs [3] [4] [83]. Cependant, ces nouveaux modes de combustion nécessitent des stratégies spécifiques d'injection de carburant et des conditions dans les cylindres, nécessitant des systèmes de contrôle plus fiables, complexes et technologiques.

La boucle d'air joue un rôle crucial dans le développement des moteurs modernes. Le contrôle de la chaîne d'air a un impact direct sur la performance du moteur ainsi que sur ses niveaux d'émissions de polluants. En effet, les stratégies de contrôle agissant sur le système d'air permettent de réguler les composants introduits dans le cylindre, ce qui est un moyen rentable de réduire les émissions polluantes. En conséquence, les systèmes d'air des automobiles sont devenus de plus en plus complexes afin de parvenir à la réduction des émissions polluantes et de la consommation de carburant.

La double boucle de recirculation de gaz d'échappement (RGE) avec la recirculation à haute (HP) et basse (BP) pressions, est une des nouvelles stratégies qui permet de parvenir à des conditions appropriées pour la mise en œuvre de modes de combustion multiples [53]. En effet, la quantité nette de RGE dans le cylindre ainsi que le rapport entre la RGE à haute pression (HP-RGE) et le RGE à basse pression (BP-RGE) permettent de contrôler efficacement la combustion dans le cylindre et les émissions polluantes sortant du moteur. La régulation de la fraction de l'air frais dans le collecteur d'admission est un moyen efficace de contrôler les conditions de RGE dans les cylindres [5] [35]. Par ailleurs, pour les moteurs dotés de systèmes doubles de RGE, la fraction d'air en amont du compresseur fournit le taux LP-RGE, tandis que la fraction d'air dans le collecteur d'admission fournit le taux total de RGE. Par conséquent, si les fractions d'air de chaque section sont bien contrôlées, les boucles de recirculation HP et BP-RGE peuvent également être efficacement contrôlées. Cependant, assurer les conditions adéquates dans le cylindre est toujours une tâche très difficile parce que l'introduction de la RGE implique la solution à de nombreux défis en raison de l'absence des mesures de débits RGE et de la fraction d'air.

Le besoin de fournir de l'air frais au moteur, même sous des taux de RGE élevés, rend essentielle l'utilisation de dispositifs de pointe pour la suralimentation, comme les turbocompresseurs de Turbine à Géométrie Variable (TGV). Ces dispositifs permettent au moteur de fonctionner avec des modes de combustion alternatifs car les TGV assurent un contrôle précis de la différence de pression sur le moteur, ainsi qu'une réponse très rapide durant les transitoires. Néanmoins, le positionnement de la TGV est un problème très complexe dans les moteurs suralimentés, en raison des non linéarités du système, du manque de mesures fiables, de la forte dépendance des conditions de fonctionnement du moteur et des contraintes physiques de l'actionneur.

En raison de la nécessité constante d'améliorer les performances et les procédures de calibration des stratégies de contrôle de la chaîne d'air, nous proposons dans ce chapitre, une architecture de contrôle du système d'air orientée vers l'industrie, qui permet de réguler efficacement les conditions du remplissage du moteur pour la mise en œuvre des modes de combustion alternatifs. Plus précisément, nous abordons le problème du contrôle de la pression, de la fraction massique de l'air frais et de la proportion de RGE dans le collecteur d'admission du moteur.

Nous estimons le débit massique de RGE basse pression et la fraction d'air circulant à travers la chaîne d'air de façon simultanée en utilisant un estimateur à modes glissants et un observateur linéaire à paramètres variant, respectivement. En utilisant ces estimations, un contrôleur LQR-LPV optimal par retour d'état est conçu pour réguler la fraction d'air dans le collecteur d'admission, ainsi que la proportion de RGE. La pression du collecteur d'échappement est estimée en utilisant un schéma numérique non itératif qui permet d'utiliser directement les cartographies extrapolées de la turbine à géométrie variable (TGV), permettant ainsi de prendre en compte l'effet de la vitesse de la turbine sur le débit massique. Enfin, on propose un régulateur de pression de suralimentation constitué par une combinaison de stratégies de contrôle en boucle ouverte et en boucle fermée. La principale différence par rapport à d'autres méthodes est l'utilisation d'un algorithme qui améliore le positionnement de la TGV. Les principales contributions présentées dans ce chapitre sont décrites dans les publications [30], [29] et [28] et dans les brevets [18], [17], [19], [16] et [20].

1.5 Chapitre 5: Modélisation 1D de la Boucle d'Air

Les modèles zéro-dimensionnels (0D) sont actuellement utilisés avec succès pour observer et contrôler la boucle d'air des moteurs Diesel. Cependant, comme la complexité de la chaîne d'air des moteurs augmente et les réglementations sur les émissions polluantes deviennent plus strictes, les limitations intrinsèques des approches 0D commencent à restreindre fortement les possibilités des stratégies de contrôle modernes. Par exemple, l'une des plus d'importantes limitations de la modélisation 0D est son incapacité à représenter le phénomène de transport de masse. Le fait de ne pas prendre en compte le transport de la fraction d'air dans les architectures avec double RGE peut introduire une dégradation systématique de la performance des émissions du moteur. L'impact négatif du transport de masse est particulièrement important lors de l'utilisation de la BP-RGE à cause de la relative longue distance entre le compresseur et le collecteur d'admission du moteur. Ainsi, il est crucial de proposer des solutions alternatives de modélisation pour améliorer l'avenir du contrôle-moteur.

La modélisation unidimensionnelle (1D) orientée-contrôle est une alternative naturelle pour la modélisation 0D, car elle permet de représenter les principales caractéristiques du régime transitoire des systèmes d'air des moteurs Diesel. En effet, la modélisation 1D de la chaîne d'air permet de résoudre plusieurs des limitations liées à des formulations 0D, y compris la représentation du transport de la fraction d'air (par exemple dans l'annexe A.1, nous présentons une illustration des avantages de l'utilisation d'une formulation 1D au lieu d'une formulation 0D pour décrire l'évolution de la fraction d'air dans un tube). Cependant, la modélisation 1D du régime transitoire du moteur implique une solution spécifique des équations d'Euler, ce qui conduit à des problèmes beaucoup plus complexes, tels que

les méthodes numériques pour résoudre les équations différentielles partielles (EDP) et la solution des conditions limites. Pour cette raison (entre autres), les stratégies de contrôle 1D sont nettement moins explorées que les approches 0D dans la littérature. Le contrôle et l'observation des systèmes 1D, et plus précisément, les systèmes décrits par des EDP, sont actuellement un sujet de recherche très actif dans la communauté de l'automatique, ce qui suggère que la modélisation 1D orientée contrôle pourrait être une évolution naturelle des stratégies de contrôle du système d'air. Par ailleurs, le développement de modèles 1D axés sur le contrôle moteur est un sujet important pour l'évolution de la chaîne d'air car il permettrait de synthétiser des stratégies de contrôles plus avancées, susceptibles d'améliorer significativement la performance du moteur par rapport aux émissions polluantes. Pour concevoir des lois de commande pour des systèmes 1D, il est essentiel de construire une plate-forme de modélisation 1D axée sur des applications contrôle (un ensemble d'outils flexibles qui permet de simuler facilement l'évolution des écoulements) avec une faible charge de calcul et une bonne précision. Malheureusement, à notre connaissance, très peu de travaux ont été réalisés dans ce domaine, d'où les très nombreuses questions à résoudre afin d'obtenir un outil approprié pour la modélisation 1D de la boucle d'air pour des applications de contrôle. Dans [69], une première approche de plate-forme de modélisation axée sur le contrôle 1D a été considérée par la formulation de solutions alternatives aux conditions frontières d'entrée et de sortie non-isentropiques (avec changement de niveau d'entropie).

En effet, la solution du problème des conditions aux frontières est l'un des sujets les plus difficiles à aborder lors de la construction d'un modèle 1D axé sur le contrôle d'un moteur Diesel. Les méthodes de résolution des problèmes frontières trouvées dans la littérature sont généralement basées sur l'hypothèse d'une contraction isentropique aux bords, ce qui simplifie considérablement le problème [10] [101]. Cependant, cette hypothèse n'est pas vérifiée expérimentalement car des débits plus élevés sont systématiquement obtenus à travers les restrictions. Par conséquent, des coefficients de décharge expérimentaux sont généralement mis en place pour faire face artificiellement à ce problème [32] [33] [91]. L'inconvénient de cette stratégie est que les mesures expérimentales doivent être effectuées, ce qui augmente le coût de la calibration du modèle. En outre, en l'absence de données expérimentales pour déterminer les coefficients de décharge, des résultats de simulation peuvent être en total désaccord avec des données issues de bancs de mesures. Une autre technique consiste à utiliser la simulation tridimensionnelle comme un banc d'essai numérique [31]. Cependant, cette technique consomme beaucoup de temps et des résultats expérimentaux sont nécessaires pour valider le banc numérique. Ses aspects motivent la recherche de modèles alternatifs de restriction et des méthodes de résolution des conditions aux bords non-isentropiques capables d'offrir plus de précision et de flexibilité.

Dans ce chapitre, nous étudions le développement d'une plate-forme 1D de simulation de la chaîne d'air orientée contrôle. Plus précisément, nous nous concentrons sur le problème de frontière non-isentropique à la sortie et à l'intérieur des conduits. Ceci est motivé par

l'écart systématique entre les méthodes traditionnelles de résolution du problème frontière (basées sur une formulation de contraction isentropique) et les résultats expérimentaux. Nous développons deux méthodes innovantes pour résoudre le problème frontière non-isentropique, qui sont indépendantes des modèles physiques des conditions limites. En effet, nos méthodes permettent l'introduction de modèles physiques des conditions limites plus prédictives dans les algorithmes de résolution du problème frontière sans qu'il soit nécessaire d'ajouter des corrections artificielles, telles que les traditionnels coefficients de décharge. Cela se fait, tout en étant toujours physiquement compatible avec la formulation non-isentropique. Les principaux avantages obtenus par les méthodes de résolution du problème frontière proposées dans ce chapitre sont les suivantes:

- l'augmentation de la flexibilité des plates-formes de modélisation 1D;
- la réduction du temps de calibration des modèles (éviter l'utilisation des coefficients de correction artificiels);
- la réduction de la charge calcul de la CPU.

qui sont des caractéristiques très intéressantes pour la modélisation orientée contrôle-commande des chaînes d'air. Les principales contributions présentées dans ce chapitre sont décrites dans les publications [27] et [23].

1.6 Chapitre 6: Contrôle et Observation Frontière de Systèmes Hyperboliques du Premier Ordre

Comme indiqué précédemment, il est très important de contrôler et d'observer efficacement la fraction d'air frais dans le collecteur d'admission des moteurs Diesel avec double boucle RGE. En effet, une bonne maîtrise de la composition du gaz permet la mise en œuvre des modes de combustion alternatifs, qui sont des éléments clés pour améliorer la performance des émissions du moteur. La plupart des méthodes de commande et d'estimation du système d'air reposent sur des stratégies de modélisation 0D, qui ont été utilisées avec succès au cours des dernières années. Cependant, comme la complexité de la boucle d'air des moteurs augmente et que les réglementations sur les émissions deviennent plus restrictives, les contraintes intrinsèques de la modélisation 0D commencent à limiter la performance des stratégies modernes de contrôle moteur. Par exemple, le transport de masse dans la chaîne d'air est un phénomène qui ne peut pas être représenté avec une formulation 0D, ce qui engendre actuellement une dégradation systématique de la performance des émissions du moteur. Par conséquent, il est crucial de proposer des stratégies alternatives de contrôle (telles que les stratégies basées sur des modèles 1D) afin de satisfaire les réglementations futures sur les émissions polluantes des moteurs.

L'utilisation de modèles 1D de la boucle d'air pour des applications de contrôle-commande semble être une approche naturelle pour résoudre un certain nombre de limitations actuelles, telles que la représentation du phénomène de transport de masse. Comme constaté dans le Chapitre 5, ces modèles de dimension infinie sont décrits par une EDP du premier ordre hyperbolique quasi-linéaire, avec des conditions aux bords qui varient en fonction de l'actionneur associé (par exemple des vannes RGE). Il est courant, pour la plupart des procédés industriels, d'avoir des capteurs et actionneurs uniquement disponibles aux frontières. En effet, cela est particulièrement vrai pour le système d'air des moteurs car aucun contrôle ou mesure n'est spatialement distribué dans les moteurs produits actuellement. Ainsi, l'utilisation de stratégies de contrôle des frontières pour les systèmes hyperboliques apparaît comme une bonne stratégie pour aborder le problème de la régulation de la fraction d'air dans les moteurs Diesel.

Le contrôle de la frontière des systèmes hyperboliques a été exhaustivement étudié dans la littérature. Cependant, la plupart des résultats considèrent que le contrôle de la frontière peut réagir beaucoup plus vite que le temps de voyage des ondes. Plus précisément, aucune limitation de temps de réponse n'est prise en compte dans les conditions aux bords. Pour de nombreuses applications, le temps de voyage des ondes peut être considéré comme beaucoup plus long que le temps de réponse de l'actionneur, comme par exemple dans la stabilisation aux frontières de canaux ouverts [9] [41]. Par conséquent, une relation statique peut être établie entre la commande d'entrée et de la condition limite. Néanmoins, il existe des applications où la dynamique associée à la condition limite ne peut pas être négligée (par exemple le contrôle de la fraction de l'air dans un moteur) et donc des stratégies de régulation alternatives doivent être proposées. Le problème de la stabilité des systèmes hyperboliques en présence d'un comportement dynamique à la frontière est un sujet beaucoup moins exploré.

Dans ce chapitre, nous examinons tout d'abord le problème de la stabilisation et de l'observation frontière dynamique des systèmes hyperboliques du premier ordre linéaires, quasi-linéaires et LPV. Nous donnons des conditions suffisantes pour la stabilité exponentielle de cette classe de systèmes de dimension infinie en utilisant des techniques basées sur des approches de types Lyapunov et inégalités matricielles. Ensuite, les principaux résultats théoriques développés dans ce chapitre sont utilisés afin de synthétiser un contrôle frontière pour réguler la fraction d'air d'un moteur Diesel fonctionnant avec RGE basse pression. Bien que nous nous concentrions sur le contrôle de la chaîne d'air de moteurs Diesel, les principaux résultats théoriques de ce chapitre s'étendent à une grande quantité d'applications industrielles de grande importance telles que les réseaux hydrauliques [85], l'écoulement polyphasique [70], les réseaux de trafic routier [51], le débit de gaz dans des pipelines [8] et la régulation du débit dans des mines profondes [102]. Les principales contributions présentées dans ce chapitre sont décrites dans les publications [25], [24], [22], [26] et [21].

1.7 Chapitre 7: Conclusions et perspectives

La thèse se termine par les conclusions générales, les orientations futures de recherche en vue d'améliorer et de compléter les méthodes développées dans cette thèse et quelques-uns des problèmes ouverts à aborder dans une perspective à long terme.

Chapter 2

Context and stakes of the study

This thesis has been developed thanks to a *Convention Industrielle de Formation par la Recherche* (CIFRE)[1] agreement, that is a program of the French agency *Association nationale de la recherche et de la technologie* (ANRT)[2], coordinated by the *Centre National de la Recherche Scientifique* (CNRS)[3]. The CIFRE program grants the French companies who engage a PhD student to carry out a research project of the company within a public research lab. For this thesis, a CIFRE agreement has been accorded between the automobile company Renault France and the scientific laboratory GIPSA-Lab in Grenoble.

2.1 Context of the study: modeling, observation and control development of the Diesel Engine

The transport powered by internal combustion engines plays a fundamental role in modern societies and individuals since the development of mobility is closely linked with how people interact, organize production and get access to services and goods. Indeed, vehicles are expected to become accessible to everybody, safer, more performing and be driven even more frequently. However, as the private transport has increased dramatically over the last decades, many undesirable consequences have appeared such as the increase fuel consumption, greater emissions of air pollutants and greater exposure of people to hazardous substances that causes serious health problems [64]. For instance, within Europe, a significant amount of studies have reported air emissions data directly linked to the vehicles use [2] [54].

The persistence of air quality degradation and health problems related to transporting

[1] Industrial Agreement for the Research and the Education
[2] Education and Research French Agency
[3] French National Center of Scientific Research

have triggered several policy responses, which are targeted to lower the emissions originated from light-duty vehicles [100]. Such policies are becoming more and more stringent worldwide with:

- the introduction of more stringent emission limits for light-duty vehicles with Euro 5 normative in 2011 and Euro 6 normative in 2014 [87];
- the replacement of the currently applied New European Driving Cycle (NEDC) by a world-wide harmonized driving cycle in 2014 [100];
- potentially, the implementation of supplementary measures for verifying vehicles emissions outside with a single standardized driving cycle in 2014.

Table 2.1 shows a summary of the main regulations and the evolution of the emissions legislation in the European community from its apparition. Figure 2.1 illustrates its evolution.

Stage	Date	CO	HC+NOx	NOx	PM
Euro 1*	1992.07	2.72 (3.16)	0.97 (1.13)	-	0.14 (0.18)
Euro 2	1996.01	1	0.7	-	0.08
Euro 3	2000.01	0.64	0.56	0.5	0.05
Euro 4	2005.01	0.5	0.3	0.25	0.025
Euro 5	2011.09	0.5	0.23	0.18	0.005
Euro 6	2014.09	0.5	0.17	0.08	0.005
* Values in brackets are conformity of production (COP) limits					

Table 2.1: EU Emission Standards for Diesel Passenger Cars (Category M1*), g/km.

In spite of the stringent emission limits, the road transport remains the most important source of urban air pollution in Europe with respect to NOX (nitrogen oxides) and CO (carbon monoxide) [100]. Another stringent issue on the vehicle development is the limitation of fossil fuel. Given that the consumption of petroleum represents 35% of world primary energy use, with natural gas and coal making up 24% and 28% respectively, it is an understatement to say that the world economy depends critically on these non-renewable resources. Since oil, natural gas and coal are finite natural resources, it is clear that at some point, the production will reach a maximum and begin to decline [13].

The energetic issues, the limitation of fuel, the health concerns, the environment together with the pollutant emissions normative are some of the main problems to address at an international level, especially in the automobile and the transportation sector. Those aspects force the car makers to develop new technologies to increase the fuel economy and

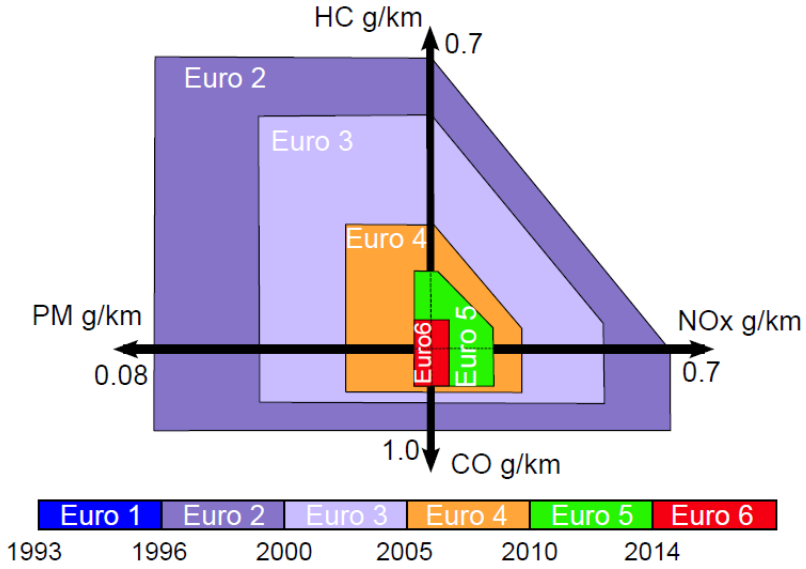

Figure 2.1: European legislation emission limits for Diesel engines [69]

decrease the emissions, while maintaining or even improving the engine's performance. Several new technologies and alternative engine architectures have allowed to mitigate some of the negative aspects inherent in the internal combustion engines, showing that increasing the complexity of the engine helps to enhance the engine's efficiency.

Because of the complexity of the new devices and technologies developed in the vehicle to overcome the current requirements on pollutant emissions, there is a strong demand to explore new modeling and control concepts capable of satisfying the stringent emission standards while maintaining the engine performance. One of the strategies adopted to overcome these aspects is the engine model-based control. With this approach, physical models of the various elements that constitute the vehicle are developed so as to represent, as best as possible, their physical behavior. This scheme allows evaluating and implementing, in a very cost-effective way, new concepts and strategies that potentially enable the improvement of the engine performance.

Currently, the research and development of the engine model-based control are made mostly in a zero-dimensional (0D) framework. However, one-dimensional (1D) approaches are starting to emerge since the intrinsic limitations of 0D modeling constrain the performance of modern engine control strategies. The $0D$ engine modeling only considers the variable dynamics with respect to time while 1D schemes allow describing the evolution of a variable along time and space. Evidently, 0D models are significantly less complex than 1D models and for that reason (among others), 0D models are usually used to design and evaluate the engine control strategies.

Using 0D-1D model-based control strategies has many advantages over engine data-map based control (static algorithms based on look-up tables), as the second ones are only

valid over the engine operating points from which they were calibrated. Moreover, since the engine control based on data-maps is a completely static approach, it introduces important errors under engine transient conditions. Using physical models to control the engine provides other advantages, such as a reduction in the development time and the use of engine benchmarks, which reduces significantly the costs of engine control design.

2.2 Objective of the study

The engine air-path has become a crucial part in the development of modern engines. The control of the air-path has a direct impact on the engine performance as well as on its pollutant emission level. Indeed, air system strategies allow controlling the species that are introduced in the cylinder, which is a cost-effective way to reduce pollutant emissions. As a consequence, the automotive air systems have become increasingly complex in order to achieve pollutant reduction strategies and to allow fuel consumption reductions.

In this context, this thesis focuses on the modeling and control of the air-path of Diesel engines. We divide this work into short-term developments and medium-long term developments.

In the short-term developments (namely Chapters 3 and 4), we address many of the current Renault's concerns regarding the control of the engine air-path. We provide industry-oriented solutions suitable for implementation, taking into account the resources currently available for production engines. Specifically, we address the problems of:

- the design of an engine air-path architecture that uses the EGR proportion as a performance variable;
- the simultaneous closed-loop estimation of the low-pressure EGR mass flow rate and the air fraction in the intake manifold;
- controlling the fresh air mass fraction in the intake manifold while satisfying a desired EGR proportion (between low pressure EGR and high pressure EGR);
- the estimation of the exhaust manifold pressure, taking into account the effect of the turbine speed;
- the improvement of the algorithm to position the variable geometry turbine (VGT).

In the medium-long term developments (namely Chapters 5 and 6), we are concerned with some of the challenges that have to be addressed in order to meet the future emission legislations. More precisely, we focus on the modeling, estimation and control of the mass transport phenomenon in the engine air-path. We contribute with the development of

boundary resolution methods for 1D modeling control-oriented platforms of the engine air-path and we build a part of the theoretical framework to enable the control and estimation of the intake manifold air fraction within an infinite dimensional approach. Particularly, we address the following issues:

- the completely non-homentropic boundary resolution methods for outflow and intra-pipe restrictions for $1D$ unsteady flow modeling;
- the dynamic boundary stabilization and observation of linear, LPV and quasi-linear first-order hyperbolic systems;
- the control and observation of the fresh air mass fraction in the intake manifold, taking into account the mass transport phenomenon.

2.3 Manuscript outline

This manuscript is organized as follows:

2.3.1 Chapter 3: Control-Oriented 0-D Engine Air-Path Modeling

In this chapter, a 0D mean-value engine air-path model is developed for control and observation purposes. This model is intended to serve as a platform for the synthesis and evaluation of control and observation laws. The aim is to illustrate the development of a 0D engine air-path model for control applications and to provide the required basis and notation for the control strategies that are proposed in the following chapters. At the end of this chapter we present a steady as well as a transient benchmark validation of the model in order to show that it is representative of the actual engine. This model is partly inspired by the works of [5], [43], [55] and [94] among others, where 0D engine air-path modeling has been successfully used for control purposes.

2.3.2 Chapter 4: 0D Model-Based Air-Path Control

Due to the constant need for improving the performance and the calibration procedures of the engine air-path control strategies, we propose, in this chapter an industrial-oriented air-path control architecture that enables to efficiently regulate the in-cylinder conditions to implement alternative combustion modes. More precisely, we address the problem of controlling the pressure, fresh air mass fraction and EGR proportion in the engine intake manifold.

We estimate the low-pressure EGR mass flow rate and the air fraction along the air-path simultaneously by means of a sliding mode and a linear parameter varying observer, respectively. Using these estimations, an optimal LQR-LPV state feedback controller is designed to regulate the air fraction in the intake manifold as well as the EGR proportion. The exhaust manifold pressure is estimated using a non-iterative numerical scheme, which allows using directly the extrapolated data-maps of the variable geometry turbine (VGT) and thus enabling to take into account the effect of the turbine speed on the turbine mass flow rate. Finally, we propose a boost pressure regulator constituted by a combination of open and closed-loop control strategies. The main difference with respect to other approaches is the use of an improved VGT positioning algorithm. The main contributions presented in this chapter are mostly described in the publications [30], [29] and [28] and the patents [18], [17], [19], [16] and [20].

2.3.3 Chapter 5: 1D Engine Air-Path Modeling

As the complexity of the engine air-path increases and the engine emission regulations become stricter, the intrinsic limitations of 0D approaches prevent to develop modern air-path control strategies able to satisfy these regulations. Thus, it is crucial to explore alternative modeling solutions (such as 1D modeling) to improve the future model-based control of Diesel engines. In this chapter, we investigate the development of a 1D air-path simulation platform for control purposes. More precisely, we focus on the non-homentropic outflow and intra-pipe boundary problem. This is motivated by the systematic disagreement of traditional boundary resolution methods (isentropic contraction-based formulations) with respect to experimental results. We develop two innovative non-homentropic boundary resolution methods which are independent of the physical models of the boundary. Indeed, these schemes permit introducing more predictable physical boundary models into the boundary resolution schemes without the need for adding artificial correction such as the traditional discharge coefficients. This is done while always being physically consistent with the non-homentropic formulation. The principal benefits obtained by the proposed boundary resolution methods are:

- the increase of the flexibility of the 1D modeling platforms;
- the reduction of model calibration (avoidance of artificial correction coefficients);
- the reduction of CPU calculation load.

which are very interesting features for the control-oriented modeling of the engine air-path. The main contributions presented in this chapter are mostly described in the publications [27] and [23].

2.3.4 Chapter 6: Boundary Control and Observation of First-Order Hyperbolic Systems

Models capable of representing the mass transport phenomenon (such as the equations that describe the evolution of a unsteady flow in a pipe) are often described by first-order hyperbolic partial differential equations. In many applications such as in the engine air-path, it is only possible to act at the boundaries, which implies that strategies based on boundary control have to be applied to stabilize these systems.

In this chapter, we first address the problem of the dynamic boundary stabilization and the boundary observation of linear, quasi-linear and LPV first-order hyperbolic systems. We give sufficient conditions for the exponential stability for this class of infinite dimensional systems by means of Lyapunov based techniques and matrix inequalities. Then, an air fraction boundary control for a Diesel engine operated with LP-EGR is proposed using some of the main results developed in this chapter. Although we focus on the control of the air-path of Diesel engines, the main theoretical results of this chapter extend to a large amount of industrial applications of significant importance such as hydraulic networks [85], multiphase flow [70], road traffic networks [51], gas flow in pipelines [8] and flow regulation in deep pits [102]. The main contributions presented in this chapter are mostly described in [25], [24], [22], [26] and [21].

2.3.5 Chapter 7: Conclusions and Perspectives

The thesis ends with the general conclusions, the future work directions to improve and complement the methods developed in this thesis and some of the open problems to be addressed in a long term perspective.

2.4 Publications and Patents

The main contributions of this thesis are the principal subject of the following publications:

Journal issues:

- F. Castillo, E. Witrant, C. Prieur, and L. Dugard. Boundary Observers for Linear and Quasi-Linear Hyperbolic Systems with Application to Flow Control. *Automatica, 10.1016/j.automatica.2013.07.027*;

International Conferences:

- F. Castillo, E. Witrant, C. Prieur, and L. Dugard. Dynamic boundary stabilization of linear and quasi-linear hyperbolic systems. Proceedings of the 51st IEEE Control and Decision Conference, Maui, Hawai, 2012;

- F. Castillo, E. Witrant, L. Dugard. Dynamic Boundary Stabilization of Linear Parameter Varying Hyperbolic Systems: Application to a Poiseuille Flow. Proceedings of the 11th IFAC Workshop on Time-Delay Systems, Grenoble, France. 2013;

- F. Castillo, E. Witrant, V. Talon, L. Dugard. Simultaneous Air Fraction and Low-Pressure EGR Mass Flow Rate Estimation for Diesel Engines . 5th IFAC Symposium on System Structure and Control Grenoble, France. 2013;

- F. Castillo, E. Witrant, V. Talon, L. Dugard. Exhaust Manifold Pressure Estimation Diesel Equipped with a VGT Turbocharger , SAE Technical Paper 2013-01-1752, doi:10.4271/2013-01-1752, 2013;

- F. Castillo, E. Witrant, L. Dugard, V. Talon, David Chalet, Pascal Chesse. Intra-Pipe Restriction Non-Homentropic Boundary Resolution Method, SAE Technical Paper 2013-01-0582, doi:10.4271/2013-01-0582, 2013.

- F. Castillo, E. Witrant, V. Talon, L. Dugard. Restriction Model Independent Method for Non-Isentropic Outflow Valve Boundary Problem Resolution, SAE Technical Paper, doi:10.4271/2012-01-0676, 2012;

- F. Castillo, E. Witrant, L. Dugard. Contrôle de température dans un flux de Poiseuille. Proceedings of the IEEE Conférence Internationale Francophone d'Automatique, Grenoble, France. 2012.

Patents

- F. Castillo, V. Talon, E. Witrant. Procédé d'Acquisition de la Composition des Gaz d'Admission dans un Repartieur d'Air d'un Moteur a Combustion Interne. INPI No FR 2973441;

- F. Castillo, V. Talon, E. Witrant. Estimation de la Pression Avant Turbine en Vue d'un Contrôle de la Suralimentation des Moteurs à Combustion Interne. INPI No FR 1251468;

- F. Castillo, V. Talon, E. Witrant, L. Dugard. Procédé de Regulation d'un Turbocompreseur a Geometrie Variable. INPI No FR 1260352;

- F. Castillo, V. Talon, E. Witrant, L. Dugard. Système et procédé de détermination de la fraction massique de gaz frais dans le collecteur d'admission d'un moteur à combustion interne de véhicule automobile. INPI No FR 1355045

Submitted journals and patents

- F. Castillo, E. Witrant, C. Prieur, V. Talon and L. Dugard. Engine Fresh Air Mass Fraction Control Using Dynamic Boundary Stabilization of Linear Parameter Varying Hyperbolic Systems. *Submitted to IEEE Transactions on Control Systems Technology*;
- F. Castillo, E. Witrant, V. Talon and L. Dugard. Air Fraction Estimation Taking into Account the Mass Transport Time in Diesel Engines. *Submitted to Control Engineering and Practice*;
- F. Castillo, E. Witrant, V. Talon and L. Dugard. Air Fraction and EGR Proportion Control for Dual Loop EGR Diesel Engines. *Submitted to Revista Ingenieria y Universidad*;
- V. Talon, F. Castillo, G. Mauviot. Estimation des émissions de NOx pour moteur Diesel sans utilisation de capteur de pression cylindre (Submitted Patent);

2.5 Nomenclature

Unless it is specified, all variables are in SI Metric Units.

Variables

α_{EGR}	$1/EGR_p - 1$
C	Cross sectional area
dQ	Thermal exchanges
dW	Work
DP	Differential pressure
d_u	Input disturbance
e	Specific internal energy
EGR_p	EGR proportion
F	Air fraction
h	Specific enthalpy
H	Enthalpy
m	Mass
N	Rotation speed in rpm

η	Efficiency
p	Pressure
P	Power
PR	Pressure ratio
q	Heat transfer per unit of mass
Q	Mass flow rate
ρ	Density
sat	Saturation
T	Temperature
U	Internal energy
V	Volume
x	Position

Sub-indexes

air	Atmosphere
$coolant$	Coolant fluid
$comp$	Compressor
cr	Critical
dc	Downstream of the compressor
de	Downstream of the high pressure cooler
dhe	Volume downstream of the heat exchanger
dt	Downstream of the turbine
$egrl$	Low pressure exhaust gas recirculation
$egrh$	High pressure exhaust gas recirculation
em	Exhaust manifold
$EMGC$	per revolution per cylinder
eng	Engine
eo	Engine output
exh	Exhaust
f	Fuel
fap	Post-treatment systems
$filter$	Filter

he	High pressure cooler
im	Intake manifold
it	Iteration
$lphe$	Low pressure EGR cooler
L^2	L^2-norm
L^∞	L^∞-norm
mp	motion planning
ref	Reference
SP	Set-point
$sural$	Between compressor discharge and intake manifold
t	Turbine
th	High pressure throttle
uc	Upstream of the compressor
uhe	Volume upstream of the heat exchanger
v	Volumetric

Constant parameters

α_t	Exhaust manifold pressure estimator convergence parameter
C_v	Heat constant at constant volume
C_p	Heat constant at constant pressure
dt	Simulation time step
f	Friction factor
γ	Heat ratio
H_j	Lower heating value of the Diesel
I	Identity matrix
J_t	Turbine inertia
λ_s	Stoichimetric air to fuel ratio
r	Specific gas constant
τ_t	Turbine lag power time constant

Acronyms

0D	Zero-dimensional
1D	One-dimensional
AFR	Air to fuel ratio
CFD	Computational fluid dynamics
DEM	Discrete event model
DOC	Diesel oxidation catalyst
DPF	Diesel particle filter
EGR	Exhaust gas recirculation
HC	High hydrocarbon
HCCI	Homogeneous charge compression ignition
HP-EGR	High pressure exhaust gas recirculation
IFP	Institut francais du pétrole
LP-EGR	Low pressure exhaust gas recirculation
LPV	Linear parameter varying
LQR	Linear quadratic regulator
LTC	Low temperature combustion
LTI	Linear time invariant
MOC	Method of characteristics
MVM	Mean value model
NL	Non-linear
NR	Newton Raphson
PCCI	Premixed controlled compression ignition
QS	Quasi-steady
RMSD	Root-mean-squared deviation
SMC	Sliding mode controller
UEGO	Universal exhaust gas oxygen
VGT	Variable geometry turbine

Chapter 3

Control-Oriented 0D Engine Air-Path Modeling

The engine modeling is a multidisciplinary subject that involves thermodynamics, fluid mechanics, chemical reactions, mathematical analysis, turbulence, heat transfer, combustion and numerical methods. Different levels of modeling have been used to represent the behavior of the engine. Such models go from basic air standard engine cycles to more complex three-dimensional (3D) models including turbulence, chemical reactions, spray dynamics, mass transport delay, engine geometry, etc. The engine modeling is commonly classified into three categories: zero dimensional (0D) models, one-dimensional (1D) models and multidimensional models (2D and 3D).

In 0D models, the engine is usually represented as a network of control volumes (e.g. the intake and exhaust manifolds), which are interconnected among them using different devices such as valves, turbines, filters, etc. These models have a high computational efficiency and a good degree of predictability with respect to the engine performance. For control applications, the zero-dimensional modeling is the most spread technique for modeling the engine air-path due to its relative simplicity, versatility and low computational demand. Moreover, these models are represented by sets of ordinary differential equations (ODEs), which are suitable for the synthesis of control and observations laws.

1D models give major features of unsteady flow in the engine, allowing to verify the engine air-path configuration and to investigate the dynamics of the engine power output under transient conditions. With 1D models, it is possible to study the fuel economy, the turbocharger operation and the engine efficiency for different engine operating conditions. In the engine control domain, very few works have been done using 1D models because of the complexity of the partial differential equations (PDEs) that describe the unsteady flow, as well as the difficulty to deal with the boundary conditions. However, the control of systems described by PDEs is a very active subject in the control community and many

efforts are being done to develop control laws for this class of systems.

On the other hand, 2D and 3D computational fluid dynamics (CFD) codes are very useful to explore and better understand the physical processes occurring inside the engine. Hence, these modeling techniques are widely used in the design of new engine concepts. The principal idea of 2D and 3D modeling consists in describing locally a large variety of variables such as pressures, temperatures, gases velocities and gas composition. Besides, this kind of physical representation helps to relate the global engine parameters to various engine geometrical data. This deep modeling scheme helps to improve the learning of the engine physical processes, which provides a better description of the physical phenomena and enables to build simpler modeling schemes for a wide range of applications. The computational resources required for the 2D-3D modeling are evidently high, therefore these models are not suitable for model-based engine control design.

Taking into account the characteristics of the three engine modeling strategies described previously, in this thesis we initially choose a 0D modeling strategy for the development of a control-oriented model of the engine air-path. This modeling strategy seems to be the best adapted for control purposes (at least in a short term scenario) due to its versatility and low computational load. To obtain an effective control-oriented model, it is essential to propose a model that is representative of the engine over a wide range of operating conditions. However, a model with greater predictability over a large operating range typically implies a model with greater calculation load. Therefore, it is crucial to establish the adequate trade-off between the calculation load and the model predictability.

For reciprocating engines of passenger cars, at least two main aspects of their operation are modeled by a 0D modeling approach [49]:

- the combustion process itself which is highly transient (cycle with large and rapid temperature and pressure variations);
- the thermodynamics of the engine air-path that governs the combustion process (intake pressure and temperature, gas composition, etc.).

The thermodynamics and kinetic process in the combustion process are very fast and usually not accessible for control purposes. Moreover, the models necessary to describe these phenomena are rather complex and rarely useful for real-time controller design. Therefore, these kinds of phenomena are not considered in the models developed in this thesis. We simplify the fast combustion characteristics by means of static expressions, which implies that the combustion itself evolves in an identical way each time. Clearly, these models will not represent all phenomena occurring in the engine (e.g. random combustion pressures) but for engine control proposes, this combustion representation method has shown to be appropriate.

In this chapter, we focus on the processes involved in the engine air-path, which are usually modeled using two different strategies:

- mean value models (MVM): continuous models that neglect the discrete cycles on the engine and assume that all processes and effects are spread out over the engine cycle;
- discrete event models (DEM): models that explicitly take into account the reciprocating behavior of the engine.

In MVM, the independent variable is the time, while in DEM, the engine crankshaft angle is the independent variable. The proper choice of the model class depends upon the problem to be solved. For example, MVM are well suited for relatively slow processes in the engine periphery such as the engine air-path, while DEM are useful for air/fuel ratio feedforward control and misfire detection algorithms.

In this chapter, a 0D MVM engine air-path model is developed for control and observation purposes. More precisely, this model is intended to serve as a platform for the synthesis and evaluation of control and observation laws. Our aim is to illustrate the development of a 0D engine air-path model for control applications and to provide the required basis and notation for the control strategies that are proposed in the following chapters. A steady-state as well as transient benchmark validation of the model are presented at the end of this chapter in order to show that the developed model is representative of the engine over a wide range of operating conditions. The model presented in this chapter is inspired by the works of [5], [49], [43], [55] and [94] among others, where the 0D engine air-path modeling has been successfully used for control purposes.

Chapter Structure This chapter begins with a description of the considered engine air-path, its main components and its basic philosophy of operation. In Section 3.2, the fundamental equations involved in the modeling of a 0D control volume approach are developed. In Section 3.3, the modeling problem considered in this chapter is presented along with the engine air-path control volume formulation. The dynamics of each section of the air-path are given in details and the static equations that allow interconnecting the control volumes are described. Finally in Section 3.4, a steady-state and a transient validation of the model is performed in order to demonstrate that the considered engine air-path modeling strategy is representative of the actual engine.

3.1 Dual Loop EGR Diesel Engine Air-Path

The engine air-path architecture considered in this work is based on a modern light-duty four-cylinder Diesel 1.6 liter engine with dual-loop exhaust gas recirculation (EGR) and

variable geometry turbine (VGT). Its schematic is depicted in Figure 3.1.

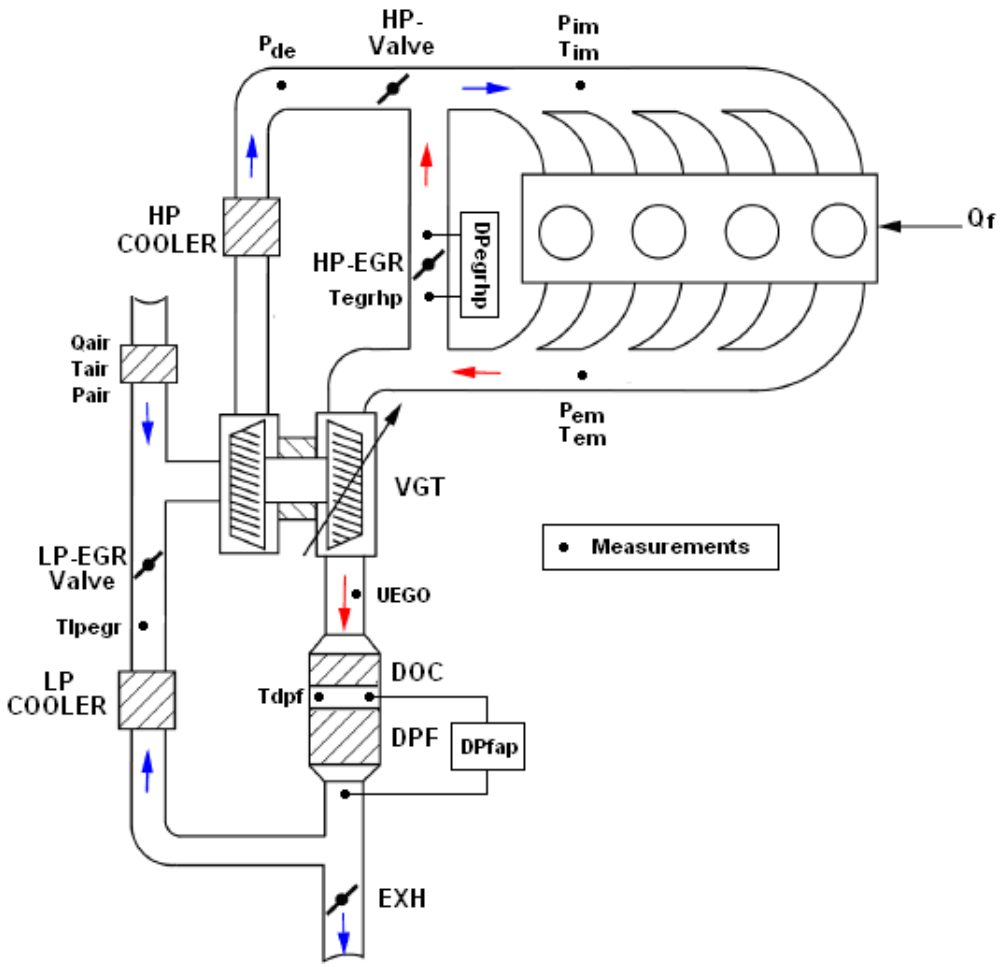

Figure 3.1: Schematic of the dual-loop EGR engine air-path

The engine shown in Figure 3.1 is equipped with a variable geometry turbocharger (VGT), a dual-loop EGR system (high-pressure valve, as well as low-pressure valve) and exhaust-treatment systems such as a Diesel Particle Filter (DPF) and Diesel Oxidation Catalyst (DOC). For Diesel engines, the combustion is usually lean, which means that there is excessive air (in comparison with the stoichiometric amount) in the cylinder mixture. Therefore, the exhaust gas contains unburned air and it could be recirculated back into the intake manifold through the EGR valves. With the high pressure EGR (HP-EGR), the burnt gases from the exhaust manifold are reintroduced into the intake manifold. The HP-EGR is used at the beginning of a cycle in order to obtain combustions with higher temperature, allowing to heat up the DOC (required for its proper operation) as quickly as possible. This configuration reduces the turbine flow and thus its power. However, the HP-EGR has a faster settling time and gives better HC and CO emission reduction in comparison with the low pressure EGR (LP-EGR) [15].

With the LP-EGR, the burnt gases are taken downstream of the exhaust post-treatment systems and reintroduced upstream of the compressor. The LP-EGR is then used instead of the HP-EGR because it is cooler, thus allowing to introduce more mass and EGR into the cylinders. With the LP-EGR, all the exhaust gases pass through the turbine allowing the supercharging system to operate optimally. Nevertheless, with the LP-EGR, the intake manifold air fraction settling time is longer than with the HP-EGR. The dual-loop EGR configuration presented in Figure 3.1 combines the advantages of the HP-EGR and the LP-EGR. With this EGR architecture, the mixing of hot HP-EGR gas and cold LP-EGR gas can be set to reach the optimal temperature regarding the HC-CO emission reduction. Also a prioritization of HP-EGR can be performed when short intake manifold air fraction settling time is required while the LP-EGR can be prioritized when supercharging performance is needed.

One of the challenges with engines operating with alternative combustion modes is to maintain the appropriate conditions in the cylinders. The need for providing fresh air to the engine even under high EGR rates makes necessary the use of advanced turbocharging devices such as variable geometry turbine (VGT) turbochargers. VGT are of particular interest to advanced Diesel powertrains since they are viewed as the key enabler for the application of the EGR system, thus allowing to meet legislated, current and future, emissions standards. This is due to the fact that VGT systems do have the potential to provide accurate control of the pressure difference across the engine, as well as a very quick response during engine transients. In this context, a turbocharged system provides two main benefits: first, it enables to extend the alternative combustion domain at high EGR levels and second it increases the engine power by augmenting the quantity of the air mass in the cylinders at high engine loads.

The high-pressure throttle depicted in Figure 3.1, denoted as HP-valve, allows increasing the HP-EGR rate at light load, reduces the air mass flow rate during the DPF regeneration phases and blocks the air flow when operating the start-stop system. The high pressure cooler (HP-Cooler) increases the gas density which allows obtaining more stable combustions and more mass inside the cylinders. The universal exhaust gas oxygen (UEGO) sensor is installed downstream of the VGT in order to avoid high-pressure at the UEGO sensor. The LP-EGR includes an EGR valve, an EGR cooler and the exhaust valve, denoted as EXH, which is required to create the necessary pressure drop in the LP-EGR system to ensure the EGR flow.

With this, we conclude the basic description of the engine air-path considered in this thesis. In the next sections, we address the modeling issues of the engine air-path by means of a control volume approach.

3.2 Development of 0D Basic Equations

For the development of the basic equations for 0D air-path modeling, consider the classical control volume approach represented in Figure (3.2):

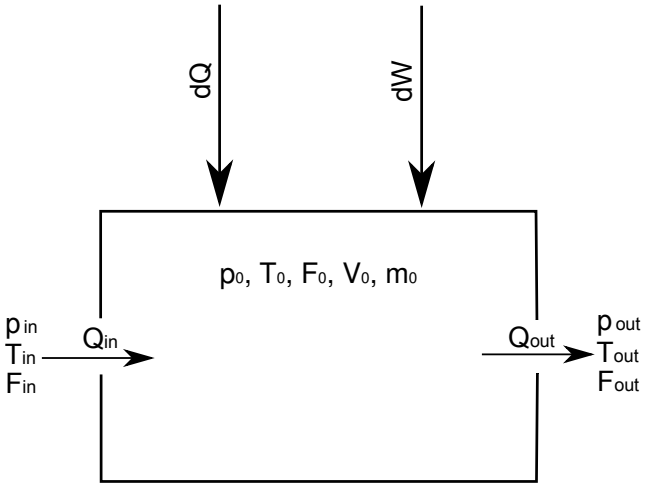

Figure 3.2: Control volume approach

For the sake of clarity, all the variables in this chapter are time dependent unless the contrary is specified. Q_{in} and Q_{out} are the sums of all mass flow rates going in and out of the control volume, respectively, dQ the thermal exchanges, dW the work performed by the gas (e.g. piston inside a combustion chamber), V_0 the volume which is constant, p_0 the pressure, T_0 the temperature and F_0 the fresh air mass fraction (from now on denoted as air fraction). p_{in} and p_{out} are the input and output pressures, T_{in} the input temperature and F_{in} and F_{out} the input and output air fractions, respectively.

To describe the dynamics inside the control volume, let us consider the Joule's second law:

$$U_0 = m_0 C_v T_0 \tag{3.2.1}$$

$$H_0 = m_0 C_p T_0 \tag{3.2.2}$$

where m_0 is the mass, U_0 is the internal energy, H_0 in the enthalpy, C_v is the heat constant at constant volume and C_p is the heat constant at constant pressure. Assuming an ideal behavior of the gas, the mass inside the control volume is given by the ideal gas law as follows:

$$m_0 = \frac{p_0 V_0}{r T_0} \tag{3.2.3}$$

where r is the specific gas constant. The time derivative of the internal energy of the gas inside the control volume is defined by the first law of thermodynamics as:

$$\dot{U}_0 = \sum_{i=1}^{n} h_i Q_i + dQ + dW \tag{3.2.4}$$

where n is the number of interacting enthalpic flows and h_i is the specific enthalpy of the respective enthalpy flow Q_i. For the development of the basic equations for a control volume, we assume that the heat transfers with the outside as well as the frictions are negligible. This implies that $dQ = 0$ and $dW = 0$. Deriving (3.2.1) with respect to time and replacing $\dot{U}_0$ in (3.2.4) gives:

$$\dot{m}_0 C_v T_0 + m_0 C_v \dot{T}_0 = \sum_{in=1}^{n} h_{in} Q_{in} - \sum_{out=1}^{l} h_0 Q_{out} \tag{3.2.5}$$

where n is the number of inputs and l is the number of outputs. The dynamics of the mass inside the volume are given by the following expression:

$$\dot{m}_0 = \sum_{in=1}^{n} Q_{in} - \sum_{out=1}^{l} Q_{out} \tag{3.2.6}$$

Combining (3.2.6) with (3.2.5) and writing the specific enthalpy in terms of the heat capacity at constant pressure and temperature (according to (3.2.2)), allows obtaining the following:

$$\dot{T}_0 = \frac{1}{m_0} \left[\gamma \sum_{in=1}^{n} Q_{in} T_{in} - \gamma \sum_{out=1}^{l} Q_{out} T_0 - \left(\sum_{in=1}^{n} Q_{in} - \sum_{out=1}^{l} Q_{out} \right) T_0 \right] \tag{3.2.7}$$

where γ is the heat ratio. By replacing m_0 with (3.2.3) in (3.2.7), we determine the following dynamics for the temperature inside the control volume:

$$\dot{T}_0 = \frac{r T_0}{p_0 V_0} \left[Q_{in} \sum_{in=1}^{n} (\gamma T_{in} - T_0) + Q_{out} \sum_{out=1}^{l} (T_0 - \gamma T_0) \right] \tag{3.2.8}$$

We take the derivative of the perfect gas law with respect to time in order to define the dynamics of the pressure inside the control volume. This gives the following:

$$\dot{p}_0 = \frac{r m_0}{V_0} \dot{T}_0 + \frac{r T_0}{V_0} \dot{m}_0 \tag{3.2.9}$$

We obtain the following dynamics of the pressure inside the control volume by plugging (3.2.8) into (3.2.9) and using (3.2.3) to represent the mass:

$$\dot{p}_0 = \frac{r\gamma}{V_0} \left[\sum_{in=1}^{n} Q_{in} T_{in} - \sum_{out=1}^{l} Q_{out} T_0 \right] \tag{3.2.10}$$

Let us define the air fraction in the control volume as:

$$F_0 = \frac{m_{air}}{m_0} \tag{3.2.11}$$

where m_{air} is the mass of the fresh air in the control volume. Using the principle of conservation of mass, the dynamics of the air fraction can be written as follows:

$$\dot{F}_0 = \frac{rT_0}{p_0 V_0} \left[\sum_{in=1}^{n} (F_{in} Q_{in}) - F_0 \sum_{out=1}^{l} Q_{out} \right] \tag{3.2.12}$$

where F_{in} is the input air fraction. Equations (3.2.8), (3.2.10) and (3.2.12) constitute the basic dynamic equations required for the 0D air-path modeling considered in this chapter. In the next section, we use these equations to address the 0D modeling of the dual-loop EGR engine air-path presented in Figure 3.1.

3.3 Dual-EGR Engine Air Path Model

Before to start developing the engine air-path model, it is important to define precisely the modeling problem as well as some essential considerations that are required for the appropriate formulation of a control-oriented model. Let us start by defining the system's inputs, which are divided into exogenous inputs and control inputs. We consider as exogenous the following inputs:

- Engine speed;
- Amount of fuel injected;
- Atmospheric temperature and pressure.

The definition of these inputs implies that the modeling of the vehicle dynamics and the fuel injection system is not considered in the control-oriented model described in this chapter. We define the control inputs according to the actuators available in the engine air-path (see Figure 3.1) as follows:

- Position of the exhaust valve (EXH);
- Position of the EGR valves (HP-EGR and LP-EGR);
- Position of the VGT;
- Position of the high pressure throttle (HP-Valve).

The objective of the model considered in this chapter is to obtain from the previously defined inputs, all the pressures, mass flows, temperatures and air fractions at every section of the engine air-path. However, achieving this task is very challenging due to the complexity of the engine air-path and therefore, it is crucial to perform some reductions in order to facilitate the modeling process and reduce the calculation load. Neglecting some dynamics and phenomena inside the system can greatly simplify the engine analysis without compromising significantly the predictability of the control-oriented model. Thus, the following assumptions are considered:

Assumptions 3.3.1.

- there are no temperature losses through the walls;
- there are no friction losses in the tubes;
- C_p and r are equal for the burned and fresh gases;
- the gases are considered as ideal ones;
- the fresh and burned gases mix instantaneously;
- the heat exchangers efficiency is independent of the mass flow;
- the turbocharger dynamics behaves as a first order system;
- the volumes associated with the exhaust gas recirculation are considered small.
- the pressure drop across the LP-EGR cooler is neglected.

The previous assumptions reduce significantly the air-path modeling problem, allowing to obtain a low computational CPU load while keeping a good predictability as it is shown later in the model validation in Section 3.4. For example, it is possible to not take into account the temperature losses through the air-path walls as the thermal exchanges associated with them are small in comparison with the energy coming from the enthalpic flows. With this hypothesis, the thermal exchanges which can be very complex, do not have to be represented in our control-oriented model, resulting in a significant reduction of calculation load. Similar considerations are done for the rest of the Assumptions 3.3.1.

To apply the modeling strategy detailed in Section 3.2, the engine air-path has to be divided into sections or control volumes. Different control volumes approaches can be defined for the engine air system architecture shown in Figure 3.1. However in this thesis, we consider the seven volumes depicted in Figure 3.3, which are enumerated according to the following list:

1. Compressor suction volume

2. Compressor discharge volume
3. Heat exchanger discharge volume
4. Intake manifold
5. Exhaust manifold
6. Turbine discharge volume
7. Exhaust

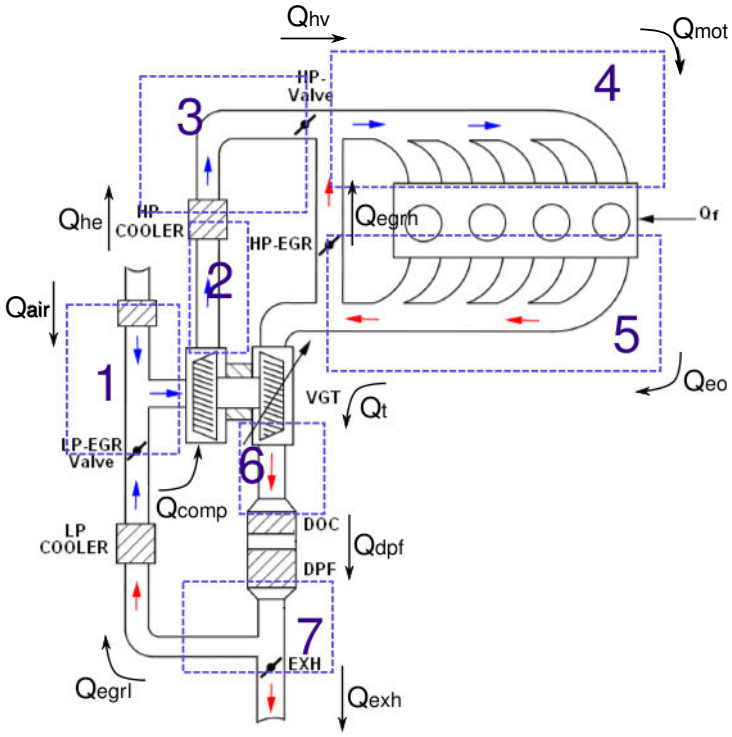

Figure 3.3: Control volume definition

Each of these seven volumes is characterized by a set of static as well as dynamic expressions that describe its own physical behavior and its interaction with the other air-path sections. For sake of illustration purposes, in this chapter we separate the dynamic equations from the static ones. In the next sections (namely Sections 3.3.1 and 3.3.2), we describe the dynamic and static equations of the control-oriented model according to Figure 3.3, respectively. It is important to remark that in this chapter, only a brief description of the air-path model equations is given because it is not our intention to provide a detailed development. The objective of this chapter is to present the required expressions to built the proposed control-oriented model and to show that it is representative of the actual engine air-path so that it can be used later for the synthesis and evaluation of the control laws. For further details on the development of 0D air-path control-oriented models, refer to [49], [60] and [88].

3.3.1 Dynamics of the Engine Air-Path Model

Based on the equations developed in Section 3.2 (namely (3.2.8), (3.2.10) and (3.2.12)), the dynamics of each of the control volumes described in Figure 3.3 are presented. Some of these equations have been already considered for control purposes in the works of [5], [55] and [94], among others.

3.3.1.1 Compressor suction (Volume 1)

At the suction of the compressor, there are three mass flow rates interacting with the control volume: the fresh air, the compressor and the LP-EGR mass flow rates denoted as Q_{air}, Q_{comp} and Q_{egrl}, respectively.

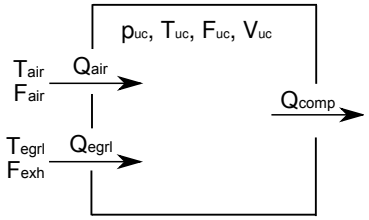

Figure 3.4: Schematic of the control volume 1

The following equations describe the pressure, temperature and air mass fraction dynamics for the compressor suction according to (3.2.8), (3.2.10) and (3.2.12):

$$\dot{p}_{uc} = \frac{r\gamma}{V_{uc}}(Q_{air}T_{air} + Q_{egrl}T_{egrl} - Q_{comp}T_{uc}) \tag{3.3.1}$$

$$\dot{T}_{uc} = \frac{rT_{uc}}{p_{uc}V_{uc}}(Q_{air}(\gamma T_{air} - T_{uc}) + Q_{egrl}(\gamma T_{egrl} - T_{uc}) + Q_{comp}T_{uc}(1-\gamma)) \tag{3.3.2}$$

$$\dot{F}_{uc} = \frac{rT_{uc}}{p_{uc}V_{uc}}(Q_{air} + F_{exh}Q_{egrl} - F_{uc}Q_{comp}) \tag{3.3.3}$$

where p_{uc}, T_{uc} and F_{uc} are the pressure, temperature and air fraction at the compressor suction, respectively. T_{air} is the atmospheric temperature, V_{uc} is the volume associated with the compressor suction, F_{exh} is the air fraction of the exhaust and T_{egrl} is the temperature of the LP-EGR. The equations that provide the mass flow rates are given in Section 3.3.2.

3.3.1.2 Compressor discharge (Volume 2)

At the compressor discharge, there are two mass flow rates to be considered: the compressor mass flow rate and the heat exchanger mass flow rate Q_{he}.

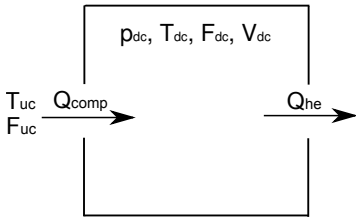

Figure 3.5: Schematic of the control volume 2

The following equations describe the pressure, temperature and air mass fraction dynamics at the compressor discharge:

$$\dot{p}_{dc} = \frac{r\gamma}{V_{dc}}(Q_{comp}T_{comp} - Q_{he}T_{dc}) \tag{3.3.4}$$

$$\dot{T}_{dc} = \frac{rT_{dc}}{p_{dc}V_{dc}}(Q_{comp}(\gamma T_{comp} - T_{dc}) + Q_{he}T_{dc}(1-\gamma)) \tag{3.3.5}$$

$$\dot{F}_{dc} = \frac{rT_{dc}}{p_{dc}V_{dc}}(Q_{comp}F_{uc} - Q_{he}F_{dc}) \tag{3.3.6}$$

where p_{dc}, T_{dc} and F_{dc} are the pressure, temperature and air fraction at the compressor discharge, respectively. T_{comp} is the gas temperature at the discharge of the compressor and V_{dc} is the volume associated with the compressor discharge.

3.3.1.3 Heat exchanger discharge (Volume 3)

There are two mass flow rates associated with the discharge of the heat exchanger: the heat exchanger mass flow rate Q_{he} and the HP-valve mass flow rate Q_{hv}.

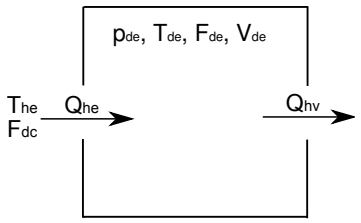

Figure 3.6: Schematic of the control volume 3

The following equations describe the dynamics at the heat exchanger discharge:

$$\dot{p}_{de} = \frac{r\gamma}{V_{de}}(Q_{he}T_{he} - Q_{hv}T_{de}) \tag{3.3.7}$$

$$\dot{T}_{de} = \frac{rT_{dc}}{p_{de}V_{de}}(Q_{he}(\gamma T_{he} - T_{de}) + Q_{hv}T_{de}(1-\gamma)) \tag{3.3.8}$$

$$\dot{F}_{de} = \frac{rT_{de}}{p_{de}V_{de}}(Q_{he}F_{dc} - Q_{hv}F_{de}) \tag{3.3.9}$$

where p_{de}, T_{de} and F_{de} are the pressure, temperature and air fraction at the heat exchanger discharge, respectively. T_{he} the gas temperature at the discharge of the heat exchanger and V_{de} is the volume associated with the heat exchanger discharge.

3.3.1.4 Intake manifold (Volume 4)

Three mass flow rates have to be considered for the intake manifold: the HP-valve mass flow rate Q_{hv}, the HP-EGR mass flow rate Q_{egrh} and the engine intake mass flow rate Q_{eng}.

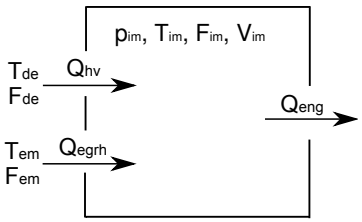

Figure 3.7: Schematic of the control volume 4

The dynamics of the intake manifold are given by:

$$\dot{p}_{im} = \frac{r\gamma}{V_{im}}(Q_{hv}T_{de} + Q_{egrh}T_{em} - Q_{eng}T_{im}) \tag{3.3.10}$$

$$\dot{T}_{im} = \frac{rT_{im}}{p_{im}V_{im}}(Q_{hv}(\gamma T_{de} - T_{im}) + Q_{egrh}(\gamma T_{em} - T_{im}) + Q_{eng}T_{im}(1-\gamma)) \tag{3.3.11}$$

$$\dot{F}_{im} = \frac{rT_{im}}{p_{im}V_{im}}(Q_{hv}F_{de} + Q_{egrh}F_{em} - Q_{eng}F_{im}) \tag{3.3.12}$$

where p_{im}, T_{im} and F_{im} denote the pressure, temperature and air fraction in the intake manifold, respectively. V_{im} is the intake manifold volume and T_{em} is the exhaust manifold temperature.

3.3.1.5 Exhaust manifold (Volume 5)

In the exhaust manifold, three mass flow rates interact with the control volume: the gas flow rate coming out from the cylinders Q_{eo}, the turbine mass flow rate Q_t and the HP-EGR mass flow rate Q_{egrh}.

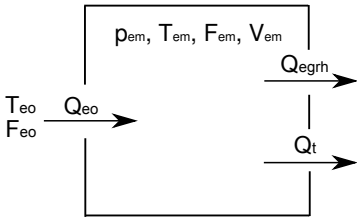

Figure 3.8: Schematic of the control volume 5

Consider the following dynamics for the exhaust manifold:

$$\dot{p}_{em} = \frac{r\gamma}{V_{em}}(Q_{eo}T_{eo} - Q_{egrh}T_{em} - Q_tT_{em}) \tag{3.3.13}$$

$$\dot{T}_{em} = \frac{rT_{em}}{p_{em}V_{em}}(Q_{eo}(\gamma T_{eo} - T_{em}) + Q_{egrh}T_{em}(1-\gamma) + Q_tT_{em}(1-\gamma)) \tag{3.3.14}$$

$$\dot{F}_{em} = \frac{rT_{em}}{p_{em}V_{em}}(Q_{eo}F_{eo} - Q_tF_{em} - Q_{egrh}F_{em}) \tag{3.3.15}$$

where T_{eo} and F_{eo} are the gas temperature and air fraction coming out of the cylinders and V_{em} is the volume of the exhaust manifold.

3.3.1.6 Turbine discharge (Volume 6)

Two flows interact with the turbine discharge control volume: the flow through the after-treatment system Q_{dpf} and the turbine mass flow rate Q_t.

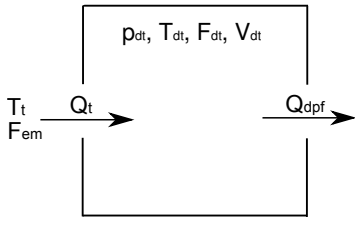

Figure 3.9: Schematic of the control volume 6

The following equations describe the dynamics for this air-path section:

$$\dot{p}_{dt} = \frac{r\gamma}{V_{dt}}(Q_tT_t - Q_{dpf}T_{dt}) \tag{3.3.16}$$

$$\dot{T}_{dt} = \frac{rT_{dt}}{p_{dt}V_{dt}}(Q_t(\gamma T_t - T_{dt}) + Q_{dpf}T_{dt}(1-\gamma)) \tag{3.3.17}$$

$$\dot{F}_{dt} = \frac{rT_{dt}}{p_{dt}V_{dt}}(Q_t F_{em} - F_{dt}Q_{dpf}) \tag{3.3.18}$$

where p_{dt}, T_{dt} and F_{dt} are the pressure, temperature and air fraction downstream of the turbine, respectively. T_t the gas temperature coming from the turbine and V_{dt} is the volume associated with the discharge of the turbine.

3.3.1.7 Exhaust (Volume 7)

There are three mass flow rates interacting with the exhaust volume: the mass flow rate through the exhaust valve Q_{exh}, the LP-EGR mass flow rate Q_{egrl} and the mass flow rate of the after-treatment system Q_{dpf}.

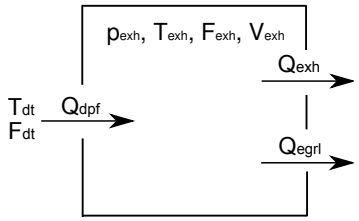

Figure 3.10: Schematic of the control volume 7

The dynamics of the exhaust volume are given by the following equations:

$$\dot{p}_{exh} = \frac{r\gamma}{V_{exh}}(Q_{dpf}T_{dt} - Q_{egrl}T_{dt} - Q_{exh}T_{dt}) \tag{3.3.19}$$

$$\dot{T}_{exh} = \frac{rT_{exh}}{p_{exh}V_{exh}}(Q_{dpf}(\gamma T_{dt} - T_{exh}) + Q_{egrl}T_{exh}(1-\gamma) + Q_{exh}T_{exh}(1-\gamma)) \tag{3.3.20}$$

$$\dot{F}_{exh} = \frac{rT_{exh}}{p_{exh}V_{exh}}(Q_{dpf}F_{dt} - Q_{egrl}F_{exh} - Q_{exh}F_{exh}) \tag{3.3.21}$$

where p_{exh}, T_{exh} and F_{exh} are the pressure, temperature and air fraction at the exhaust, respectively and V_{exh} is the volumes of the exhaust.

3.3.1.8 Turbocharger Power

The dynamics of the VGT turbocharger are directly linked to the exhaust gas. A part of the energy of the exhaust gas is transferred from the turbine to the compressor by the turbocharger shaft. The rotational speed N_t of this system depends on the power balance between the turbine and compressor powers as [48]:

$$\frac{d}{dt}\left(\frac{1}{2}J_t N_t^2\right) = P_t - P_{comp} \tag{3.3.22}$$

where J_t is the turbocharger shaft inertia, P_t is the turbine power and P_{comp} is the compressor power. A simplification of (3.3.22) can be performed by modeling the compressor power as a first-order lag power transfer with time constant τ_t. This reduction results convenient for control purposes as discussed for instance in [55] and [94], among other references. After this simplification, the following power dynamics for the compressor are obtained:

$$\dot{P}_{comp} = \frac{1}{\tau_t}(P_t - P_{comp}) \tag{3.3.23}$$

The time constant τ_t is a value to be identified from the engine benchmark measurements in transient conditions. The dynamics of turbine speed N_t are replaced by a compressor data-map inversion which is detailed in Section 3.3.2.4.

3.3.2 Statics of the Engine Air-Path Model

As previously mentioned, the network of control volumes presented in Figure 3.3 is made up of a large variety of interconnected models that represent the behavior of the engine air-path. In this section, we present how the model interconnections are made by representing the flow through valves, filters, heat-exchanger, after-treatment systems, turbines and compressors as well as the engine gas outflow properties and the engine intake mass flow rate.

3.3.2.1 Saint-Venant Based Equations

The Saint-Venant equation is one of the most commonly used ways to model the gas mass flow rate through an orifice such as an orifice plate or a valve. Nonetheless, this equation is often also used to model the flow through many other flow restricting devices (e.g. filters and after-treatment systems). To illustrate how this formulation is applied in the engine air-path modeling, let us consider the modeling of the mass flow rate through the HP-Valve.

Two expressions are formulated, depending on whether the gas speed at the restriction throat is sonic or not [88]. For subsonic flow:

$$Q_{hv} = \frac{A_{hv}(x_{hv})p_{de}}{\sqrt{rT_{de}}}\sqrt{\frac{\gamma}{\gamma-1}\left(\left(\frac{p_{im}}{p_{de}}\right)^{\frac{2}{\gamma}} - \left(\frac{p_{im}}{p_{de}}\right)^{\frac{\gamma+1}{\gamma}}\right)} \tag{3.3.24}$$

and for sonic flow:

$$Q_{hv} = \frac{A_{hv}(x_{hv})p_{de}}{\sqrt{rT_{de}}}\sqrt{\gamma}\left(\frac{2}{\gamma+1}\right)^{\frac{\gamma+1}{2(\gamma-1)}} \tag{3.3.25}$$

where Q_{hv} is the mass flow rate through the HP-Valve valve and A_{hv} is the valve's effective area that is typically a function of the valve position x_{hv}. This function is usually found empirically. In this thesis, the functions that relate the area to the valve position have been provided by the direction of engine control and calibration of Renault. The effective area is controlled by the valve's position, which allows imposing a desired mass flow rate through the valve. In this sense, one can set the HP-Valve mass flow rate from the knowledge of p_{de}, T_{de}, p_{im} and the relationship between the effective area and the valve position.

The mass flow rates associated with the HP-EGR, LP-EGR and EHX valves can also be modeled by using the same formulation as in (3.3.24) and (3.3.25). To model the flow through the intake filter, the same approach can also be applied, with the difference that in this case, the effective area is constant. On the other hand, the modeling of the flow through the after-treatment system is a more complex issue as its flow parameters change with respect to time, implying that the after-treatment effective area, denoted as A_{dpf}, is time dependent. However, for a control oriented-model, the Saint-Venant approach can give suitable results using a time average of the effective area. Moreover, since the differential pressure across the particle filter DP_{dpf} is measured (refer to Figure 3.1), modeling the DPF flow variations is not crucial for the air-path control design.

3.3.2.2 Engine Intake Mass Flow Rate

We model the engine intake mass flow rate by considering the time average of the mass flow rate sucked-in by the cylinders, which is consistent with the MVM formulation. This quantity depends on the intake manifold pressure and temperature, the engine speed and the volumetric efficiency η_v and its behavior is described by the well-known speed density equation [94]:

$$Q_{eng} = \frac{\eta_v p_{im} N_{eng} V_{eng}}{120 T_{im} r} \tag{3.3.26}$$

where V_{eng} is the engine volume. The volumetric efficiency η_v depends on N_{eng}, p_{im} and T_{im}, which is very challenging to describe using a physical-based formulation. Therefore, empirical strategies are often used to address this issue. Among these strategies we can find the use of polynomials, data-maps and neural networks, which are derived from measurements taken at steady-state over a large range of engine operating conditions [68]. In [86], it has been shown that the quasi-steady assumption on the volumetric efficiency (since it is found using measurements in steady-state) is also valid under transient conditions. In this work, the empirical function for η_v has been identified using steady-state engine benchmark measurements along with a polynomial approach of order 3 that minimizes a linear least-squares criterion by using the Moore-Penrose pseudo-inverse.

3.3.2.3 Parametric Combustion Model

Since the interest of this study is to provide a suitable tool for the synthesis and evaluation of engine air-path control strategies, the engine combustion model is developed using a parametric combustion approach, which intends to describe the rate of heat release of the fuel using several input parameters. Indeed, this strategy has the advantage of consuming very few computational resources and having a low complexity when compared with other 0D combustion models such has high frequency DEM 0D combustion models [12] [82]. Therefore, parametric combustion models are widely spread in applications related to control, indirect identification and optimization processes.

Our parametric combustion model provides three of the essential quantities for the engine air-path modeling: the engine output gas temperature T_{eo}, air fraction F_{eo} and mass flow rate Q_{eo}. Let us consider the following equation for the engine output temperature (derived from the energy conservation for the engine block) [5]:

$$T_{eo} = T_{im} + \eta_{eng} \frac{Q_{EMGC} H_j}{\left(Q_{EMGC} + \frac{30 Q_{eng}}{N_{eng}}\right) c_p} \tag{3.3.27}$$

where Q_{EMGC} is the fuel mass injected per revolution per cylinder, H_i is the lower heating value of the Diesel and η_{eng} is the fraction of the heat release from the combustion process that remains in the exhaust gas. In other words, $\eta_{eng} = (1 - \eta_e - \eta_{wall})$ where η_e is the engine efficiency and η_{wall} is the fraction of heat transferred to the cylinder walls. As in the case of the volumetric efficiency η_v, determining a physical formulation for η_{eng} is a very challenging issue; hence, empirical representations of this efficiency are traditionally developed for MVM models. For the control-oriented model developed in this chapter, we consider η_{eng} as a function of p_{im}, N_{eng} and T_{im} and the empirical function is determined using benchmark measurements over a large range of steady-state engine operating conditions along with a polynomial approach of order 4 that minimizes a linear least-squares criterion.

The air fraction coming out from the cylinders F_{eo} can be estimated based on the fueling rate Q_f and the stoichiometric air to fuel ratio (AFR) λ_s as [96]:

$$F_{eo} = \frac{Q_{eng} F_{im} - Q_f \lambda_s}{Q_{eng} + Q_f} \tag{3.3.28}$$

The fueling rate Q_f can be represented in terms of Q_{EMGC} as follows:

$$Q_f = \frac{Q_{EMGC} N_{eng}}{30} \tag{3.3.29}$$

and the mass flow rate coming out from the cylinders Q_{eo} is given by:

$$Q_{eo} = Q_f + Q_{eng} \tag{3.3.30}$$

3.3.2.4 Compressor

In this part, three required variables for the engine air-path model are found: the compressor mass flow rate Q_{comp}, the turbine speed N_t and the compressor discharge temperature T_{dc}. Real-time compressor models are usually based upon performance data-maps since these models are easy to upload into the vehicle CPU, have low calculation load and are suitable for control applications. Indeed, data relative to the compressor are typically read from tables that are the results of extrapolation procedures from the data provided by the suppliers [50].

Let us consider for our model, the following compressor data-maps:

$$PR_{comp} = datamap_{PRcomp}\left(Q_{compcorr}, N_{tcorr}\right) \tag{3.3.31}$$

$$\eta_{comp} = datamap_{etacomp}\left(Q_{compcorr}, N_{tcorr}\right) \tag{3.3.32}$$

where

$$PR_{comp} = \frac{p_{dc}}{p_{uc}}, \quad Q_{compcorr} = Q_{comp}\frac{\sqrt{T_{uc}}p_{ref}}{\sqrt{T_{ref}}p_{uc}}, \quad N_{tcorr} = \frac{\sqrt{T_{ref}}}{\sqrt{T_{uc}}} \tag{3.3.33}$$

PR_{comp} is the compressor pressure ratio, η_{comp} is the compressor efficiency and p_{ref} and T_{ref} are some pressure and temperature references used for the correction of the compressor mass flow rate and the turbocharger speed. $Q_{compcorr}$ and N_{tcorr} are the corrected compressor mass flow rate and the corrected turbocharger speed, respectively. For further understanding of the significance of these corrections refer to [99].

The data-map (3.3.31) is invertible, implying that the turbocharger speed can be written as a function of the compressor pressure ratio and the mass flow rate as follows [104]:

$$N_t = datamap_{N_t}\left(Q_{comp}\frac{\sqrt{T_{uc}}p_{ref}}{\sqrt{T_{ref}}p_{uc}}, PR_{comp}\right)\frac{\sqrt{T_{uc}}}{\sqrt{T_{ref}}} \tag{3.3.34}$$

To find the compressor mass flow rate, let us consider the compressor power given by:

$$P_{comp} = Q_{comp}c_pT_{uc}\frac{1}{\eta_{comp}}\left[\left(\frac{p_{dc}}{p_{uc}}\right)^k - 1\right], \quad k = \frac{\gamma - 1}{\gamma} \tag{3.3.35}$$

As the value of the compressor power is available from (3.3.23), then the compressor mass flow rate can be found using:

$$Q_{comp} = \frac{P_{comp}}{c_pT_{uc}\frac{1}{\eta_{comp}}\left[\left(\frac{p_{dc}}{p_{uc}}\right)^k - 1\right]} \tag{3.3.36}$$

However, the solution of (3.3.36) cannot be solved analytically because the compressor pressure ratio PR_{comp} and the compressor efficiency η_{comp} depend on the compressor mass flow rate creating an algebraic loop. Therefore, numerical schemes have to be used every simulation time step to solve Q_{comp}.

The compressor discharge temperature is easily found by solving the following [5]:

$$T_{dc} = T_{uc} + \frac{P_{comp}}{c_p Q_{comp}} \tag{3.3.37}$$

3.3.2.5 Turbine

As in the compressor, the turbine model provides three essential variables for the 0D model: the turbine mass flow rate, power and discharge temperature. The turbine model is also represented by data-maps extrapolated from the data provided by the turbocharger supplier [47]. For a VGT, the mass flow rate and its efficiency can be represented as follows:

$$Q_{tcorr} = datamap_{Qt}\left(x_{vgt}, N_{tcorr}, \frac{p_{em}}{p_{dt}}\right) \tag{3.3.38}$$

$$\eta_t = datamap_{etat}\left(x_{vgt}, N_{tcorr}, \frac{p_{em}}{p_{dt}}\right) \tag{3.3.39}$$

where the corrected turbine speed is defined as:

$$N_{tcorr} = \frac{\sqrt{T_{ref}}}{\sqrt{T_{em}}} \tag{3.3.40}$$

and the turbine mass flow rate Q_t is obtained from:

$$Q_t = Q_{tcorr}\frac{\sqrt{T_{ref}}p_{em}}{\sqrt{T_{em}}p_{ref}} \tag{3.3.41}$$

x_{vgt} is the VGT position and T_{ref} and p_{ref} are some references used for the correction of the turbine mass flow rate and the turbine speed. These references are not necessarily the same for the compressor and the turbine. From (3.3.38), the turbine mass flow rate and efficiency can be directly calculated using the VGT position, the turbine speed given by the compressor model (3.3.34) and the turbine pressure ratio. The turbine power can be obtained using the following equation [104]:

$$P_t = Q_t c_p T_{em} \eta_t \left[1 - \left(\frac{p_{dt}}{p_{em}}\right)^k\right] \tag{3.3.42}$$

To calculate the turbine discharge temperature, the following expression is used [5]:

$$T_{dt} = T_{em} - \frac{P_t}{c_p Q_t} \tag{3.3.43}$$

3.3.2.6 Heat Exchangers (HP-Cooler and LP-EGR Cooler)

The heat exchanger models provide the temperatures downstream of the heat exchangers as well as the mass flow rate passing through them. To model the gas temperature decrease obtained from the heat exchangers HP-Cooler and LP-EGR Cooler, a constant heat exchanger effectiveness is considered along with the following linear approximation [94]:

$$T_{he} = \eta_{he} T_{coolant} + (1 - \eta_{he}) T_{dc} \tag{3.3.44}$$

$$T_{egrl} = \eta_{lphe} T_{coolant} + (1 - \eta_{lphe}) T_{dt} \tag{3.3.45}$$

where $T_{coolant}$ is the engine coolant temperature and η_{he} and η_{lphe} are the HP-Cooler and LP-EGR Cooler efficiencies, respectively. To model the pressure drop across the HP-Cooler, an empirical function is used, allowing to represent this relation in terms of the HP-cooler mass flow rate as follows:

$$\Delta p_{he} = f_{\Delta p}(Q_{he}) \tag{3.3.46}$$

where $\Delta p_{he} = p_{dc} - p_{de}$. The function $f_{\Delta p}$ is found using polynomial approximations over a representative amount of steady-state engine operating conditions. Since $f_{\Delta p}$ is an invertible function, then the HP-Cooler mass flow rate Q_{he} is found from the differential pressure across the heat exchanger.

With this, we conclude the fundamental dynamic and static equations (Section (3.3.1) and Section (3.3.2), respectively) for our control-oriented engine air-path model. In the next section, we validate the proposed model with engine benchmark measurements in steady-state as well as in transient conditions.

3.4 Model Benchmark Validation

In this section we propose a benchmark model validation to show that the air-path model developed in the previous section is representative of the actual engine. Two validations are performed: one under engine steady-state conditions and a second one in engine transient conditions. Each validation allows verifying different characteristics of the air-path model performance. The steady-state validation permits to corroborate whether the statics of the engine air-path are well posed and whether the identified parameters, such as η_v and η_{eng} have been accurately described over a wide range of engine operating conditions. The validation in transient conditions allows verifying whether the dynamics for the engine air-path formulated in Section (3.3.1) are representative.

3.4.1 Model and Simulation Parameters

The parameters considered for the engine air-path model correspond to a 1.6 liter Diesel engine with dual-loop EGR and VGT according to the architecture shown in Figure 3.1. The parameters of the engine model are given in Table 3.1.

Variable	Value	Variable	Value
p_{air}	$1 \times 10^5\ Pa$	V_{uc}	$0.0054\ m^3$
T_{air}	$300\ K$	V_{dc}	$0.0049\ m^3$
r	$247\ Jkg^{-1}K^{-1}$	V_{de}	$0.0038\ m^3$
C_p	$1004\ Jkg^{-1}K^{-1}$	V_{im}	$0.002\ m^3$
C_v	$717\ Jkg^{-1}K^{-1}$	V_{em}	$0.001\ m^3$
λ_s	14.7	V_{dt}	$0.002\ m^3$
H_j	$43.5 \times 10^6\ Jkg^{-1}$	V_{exh}	$0.003\ m^3$
$T_{coolant}$	$300\ K$	V_{eng}	$0.0016m^3$
τ_t	$0.2\ s$	dt	$0.005\ s$
A_{dpf}	$0.0013\ m^2$	A_{filter}	$0.0013\ m^2$
γ	1.4	η_{he}	0.8
η_{lphe}	0.8		

Table 3.1: Engine model parameters

The volumes of the air-path correspond to the geometry of the engine, the constant τ_t in Table 3.1 has been identified using a gradient based optimization algorithm that minimizes the root-mean-square deviation of p_{im} with respect to its benchmark measurement and dt is the simulation time step. The rest of the parameters is set according to the experimental conditions of the benchmark and the data provided by the direction of engine control and calibration of Renault. The control-oriented model described in this section has been implemented in Matlab-Simulink ® and simulated with the fixed step solver *ode*2. A computation performance of $0.17\ s$ of calculation time for every second of simulation has been obtained with a Intel Xeon processor W3690 running at $3.47GHz$, which is suitable for control and observer design and evaluation purposes.

3.4.2 Steady State Validation

The steady-state validation is performed using a wide range of the engine operating conditions at steady-state (147 different points). The validation has been done using the measurements of the intake manifold pressure p_{im}, the temperature after the turbine T_{dt}, the percentage of EGR at the intake manifold $\%EGR$, the exhaust manifold temperature T_{em}, the pressure after turbine p_{dt} and the fresh air mass flow Q_{air}. Figure

3.11 depicts a comparison of the 147 benchmark engine operating points with respect the control-oriented model.

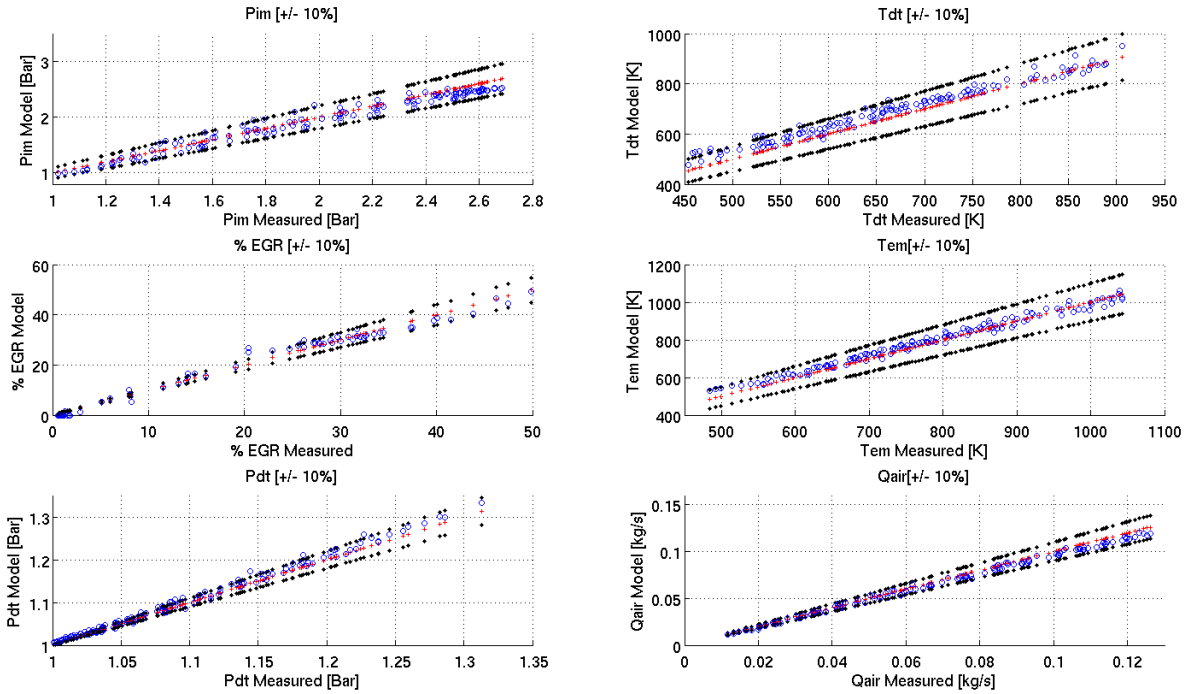

Figure 3.11: Steady state validation with 147 operating points

As shown in Figure 3.11, the model shows a good agreement with respect to the measurements taken on the engine. An accuracy better than 10% has been obtained for most of the 147 operating points over the six measurements considered. The dispersion obtained is intrinsic to the modeling process and it can come from many different sources such an unmodeled phenomena, inaccuracies in the parametric identifications and measurement noise. Table 3.2 presents the root-mean-square deviation (RMSD) of the model with respect to the 147 engine operating conditions.

Variable	RMSD	Variable	RMSD
p_{im}	4.1 %	T_{dt}	4.4 %
$\%EGR$	2.5 %	T_{em}	2.5 %
p_{dt}	0.62 %	Q_{air}	4.2%

Table 3.2: Model root-mean-square deviation percentage error in steady-state for 147 engine operating points

The results of Table 3.2 show that the developed 0D model has an overall accuracy better than 5%, which allows us to consider it as representative of the engine in steady-state conditions.

3.4.3 Transient Validation

The validation under transient conditions is done using three different engine cycles: Cycle 1 is a cycle with HP-EGR and LP-EGR and not much supercharging, Cycle 2 is a well supercharged cycle with LP-EGR and Cycle 3 is the new motor vehicle emissions group (NMVEG) engine cycle. Figures 3.12, 3.13 and 3.14 present the results obtained for the transient validation using as a reference, the measurements of p_{im}, p_{em} and Q_{air}.

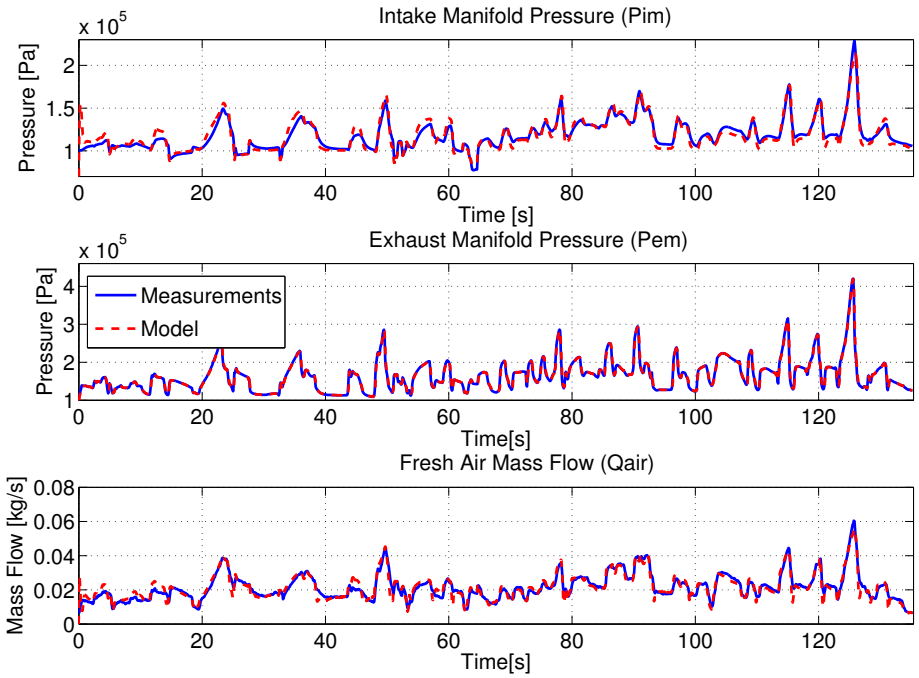

Figure 3.12: Validation in transient with Cycle 1

As depicted in Figures 3.12, 3.13 and 3.14, the model shows a good agreement with the benchmark engine measurements. Some parts of the cycles are deviated from the reference, however, we can see that the overall dynamics are well represented by the model. Table 3.3 shows the RMSD of each cycle with respect the benchmark measurements.

Variable/Cycle	Cycle 1	Cycle 2	NMVEG Cycle
p_{im}	3.7 %	4.6%	3.9%
p_{em}	1.8 %	1.2%	1.7 %
Q_{air}	8.6 %	6.0%	4.6%

Table 3.3: Model root-mean-square deviation percentage error in transient of three different engine cycles

As illustrated in Table 3.3, the accuracy obtained over transient conditions is better

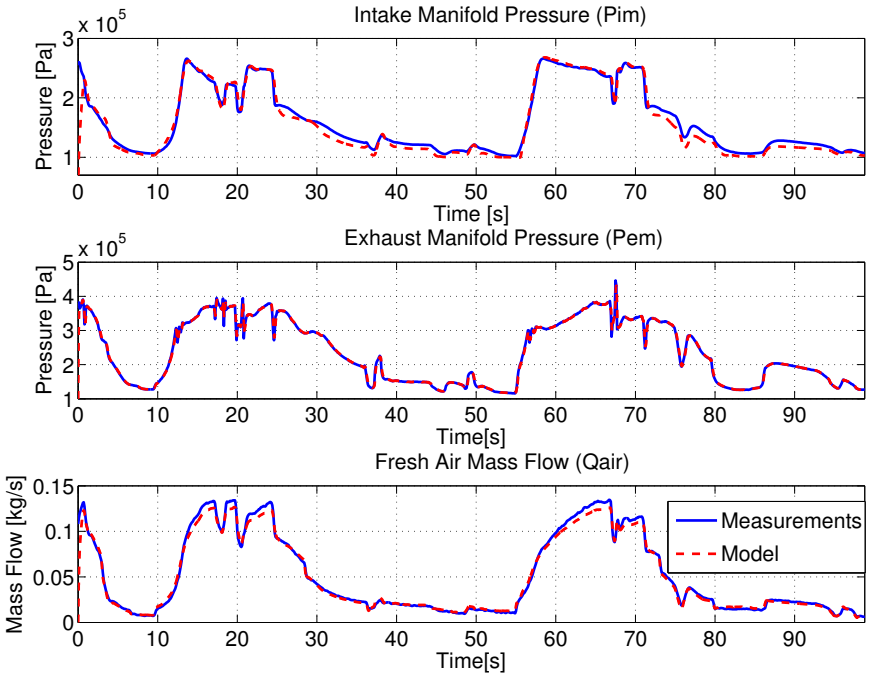

Figure 3.13: Validation in transient with Cycle 2

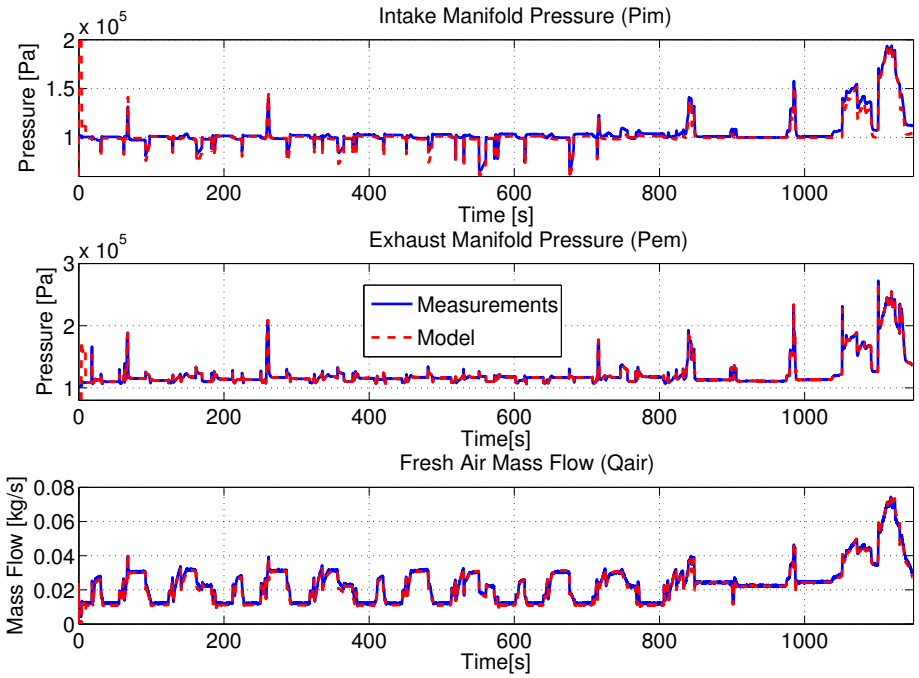

Figure 3.14: Validation in transient with Cycle 3

than 9%. We can see that the least well represented variable of the three considered in this validation is the fresh air mass flow rate Q_{air}. This could be due to the unmodeled phenomena of the compressor and the volumetric efficiency. Nonetheless, the results

obtained are considered good enough for control purposes.

The results of Sections 3.4.2 and 3.4.3 confirm that the Assumptions 3.3.1 are appropriate for a control-oriented air-path model as a good predictability is obtained while reducing significantly the CPU calculation load. The obtained model is accurate enough for the evaluation and synthesis of control laws and therefore it will be used for the developments presented in the next chapter.

3.5 Chapter Summary

In this chapter, a 0D model for control purposes has been developed and validated with engine benchmark measurements. First, the engine air-path considered in this work is presented along with a brief explanation of each of its main components. Then, the basic equations for the control volume modeling strategy are derived. Based on this approach, an air-path modeling formulation is developed on the basis of some important assumptions that simplify the modeling problem. The dynamics of each of the considered control volumes are defined and a first order lag power transfer is established for the turbocharger.

The interconnection between the control volumes is formulated using static relationships. The intake manifold mass flow rate is modeled using the speed density equation. The valves, filters and after-treatment system are represented by the traditionally used Saint-Venant equations. A parametric combustion model is considered to model the engine output variables because of its low calculation load and its simplicity for control purposes. The compressor and turbine are modeled using extrapolated data-maps which are suitable for control applications as they can be easily uploaded into vehicle CPU. The heat exchangers are approximated by a linear heat exchange model and their pressure drop is modeled by means of an empirical approach.

A steady-state as well as a transient validation of the model have been performed using benchmark measurements on the corresponding engine. The results obtained have shown that the developed control-oriented air-path model is representative of the engine air-path, which allows considering the model as a platform to develop and evaluate control and observation laws.

Chapter 4

0D Model-Based Air-Path Control

Regulations of Diesel engine emissions have become stricter, and satisfying simultaneously the emissions legislations and the desired engine drivability objectives is a particularly challenging issue. Although significant improvements were made over the past years, there are still many technical issues that need to be addressed in order to meet the future regulation laws on emissions. The introduction of sophisticated alternative combustion modes such as homogeneous charge compression ignition (HCCI), low temperature combustion (LTC) and premixed controlled compression ignition (PCCI) offers a great potential to reduce the emission level of engines [3] [4] [83]. However, these new modes require specific fueling strategies and in-cylinder conditions, thus creating the need for more complex, reliable and precise control systems and technologies.

The engine air-path has become a crucial part in the development of modern engines. The control of the air-path has a direct impact on the engine performance as well as on its pollutant emission level. Indeed, air system strategies allow controlling the species that are introduced in the cylinder, which is a cost-effective way to reduce pollutant emissions. As a consequence, the automotive air systems have become increasingly complex in order to achieve pollutant reduction strategies and to allow fuel consumption reductions.

Dual-loop exhaust gas recirculation (EGR) with both high (HP) and low-pressure (LP) recirculation is one of the new strategies that can provide the appropriate conditions for multiple combustion modes [53]. Indeed, the total in-cylinder EGR amount as well as the ratio between the high-pressure EGR (HP-EGR) and the low-pressure EGR (LP-EGR) allow controlling efficiently the in-cylinder combustion and the engine-out emissions. The air fraction regulation in the intake manifold is an effective way to control the in-cylinder EGR conditions [5] [35]. Moreover, for engines with dual EGR systems, the air fraction upstream of the compressor provides the LP-EGR rate while the air fraction in the intake manifold provides the total EGR rate. Therefore, if the air fractions in each section are well regulated, then the HP and LP-EGR can also be efficiently controlled. However,

ensuring the adequate in-cylinder conditions is still a very difficult task, as the introduction of the EGR implies to solve many control challenges due to the lack of EGR flow rates and air fraction measurements.

The need for providing fresh air to the engine even under high EGR rates makes necessary the use of advanced turbo charging devices, such as a variable geometry turbine (VGT) turbochargers. These devices allow the engine to operate with alternative combustion modes as the VGT systems provide accurate control of the pressure difference across the engine, as well as very quick response during engine transients. Nevertheless the positioning of the VGT is a very complex problem in turbocharged engines, due to the system nonlinearities, the lack of reliable measurements, the strong dependency on the engine operating conditions and the actuator physical constraints.

There is a constant need for improving the engine air-path control strategies in order to propose more robust, optimal and easy to calibrate control structures. With the aim to improve the performance of the air-path control of dual-loop EGR engines with VGT, we propose in this chapter an industry-oriented air-path control architecture that enables to regulate efficiently the in-cylinder conditions for implementing alternative combustion modes. More precisely, we address the problem of controlling the pressure, fresh air mass fraction and EGR proportion in the engine intake manifold. The proposed air-path control approach is designed according to the following industrial specifications:

Specifications 4.0.1.

- *low time consuming and simple control calibration procedures that can be performed by a technician with no advanced knowledge on control theory;*
- *solutions relatively simple to industrialize;*
- *use a similar air-path control architecture as the one currently used in Renault;*
- *reduction of the number of sensors involved in the engine air-path control.*

Chapter Structure This chapter is introduced with a review of some of the most representative strategies to control the Diesel engine air-path. In Section 4.2, a LP-EGR mass flow rate estimation method and a robust air fraction observer for a Diesel engine with a dual-loop EGR system are developed. Both observers are designed to simultaneously operate in closed-loop. A sliding mode observer is designed to estimate the LP-EGR mass flow rate using the standard sensors available in commercial Diesel engines. Then, a linear parameter varying (LPV) observer is designed to estimate the air fraction in the intake manifold. In Section 4.3, a linear quadratic regulator (LQR) for LPV systems is proposed to control the air fraction in the intake manifold of dual-loop EGR Diesel engines. This control strategy allows satisfying a desired EGR proportion (between LP-EGR and

HP-EGR) while minimizing a quadratic performance index. The existence of the optimal state feedback control is guaranteed inside a convex set of parameters by means of a polytopic approach.

In Section 4.4, we present an exhaust manifold pressure estimation method for a Diesel engine equipped with a variable geometry turbine (VGT) turbocharger. Extrapolated VGT data-maps are used directly for the estimation of the exhaust pressure using a non-iterative method suitable for real-time applications. This approach can give more accurate estimations than traditional methods as it takes into account the turbine speed effect on the turbine mass flow rate. Finally, in Section 4.5, we develop a novel VGT positioning algorithm to control the boost pressure in Diesel engines without measuring the exhaust manifold pressure. A model-based open-loop control is used to generate a turbine power set-point from a boost pressure reference. This control is completed by a closed-loop PI regulator that allows adjusting the turbine power set-point according to the boost pressure error. 90% of the control effort is done by the open-loop control while the remaining is performed by the PI. From the generated turbine power set-point and the engine operating conditions, we propose a method that provides a unique VGT position. This position allows approaching, as much as possible, the turbine power target while respecting the turbocharger physical constraints.

Publications and Patents

The main contributions presented in this chapter are the principal topic of the following publications:

- F. Castillo, E. Witrant, V. Talon and L. Dugard. Air Fraction Estimation Taking into Account the Mass Transport Time in Diesel Engines. *Submitted to Control Engineering and Practice*;
- F. Castillo, E. Witrant, V. Talon and L. Dugard. Air Fraction and EGR Proportion Control for Dual Loop EGR Diesel Engines. *Submitted to Revista Ingenieria y Universidad*;
- F. Castillo, E. Witrant, V. Talon, L. Dugard. Simultaneous Air Fraction and Low-Pressure EGR Mass Flow Rate Estimation for Diesel Engines . 5th IFAC Symposium on System Structure and Control. Grenoble, France. 2013;
- F. Castillo, E. Witrant, V. Talon, L. Dugard. Exhaust Manifold Pressure Estimation Diesel Equipped with a VGT Turbocharger , SAE Technical Paper 2013-01-1752, doi:10.4271/2013-01-1752, 2013.

and the patents:

- F. Castillo, V. Talon, E. Witrant. Procédé d'Acquisition de la Composition des Gaz d'Admission dans un Répartieur d'Air d'un Moteur a Combustion Interne. INPI No FR 2973441;

- F. Castillo, V. Talon, E. Witrant. Estimation de la Pression Avant Turbine en Vue d'un Contrôle de la Suralimentation des Moteurs à Combustion Interne. INPI No FR 1251468;

- F. Castillo, E. Witrant, V. Talon, L. Dugard. Procédé de Régulation d'un Turbo-compresseur à Géométrie Variable. INPI No FR 1260352;

- F. Castillo, V. Talon, E. Witrant, L. Dugard. Système et procédé de détermination de la fraction massique de gaz frais dans le collecteur d'admission d'un moteur à combustion interne de véhicule automobile. INPI No FR 1355045;

- V. Talon, F. Castillo, G. Mauviot. Estimation des émissions de NOx pour moteur diesel sans utilisation de capteur de pression cylindre. (Submitted).

4.1 Background on Diesel Engine Air-Path Control

The problem of controlling a turbocharged Diesel engine with EGR has been exhaustively investigated in the literature. A large number of model-based air-path control and estimation techniques have been proposed over the years to meet the required engine drivability and emission performance. Some of the most representative architectures to control the air-path of Diesel engines are given in [48], [93] and [94]. Furthermore, in [103], a singular perturbation methodology is proposed to control the intake manifold pressure, temperature and air fraction in a dual-loop EGR engine. In [52], a nonlinear model predictive control of a turbocharged Diesel engine with single-loop EGR is developed. A strategy based on motion planning is proposed for air-path control with the purpose of managing the air and burned gas masses in the cylinders [36]. In [55], a constructive Lyapunov control design is considered to regulate the air-fuel ratio and the fraction of EGR to their respective set-points and in [56], a robust gain-scheduled controller is designed based on a LPV model for turbocharged diesel engine.

In the next sections, a more detailed description of the works of [48], [93] and [94] is introduced, using the same nomenclature as in Chapter 3.

4.1.1 Hybrid Robust Control for Diesel Engines Operated in Low Temperature and Conventional Combustion Modes (Junmin Wang)

This work describes a hybrid robust nonlinear control approach for modern Diesel engines operating multiple combustion modes; in particular, low temperature combustion and conventional Diesel combustion modes [94]. The control strategy is based on a reduction of a 0D engine air-path model (as the one described in Chapter 3) which is expressed in a control affine form as follows:

$$\dot{x} = f(x, \xi) + g(x, \xi)u \tag{4.1.1}$$

where $x = [p_{im}, p_{de}, p_{em}, P_c, F_{im}]^T$ and $u = [Q_{ht}, Q_{egrh}, Q_t]^T$. The functions f and g depend on the engine operating conditions ξ, which are defined in details in [94]. A supervisory controller conducts the switching between different combustion mode controllers and prevents the appearance of singularities. Figure 4.1 depicts an schematic of the control architecture proposed by J. Wang.

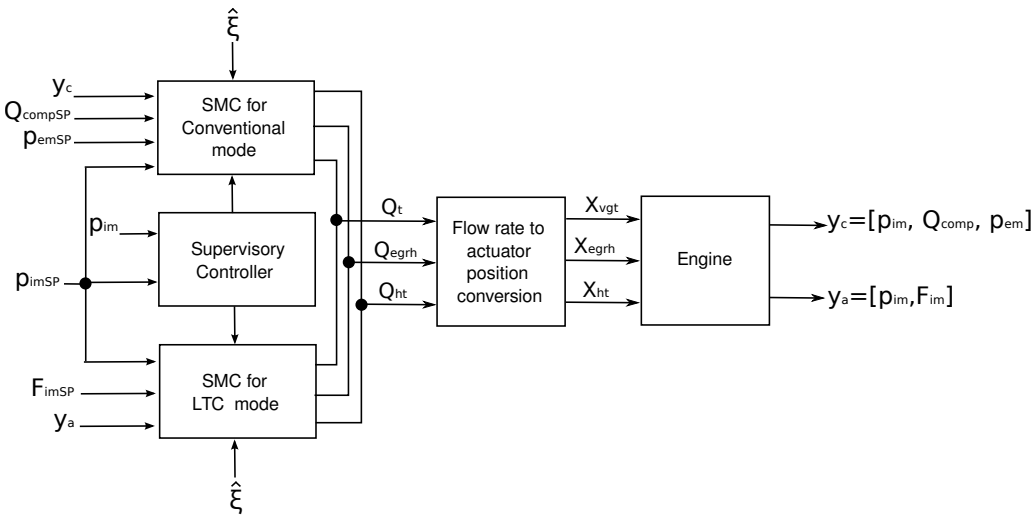

Figure 4.1: Junmin Wang Control Architecture

As shown in Figure 4.1, two different controllers are designed: one for a conventional combustion mode and a second for a low temperature combustion (LTC) mode. The intake manifold pressure, the compressor mass flow rate and the exhaust manifold pressure are chosen as performance variables for the conventional Diesel combustion controller while the intake manifold pressure and air fraction are considered for the LTC controller. The intake air fraction is estimated using the air to fuel ratio measurement in the exhaust manifold. In [96], an air fraction estimation method for dual-loop EGR is proposed by means of an LPV representation and a Lyapunov-based observer formulation.

Due to some parametric uncertainties and un-modeled dynamics involved in (4.1.1), a MIMO sliding mode control (SMC) is chosen for its inherent robustness. SMC is a non-linear control method that uses a discontinuous control signal to force the system along a sliding surface generated from the system's normal behavior (see [76]). The sliding surface for the conventional Diesel combustion controller is defined as follows:

$$S_c = \lambda_c(y_c - y_{cd}) + \varphi_c\rho_c, \quad \dot{\rho}_c = (y_c - y_{cd}) \tag{4.1.2}$$

where $y_c = [p_{im}, Q_{comp}, p_{em}]^T$, y_{cd} is the vector of desired values and λ_c and φ_c some positive definite diagonal matrices of the sliding surface parameters to be calibrated. The dynamics of the system output y_c is given in the following form after developing (4.1.1):

$$\dot{y_c} = a(x, \xi) + b(x, \xi)u \tag{4.1.3}$$

where $b(x, \xi)$ is an invertible matrix. By defining a quadratic Lyapunov function candidate, it is found in [94] that the control:

$$u = \hat{b}^{-1}(x, \hat{\xi})\lambda_c^{-1}\left[\lambda_c\dot{y}_{cd} - \lambda_c\hat{a}(x, \hat{\xi}) - \varphi_c y_c + \varphi_c y_{cd} - sat\left(\frac{S_c}{\Phi_c}\right)K_c\right] \tag{4.1.4}$$

stabilizes the system at the equilibrium $(y_c - y_{cd}) = 0$. The control input (4.1.4) provides the mass flow rates Q_{ht}, Q_{egrh} and Q_t in terms of the vector of desired values y_{cd}, the dynamics of the output y_c and the sliding surface S_c. To avoid chattering effects around the sliding surfaces caused by the *sgn* functions, a continuous approximation with thickness Φ_c is used to smooth out the control discontinuity.

A similar sliding mode approach is developed for the LTC control mode by defining the performance variable $y_a = [p_{im}, F_{im}]$. The control inputs given by the controllers in terms of mass flow rate are converted into actuator positions by inverting the orifice equations given in Section 3.3.2.1. This air-path control strategy has shown significant benefits compared with conventional control approaches in terms of smoothness, speed and robust torque responses, as well for as pollutant emission reductions.

4.1.2 Control of a Turbocharged Diesel Engine Fitted with High Pressure and Low Pressure Exhaust Gas Recirculation Systems (Olivier Grondin, Philippe Moulin, Jonathan Chauvin)

This work describes a control structure based on flow observations and a motion planning strategy for Diesel engines with dual-loop EGR systems and VGT turbocharger. The air-path model for the control synthesis is very similar to the one considered in [94]. However, the problem of controlling the engine air-path is addressed in a very different way. The

proposed control is based on the architecture of the Institut Français du Pétrole (IFP), which regulates the intake manifold pressure and air fraction using two separate control loops [48]. The IFP architecture is depicted in Figure 4.2.

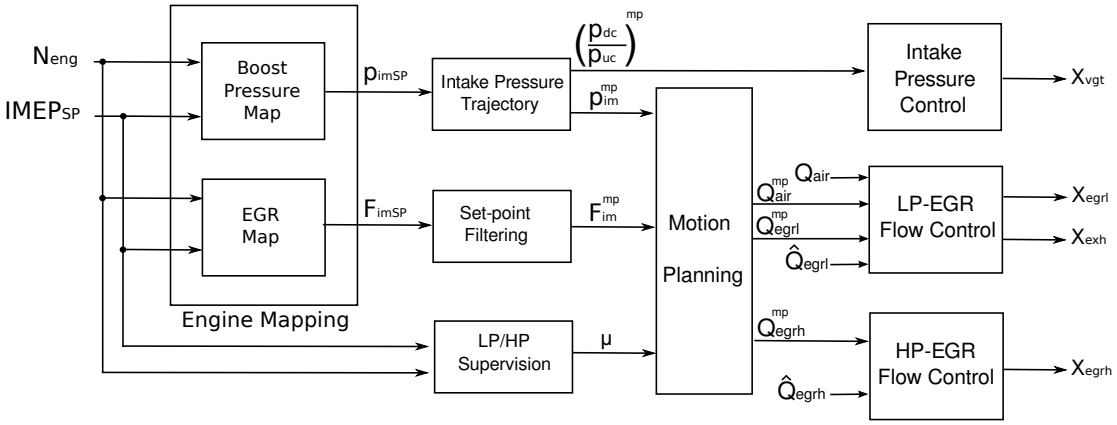

Figure 4.2: IFP Control Architecture

Two observers are designed to estimate the mass flow rates coming from the HP and LP-EGR loops, and the air fraction in the intake manifold. The EGR mass flow rates are estimated based on a reduced version of the intake manifold pressure dynamics (3.3.10), while the air fraction is estimated using an open-loop approach. One of the main advantages of this strategy is the economy of extra sensors.

For the EGR flow control, two operation modes are defined: an LP-EGR mode and a HP-EGR mode. Both are based on computing the motion planning for flows presented in [36], which is an implicit inversion of the dynamics of the intake manifold pressure and air fraction (see the motion planning block in Figure 4.2). From the inversion of these dynamics, three functions are defined to determine the LP-EGR, HP-EGR and the fresh air mass flow rate in terms of the engine operating conditions, the set-points and their first derivatives. These functions are denoted as f_1, f_2 and f_3, respectively. For LP-EGR operation, the following controller is given:

$$Q_{egrl}^{mp} = (1-\mu) f_1(T_{im}, N_{eng}, F_{em}, p_{im}^{mp}, \dot{p}_{im}^{mp}, F_{im}^{mp}, \dot{F}_{im}^{mp}) \tag{4.1.5}$$

where μ is a signal from the LP/HP supervision block that allows choosing between an LP and a HP-EGR operation and the index mp stands for the motion planning trajectories. For the second EGR control mode, the following expressions are considered:

$$Q_{egrh}^{mp} = \mu f_2(T_{im}, N_{eng}, F_{em}, p_{im}^{mp}, \dot{p}_{im}^{mp}, F_{im}^{mp}, \dot{F}_{im}^{mp}) \tag{4.1.6}$$

$$Q_{air}^{mp} = \mu f_3(T_{im}, N_{eng}, F_{em}, p_{im}^{mp}, \dot{p}_{im}^{mp}, F_{im}^{mp}, \dot{F}_{im}^{mp}) \tag{4.1.7}$$

To position the EGR and the HP valves, an integral term along with a feedforward control are used according to [48]. For the pressure control, an open-loop control allows getting a

trajectory for the compressor pressure ratio, which is obtained from the set-point of the intake manifold pressure and the engine operating conditions. This trajectory ensures a continuously differentiable set-point that respects the VGT actuator physical constraints. Then, this trajectory is transformed into a VGT position by using the backstepping control law detailed in [104]. The pressure control dynamics can be tuned according to static as well as dynamic constraints. For EGR, the motion planning is a very efficient strategy to tune the flow dynamics while including constraints on set-point feasibility.

4.1.3 Nonlinear Input Transformation for EGR and VGT Control in Diesel Engines (Johan Wahlström and Lars Eriksson)

This work describes a control structure based on the control of the performance variables F_{EGR} and λ_0 (EGR fraction and oxygen/fuel ratio, respectively). This selection is considered to be more suitable for emission control than the traditional air/fuel ratio formulation because the oxygen content has a direct impact in the engine emission performance. The main idea is to use the oxygen content of the cylinder instead of the air mass flow rate. These performance variables are equivalent to the cylinder air/fuel ratio and burned gas ratio, which are a frequent choice for performance variables. Figure 4.3 presents the control architecture proposed in [93].

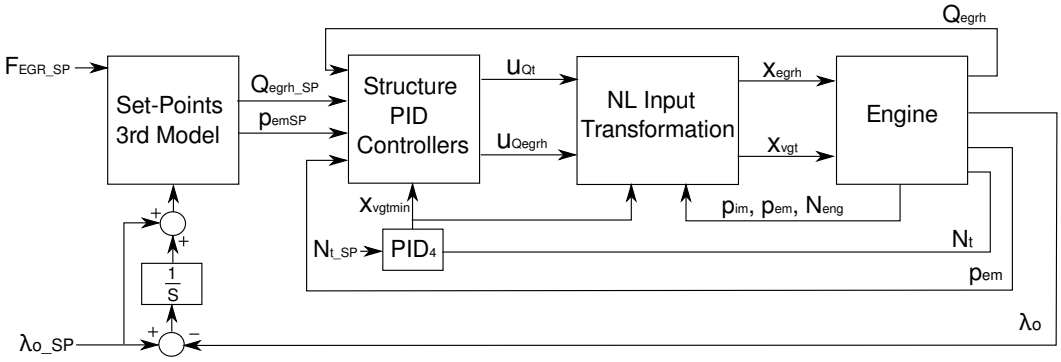

Figure 4.3: Wahlström and Eriksson Control Architecture

In this work a third order model is used to transform the EGR fraction set-point F_{EGR_SP} and an oxygen/fuel ratio set-point λ_{0_SP} into a EGR mass flow rate set-point Q_{egrhSP} and an exhaust manifold pressure set-point p_{emSP}. To compensate the errors caused by the model simplification, an integral action is used on the oxygen/fuel tracking error. A control structure with PID controllers and min/max-selectors is then proposed to regulate the turbine and EGR mass flow rate according to Figure 4.3. The two main PIDs are defined as follows:

$$u_{Qegrh} = PI_1\left(Q_{egrhSP}, Q_{egrh}\right), \quad u_{Qt} = PI_2\left(p_{emSP}, p_{em}\right) \tag{4.1.8}$$

where u_{Qegrh} and u_{Qt} are the control EGR and turbine mass flow rates. Ideally, if no modeling errors are considered, $u_{Qegrh} = Q_{egrh}$ and $u_{Qt} = Q_t$. Two other PIDs are considered for additional control modes (see [93]). A nonlinear input transformation, which is an inversion of the EGR and turbine flow models, is considered to transform the control inputs u_{Qegrh} and u_{Qt} into valve and VGT positions. This control strategy with nonlinear input transformation has shown to improve the performance of the air-path control as the same time response is achieved for different flow conditions, which implies that this control strategy handles efficiently the nonlinear effects.

One of the objectives of this thesis is to propose an alternative control approach for the engine air-path capable of regulating the pressure, air fraction and the EGR proportion in the intake manifold. Besides this objective, the developments in this works have to fulfill the design criteria imposed by the Specifications 4.0.1. To this aim, we propose the air-path control architecture depicted in Figure 4.4. This architecture is an evolution of the actual control architecture used by Renault, which is inspired in the IFP architecture introduced in Section 4.1.2.

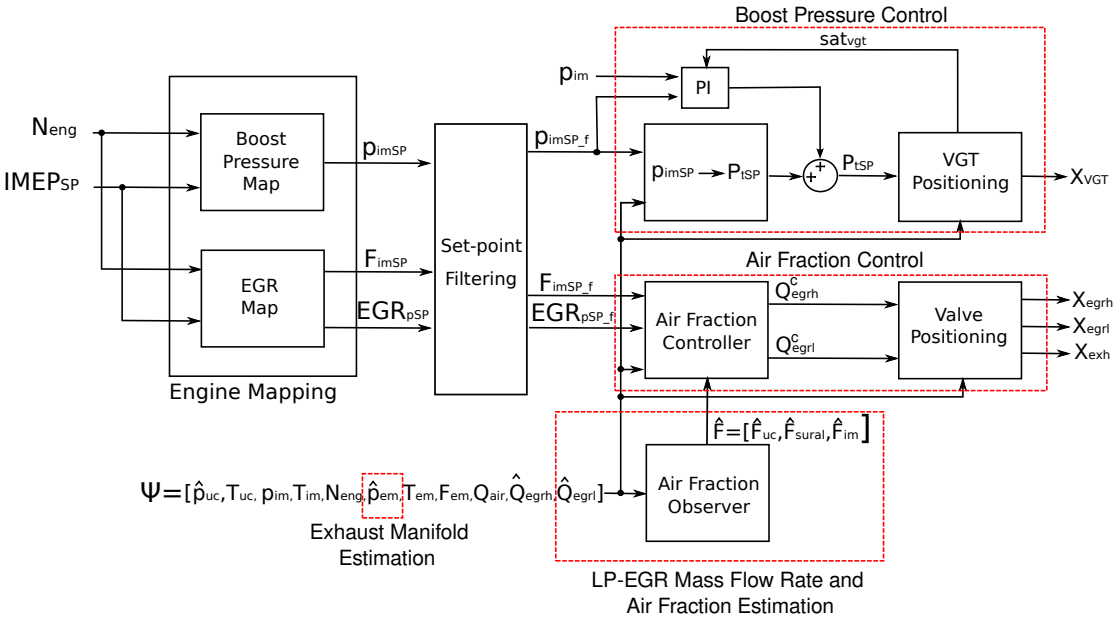

Figure 4.4: Proposed air-path control architecture

The first part of Figure 4.4, from left to right, corresponds to the engine mapping resulting from a complex calibration phase, not detailed in this work. The intake manifold pressure, air fraction and EGR proportion set-points (p_{imSP}, F_{imSP} and EGR_{pSP}, respectively) are mapped according to an indicated mean effective pressure (IMEP) set-point imposed by the driver and the measured engine speed N_{eng}. EGR_{pSP} determines the EGR proportion that must be applied. The set-points are then filtered in order to obtain feasible trajectories that respect the system and actuators dynamics and avoid discontinuities. These trajectories are tuned according to the desired performances.

We divide the remaining the air-path control architecture into four blocks (see Figure 4.4): a LP-EGR mass flow rate and air fraction estimator, a state feedback air fraction controller, an exhaust pressure manifold estimator and an boost pressure control. The details on each of these blocks are given in Sections 4.2, 4.3, 4.4 and 4.5, respectively. All these blocks together allow positioning the engine air-path actuators (namely the VGT position, the LP-EGR and HP-EGR valves, and the exhaust valve) according to the filtered set-points, the engine operating conditions (denoted in Figure 4.4 as Ψ) and the system physical constraints.

The main improvements obtained with the air-path control strategy developed in this chapter can be summarized as follows:

- control architecture that takes into account the EGR proportion as a performance variable;
- closed-loop formulation for the simultaneous estimation of the LP-EGR mass flow rate and the air fraction in the intake manifold;
- avoiding the need for an exhaust manifold pressure measurement to control the engine air-path;
- a more efficient strategy to position the VGT.

4.2 Simultaneous Air Fraction and Low-Pressure EGR Mass Flow Rate Estimation for Diesel Engines

Controlling the air fraction is a difficult task, because its direct measurement is not available on production engines and the dynamics of the admission air-path can be highly complex. Moreover, measurements of the EGR mass flow rates are often inaccurate due to the small pressure drop across the EGR valves as well as the intrinsic valve fabrication dispersion. Therefore, several air fraction/EGR rate estimation methods have been proposed in the literature to address these issues. In [34], [35] and [61], estimators of burned gas fraction in the intake manifold have been designed for single-loop EGR. In [96], a method for estimating the air fraction in each section of the engine has been proposed for dual-loop EGR systems. However, to the best of our knowledge, a simultaneous closed-loop estimation method for the air fraction and the LP-EGR mass flow rate has not been found in the literature.

In this section, we propose two novel model-based methods to estimate the LP-EGR mass flow rate and the air fraction in the intake manifold. The observers are derived to work simultaneously, reducing the need for adding new sensors to the engine air-path. In

Section 4.2.1, a reduced observation-oriented model of the pressure in the intake manifold and the air fraction along the engine air-path is derived. Then in Sections 4.2.2 and 4.2.3, a sliding mode and an LPV air fraction observer are designed to estimate the LP-EGR mass flow rate and the air fraction in the intake manifold, respectively. Finally in Section 4.2.4, an evaluation of both observers working simultaneously is performed to illustrate the effectiveness of the proposed strategies.

4.2.1 Model Reduction for the Air Fraction and LP EGR Mass Flow Rate Estimation

In order to build a reduced model of the intake manifold and the air fraction dynamics, the following assumptions are made:

Assumptions 4.2.1.

- *the dynamics of the temperature is much slower than the pressure dynamics;*
- *the volumes associated with the exhaust gas recirculation are considered small;*
- *the HP-Valve is completely open during LP-EGR operation;*
- *the volumes between the compressor discharge and the HP-Valve are considered as a single one.*

These assumptions allow simplifying the dynamics of the pressure in the intake manifold and the air fraction in the engine admission path. Similarly to the models proposed in [36] and [96], the dynamics of the intake manifold pressure and the air fraction can be approximated by:

$$\dot{p}_{im} = \frac{rT_{im}}{V_{eqv}}(Q_{air} + Q_{egrl} + Q_{egrh} - Q_{eng}) \tag{4.2.1}$$

$$\begin{aligned}\dot{F}_{em} =& \frac{rT_{em}}{p_{em}V_{em}}((Q_{air} + Q_{egrl} + Q_{egrh})F_{im} - (Q_{air} + \\ & Q_{egrl} + Q_{egrh} + Q_f)F_{em} - PCOQ_f)\end{aligned} \tag{4.2.2}$$

$$\dot{F}_{uc} = \frac{rT_{air}}{p_{air}V_{uc}}((F_{em} - 1)Q_{egrl} + (1 - F_{uc})(Q_{air} + Q_{egrl})) \tag{4.2.3}$$

$$\dot{F}_{sural} = \frac{rT_{im}}{p_{de}V_{sural}}(Q_{air} + Q_{egrl})(F_{uc} - F_{sural}) \tag{4.2.4}$$

$$\dot{F}_{im} = \frac{rT_{im}}{p_{im}V_{im}}((Q_{air} + Q_{egrl})(F_{sural} - F_{im}) + Q_{egrh}(F_{em} - F_{im})) \tag{4.2.5}$$

where the index *sural* corresponds to the volume between the compressor discharge and the HP-Valve, PCO is the stoichiometric air to fuel ratio and V_{eqv} is an equivalent volume for the 0D pressure dynamics defined as $V_{eqv} = V_{dc} + V_{de} + V_{he} + V_{im}$. V_{he} is the HP-cooler volume. According to the schematic presented in Figure 3.1, the only measured states in (4.2.1) - (4.2.5) are p_{im} and F_{em} (UEGO sensor). Note that p_{em}, T_{em}, T_{im} and Q_{air} are measured directly in the engine. However, in this thesis, p_{em} is estimated using the results obtained in Section 4.4 and T_{em} is often given by a data-map with the purpose of improving the time response (the measurement of T_{em} is typically slow).

The mass flow rates Q_{egrh} and Q_{egrl} still have to be taken into account in order to complete the information to solve system (4.2.1)-(4.2.5). These variables have a large degree of uncertainty due to the inaccurate measurement of the differential pressure across the EGR valves and the uncertainties associated with the valve's effective empirical function. It would be desirable to achieve an estimation of both mass flows rates from system (4.2.1)-(4.2.5), but the measurements available on the engine described in Figure 3.1 do not allow estimating both Q_{egrh} and Q_{egrl} at the same time. Since p_{im} is measured, it is possible to solve (4.2.1) by searching the right value for the sum of $Q_{egrh} + Q_{egrl}$. However, it is clear that Q_{egrh} and Q_{egrl} cannot be distinguished. The differential pressure across the low-pressure EGR valve is much smaller than the one across the HP-EGR valve, making this measurement more complex and inaccurate. That is why the estimation of the LP-EGR mass flow rate is addressed in this work. For the estimation of Q_{egrh} we use the Saint-Venant equations along with DP_{egrh}, p_{em} and T_{em}.

In the next sections, we consider the problem of estimating the air fraction and LP-EGR mass flow rate as two separate problems since the dynamics of the intake manifold pressure is much faster than the dynamics of the air fraction. Moreover, this approach is suitable because the air fraction does not influence the pressure dynamics, as described by (4.2.1)-(4.2.5).

4.2.2 Low Pressure EGR Flow Rate Observer Design

In this subsection, an input observer is designed to obtain an estimation of Q_{egrl}, denoted as $\hat{Q}_{egrl}$. This estimation problem is formulated as a state observation by considering the state extension $\dot{Q}_{egrl} = 0$, to include the variations of $\hat{Q}_{egrl}$ as:

$$\dot{\hat{p}}_{im} = \frac{rT_{im}}{V_{eqv}}(Q_{air} + \hat{Q}_{egrl} + Q_{egrh} - Q_{eng}) + u_1 \tag{4.2.6}$$

$$\dot{\hat{Q}}_{egrl} = u_2 \tag{4.2.7}$$

The estimation problem is to find u_1 and u_2 such that the convergence of the estimation errors $p_{im} - \hat{p}_{im}$ and $Q_{egrl} - \hat{Q}_{egrl}$ to zero is guaranteed. From the fact that system (4.2.6) - (4.2.7) is already in an additive triangular form, a sliding mode observer (suitable for this class of systems) is chosen for its inherent robustness and its implementation simplicity [76].

Define the first sliding surface with integral action as:

$$S_1 = k_1(\hat{p}_{im} - p_{im}) + k_2 \int (\hat{p}_{im} - p_{im})dt \tag{4.2.8}$$

where k_1 and k_2 are some constant parameters. Consider the following Lyapunov function candidate:

$$V(t) = \frac{1}{2} S_1^2(t) \tag{4.2.9}$$

The following is obtained after taking the derivative of V along the trajectories of (4.2.1) and (4.2.6):

$$\dot{V} = S_1(k_1 \left(\frac{rT_{im}}{V_{eqv}} (\hat{Q}_{egrl} - Q_{egrl}) + u_1 \right) + S_1 k_2 (\hat{p}_{im} - p_{im}) \tag{4.2.10}$$

Define the first observer input u_1 as follows:

$$u_1 = h_1 \lambda_1 sign(S_1) + h_2(\hat{p}_{im} - p_{im}) \tag{4.2.11}$$

where h_1 and h_2 are time-varying variables precised later and λ_1 is a tuning parameter. This leads to:

$$\begin{aligned} \dot{V} =& S_1 \left(k_1 \frac{rT_{im}}{V_{eqv}} (\hat{Q}_{egrl} - Q_{egrl}) + k_1 h_1 \lambda_1 sign(S_1) + k_1 h_2 (\hat{p}_{im} - p_{im}) \right) \\ &+ S_1 k_2 (\hat{p}_{im} - p_{im}) \end{aligned} \tag{4.2.12}$$

By choosing h_1 and h_2 as follows:

$$h_1 = \frac{rT_{im}}{V_{eqv}}, \quad h_2 = -\frac{k_2}{k_1} \tag{4.2.13}$$

we obtain:

$$\dot{V} = S_1 k_1 \frac{rT_{im}}{V_{eqv}} \left(\hat{Q}_{egrl} - Q_{egrl} + \lambda_1 sign(S_1) \right) \tag{4.2.14}$$

In order to ensure the asymptotic stability of the pressure estimation error, the parameters λ_1 and k_1 have to respect the following inequalities (to ensure that $\dot{V} < 0$):

$$|\hat{Q}_{egrl} - Q_{egrl}| < |\lambda_1|, \quad \lambda_1 < 0, \quad k_1 > 0 \tag{4.2.15}$$

It can be easily shown that when the estimation error $e = \hat{p}_{im} - p_{im}$ is at steady-state ($\dot{e} = 0$), the following expression is obtained:

$$Q_{egrl} = \hat{Q}_{egrl} + \lambda_1 sign(S_1) - \frac{k_2}{k_1}\frac{V_{eqv}}{RT_{im}}(\hat{p}_{im} - p_{im}) \tag{4.2.16}$$

Equation (4.2.16) permits to define a second sliding surface as follows:

$$S_2 = k_3(\hat{Q}_{egrl} - Q_{egrl}) + k_4 \int (\hat{Q}_{egrl} - Q_{egrl})dt \tag{4.2.17}$$

where k_3 and k_4 are constants. Using the same Lyapunov function candidate (4.2.9) for the sliding surface S_2, denoted as V_2, the following is obtained by taking into account that $\dot{Q}_{egrl} = 0$ (defined for the state insertion):

$$\dot{V}_2 = S_2(k_3 u_2 + k_4(\hat{Q}_{egrl} - Q_{egrl})) \tag{4.2.18}$$

Define the second observer input u_2 as:

$$u_2 = \lambda_2 sign(S_2) + h_3(\hat{Q}_{egrl} - Q_{egrl}) \tag{4.2.19}$$

where λ_2 and h_3 are constant tuning parameters. Then, (4.2.18) can be written as:

$$\dot{V}_2 = S_2(k_3(\lambda_2 sign(S_2) + h_3(\hat{Q}_{egrl} - Q_{egrl})) + k_4(\hat{Q}_{egrl} - Q_{egrl})) \tag{4.2.20}$$

To ensure that the time derivative of the Lyapunov function is strictly negative, the following conditions for λ_2, k_3 and h_3 are established:

$$\lambda_2 < 0, \quad k_3 > 0, \quad h_3 = -\frac{k_4}{k_3} \tag{4.2.21}$$

which guarantees the asymptotic convergence of the Q_{egrl} estimation error. Conditions (4.2.15) and (4.2.21) describe the regions of the tuning parameters for which the estimation error converges asymptotically to zero in finite time. The magnitude of λ_1 and λ_2 determines the convergence speed of the observer. It is important to note that the convergence of the observer (4.2.6)-(4.2.7) does not depend on F_{em}, F_{uc}, F_{sural} and F_{im}, which confirms that the estimation of the LP-EGR mass flow rate can be considered independently from the air fraction.

4.2.3 Air Fraction Observer

In this section, an air fraction observer is designed based on an LPV representation of the simplified air fraction model (4.2.2) - (4.2.5). The convergence and performance are guaranteed taking into account the time variation of the system by means of a polytopic representation of model (4.2.2) - (4.2.5) and the use of a LMI formulation for the observer

design. The effect of the estimation of Q_{egrl} on the stability of the air fraction observer is discussed at the end of this section.

In comparison with the approach presented in [96], where an estimation of the intake manifold air fraction F_{im} is considered as system output for the observer design, the air fraction estimation proposed in this thesis uses directly the measurement obtained from the UEGO sensor (F_{em}) as system output. The advantage of this formulation is that the complete air fraction dynamics is taken into account during the air fraction estimation.

Start by considering the following LPV representation of system (4.2.2)-(4.2.5):

$$\begin{aligned} \dot{X} &= A(\varphi)X + W(\varphi) + \xi_x \\ y &= CX + \xi_y \end{aligned} \tag{4.2.22}$$

where ξ_x is a stochastic process vector with covariance matrix $V = V^T$, ξ_y is the measurement noise with covariance W_y, $X = [F_{em}\, F_{uc}\, F_{sural}\, F_{im}]^T$, $C = [1\,0\,0\,0]$ and

$$A(\varphi) = \begin{bmatrix} -\varphi_1 - \varphi_2 & 0 & 0 & \varphi_1 \\ \varphi_3 & -\varphi_3 - \varphi_4 & 0 & 0 \\ 0 & \frac{\varphi_5}{V_{sural}} & -\frac{\varphi_5}{V_{sural}} & 0 \\ \varphi_6 & 0 & \frac{\varphi_5}{V_{im}} & -\frac{\varphi_5}{V_{im}} - \frac{\varphi_6}{V_{im}} \end{bmatrix}, \quad W(\varphi) = \begin{bmatrix} -PCO\varphi_2 \\ \varphi_4 \\ 0 \\ 0 \end{bmatrix}$$

with the varying parameters defined as follows:

$$\begin{aligned} \varphi_1 = \frac{rT_{em}}{p_{em}V_{em}}(Q_{air} + Q_{egrl} + Q_{egrh}), \quad \varphi_2 = \frac{rT_{em}}{p_{em}V_{em}}Q_f, \quad \varphi_3 = \frac{rT_{air}}{p_{air}V_{uc}}Q_{egrl}, \\ \varphi_4 = \frac{rT_{air}}{p_{air}V_{uc}}Q_{air} \quad \varphi_5 = \frac{rT_{im}}{p_{im}}(Q_{air} + Q_{egrl}), \quad \varphi_6 = \frac{rT_{im}}{p_{im}}Q_{egrh} \end{aligned} \tag{4.2.23}$$

In the general case, the parameter vector φ consists of n_φ varying parameters $[\varphi_1, \varphi_2, ..., \varphi_{n_\varphi}]$ where each varying parameter φ_i is bounded by a minimum and maximum value $\underline{\varphi_i}$ and $\overline{\varphi_i}$, respectively. The admissible values of the vector φ are constrained in an hyperrectangle in the parameter subset $Z_\varphi \subset \mathbb{R}^{n_\varphi}$ with $N_\varphi = 2^{n_\varphi}$ vertices $\{w_1, w_2, ...w_{N_\varphi}\}$. The images of the matrix $A(\varphi)$ for each vertex w_i corresponds to a set $\{\Omega_1, ..., \Omega_{N_\varphi}\}$. The components of the set $\{\Omega_1, ..., \Omega_{N_\varphi}\}$ are the extrema of a convex polytope that contains the images for all admissible values of φ if the matrices $A(\varphi)$ and $W(\varphi)$ depend linearly on φ.

It has been shown in [7] (among other references) that the LPV system (4.2.22) can be written in the following equivalent linear polytopic form:

$$\dot{X} = \sum_{i=1}^{N_\varphi} \alpha_i(\varphi)(A(w_i)X + W(w_i)u) + \xi_x \tag{4.2.24}$$

where the scheduling functions $\alpha_i(\varphi)$ are defined as:

$$\alpha_i(\varphi) = \frac{\prod_{k=1}^{n_\varphi} |\varphi_k - C(w_i)_k|}{\prod_{k=1}^{n_\varphi} |\overline{\varphi}_k - \underline{\varphi}_k|} \tag{4.2.25}$$

where:

$$C(w_i)_k = \left\{ \varphi_k \middle| \begin{array}{c} \varphi_k = \overline{\varphi}_k \text{ if } (w_i)_k = \underline{\varphi}_k \\ \varphi_k = \underline{\varphi}_k \text{ otherwise} \end{array} \right\} \tag{4.2.26}$$

and the scheduling function α_i have the following properties:

$$\alpha_i(\varphi) \geq 0, \quad \sum_{i=1}^{N_\varphi} \alpha_i(\varphi) = 1 \tag{4.2.27}$$

Consider the following LPV Luenberger-like observer for the system (4.2.22):

$$\dot{\hat{X}} = A(\varphi)\hat{X} + W(\varphi) + L(F_{em} - \hat{F}_{em}) \tag{4.2.28}$$

where L is a constant observer gain vector that ensures the asymptotic stability of the estimation error for all $\varphi \in Z_\varphi$. This approach may give relatively conservative results when compared with a φ dependent observer gain $L(\varphi)$. However, its simplicity to implement, its low calculation load (required from Specifications 4.0.1) and the good results that can be obtained suggest that (4.2.28) is an appropriate approach for the estimation of the air fraction in the intake manifold.

The following theorem is considered for the calculation of observer gain.

Theorem 4.2.2. *[82]: Consider system (4.2.22). If there exists a symmetric positive definite matrix $P > 0$, a matrix Y and a symmetric matrix X, for a given diagonal process covariance matrix $V > 0$ and a diagonal measurement covariance matrix $W_y > 0$, such that the following linear matrix inequalities are satisfied for all $i \in [1, \ldots, N_\varphi]$:*

$$A(w_i)^T P + P A(w_i) + C^T Y + Y^T C + I \prec 0 \tag{4.2.29}$$

$$\begin{bmatrix} X & W_y^{\frac{1}{2}} Y \\ Y^T W_y^{\frac{1}{2}} & P \end{bmatrix} \succ 0 \quad L = YP^{-1} \tag{4.2.30}$$

subject to:

$$\arg \min_{P,X,Y} \{Tr(VP) + Tr(X)\} \tag{4.2.31}$$

then, (4.2.28) is an observer of system (4.2.22) for all $\varphi \in Z_\varphi$.

Theorem 4.2.2 is very interesting as it guarantees the convergence of the estimation error for all $\varphi \in Z_\varphi$ while minimizing the quadratic performance index (4.2.31). Moreover, note also that Theorem 4.2.2 is formulated in terms of LMIs, which allows calculating numerically the observer gain L using convex optimization methods. With this approach, convergence and performance are achieved despite the system time variation.

As presented in (4.2.23), the LP-EGR mass flow rate is a part of the varying parameters considered for the LPV representation of system (4.2.2) - (4.2.5). In order to ensure that the effect of the estimation of Q_{egrl} does not destabilize the air fraction observer, the only condition to fulfill is to guarantee that $\hat{Q}_{egrl}$ does not drive φ out of the defined polytope. As long as this condition is satisfied, both estimators errors simultaneously converge to zero.

Remark 4.2.1. The air fraction estimation approach considered in this section is extended to take into account the mass transport time in Appendix A.4.

4.2.4 Estimation Results

In this section, the performance of the estimators working simultaneously is evaluated using as a reference the validated engine air-path model presented in Chapter 3. The evaluation is done with an engine cycle that presents strong transient conditions with the purpose of evaluating the time response of the proposed observers.

4.2.4.1 LP-EGR mass flow rate estimator evaluation

Figure 4.5 shows the LP-EGR mass flow rate estimation results obtained using the sliding mode estimator presented in Section 4.2.2. The parameters of the sliding mode estimator, which have been calibrated in simulation, are given in Table 4.1.

Parameter	Value
k_1	0.003
k_2	0.04
λ_1	-0.005
k_3	0.02
k_4	0.03
λ_2	-0.03

Table 4.1: Simulation parameters of the sliding mode estimator

Figure 4.5 shows a zoom in the engine cycle simulation in order to better illustrate the observer performance. As depicted in the figure, the observer quickly converges to the

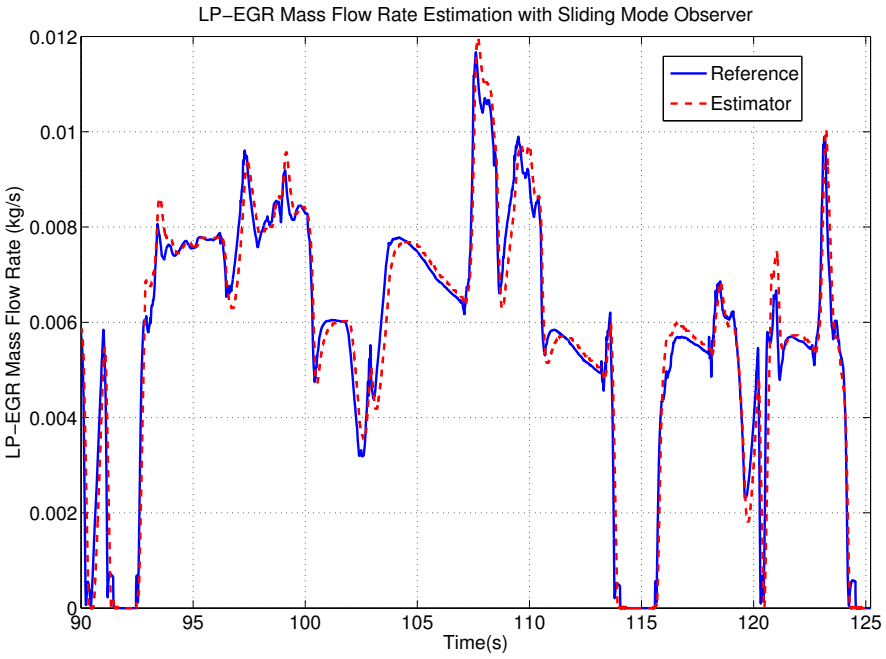

Figure 4.5: Zoom on the LP-EGR mass flow rate estimator results

virtual air-path LP-EGR mass flow rate provided by the air-path model. Some slight estimation errors are found in Figure 4.5, which are originated from the model reductions effectuated for the observer synthesis (Section 4.2.1). However, the overall observer performance is satisfactory. Figure 4.6 presents the LP-EGR mass flow rate estimation error for a larger time interval of the engine cycle. In this figure we can observe that the estimator responds quickly to strong changes of LP-EGR mass flow rate (sudden opening and closing of the LP-EGR valve). Note also that the estimation error remains bounded by $|Q_{egrl} - \hat{Q}_{egrl}| < |\lambda_1| = 0.005$, which according to the parameter conditions given in (4.2.15) guarantees the convergence of the observer.

4.2.4.2 Air fraction observer evaluation

An evaluation of the air fraction observer presented in Section 4.2.3 is performed using the same engine cycle as the one used in the previous section. This to evaluate the performance of both observers working simultaneously.

The bounds of the parameter vector φ are found using engine benchmark measurements over representative engine operating conditions. The resulting parameter limits are given in Table 4.2.

Applying Theorem 4.2.2 with $V = 0.01 \times I^{n\times n}$ and $W_y = 0.01$ (the respective process and measurement noise covariance matrices added in the engine model), the following

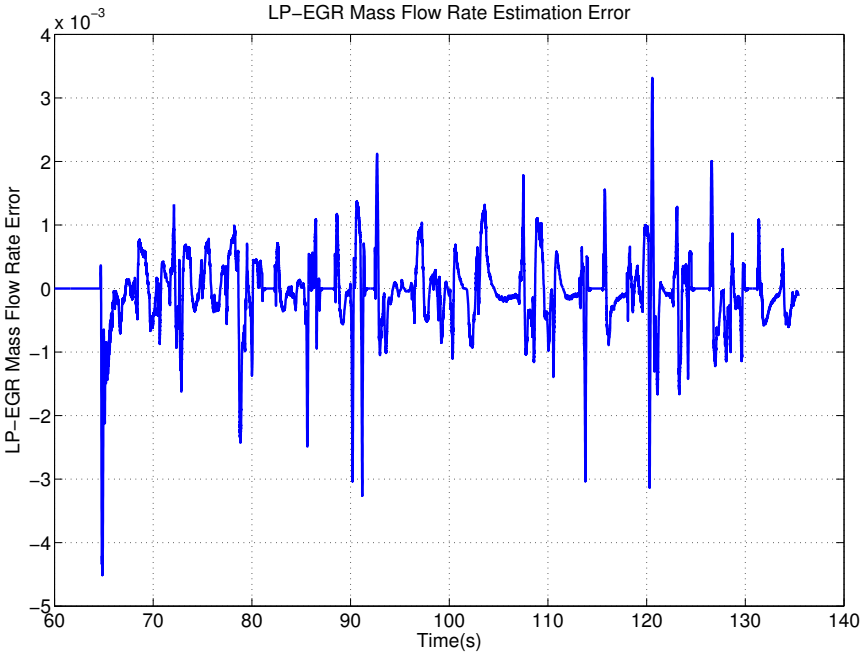

Figure 4.6: LP-EGR mass flow rate estimator error

Parameter	ValueMin	ValueMax
φ_1	8.33	49.02
φ_2	0	2.17
φ_3	0	2.98
φ_4	0.98	9.38
φ_5	0.0051	0.033
φ_6	0	0.0073

Table 4.2: Bounds on the parameter vector φ

observer gain is obtained using a classical convex optimization algorithm:

$$L = [1.36,\ 0.63,\ 1.00,\ 1.21]^T \tag{4.2.32}$$

Figure 4.7 illustrates the observer effectiveness over the same time interval as the one used in Figure 4.5. As depicted, the air fraction in the intake manifold shows a good agreement with the air fraction reference. Although some estimation errors appear in Figure 4.7 due to the un-modeled dynamics in (4.2.1)-(4.2.5) and the estimation errors of the LP-EGR mass flow rate sliding mode observer, the overall performance of the air fraction estimation is very satisfying. This confirms that a constant observer gain L for the air fraction estimator is suitable and has the advantage of introducing a reasonable calculation load. Due to the good behavior of the LP-EGR mass flow rate estimator, the parameter vector φ is not driven out of the polytope formed by the parameter extremities

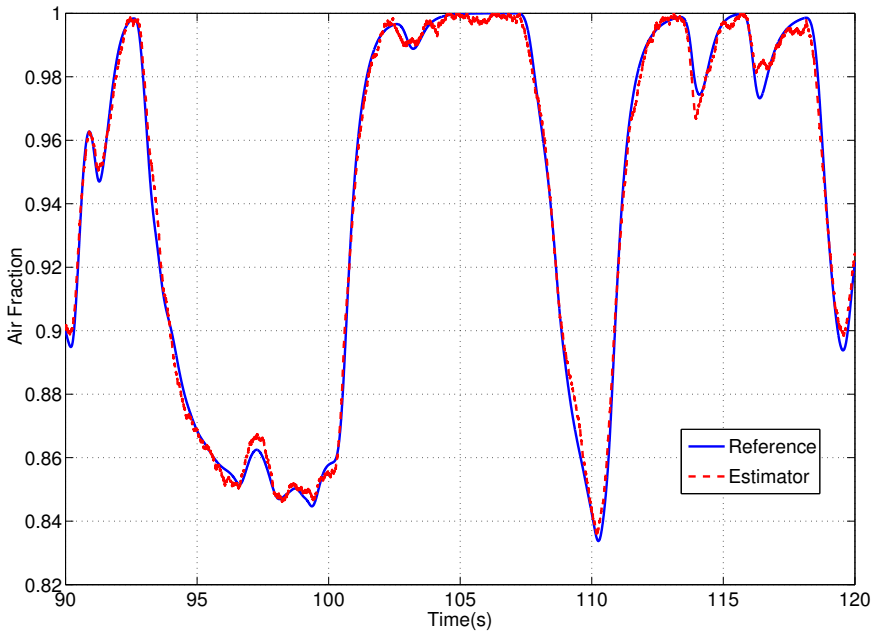

Figure 4.7: Zoom of the intake manifold air fraction estimation

given in Table 4.2, ensuring also the convergence of the air fraction estimation error.

One of the advantages of the air fraction observer proposed in (4.2.28), is that it gives an estimation of the air fraction along the engine air-path (at each of the defined air-path sections). This allows formulating a state feedback air fraction control for system (4.2.2)-(4.2.5), which is the main concern of the next section.

4.3 Air Fraction and EGR Proportion Control for Dual Loop EGR Diesel Engines

An efficient control of the in-cylinder combustion and engine-out emissions not only involves the total in-cylinder EGR, but also the ratio between the HP-EGR and LP-EGR. With the HP-EGR the burnt gases from the exhaust manifold are reintroduced into the intake manifold reducing the turbine flow and thus its power. However, the HP-EGR has a faster settling time and gives better HC and CO emission reduction than the LP-EGR [15]. With the LP-EGR the burnt gases are taken downstream of the exhaust after-treatment systems and reintroduced upstream of the compressor. With the LP-EGR all the exhaust gases pass through the turbine, allowing the supercharging system to operate optimally. Nevertheless, with the LP-EGR, the settling time of the air fraction in the intake manifold is longer than with the HP-EGR. The dual-loop EGR configuration combines the advantages of the HP-EGR and the LP-EGR. With this EGR architecture,

the mixing of hot HP-EGR gas and cold LP-EGR gas can be set to reach the optimal temperature regarding the HC-CO emission reduction. A prioritization of HP-EGR can be performed when a short settling time of the air fraction in the intake manifold is required, while the LP-EGR can be prioritized when supercharging performance is needed. Thus, designing an air fraction control that allows regulating the EGR proportion is of significant importance.

The control of the air fraction in the intake manifold has been exhaustively investigated for single-loop EGR architectures; as reported in [36], [52] and [94], among other references. In [48], the air fraction control in dual-loop EGR engines has been considered to manage either the HP-EGR or the LP-EGR. In [103], a cooperative dual-EGR control methodology has been proposed based on a singular perturbation methodology. However, the control of the air fraction, together with the EGR proportion has been less explored in the literature.

In this section, we address the problem of controlling the air fraction as well as the EGR proportion in dual-loop EGR architectures. We modify an air fraction model with the purpose of having the required EGR proportion as a system input. Then, this modified model is expressed in an LPV form by defining the LP-EGR mass flow rate in terms of a virtual input that allows canceling out the system's exogenous inputs. Based on the LPV model, an optimal LPV-LQR state feedback air fraction controller is designed. To ensure the existence of the optimal LPV-LQR state feedback control, the controllability of the LPV system is verified for all the varying parameters that belong to a defined parameter convex set. The effectiveness of the air fraction control is evaluated using as a reference, the experimentally validated engine model presented in Chapter 3.

4.3.1 Air-Path Air Fraction Control Model

With the purpose of writing the reduced dynamics of the air fraction (4.2.2) - (4.2.5) in terms of the EGR proportion, the EGR proportion is defined as follows:

$$EGR_p = \frac{Q_{egrl}}{Q_{egrl} + Q_{egrh}} \tag{4.3.1}$$

From (4.3.1), Q_{egrh} can be written in terms of Q_{egrl} and EGR_p as:

$$Q_{egrh} = \alpha_{EGR} Q_{egrl} \tag{4.3.2}$$

where $\alpha_{EGR} = \left(\frac{1}{EGR_p} - 1\right)$. Rewriting (4.2.3) - (4.2.5) with (4.3.2) gives:

$$\dot{F}_{uc} = -\gamma_{uc}(Q_{air} + Q_{egrl})F_{uc} + \gamma_{uc}F_{em}Q_{egrl} + \gamma_{uc}Q_{air} \tag{4.3.3}$$

$$\dot{F}_{sural} = \gamma_{sural}(Q_{air} + Q_{egrl})(F_{uc} - F_{sural}) \tag{4.3.4}$$

$$\begin{aligned}\dot{F}_{im} =&\gamma_{im}(Q_{air}+Q_{egrl})F_{sural}-\gamma_{im}(Q_{air}+(1+\alpha_{EGR})Q_{egrl})F_{im}\\&+\gamma_{im}F_{em}\alpha_{EGR}Q_{egrl}\end{aligned} \tag{4.3.5}$$

where

$$\gamma_{uc}=\frac{rT_{air}}{p_{air}V_{uc}},\quad \gamma_{im}=\frac{rT_{im}}{p_{im}V_{im}},\quad \gamma_{sural}=\frac{rT_{im}}{p_{de}V_{sural}} \tag{4.3.6}$$

With this representation of the air fraction dynamics, Q_{egrl} and α_{EGR} are defined as control inputs, which is convenient since the EGR proportion in the intake manifold is hardly distinguishable from the measurements currently available in production engines. The dynamics of the exhaust manifold air fraction F_{em} is not considered for the air fraction control as this quantity is measured in productions engines. Therefore, it can be considered as an exogenous input. For small EGR proportions, the LP-EGR mass flow rate becomes also small, making it harder to measure or estimate. Moreover, as the LP-EGR vanishes, there is no longer the need for considering model (4.2.3) - (4.2.5) since (4.2.5) would be sufficient. This is why we consider for dual-loop EGR operation, that the variation range of EGR_p is between 0.2 and 1 (equivalent to $\alpha_{EGR}\in[0,4]$). If only HP-EGR is required, a classical HP-EGR air fraction control can be used.

4.3.2 Air Fraction Control

The inputs associated with the air fraction controller are the filtered air fraction and the EGR proportion set-points, the engine operating conditions Ψ and the estimated air fractions at each section of the air-path (see Figure 4.4). The outputs of the air fraction controller are the objective HP and LP EGR mass flows rates (denoted as Q^c_{egrh} and Q^c_{egrl}, respectively), which are then transformed into valve position by the valve positioning block.

In order to control the air fraction in the intake manifold, we define the air fraction error at each of the defined air-path sections as:

$$\begin{gathered}e_{uc}=F_{uc}-F_{ucSP};\quad e_{sural}=F_{sural}-F_{suralSP};\\e_{im}=F_{im}-F_{imSP}\end{gathered} \tag{4.3.7}$$

where the index SP stands for set-point. Taking into account that $F_{suralSP}=F_{ucSP}$, the dynamics of (4.3.7) are given as follows:

$$\begin{aligned}\dot{e}_{uc}=&-\gamma_{uc}(Q_{air}+Q_{egrl})e_{uc}+\gamma_{uc}F_{em}Q_{egrl}+\gamma_{uc}Q_{air}\\&-\gamma_{uc}(Q_{air}+Q_{egrl})F_{ucSP}\end{aligned} \tag{4.3.8}$$

$$\dot{e}_{sural}=\gamma_{sural}(Q_{air}+Q_{egrl})(e_{uc}-e_{sural}) \tag{4.3.9}$$

$$\begin{aligned}\dot{e}_{im} =&\gamma_{im}(Q_{air}+Q_{egrl})e_{sural}-\gamma_{im}(Q_{air}+(1+\alpha_{EGR})Q_{egrl})e_{im}\\&+\gamma_{im}F_{em}\alpha_{EGR}Q_{egrl}+\gamma_{im}(Q_{air}+Q_{egrl})F_{ucSP}\\&-\gamma_{im}(Q_{air}+(1+\alpha_{EGR})Q_{egrl})F_{imSP}\end{aligned} \tag{4.3.10}$$

With the purpose of canceling out the additive terms of (4.3.8) - (4.3.10) (namely the last two terms in (4.3.8) and (4.3.10)), we define a virtual control input u_v and the air fraction set-point F_{ucSP} as follows:

$$u_v = Q_{egrl}F_{em}-\frac{(F_{imSP}-1)Q_{air}}{(1+\alpha_{EGR})(F_{em}-F_{imSP})} \tag{4.3.11}$$

$$F_{ucSP} =\frac{1}{Q_{air}+Q_{egrl}}((Q_{air}+(1+\alpha_{EGR})Q_{egrl})F_{imSP}-F_{em}\alpha_{EGR}Q_{egrl}) \tag{4.3.12}$$

Using (4.3.11) and (4.3.12), system (4.3.8) - (4.3.10) can be expressed in the following LPV representation:

$$\dot{X} = A(\varphi)X + B(\varphi)u_v \tag{4.3.13}$$

where $\varphi \in \mathbb{R}^{n_\varphi}$ is a varying parameter vector that takes values in a parameter space Z_φ, n_φ is the amount of varying parameters, $X \in \mathbb{R}^3$, $u_v \in \mathbb{R}$, $A(\varphi) : Z_\varphi \to \mathbb{R}^{3\times3}$ and $B(\varphi) : Z_\varphi \to \mathbb{R}^{3\times1}$. The respective LPV matrices of (4.3.13) are given as follows:

$$A(\varphi) = \begin{bmatrix} -\varphi_1 & 0 & 0 \\ \varphi_3 & -\varphi_3 & 0 \\ 0 & \varphi_4 & -\varphi_4-\varphi_5 \end{bmatrix}, B(\varphi) = \begin{bmatrix} \varphi_2 \\ 0 \\ \varphi_6 \end{bmatrix} \tag{4.3.14}$$

where the varying parameters are defined as:

$$\begin{aligned}&\varphi_1 = \gamma_{uc}(Q_{air}+Q_{egrl}), \quad \varphi_2 = \gamma_{uc}, \quad \varphi_3 = \gamma_{sural}(Q_{air}+Q_{egrl}),\\&\varphi_4 = \gamma_{im}(Q_{air}+Q_{egrl}), \quad \varphi_5 = \gamma_{im}(\alpha_{EGR}Q_{egrl}), \quad \varphi_6 = \gamma_{im}\alpha_{EGR}\end{aligned} \tag{4.3.15}$$

The aim of this section is to find a state feedback control of the form:

$$u_v = K(\varphi)X \tag{4.3.16}$$

where $K(\varphi) : Z_\varphi \to \mathbb{R}^{1\times3}$, such that system (4.3.13) is stabilized and a quadratic performance criterion is minimized for all $\varphi \in Z_\varphi$.

According to the control design Specifications 4.0.1, an LQR approach has been chosen to design the state feedback control gain $K(\varphi)$ because of its simplicity, its good stability properties as well as its inherent robustness with respect to model uncertainties [105]. Consider the LPV-LQR formulation given in the following theorem.

Theorem 4.3.1. *[6] Consider system (4.3.13) and the completely controllable pair $(A(\varphi), B(\varphi))$ for all $\varphi \in Z_\varphi$. Let $A(\varphi)$ and $B(\varphi)$ have continuous entries and the matrices $R_u(\varphi)$ and $Q_u(\varphi)$ have continuous entries, be positive definite and be symmetric, respectively. Then, the state feedback control gain*

$$K(\varphi) = -R_u^{-1}(\varphi)B^T(\varphi)P(t) \tag{4.3.17}$$

with

$$\begin{aligned}\dot{P}(t) =& P(t)A(\varphi(t)) + A^T(\varphi(t))P(t) \\ &- P(t)B(\varphi(t))R_u^{-1}(\varphi(t))B^T(\varphi(t))P(t) + Q_u(\varphi(t))\end{aligned} \tag{4.3.18}$$

and initial condition

$$P(0) = P(0)^T \succ 0 \tag{4.3.19}$$

stabilizes the system for all $\varphi \in Z_\varphi$. Moreover, the cost function:

$$J = \int_{t_0}^{\infty} \left(X^T(t)Q_u(\varphi)X(t) + u(t)^T R_u(\varphi)u(t) \right) dt \tag{4.3.20}$$

is minimized for all $t > t_0 > 0$.

With Theorem 4.3.1, an optimal state feedback control $K(\varphi)$ (with respect to (4.3.20)) can be found as long as the LPV matrices have continuous entries, condition (4.3.19) is satisfied and the pair $(A(\varphi), B(\varphi))$ is completely controllable over the convex parameter set Z_φ.

To ensure that the matrices have continuous entries, the following considerations are taken into account:

- the F_{imSP} and the EGR_{pSP} are filtered in order to avoid unfeasible trajectories and discontinuities on the parameters;
- the air-path measurements and estimations are continuous.

This allows considering the parameter vector φ to be continuous for all $t > 0$ and therefore obtaining the LPV matrices with continuous entries. To satisfy (4.3.19), the matrix P of (4.3.18) is initialized with the following algebraic Riccati equation:

$$\begin{aligned}0 =& P_0(0)A(\varphi(0)) + A^T(\varphi(0))P_0(0) \\ &- P_0(0)B(\varphi(0))R_u^{-1}(\varphi(0))B^T(\varphi(0))P_0(0) + Q_u(\varphi(0))\end{aligned} \tag{4.3.21}$$

which ensures that P_0 is symmetric positive definite and that $(A(\varphi(0)) - B(\varphi(0))K(\varphi(0))) \prec 0$ (stability at $t = 0$).

Verifying the controllability of the pair $(A(\varphi), B(\varphi))$ is not always an easy task as the system properties depend on the variation of the system's parameters. However, there are available tools to verify the controlability of LPV systems over a defined convex parameter set, which allows guaranteeing the existence of a stabilizing control $K(\varphi)$ for all $\varphi \in Z_\varphi$.

To verify the controllability of (4.3.13) over the convex set Z_φ (polytope formed by the extremities of the parameters (4.3.15)), consider the following linear polytopic representation of (4.3.13) (according to (4.2.25) - (4.2.27)) and Theorem 4.3.2:

$$\dot{X} = \sum_{i=1}^{2^l} \alpha_i(\varphi)(A(w_i)X + B(w_i)u_v) \tag{4.3.22}$$

Theorem 4.3.2. *[7] The n-dimensional polytopic system (4.2.24) is controllable only if*

$$rank(R(A_i, B_i)) = n \quad \forall\, i \in [1, ..., N_\varphi] \tag{4.3.23}$$

where

$$R(A, B) = [B, AB, A^2B, ..., A^{n-1}B] \tag{4.3.24}$$

The results of Theorem 4.3.2 allow verifying easily the controllability of (4.3.13), which fulfills the three requirements for the existence of the state feedback control $K(\varphi)$ for all $\varphi \in Z_\varphi$.

A polytopic LQR controller could be a natural strategy to control system (4.3.13). However, due to the amount of varying parameters as well as the size of the resulting polytope, an LQR gain-scheduled polytopic control or a robust LTI-LQR control, such as the ones proposed in [7] and [73], respectively, give very conservative controller gains with poor performance (this is illustrated in Section 4.3.3). The LPV-LQR control approach is suitable for the application considered in this work since the parameter vector φ is known from the engine parameters, measurements and estimations available in production engines. The implementation of (4.3.18) can be done by using an Euler method and the calibration can be easily carried out by fixing the ratio between Q_u and R_u (appropriate for technicians).

The controller (4.3.16) allows obtaining the EGR mass flow rates that need to be applied in the engine air-path. However, to implement the air fraction and the EGR proportion control, the mass flow rates have to be converted into actuators positions, namely the positions of the HP-EGR, LP-EGR and EXH valves. Typically, to model the mass flow rate through the valve, the Saint-Venant equations given in 3.3.2.1 are used [94] . However, as mentioned in the previous section, with the differential pressure sensors available in production engines, an estimation based on an orifice equation for the LP-EGR mass flow rate is inaccurate due to the low pressure drop across the LP-EGR valve and the valve

fabrication dispersion. This is why, the sliding mode LP-EGR mass flow rate observer proposed in Section 4.2.2 is also considered for the LP-EGR valve positioning.

The position of the HP-EGR valve can be obtained using (3.3.24) and (3.3.25) along with p_{em}, DP_{egrh} and T_{egrh} and the inverse of the valve's effective area. Consider the following HP-EGR valve positioning method:

$$x_{egrh}(t) = A^{-1}_{egrh}[SV^{-1}(Q^c_{egrh}, p_{em}, DP_{egrl}, T_{egrh})] \tag{4.3.25}$$

where Q^c_{egrh} is the HP-EGR mass flow rate control objective, SV^{-1} is the inverse of the Saint-Venant equations and A^{-1}_{egrh} is the inverse function of the valve effective area. Note that in (4.3.25), the valve position is obtained directly by a static equation. On the other hand, the positioning of the LP-EGR and the exhaust valve cannot be established statically as the conditions upstream of the valves are unknown. Therefore, two integrators are used for the valves' positioning:

$$x_{egrl}(t) = k_{egrl} \int_{t_0}^{t} \left(Q^c_{egrl} - \hat{Q}_{egrl} \right) dt \tag{4.3.26}$$

$$x_{exh}(t) = k_{exh} \int_{t_0}^{t} \left(Q^c_{egrl} - \hat{Q}_{egrl} \right) dt \tag{4.3.27}$$

where Q^c_{egrl} is the LP-EGR mass flow rate control objective, $\hat{Q}_{egrl}$ is the LP-EGR rate estimated by the sliding mode observer and k_{egrl} and k_{exh} are the associated integration gains for the LP-EGR and the exhaust valves positions, respectively. The ratio $\frac{k_{egrl}}{k_{exh}}$ can be used to set the effort of a valve with respect to the other. With this we conclude the air fraction control strategy.

Two main concerns may arise from the proposed air fraction controller:

- In theory, (4.3.11) and (4.3.12) cancel perfectly the additive terms in (4.3.8) - (4.3.10). However, in practice, there are multiple sources of a deviation such as measurements inaccuracies, parametric dispersion and estimation errors. Although these mismatches cannot be avoided, their effect on the intake manifold air fraction can be modeled and quantified by defining a bounded control input disturbance denoted as d_u. This allows designing the closed-loop control such that the effect of the input disturbance is rejected up to an acceptable level. To quantify the effect of these mismatches, consider the following definition:

  $$\delta = \max_{w_i} \{ \| G_{cl}(w_i) \|_\infty \} \tag{4.3.28}$$

  where $G_{cl}(w_i)$ is the transfer function from the input disturbance d_u to the air fraction in the intake manifold F_{im} in closed-loop. There are as many $G_{cl}(w_i)$

as polytope vertices and they are obtained by solving the LQR problem at each vertex of Z_φ. δ is the maximal H_∞-norm of $G_{cl}(w_i)$ among all $i \in [1, ..., 64]$. The approach (4.3.28) allows having an estimate of the largest gain from d_u to F_{im}. For smaller δ, greater input disturbance rejection is obtained. It can be proved that as the LQR parameter R_u decreases, the magnitude of $K(\varphi)$ increases. In this sense, the proposed air fraction control design allows tuning the sensitivity to input disturbances with R_u. We look a posteriori at the maximum disturbance amplification (4.3.28) to verify whether $\delta < \delta_{max}$ (δ_{max} a control design criterion) and change R_u if necessary.

- The time-varying parameters φ are also not exactly known in the real application, which implies that modeling uncertainties affect the controller performance. The effect of these parameter deviations is not easy to quantify, however, as previously mentioned, the LQR formulation typically behaves well against model uncertainties (good gain and phase margins intrinsically obtained by an LQR formulation [105]), suggesting that the air fraction controller performance should not be significantly affected.

4.3.3 Air Fraction Controller Results

In this section, the performance of the air fraction controller is evaluated using as a reference the engine air-path model presented in Chapter 3. In order to illustrate the effectiveness of the proposed air fraction controller, simulations under strong engine transient conditions are done for three different EGR proportions. The simulations have been performed using the air fraction estimator of Section 4.2.3 for the state feedback control (according to Figure 4.4).

The bounds of the varying parameter vector φ defined in (4.3.15) are found using engine benchmark measurements over representative engine operating conditions. The obtained parameter limits are presented in Table 4.3.

Parameter	ValueMin	ValueMax
φ_1	4.9	48.2
φ_2	792.3	866.5
φ_3	0.46	5.76
φ_4	2.6	29.6
φ_5	0	38.8
φ_6	0	5437

Table 4.3: Bounds on the parameter vector φ

Using the parameter extrema given in Table 4.3, a polytope is built to verify the controllability of (4.3.13) according to Theorem 4.3.2. It has been found that the system is indeed controllable since $rank(R(A_i, B_i)) = 3$ for all $i \in [1, ..., 64]$. Applying Theorem 4.3.1 with $Q_u(\varphi) = I^{n \times n}$ and $R_u(\varphi) = 500$ (R_u calibrated in simulation), the results presented in Figures 4.8, 4.9a, 4.9b, 4.10a and 4.10b are obtained.

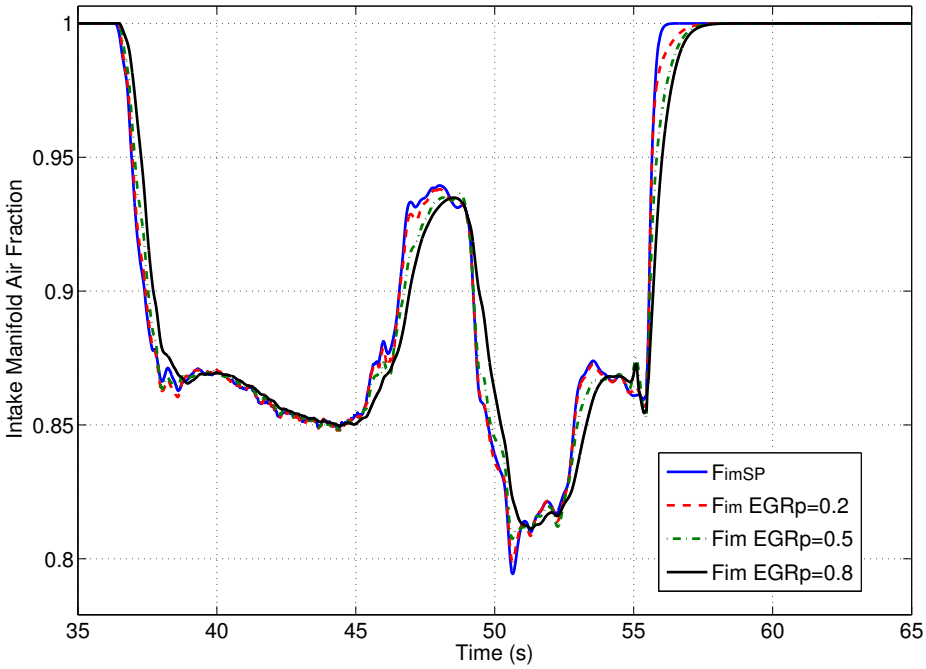

Figure 4.8: Intake manifold air fraction comparison for different EGR proportions

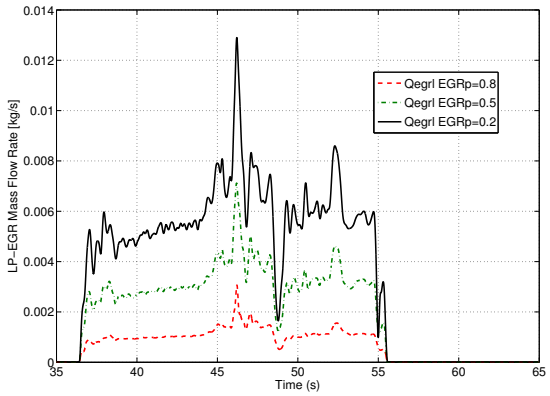

(a) Low pressure mass flow rate comparison for different EGR proportions

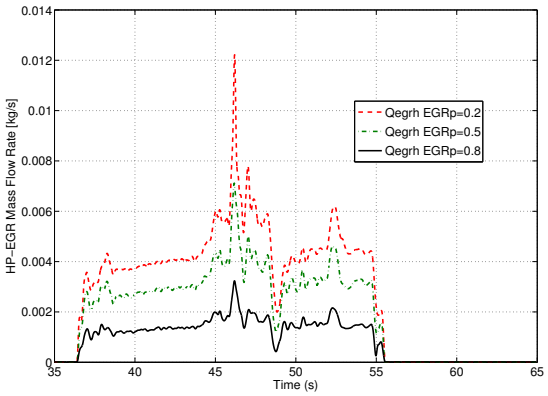

(b) High pressure mass flow rate comparison for different EGR proportions

Figure 4.9: EGR mass flow rates

In Figure 4.8, we depict the intake manifold air fraction for the EGR proportions $EGR_p = 0.2, 0.5$ and 0.8. The air fraction tracks the reference following a smooth optimal trajectory

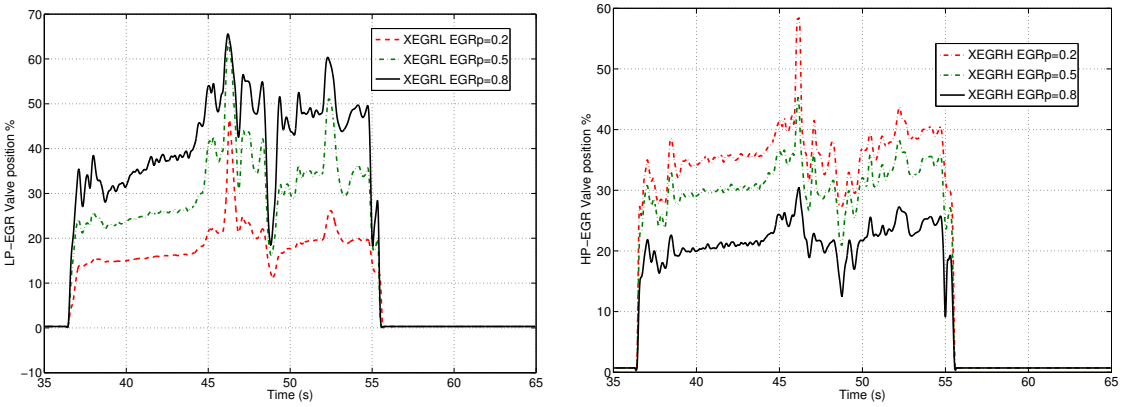

(a) Low pressure valve position comparison for different EGR proportions

(b) High pressure valve position comparison for different EGR proportions

Figure 4.10: EGR valve positions

for the three EGR proportions, as expected from the LQR formulation. We see that even under strong variations on the engine operating conditions, the air fraction controller responds efficiently. The EGR proportions are respected by the controller, as illustrated in Figures 4.9a and 4.9b, where the corresponding EGR mass flow rates are depicted. For smaller EGR proportions, the desired air fraction is reached faster as more HP-EGR is used; while for higher EGR proportions, the time response is slower due to a greater use of the LP-EGR path. Figures 4.10a and 4.10b present the EGR valves positions. We see that the valve positioning strategies given in (4.3.25), (4.3.26) and (4.3.27) are effective. Note that the valve positions are not proportional to the EGR mass flow rates, which is a consequence of the non-linearities associated with the Saint-Venant equations.

To illustrate the advantages of using the LPV-LQR control over an LTI approach, a performance comparison between a robust LTI-LQR controller (e.g. [44]) and the LPV-LQR approach is provided in Figures 4.11 and 4.12. The LTI presents significantly larger tracking errors in transient conditions and oscillations that can cause instabilities in the engine air-path.

To quantify the effect of the mismatches originated in (4.3.11) and (4.3.12), consider the input disturbance bounded as follows:

$$d_u \leq 0.1|Q_{egrl} + Q_{egrh}| \tag{4.3.29}$$

In other words, the input disturbance is bounded by the 10% of the total EGR mass flow rate. The EGR mass flow rate does not exceed the 0.016 kg/s, therefore $d_u \leq 0.0016$ kg/s. An estimation of the maximum gain from d_u to F_{im} has been found using 4.3.28, and gave $\delta = 9.2$. This implies that the input disturbance arising from the mismatches in (4.3.11) and (4.3.12) can introduce a maximal air fraction deviation of $d_u\delta = 0.012$, which is acceptable for the engine air-path control.

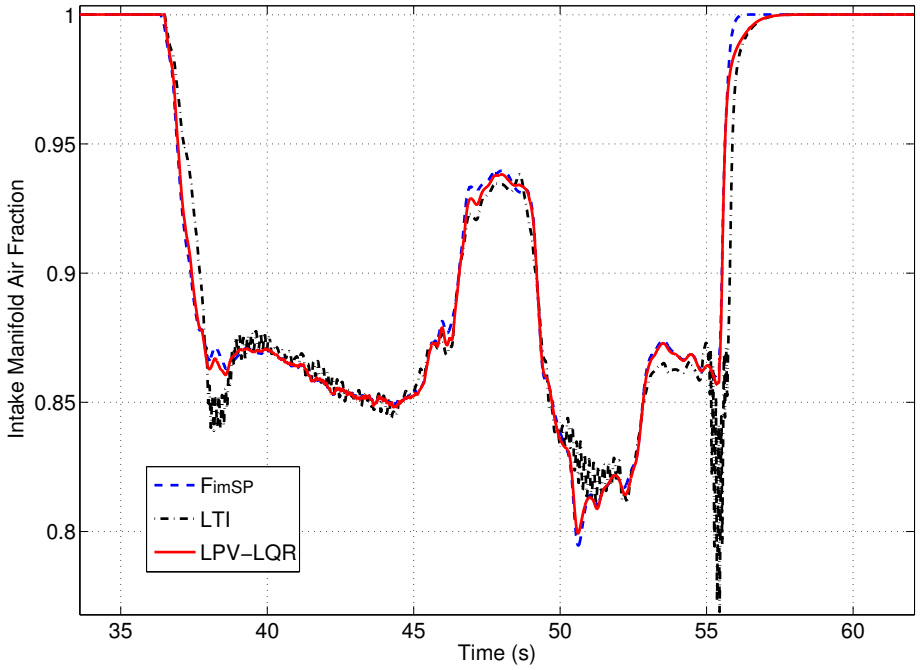

Figure 4.11: Comparison between a robust LTI control and the LPV-LQR control ($EGR_p = 0.2$)

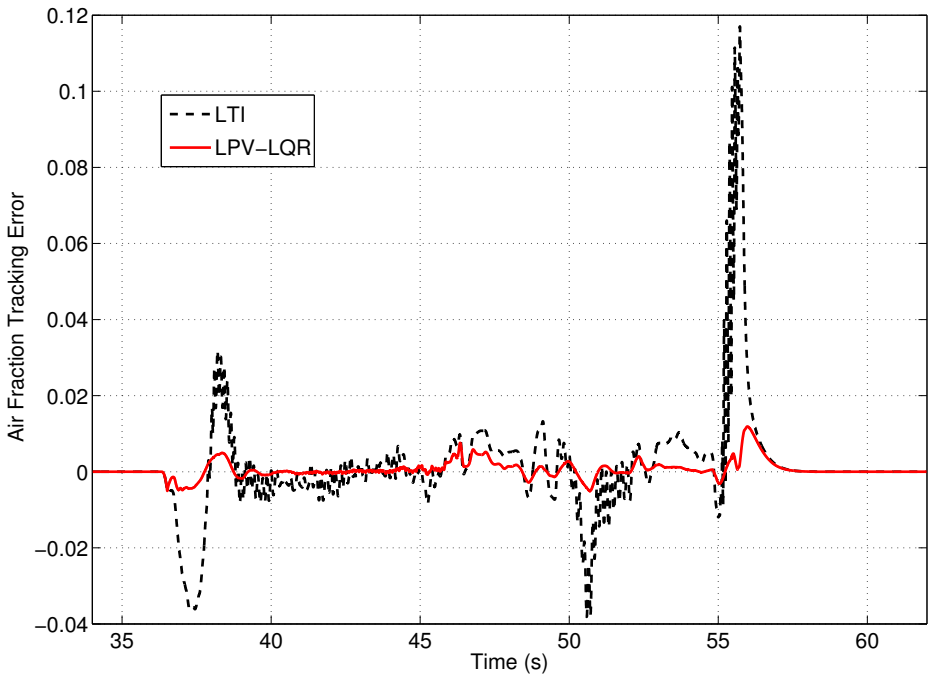

Figure 4.12: Tracking error comparison between a robust LTI control and the LPV-LQR control ($EGR_p = 0.2$)

The simulation results show that the proposed air fraction controller, together with the air fraction observer described in Section 4.2 are effective since good tracking of the air fraction set-point is obtained while ensuring the use of the adequate EGR proportions.

With this we conclude the control strategies for the air fraction regulation.

In the next sections, we consider the estimation of the exhaust manifold pressure and the boost pressure control according to the engine air-path architecture presented in Figure 4.4.

4.4 Exhaust Manifold Pressure Estimation Diesel Equipped with a VGT Turbocharger

The pressure in the exhaust manifold is one of the variables traditionally used for Diesel engine air-path control. However, its measurement is difficult and expensive due to the strong pressure oscillations and high temperature conditions in the exhaust manifold. Moreover in production engines, the measurement of the pressure in the exhaust manifold is often not reliable in some operating conditions (e.g. under high exhaust manifold temperature). To address this issue, model-based virtual sensors can be developed to estimate the exhaust manifold pressure, allowing to complement or even replace the physical sensors. Indeed, physical model-based estimators are specially attractive since these models work over a large range of operating conditions and allow estimating the mean value of the pressure over several engine cycles. For computational reasons, such this mean value is suitable for engine control purposes.

Several exhaust pressure estimators have been proposed in the literature. In [45], a non-linear model-based exhaust pressure observer is proposed for a turbocharged Diesel engine. In [74], a mean-value model for calculating the exhaust manifold pressure is derived from the compressible flow equations, treating the exhaust system as a fixed-geometry restriction. In [98], a non-linear coordinate transformation to a dimensionless model of a VGT is proposed to estimate the exhaust pressure in single-loop EGR engines. However, the VGT mass flow rate is usually approximated by a modified version of the orifice equation or a coordinate transformation, neglecting systematically the effect of the turbine speed on the turbine mass flow rate [45] [77]. Indeed, not taking into account the effect of the turbine speed can result in a degradation of the pressure estimation. Moreover, most exhaust manifold pressure estimation methods involve a manipulation of the VGT model, resulting in time consuming procedures and more data to upload into the engine controller. Therefore, it is of significant importance to search for alternative exhaust manifold pressure estimations capable of addressing these issues.

In this section, a model-based exhaust manifold pressure estimator is designed by means of a non-iterative numerical method. The estimation is done using directly the extrapolated VGT data-maps, which allows taking into account the effect of the turbine speed on the turbine mass flow rate. Since the proposed method is not iterative, it features a low calculation load, making it suitable for the implementation in production engine

controllers. This estimator is intended to relieve the physical sensor when the engine operates in the conditions where the pressure sensor looses its reliability. Nevertheless, the proposed estimator can be used in various applications, such as in VGT diagnosis and positioning, among others.

4.4.1 Problem Formulation

Neglecting the effect of the turbine speed on the turbine mass flow rate may seem an adequate assumption in some applications, such as the one addressed in [98]. Nevertheless, this assumption cannot be generalized for all the VGT because it is often found that the turbine speed has a significant effect on the turbine mass flow rate. In Figure 4.13a, we depict the turbine data-map of the turbocharger considered in this thesis for a VGT opening of 65%. In Figure 4.13b, this data-map is projected on the $Q_{tcorr} - PR_t$ plane (PR_t is the pressure ratio across the turbine) to obtain and visualize the dispersion of the curve induced by the turbine speed. We see that the turbine speed has a significant impact on the turbine mass flow rate as a variation up to a 25% is found. Consequently, neglecting the turbine speed in the pressure estimation method as proposed in previous estimation strategies can result in a significant under-estimation or over-estimation of the exhaust manifold pressure, motivating the new results proposed in this section.

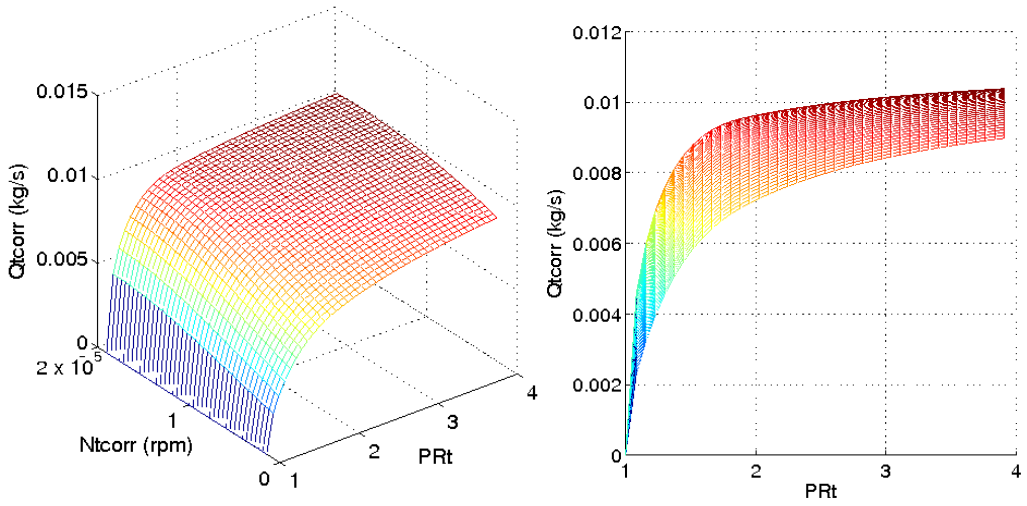

(a) Turbine data-map (b) Turbine data-map projection

Figure 4.13: Turbine flow data-map for a VGT position of 65%

Consider the turbine pressure ratio defined as follows:

$$PR_t = \frac{p_{em}}{p_{dt}} \tag{4.4.1}$$

where p_{dt} is the pressure downstream of the turbine which its value is not directly mea-

sured, thus we approximate it as follows:

$$p_{dt} = p_{air} + DP_{exh} + DP_{dpf} \tag{4.4.2}$$

where DP_{exh} is the differential pressure across the exhaust valve EXH and DP_{dpf} is the differential pressure across the particle filter. The DP_{exh} can be approximated using the mass flow rate $Q_{exh} = Q_t - Q_{egrl}$, the particle filter temperature T_{dpf} and the valve position x_{exh} along with the Saint-Venant equations. DP_{dpf} is provided by a differential pressure sensor of the particle filter.

As mentioned in Chapter 3, the mass flow rate through the turbine is typically described by data-maps, which are obtained after extrapolating the VGT characteristics provided by the suppliers [47] [50]. The three-dimensional data-maps for a VGT can be expressed in the following form (a graphical example for a fixed VGT position is depicted in Figure 4.13a):

$$Q_{tcorr} = datamap_{Qt}(x_{vgt}, N_{tcorr}, PR_t) \tag{4.4.3}$$

where x_{vgt} is the VGT position, Q_{tcorr} the corrected turbine mass flow rate and N_{tcorr} the corrected turbine speed (defined in (3.3.41) and (3.3.40), respectively). Equation (4.4.3) allows obtaining the corrected turbine flow rate for any set of inputs using look-up table techniques and trilinear interpolations as long as the inputs are contained in the defined data-map range. Expressing (4.4.3) in terms of non-corrected turbine speed and turbine mass flow rate, we obtain:

$$Q_t = datamap_{Qt}\left(x_{vgt}, N_t\frac{\sqrt{T_{ref}}}{\sqrt{T_{em}}}, \frac{p_{em}}{p_{dt}}\right)\frac{p_{em}\sqrt{T_{ref}}}{p_{ref}\sqrt{T_{em}}} \tag{4.4.4}$$

Note that in (4.4.4) the turbine mass flow rate can be explicitly found using the data-map along with the VGT position, the turbine speed and the exhaust pressure (solving (4.4.2) for p_{dt}). However, as our goal is to solve the inverse problem (finding the exhaust pressure for a given turbine mass flow rate), the solution of (4.4.4) becomes difficult since the exhaust manifold pressure cannot be written explicitly in terms of the turbine mass flow rate, turbine speed and position. Moreover, as (4.4.4) is not an analytical expression, its inversion can be very challenging and a generalization difficult to formulate.

In the next section, we propose an efficient strategy to perform this inversion, allowing us to estimate the exhaust manifold pressure from the turbine mass flow rate, the VGT position and the engine operating conditions.

4.4.2 Exhaust Pressure Estimation

Three main approaches are found in the literature to estimate the exhaust manifold pressure: an observer-based strategy set on a non-linear dynamical model [45], a modified

version of the orifice equation [74] and a non-linear coordinate transformation that provides a dimensionless VGT model [98]. However, to the best of our knowledge, these existing exhaust manifold pressure estimation techniques neglect the effect of the turbine speed on the turbine mass flow rate. Moreover, a manipulation of the data-maps and/or the development of approximated models are required for describing the turbine mass flow rate. This increases the calibration time and storage load of the engine control system since supplementary data needs to be uploaded into the vehicle controller.

In this section we design a pressure estimator for the exhaust manifold, which is directly based on the traditional extrapolated turbine data-maps (easily available in the vehicle CPU). The main benefits obtained from this approach are:

- no approximated model calibration has to be performed for estimation purposes as the turbine data-maps are directly used;
- the turbine speed's effect on the mass flow rate is considered;
- the time response of the estimator can be chosen;
- it is not an iterative method, making it suitable for real-time applications.

Let us define the following formulation to solve of the inverse problem of (4.4.4):

$$f_t(\hat{PR}_t, \varpi) = Q_t - datamap_{Qt}\left(x_{vgt}, N_t\frac{\sqrt{T_{ref}}}{\sqrt{T_{em}}}, \hat{PR}_t\right)\frac{\hat{PR}_t p_{dt}\sqrt{T_{ref}}}{p_{ref}\sqrt{T_{em}}} = 0 \tag{4.4.5}$$

where f_t is the difference between the turbine mass flow rate and the estimated mass flow rate, which is obtained from the evaluation of (4.4.4) with the pressure ratio estimate $\hat{PR}_t$ and the engine operating conditions $\varpi = [Q_t, x_{vgt}, N_t, T_{em}, p_{dt}]$. In other words, $\hat{PR}_t$ is the solution of the inverse problem of (4.4.4) when $f_t(\hat{PR}_t, \varpi) = 0$.

Since (4.4.5) does not have an analytical solution, numerical methods such as the Newton-Raphson (NR) method are typically used. Consider the following NR formulation for (4.4.5).

$$\hat{PR}_t^{it+1} = \hat{PR}_t^{it} - \alpha_{NR}\frac{f_t(\hat{PR}_t^{it})}{f_t'(\hat{PR}_t^{it})} \tag{4.4.6}$$

where $0 < \alpha_{NR} < 1$ is a constant, f_t is considered a well-behaved function and f_t' is the derivative of f_t with respect to $\hat{PR}_t$. Define $\hat{PR}_t^*$ as a root of f_t, which implies that $f_t(\hat{PR}_t^*) = 0$. The convergence criterion for the NR method is usually defined by $| f_t(\hat{PR}_t) | < \epsilon$, where ϵ is a small constant. To find an approximate of $\hat{PR}_t^*$, (4.4.6) is evaluated until the convergence criterion is satisfied. More precisely, when $\hat{PR}_t^{it} \approx \hat{PR}_t^*$

(being it the iteration step). To obtain a better accuracy in the solution of (4.4.5), smaller values of ϵ have to be chosen. Nonetheless more iterations have to be performed to satisfied the convergence criterion.

The parameter α_{NR} allows setting the convergence speed of the algorithm; the smaller its value, the slower the convergence. However, as α_{NR} decreases, the robustness of the method increases, a property that is considered later in the proposed exhaust manifold pressure estimation method. Note that $f_t'(\hat{PR}_t^{it})$ has to be evaluated in every iteration to update $\hat{PR}_t^{it}$, which is not always an easy task.

One of the main drawbacks of the NR method is that it is an iterative method whose convergence cannot be always guaranteed. Besides, the amount of iterations to reach the solution is usually unknown, which is highly undesirable for the real-time implementation in a vehicle controller. However, a gradient based method, such as the NR method, is a good approach to solve an equation like (4.4.4) because, as depicted in Figure 4.13, the turbine mass flow rate data-map is typically convex downward [50]. Indeed, this characteristic allows approaching the solution using the information given by the derivative.

To solve the inverse problem of (4.4.5), we define the following dynamics for the function f_t:

$$\dot{f}_t(\hat{PR}_t, \varpi) + \lambda_t f_t(\hat{PR}_t, \varpi) = 0 \tag{4.4.7}$$

which allows us to obtain for all $\lambda_t > 0$ an exponential convergence of our function f_t and thus a solution of our inverse problem in finite time. To define the dynamics of the estimate of the pressure ratio across the turbine $\hat{PR}_t$, consider the following hypothesis:

Hypothesis 4.4.1.

- *the variation in time of the engine operating conditions are much slower than the convergence time of* (4.4.7).

From Hypothesis 4.4.1 and (4.4.7), the dynamics of $\hat{PR}_t$ can be established as follows:

$$\dot{\hat{PR}}_t = -\lambda_t \frac{f_t(\hat{PR}_t, \varpi)}{f_t'(\hat{PR}_t, \varpi)} \tag{4.4.8}$$

By approximating the time derivative in (4.4.8), the following upgrade method is obtained to estimate of the pressure ratio across the turbine (no iterations are performed):

$$\hat{PR}_t^{n+1} = \hat{PR}_t^{n} - \alpha_t \frac{f_t(\hat{PR}_t^{n})}{f_t'(\hat{PR}_t^{n})} \tag{4.4.9}$$

where $\hat{PR}_t^{n+1}$ is the estimation of the turbine pressure ratio at the time step $n+1$, $\hat{PR}_t^{n}$ is the estimation at the current time step n, $\alpha_t = \lambda_t \Delta t$ is a parameter to calibrate the

speed of convergence of the algorithm and Δt is the estimator time step. Note that α_t is similar to α_{NR}.

Evaluating the derivative of f_t with respect to $\hat{PR}_t$ is essential for the proposed pressure estimator (4.4.9). However, this task is very demanding due to the complexity of (4.4.5) and the non-analytical form of the turbine data-maps. Indeed, the calculation of the derivative of f_t gives a large expression with a supplementary data-map representing the derivative of Q_t with respect to PR_t, which is highly inconvenient in terms of CPU calculation load and storage. Usually, it is more efficient to approximate $f_t^{'}$ to avoid the computation of the analytical derivative, thus allowing to significantly reduce linear algebra work and matrix storage. The price of such an approximation is a decrease in the convergence speed of (4.4.9). However, the overall cost of the solution is significantly less expensive [59].

To approximate (4.4.9), we consider the following upgrade function to estimate the turbine pressure ratio:

$$\hat{PR}_t^{n+1} = \hat{PR}_t^n - \alpha_t \frac{\delta PR\, f_t(\hat{PR}_t^n)}{f_t(\hat{PR}_t^n + \delta PR) - f_t(\hat{PR}_t^n)} \tag{4.4.10}$$

where δPR is a defined small variation of pressure ratio. Equation (4.4.10) is a simple approach to estimate PR_t, which is very interesting for the industrialization in productions engines. Figure 4.14 shows the schematic of the proposed estimation method.

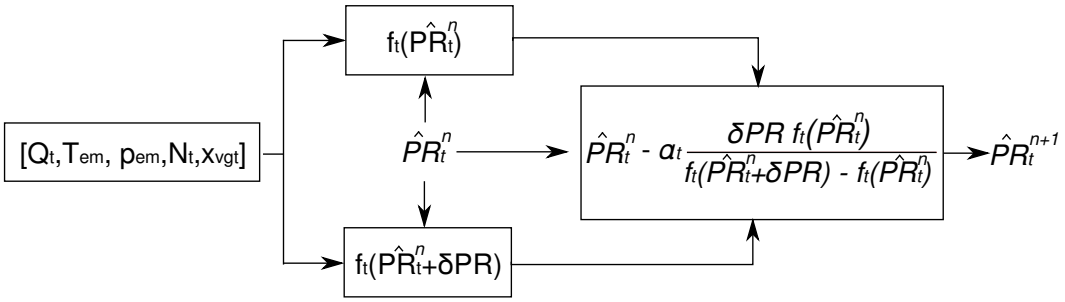

Figure 4.14: Proposed method schematic

As depicted in Figure 4.14, the function f_t is computed twice using the engine operating conditions ϖ and the turbine pressure ratio at time n. Then, the upgrade function (4.4.10) is evaluated to obtain the turbine pressure ratio at time $n+1$. To implement the proposed estimation method, it is only required to evaluate the turbine data-maps twice in order to compute the estimated turbine pressure ratio in the next time step. This gives the same calculation load every time step, which is very convenient when working with real-time applications.

To transform the estimation of the turbine pressure ratio into the exhaust manifold pressure estimation, the following is done:

$$\hat{p}_{em}^n = \hat{PR}_t^n p_{dt} \tag{4.4.11}$$

The estimator (4.4.10) has to be initialized with a suitable PR_t^0. If a p_{em} measurement is available, it can be used to initialize the method. Also a predefined initial value, close enough to the actual exhaust manifold pressure can be used to converge as fast as possible. However, it is not essential to initialize the estimator close to the solution as long as PR_t^0 is inside the data-map range. This is due to the fact that the turbine flow data-map is considered to be convex downward, therefore ensuring a good behavior of the gradient based method. The parameter α_t can be fixed between 0 and 1 to set the desired convergence speed of the estimator. As the magnitude of α_t increases, also the convergence speed of the method does, however the robustness of the numerical scheme decreases.

With this we conclude the presentation of our exhaust manifold pressure estimator. In the next section we evaluate it using two different engine cycles and illustrate the effect of the parameter α_t on the estimator convergence speed.

4.4.3 Exhaust Manifold Pressure Estimation Results

In this section, the performance of the estimator is evaluated in simulation using as a reference the validated engine model presented in Chapter 3. A comparison with respect to an orifice-based estimation method is performed with the purpose of illustrating the gain in terms of estimation accuracy. The estimator evaluation is done using two different engine cycles.

Figures 4.15 and 4.16 show the simulation results obtained with $\alpha_t = 0.02$, $\delta PR = 0.01$ and sampling time of 5 ms. Both figures provide the results given by the proposed estimation method and the orifice-based strategy.

As depicted in Figures 4.15 and 4.16, the proposed estimator rapidly reaches the reference. On the other hand, the orifice-based method presents some significant inaccuracies for light and heavy engine loads. These inaccuracies can have an important effect on the engine control. Indeed, the orifice-based method over-estimates the pressure (see Figure 4.15), which causes a surpassing of the maximum allowable exhaust manifold pressure (around 4 bars). This can have a significant effect on the engine air-path control performance due to the unnecessary activation of the air-path high pressure protections.

To provide a better comparison between the reference and the proposed estimation method, the estimation error obtained in the second cycle (Figure 4.16) is shown in Figure 4.17. As depicted, the estimation error converges quickly even with strong transient conditions. To illustrate the effect of the convergence parameter α_t on the pressure estimation, we perform a comparison using three different values of α_t. Figure 4.18 presents in details the results obtained (a zoom on strong transient is shown to better show the estimation results).

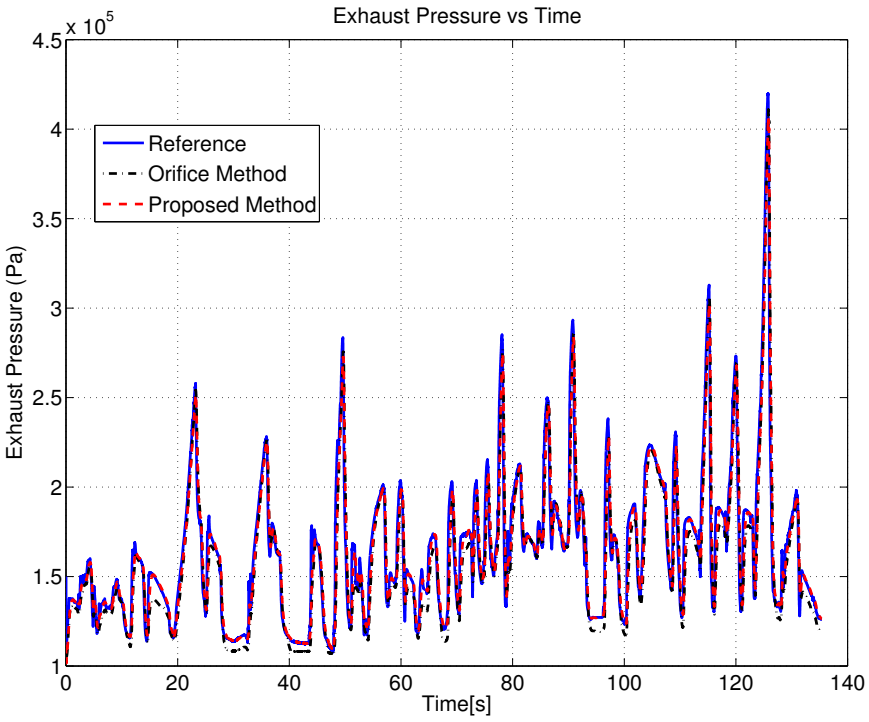

Figure 4.15: Exhaust manifold pressure estimation (Cycle 1)

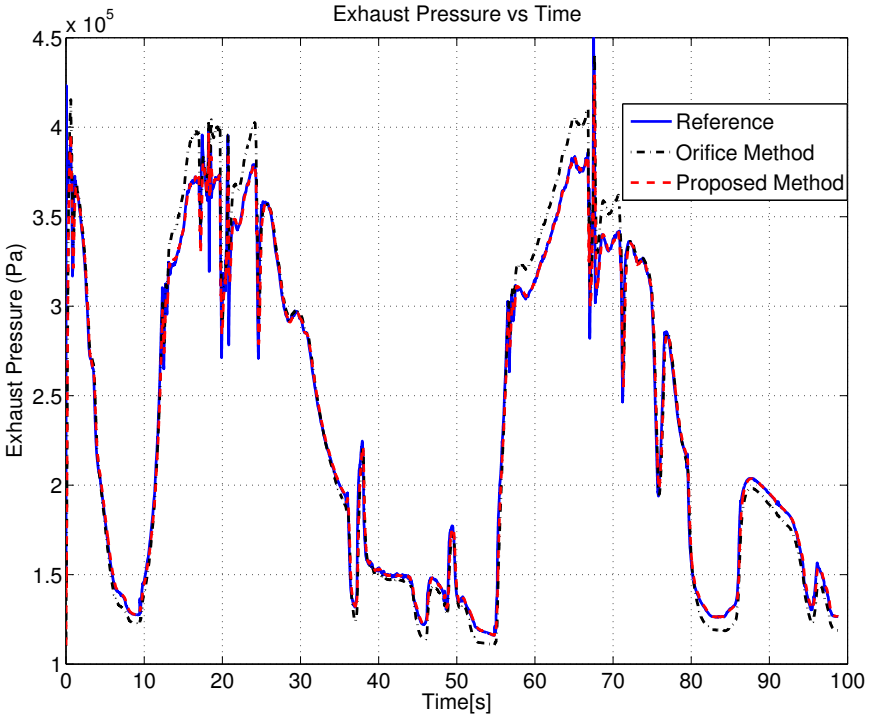

Figure 4.16: Exhaust manifold pressure estimation (Cycle 2)

As depicted in Figure 4.18, when α_t is increased, the estimator response becomes faster.

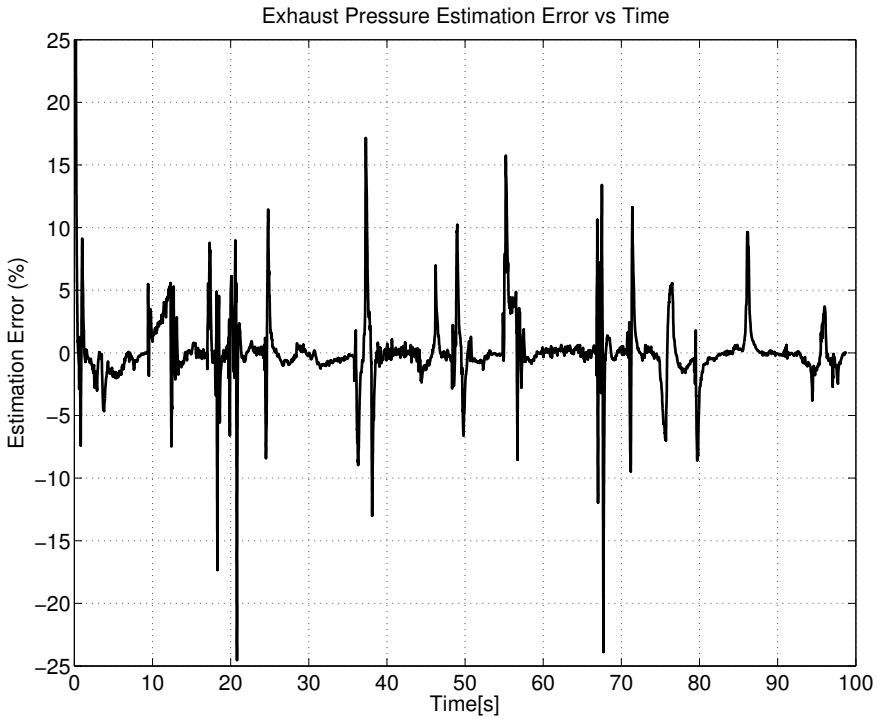

Figure 4.17: Exhaust manifold pressure estimation error (Cycle 2)

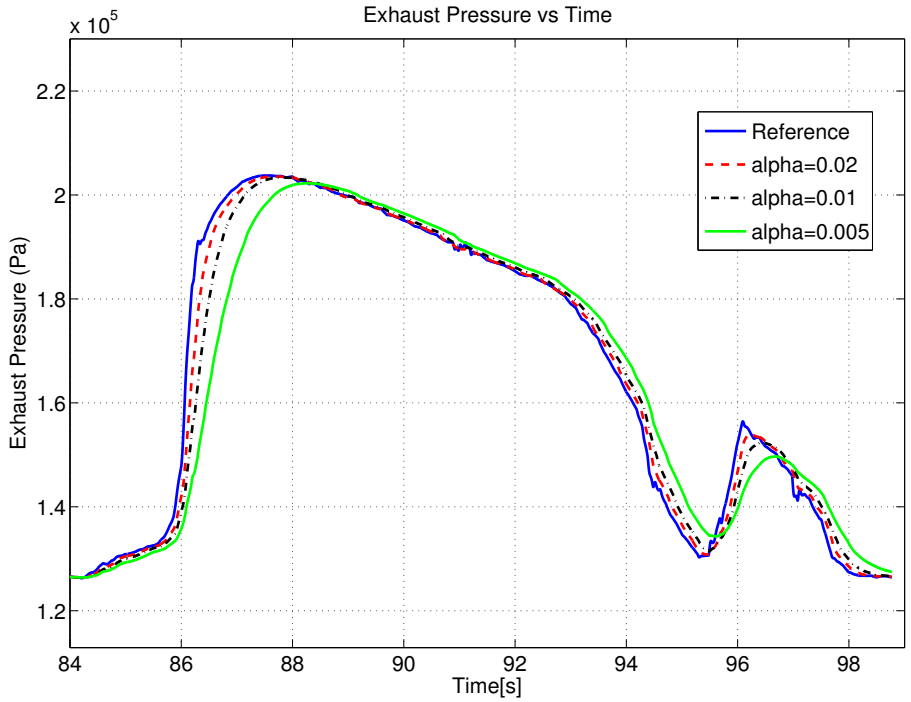

Figure 4.18: Response comparison between different α_t

Nevertheless, it is important to take into account that as α_t increases, the robustness of the estimator decreases. For this application, the value $\alpha_t = 0.02$ has shown to be a good

choice for the exhaust manifold pressure estimation (calibrated in simulation).

Besides estimating the exhaust manifold pressure, the estimation method considered in this section has various potential applications. For example, it can be used to position the VGT without the need for having an exhaust manifold pressure measurement. This application is presented in the next section.

4.5 Boost Pressure Control Using a Novel VGT Positioning Algorithm

There is a constant need for improving the turbocharger control strategies in order to propose more robust, optimal and easy to calibrate control structures for complex turbocharged architectures. The control of turbocharged Diesel engines with EGR has been exhaustively investigated, as reported in [36], [52], [97], among other references. For dual-loop EGR architectures, [48], [57], [103] are some of the most representative references. In [48], the authors proposed a dual-loop EGR control method, which deals with HP-EGR and LP-EGR separately by motion planning. In [57], a robust non-linear lean-rich switching control is developed using sliding mode controllers. In [103], a singular perturbation methodology is proposed to control the intake manifold pressure, temperature and air fraction.

When the engine operates at light loads, the controllability of the supercharging system is significantly reduced, making a purely closed-loop control strategy very difficult to implement. This is why, a combination of open and closed loop control for the boost pressure regulation is often found in the literature (see for instance [36]) as well as in the industry. Typically, most of the control effort is done by the open-loop controller while the closed-loop control is used for pressure adjustment.

The positioning of the VGT is a very challenging issue in turbocharged engines because of the system nonlinearities, the lack of reliable measurements, the strong dependence with respect to the engine operating conditions and the actuator physical constraints. Many different approaches have been proposed in the literature to address this issue. In [95], the desired VGT position is calculated inversely from an orifice equation once the turbine flow rate is specified by the controller. In [104], the VGT position is computed from a desired turbine pressure ratio by inverting an approximation of the turbine flow data-map. In [93], the VGT positioning is performed by an input transformation achieved by the inversion of the turbine flow model. However, to the best of our knowledge, most VGT positioning strategies require the measurement of the exhaust manifold pressure. As previously mentioned, the measurement of the exhaust manifold pressure is difficult and expensive due to strong pressure oscillations and high temperature conditions in the exhaust manifold. Therefore, it is of great interest to develop VGT positioning algorithms

that do not require this measurement.

One difficulty that arises from the VGT is the determination of the actuator saturation. This information is very important because it allows activating the anti-windup algorithms for the integral action of the turbocharger controllers, and thus avoiding possible instabilities. The saturations of the VGT are typically established by the engine operating conditions and the minimal and maximal admissible VGT positions [93]. However, as is illustrated in this work, it is more convenient to determine the VGT saturation in terms of turbine power instead of VGT position.

In this section, we propose a boost pressure control architecture (see Figure 4.4) inspired by the combination of open and closed-loop control strategies currently used in Renault's engines, which has shown to be very robust and effective. The main differences with respect to other air-path control architectures come from the VGT positioning algorithm and the closed-loop control acting on the desired turbine power instead of the desired turbine pressure ratio or turbine mass flow rate. Our main contribution is a significant improvement in the VGT positioning algorithm, which exhibits the following features:

- the exhaust manifold pressure measurement is not required;
- the VGT is positioned optimally even with turbine power saturation;
- the positioning of the VGT is done directly using the turbine data-maps;
- the effect of the turbine speed and the physical constraints of the turbine are taken into account;
- the exhaust manifold pressure is minimized, thus increasing the engine efficiency.

In Section (4.5.1), the desired turbine power (turbine power set-point) is generated using an open-loop model-based control along with a PI control that corrects the turbine power set-point depending on the intake manifold pressure tracking error. The open-loop control does 90% of the control effort while the 10% left is done by the PI. The closed-loop control is meant for pressure adjustment. In Section (4.5.1), we develop the algorithm to transform a turbine power set-point into a VGT position, taking into account the engine operating conditions, the turbocharger physical constraints and the VGT saturation in terms of power. In Section (4.5.3), simulation results are presented in order to evaluate the effectiveness of the boost pressure control strategy.

4.5.1 Towards a Turbine Power Set-Point

Consider a boost pressure set-point p_{imSP} given by an engine map according to Figure 4.4. A compressor mass flow rate set-point can be defined using the speed density equation

(3.3.26) and the HP-EGR mass flow rate as follows:

$$Q_{compSP} = \frac{\eta_v(p_{imSP}, N_{eng}) p_{imSP} N_{eng} V_d}{120 r T_{im}} - Q_{egrh} \tag{4.5.1}$$

The fresh mass flow rate set-point Q_{airSP} allows estimating the pressure upstream of the compressor, which is required to compute the compressor pressure ratio set-point. The fresh air mass flow rate set-point can be determined from (4.5.1) and the LP-EGR mass flow rate with the following expression:

$$Q_{airSP} = Q_{compSP} - Q_{egrl} \tag{4.5.2}$$

The pressure drop across the HP-Cooler and the air filter are also necessary to calculate the compressor pressure ratio set-point. Both differential pressures can be determined from empirical functions (denoted as f_{he} and f_{filter}, respectively) that are obtained from measurements taken in an engine benchmark operating at steady-state conditions. These functions provide the pressure drop as a function of the mass flow rate as follows:

$$p_{ucSP} = p_{air} - \Delta p_{filterSP}, \tag{4.5.3}$$

$$p_{dcSP} = p_{imSP} + \Delta p_{heSP} \tag{4.5.4}$$

where

$$\Delta p_{heSP} = f_{he}(Q_{compSP}), \quad \Delta p_{filterSP} = f_{filter}(Q_{airSP}) \tag{4.5.5}$$

From the estimated upstream and downstream compressor set-point pressures (4.5.3) and (4.5.4), the compressor pressure ratio set-point can be easily determined as follows:

$$PR_{compSP} = \frac{p_{dcSP}}{p_{ucSP}} \tag{4.5.6}$$

To obtain a compressor power set-point that allows determining the turbine power set-point, an estimation of the temperature upstream the compressor has to be performed as its measurement is not available in the engine air-path of Figure 3.1. This estimation is proposed as follows:

$$T_{uc} = \frac{Q_{air} T_{air} + Q_{egrl} T_{egrl}}{Q_{air} + Q_{egrl}} \tag{4.5.7}$$

where T_{egrl} is the LP-EGR temperature. As shown in [104], the compressor pressure ratio data-map is invertible, which implies that the turbocharger speed set-point can be written as a function of the compressor pressure ratio and the mass flow rate as:

$$N_{tSP} = datamap_{N_t}\left(Q_{compSPCorr}, PR_{compSP}\right) \frac{\sqrt{T_{uc}}}{\sqrt{T_{ref}}} \tag{4.5.8}$$

where $Q_{compSPCorr}$ is the corrected compressor mass flow rate set-point, which is given by:

$$Q_{compSPCorr} = Q_{compSP}\frac{\sqrt{T_{uc}}p_{ref}}{\sqrt{T_{ref}}p_{uc}} \tag{4.5.9}$$

To protect the turbocharger, the compressor pressure ratio set-point (4.5.6) is limited by a maximal compressor pressure ratio $PR_{compmax}$. This allows avoiding to surpass the maximal turbocharger speed N_{tmax}. According to (3.3.31), the maximal compressor pressure ratio can be defined as follows:

$$PR_{compmax} = datamap_{PRcomp}\left(Q_{comp}\frac{\sqrt{T_{uc}}p_{ref}}{\sqrt{T_{ref}}p_{uc}}, N_{tmax}\frac{\sqrt{T_{ref}}}{\sqrt{T_{uc}}}\right) \tag{4.5.10}$$

We update the compressor pressure ratio set-point by using the minimum between (4.5.6) and (4.5.10). This allows limiting the turbocharger speed. The turbine speed set-point (4.5.8) is necessary to establish the compressor efficiency at engine set-point conditions. This efficiency is calculated by using the compressor efficiency data-map (3.3.32) as follows:

$$\eta_{compSP} = datamap_{etacomp}\left(Q_{compSPCorr}, N_{tSP}\frac{\sqrt{T_{ref}}}{\sqrt{T_{uc}}}\right) \tag{4.5.11}$$

From (4.5.1), (4.5.6), (4.5.7), (4.5.11), the compressor power set-point can be expressed by using (3.3.35) as:

$$P_{compSP} = \frac{Q_{compSP}c_pT_{uc}}{\eta_{compSP}}\left[\left(\frac{p_{dcSP}}{p_{ucSP}}\right)^k - 1\right] \tag{4.5.12}$$

where $k = (\gamma-1)/\gamma$. To obtain the turbine power set-point, consider the reduced dynamics of the turbocharger given by [55]:

$$\dot{P}_{comp} = \frac{1}{\tau_t}(P_t - P_{comp}) \tag{4.5.13}$$

Solving for P_t, the turbine power set-point can finally be defined in terms of the compressor power set-point as:

$$P_{tSP} = P_{compSP} + \tau_t\dot{P}_{compSP} \tag{4.5.14}$$

With (4.5.14), the open-loop part of the boost pressure control is completed. However, in order to compensate for modeling errors associated with the turbine power set-point generation, a PI controller is added. This PI uses the boost pressure error to correct the power turbine set-point as shown in Figure 4.4. As the model used to determine the open-loop controller is assumed to be representative of the engine air system, then the

effort made by the PI controller is small (around 10% maximum) in comparison with the open-loop control. The final turbine power set-point is then given by:

$$P_{tSP} = P_{compSP} + \tau_t \dot{P}_{compSP} + K_p(p_{im} - p_{imSP}) + sat_{vgt} K_i \int (p_{im} - p_{imSP}) \tag{4.5.15}$$

where sat_{vgt} is a variable associated with an anti-windup system and K_p and K_i are the proportional and integral PI constants, respectively. This set-point is used by the VGT positioning algorithm in order get the best VGT position according to the engine operating conditions and turbine physical constraints. This VGT positioning algorithm is the main concern in the next section.

4.5.2 Optimal VGT Positioning

In this section, we propose an algorithm to obtain a VGT position from a turbine power set-point without using an exhaust manifold pressure measurement. We start by defining the turbine mass flow rate, as a function of the VGT position, the pressure ratio and some engine operating conditions vector ϖ:

$$Q_t(x_{vgt}, PR_t, \varpi) = datamap_{Qt}\left(x_{vgt}, N_t \frac{\sqrt{T_{ref}}}{\sqrt{T_{em}}}, \frac{p_{em}}{p_{dt}}\right) \frac{p_{em}\sqrt{T_{ref}}}{p_{ref}\sqrt{T_{em}}} \tag{4.5.16}$$

where $\varpi = [N_t, p_{dt}, T_{em}]$. The turbine power can also be given as a function of x_{vgt}, the turbine pressure ratio and ϖ according to (3.3.42) as:

$$P_t(x_{vgt}, PR_t, \varpi) = Q_t(x_{vgt}, PR_t, \varpi) c_p T_{em} \eta_t(x_{vgt}, PR_t, \varpi) \left[1 - \left(\frac{1}{PR_t}\right)^k\right] \tag{4.5.17}$$

where the turbine efficiency η_t is also provided by a data-map, which is a function of the corrected turbine speed N_{tcorr}, the turbine pressure ratio PR_t and the VGT position as presented in (3.3.39). The VGT positioning problem can be formulated as the problem of finding the VGT position such that the turbine power (4.5.17) is as close as possible to the desired turbine power P_{tSP}. However, as the exhaust manifold pressure p_{em} is assumed to be unavailable, this problem is very challenging.

To address the VGT positioning problem, define a vector of fixed VGT positions as follows:

$$\vec{x_{vgt}} = [x_{vgt\_1}, x_{vgt\_2}, ..., x_{vgt\_l}], \quad x_{vgt\_i} \in [0, 100\%], \text{ for all } i \in [0, 1, ..., l] \tag{4.5.18}$$

where l is the number of VGT positions considered by the positioning algorithm. The larger l, the higher the algorithm resolution. Let us first consider the following hypothesis:

Hypothesis 4.5.1.

- *The dynamics of the exhaust pressure are much faster than the dynamics of the exhaust manifold temperature and the engine output mass flow rate.*

This hypothesis implies that when a sudden change of x_{vgt} occurs, the exhaust manifold pressure changes much faster than the engine operating conditions, namely the engine output mass flow rate Q_{eo} and ϖ. In other words, after a very short period of time, the turbine mass flow rate stabilizes once again to $Q_{eo} - Q_{egrh}$. Due to the relatively large inertia of the air-path components such as the turbocharger and the engine itself, Hypothesis 4.5.1 is a reasonable assumption.

As seen in Section 4.4, the exhaust manifold pressure can be found for a given Q_t, x_{vgt} and ϖ by means of the numerically efficient method given in (4.4.10). This method can be adapted to solve the problem of estimating the turbine pressure ratio for each position described by $\vec{x_{vgt}}$ with engine operating conditions Q_t and ϖ. Using the numerical scheme of Section 4.4, the solution of (4.5.16) can be expressed in a simplified form as:

$$\vec{PR}_t = f_{PR}(\vec{x_{vgt}}, Q_t, \varpi) \tag{4.5.19}$$

where $\vec{PR}_t$ is a vector that contains the turbine pressure ratios associated with each element of $\vec{x_{vgt}}$. According to Hypothesis 4.5.1, Q_t can be defined in terms of the engine operating conditions as:

$$Q_t = Q_{eng} + Q_f - Q_{egrh} \tag{4.5.20}$$

where Q_f is the fuel mass flow rate. For each element of $\vec{x_{vgt}}$ there is a respective $\vec{PR}_t$, which can be considered as a prediction of what would be the turbine pressure ratio if the VGT position is changed for the operating conditions ϖ and Q_t. This can also be extended to the turbine power by evaluating (4.5.17) with $\vec{x_{vgt}}$ and $\vec{PR}_t$, which gives the respective turbine power $\vec{P}_t(\vec{x_{vgt}}, Q_t, \varpi)$ associated with each position VGT described by $\vec{x_{vgt}}$. In other words, $\vec{P}_t$ gives the turbine power profile with respect to the VGT position. It is clear that this power profile changes with respect to time as it depends on the engine operating conditions.

To establish the proper VGT position from $\vec{P}_t$, we define a function that describes the difference between the desired turbine power P_{tSP} and $P_t(\vec{x_{vgt}}, Q_t, \varpi)$ as:

$$\vec{G}(\vec{x_{vgt}}, Q_t, \varpi) = |P_t(\vec{x_{vgt}}, Q_t, \varpi) - P_{tSP}| \tag{4.5.21}$$

Choosing a VGT position such that $\vec{G}$ is minimized is a natural criterion to solve the VGT positioning problem. However, this criterion is not enough because there may be many VGT positions where $\vec{G}$ is minimal, implying that there are more than one VGT position such that the desired turbine power is obtained. To illustrate this issue, a case where $\vec{G}$ has more that one minimum is presented in Figure 4.19, which is a curve obtained in an actual Diesel engine cycle.

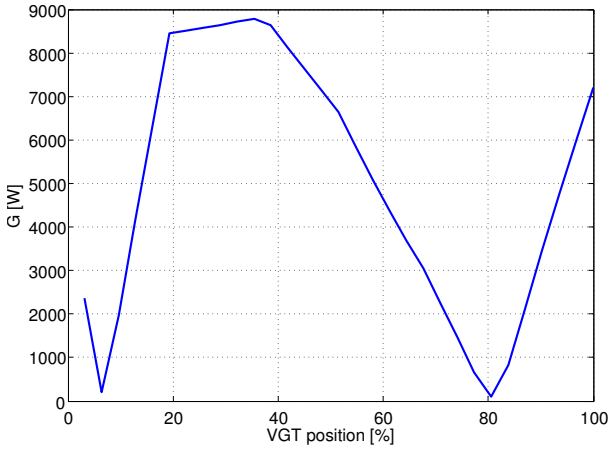

Figure 4.19: Example of a plot of $\vec{G}$

As depicted in Figure 4.19, there are two different VGT positions that give the required turbine power. The behavior of the turbine power profile is not convex and therefore, gradient based strategies should be avoided when solving the VGT positioning problem. This is why an heuristic method is considered to address this problem by defining a finite number of VGT positions in (4.5.18). For larger sizes of $x_{\vec{vgt}}$, greater resolution is obtained in the turbine power profile, but also higher CPU calculation load is required. This non-convexity of the VGT power profile is one of the reason why purely closed-loop control strategies may not be advised for boost pressure control. Another issue that arises from the formulation presented in (4.5.21) is that the physical constrains (such as the maximal admissible turbine pressure ratio of the turbocharger) are not taken into account.

To address the multiple possible VGT positioning solutions and the turbine physical constraints, we add two additional terms to (4.5.21):

$$\begin{aligned}\vec{G}_{ex}(x_{\vec{vgt}}, Q_t, \varpi) =& |\vec{P}_t(x_{\vec{vgt}}, Q_t, \varpi) - P_{tSP}| + max(\vec{PR}_t - PR_{max}, 0)R_{vgt} \\ &+ (\vec{PR}_t - 1)Q_{vgt}\end{aligned} \tag{4.5.22}$$

where PR_{max} is the maximal admissible turbine pressure ratio and R_{vgt} and Q_{vgt} are some constants that allow giving weight to each of the additional terms. With this formulation we obtain the following:

- The first term of (4.5.22) identifies the best VGT positions to reach the desired turbine power P_{tSP};
- The second term of (4.5.22) avoids the turbine pressure ratio to surpass PR_{max}. The value of R_{vgt} gives the weight for this term, which should be large in order to set a hard constraint;
- The third term of (4.5.22) allows choosing between two or more minimums of $\vec{G}$. The criterion chooses the VGT position that has the smallest associated turbine pressure

ratio. This allows increasing the engine efficiency as the engine back pressure is reduced.

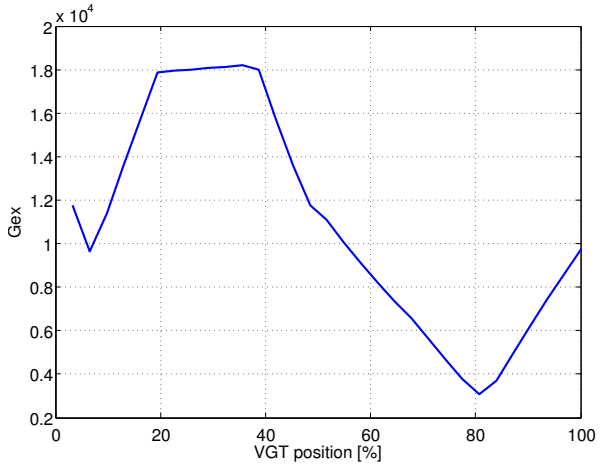

Figure 4.20: Example of a plot of $\vec{G}_{ex}$

Under the same conditions of the example presented in Figure 4.19, Figure 4.20 is obtained using (4.5.22). As depicted, only one minimum is obtained which is the VGT position that provides the turbine power closest to the set-point with the smallest turbine pressure ratio.

To control the boost pressure, the VGT positioning problem can be formulated for a given P_{tSP} as follows:

$$x^*_{vgt} = \arg\min_{x_{vgt}} \{\vec{G}_{ex}(\vec{x_{vgt}}, Q_t, \varpi)\} \tag{4.5.23}$$

where x^*_{vgt} is the optimal VGT position such that (4.5.22) is minimized. The optimization problem (4.5.23) has to be solved every time step in order to obtain the VGT position that provides the turbine power closest to P_{tSP}, and thus enabling to control the boost pressure.

Note that in (4.5.18), the VGT position can only take a finite number of values, therefore providing a piecewise continuous VGT control signal. The greater is l, the less discontinuous is the VGT position signal. These discontinuities could induce some chattering in the VGT position, which is an undesirable behavior for the air-path control. However, this problem can easily be addressed by filtering the VGT position signal by using, for example, a first order low-pass filter.

One of the most interesting features of the proposed VGT positioning algorithm is that the saturation of the VGT can be determined in terms of turbine power instead of VGT position, as usually formulated in the literature. The saturation is reached when the turbine power cannot reach the desired turbine power P_{tSP} for any VGT position. Considering directly the turbocharger saturation in terms of turbine power is a more natural

approach than using the VGT position extrema, since the turbine power is what really modifies the turbocharger dynamics. Moreover, the information from the power profile $\vec{P}_t$ gives the VGT position where the maximal or minimal turbine power is obtained, which is often not found at the VGT extrema.

In supercharged air-path architectures, it is common to operate the VGT at the saturation limits. Indeed, when the engine operates in light loads, the system controllability is very low. Controlling the boost pressure under these conditions is very challenging, specially when using closed-loop control methods. Purely closed-loop methods usually address this issue by relieving the control with a fixed VGT position. On the other hand, our strategy allows setting the VGT position such that (4.5.22) is minimized (turbine power closest to the set-point while respecting the turbine physical constraints and minimizing the engine back pressure), even if the supercharging system is saturated. Also, our approach identifies when the VGT saturates, which is a crucial information for the adequate operation of the boost pressure control since it can avoid instabilities that may arise from the PI used in the P_{tSP} generation. For example, this information can be used by an anti-windup system.

To generate a signal that allows determining whether the VGT is saturated, consider the following strategy:

$$sat_{vgt} = \left\{ \begin{array}{ll} sat_{vgt} = 0, & \text{if} \quad G(x^*_{vgt}, \varpi) < L_{vgt}(P_{tSP}) \\ sat_{vgt} = 1, & \text{otherwise} \end{array} \right\} \tag{4.5.24}$$

where $L_{vgt}(P_{tSP})$ is a threshold that allows establishing the turbine saturation. This level can be defined as a percentage of the desired turbine power. sat_{vgt} is an output that indicates whether the turbine is saturated or not and can be used to stop the integral action of a PI control as proposed in (4.5.15). With this we conclude the presentation of our boost pressure control strategy.

To summarize, the main features of the proposed VGT positioning method are:

- no further turbine model reductions have to be developed as the VGT data-maps are directly used (e.g. orifice equations and input transformations). This results in a faster conception and calibration process;
- the effect of the turbocharger speed on the turbine power is taken into account, which is often neglected when reducing the turbine models;
- the VGT is positioned optimally even when the air-path controllability is low;
- the saturation of the VGT is defined in terms of power instead of VGT position;
- the physical turbine constraints are added to the VGT positioning algorithm.

In the next section, we evaluate the performance of the proposed boost pressure control along with the novel VGT positioning method.

4.5.3 Boost Pressure Control Simulation Results

The boost pressure control approach presented in this thesis is evaluated using the model developed in Chapter 3 along with an engine cycle that requires a significant use of the supercharging system. The VGT positioning algorithm is evaluated by defining three different sizes of $\vec{x_{vgt}}$ with the purpose of illustrating the effect of increasing the resolution of the turbine power profile $\vec{P_t}$ in the boost pressure control performance. In the simulation, the complete air-path control architecture has been considered, meaning that the control of the air fraction and EGR proportion is also operative. This allows verifying the effectiveness of the complete air-path control architecture and the influence of the air fraction regulation on the boost pressure control.

For the results presented in this work, the following boost pressure controller parameters have been chosen: $K_p = 0.08$, $K_i = 0.005$, L_{vgt} has been chosen as 5% of P_{tSP}, $R_{vgt} = 10000$ and $Q_{vgt} = 0.1$. These parameters have been calibrated in simulation. Further adjustment can be easily carried out if necessary by modifying the PI control parameters. This procedure is typically well known by technicians.

Figures 4.21, 4.22 and 4.23 present the simulation results for $\vec{x_{vgt}}$ sizes of 7, 14 and 28, respectively. The boost pressure, the VGT position and the saturation signal sat_{vgt} are plotted.

As depicted in the simulation results of Figures (4.21), (4.22) and (4.23), all the three VGT positioning configurations control properly the intake manifold pressure. However, significant differences can be identified between them. In Figure 4.21, a ripple appears in the intake manifold pressure along with some glitches in the position of the VGT (see for instance Figure 4.21 at t=10, 18 and 48s). The VGT saturation signal sat_{vgt} seems to be switching excessively which suggests that the turbine power profile resolution may not be high enough. However, these issues can be addressed by increasing the amount of VGT positions in the vector $\vec{x}_{vgt}$. Figure 4.22 shows the results for 14 VGT positions. A significant improvement in terms of smoothness of the intake manifold pressure is obtained, as well as an elimination of the VGT position glitches that appear in Figure 4.21. Also, the saturation signal of the VGT is better identified in comparison with the results of Figure 4.21, which allows to better control the boost pressure. For 28 VGT positions, an even better response is obtained is terms of smoothness and VGT saturation. However, as the amount of VGT positions increases, also does the CPU calculation load. From the results obtained in this work, a $\vec{x_{vgt}}$ size of 14 seems to be suitable for intake manifold pressure control without increasing significantly the calculation time.

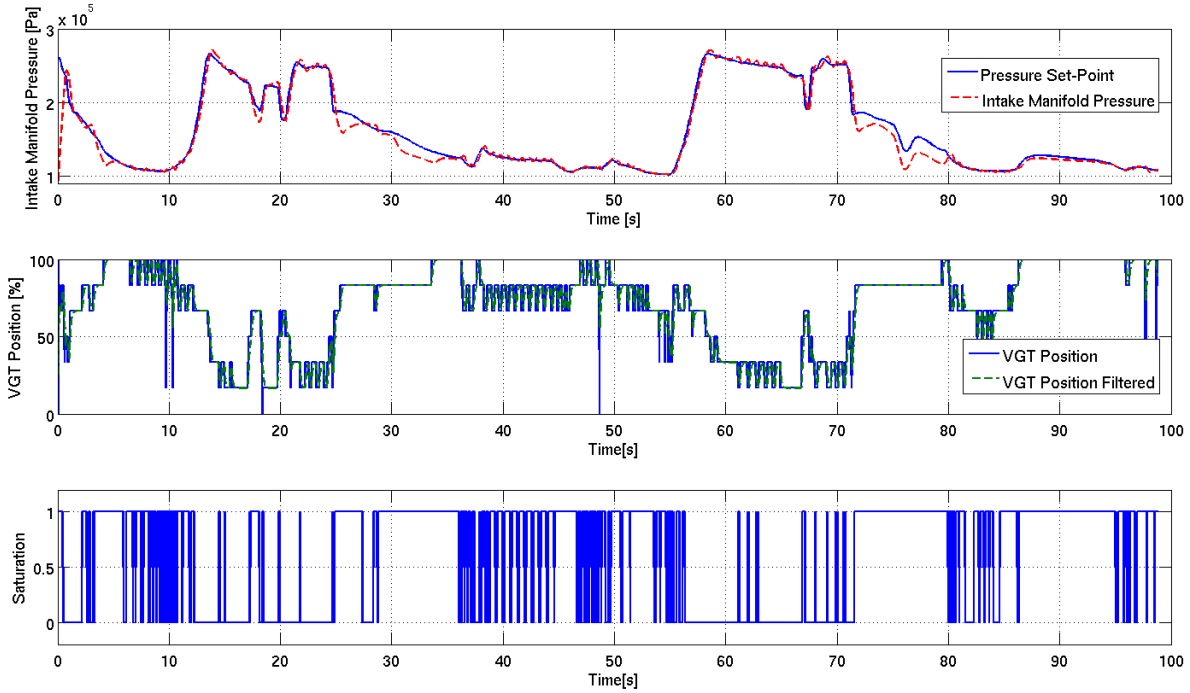

Figure 4.21: Boost pressure control simulation for a $\vec{x_{vgt}}$ size of 7

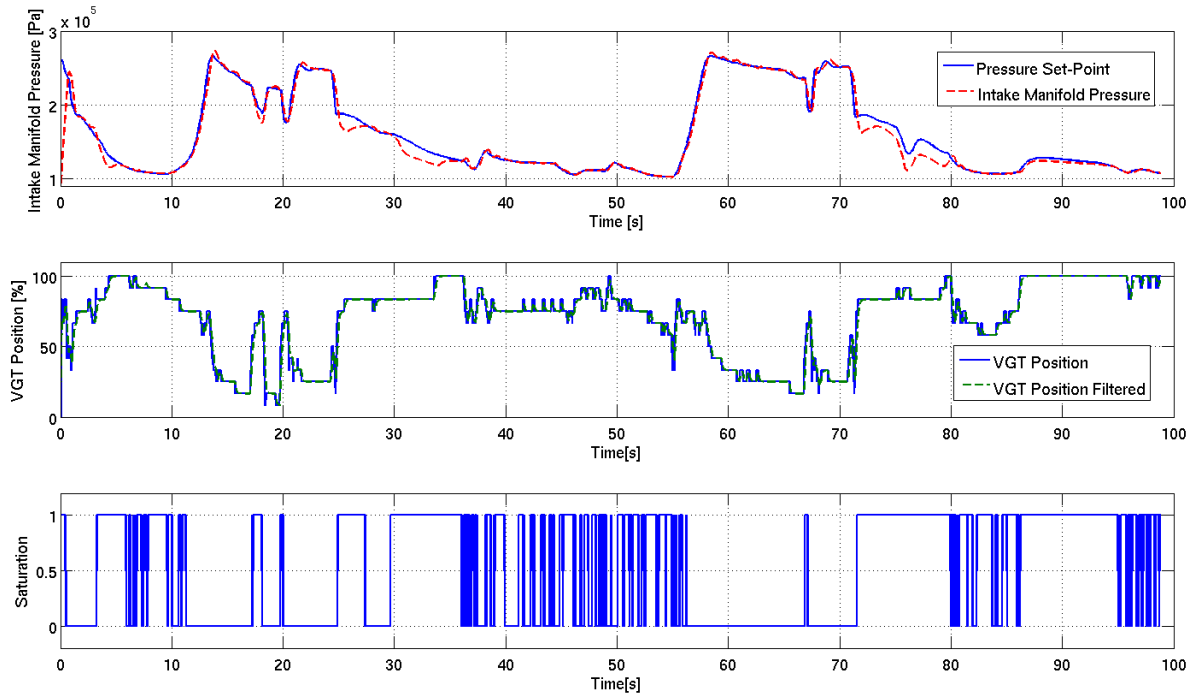

Figure 4.22: Boost pressure control simulation for a $\vec{x_{vgt}}$ size of 14

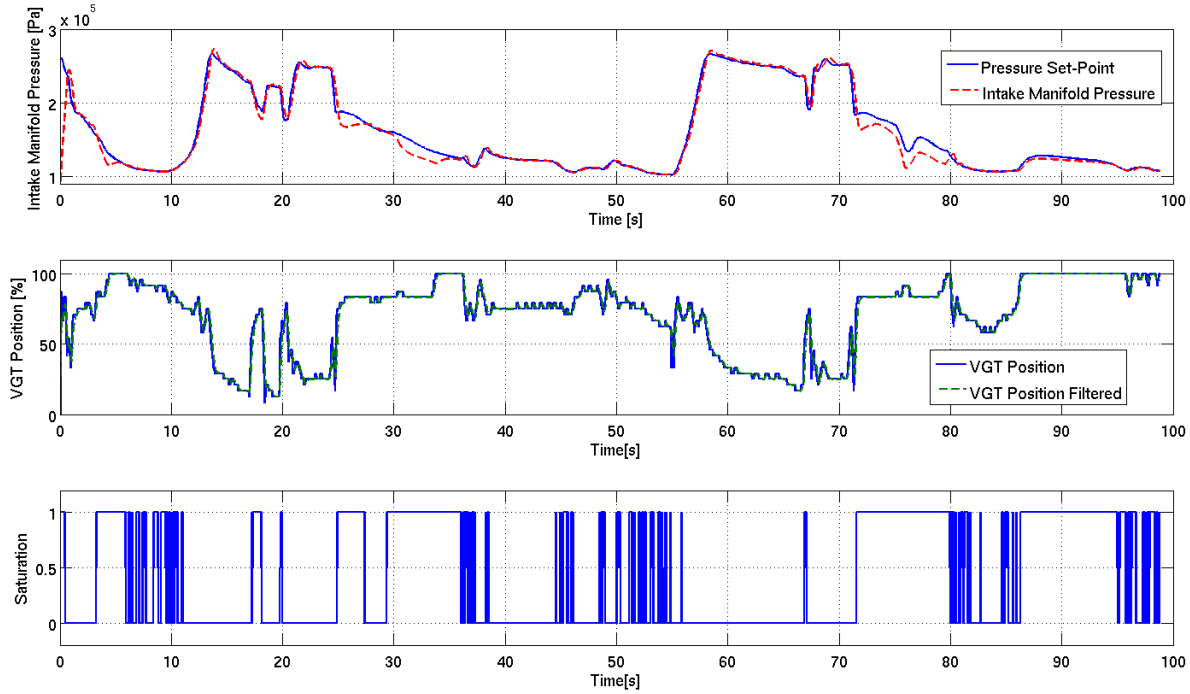

Figure 4.23: Boost pressure control simulation for a $x_{\vec{vgt}}$ size of 28

From the results of Figures 4.21, 4.22 and 4.23, some important characteristics of the air system and the boost pressure control can be observed. For example, from 25 to 35 and 72 to 80 seconds in all cases, the supercharging system is not able to reach the reference pressure, which can be confirmed by the respective saturation signals. However, note that even though the VGT is saturated, the best VGT position is set which in this case is not at the extremity of the VGT position but at 80%. This implies that a traditional VGT positioning algorithm would continue to open the VGT to try to reach the reference, which would end up in a greater intake pressure tracking error as the optimal VGT position is 80%. This is an example where working with a turbine power formulation for the VGT positioning is advantageous. From 87 to 95 seconds, the turbine is once again saturated. However in this case, the full open VGT is the appropriate VGT position. There are also some engine zones, for example from 6 to 12 seconds and 36 to 56 seconds, where the intake manifold pressure is marginally controllable, implying that the system is at the edge of saturation. These engine operating conditions are very challenging in terms of boost pressure control. Nevertheless, the proposed VGT positioning algorithm permits a good tracking of the pressure reference while having a well behaved VGT position signal.

4.6 Chapter Summary

In this chapter, an alternative air-path control architecture has been proposed in order to control the engine intake manifold pressure, fresh air fraction and the EGR proportion. The main differences obtained with respect to other existing air-path control architectures are: a closed-loop formulation to estimate the air fraction in the intake manifold, an air fraction control that takes into account the EGR proportion, the estimation of the exhaust manifold pressure and a more effective way of positioning the VGT, which allows controlling the boost pressure without a measurement of the exhaust manifold pressure.

Two 0D model-based observers were proposed to simultaneously estimate the LP-EGR mass flow rate and the air fraction in the intake manifold. The LP-EGR mass flow rate observer has been designed using a sliding mode approach while the air fraction estimation has been obtained by means of a robust Luenberger-like observer formulation. The estimators convergence is guaranteed using a Lyapunov stability approach and linear matrix inequalities for the LP-EGR mass flow rate and the air fraction, respectively.

Based on an LPV representation of a reduced physical model of the air fraction dynamics, an air fraction control that takes into account a desired EGR proportion has been considered. A virtual control input has been defined with the purpose of canceling out some additive terms which allow obtaining an appropriate air fraction LPV representation for a state feedback control design. An LPV-LQR state feedback control approach has been considered for the intake manifold air fraction control because of its simplicity as well as its intrinsic robustness with respect to model uncertainties. To ensure the existence of the optimal control, the complete controllability of the LPV system is verified using a polytopic formulation.

An exhaust manifold pressure estimator has been designed using directly the data-maps of the VGT and a non-iterative highly efficient numerical scheme. This iteration-free estimator takes into account the effect of the turbine speed on the turbine mass flow rate which allows achieving more accurate pressure estimations. A very interesting feature of the method is that no model calibration has to be performed for the estimator, the only parameter to choose being α_t (it allows adjusting the convergence speed and the robustness of the estimator).

Finally, a boost pressure control for Diesel engines has been developed. The regulator is a combination of an open and a closed-loop controller that has shown to be a good approach for addressing this control problem. Based on an engine air system model, a transformation from a boost pressure set-point to a turbine power set-point is performed. A novel VGT positioning algorithm that provides a VGT position for a given turbine power set-point while minimizing the turbine pressure ratio and respecting the physical constraints of the turbine has been proposed. This approach exhibits many advantages over traditional VGT positioning strategies such as: no exhaust manifold pressure mea-

surement required, the direct use of the turbine data-maps and a good behavior of the system for low controllability engine operating conditions. The algorithm also provides information about the power saturation of the VGT, which is valuable for anti-windup systems.

Chapter 5

1D Engine Air-Path Modeling

As seen in the previous chapter, zero-dimensional (0D) models have been successfully used to observe and control the Diesel engine air-path. However, as the complexity of the engine air-path increases and the engine emission regulations become stricter, the intrinsic limitations of 0D approaches start to restrict the capabilities of the modern control strategies. For example, one of the most significant limitations of 0D engine air-path modeling is its inability to represent the mass transport phenomenon. Indeed, the fact of not taking into account the air fraction transport in modern dual-loop EGR architectures can introduce a systematic degradation of the engine emission performance. The negative impact of the mass transport is particularly relevant when using LP-EGR due to the relative long distance between the compressor and the engine intake manifold. Thus, it is crucial to propose alternative modeling solutions to improve the future model-based control of Diesel engines.

One-dimensional (1D) modeling is a natural alternative for 0D control-oriented modeling, since it allows representing the major features of unsteady flow in the engine air-path. Indeed, 1D air-path modeling enables to address many of the limitations associated with 0D formulations, including the representation of the air fraction transport (e.g. in Appendix A.1, where we present an illustration of the advantages of using a 1D over 0D strategies to model the air fraction dynamics). However, 1D modeling of unsteady flow implies a specific resolution of Euler's equations, leading to much more complex problems, such as the wave action methods and boundary conditions resolution. For this reason (among others), 1D control strategies are significantly less explored in the literature than 0D approaches.

The control and observation of 1D systems, more precisely, systems described by 1D partial differential equations (PDE), is currently a very active research subject in the control community, suggesting that 1D modeling for control could be a natural evolution for the current engine air-path control strategies. Moreover, the development of 1D control-oriented models is of significant importance for the air-path control as it would

allow designing more advanced control and estimation strategies capable of improving the engine emission performance. To synthesize control laws for 1D systems, it is essential to built a 1D control-oriented modeling platform (a set of flexible tools that allows to easily simulate the evolution of the flow) with low calculation load, good predictability and flexibility. Unfortunately, to the best of our knowledge, very few works have been done in this area, implying that there are still many issues to address to obtain a suitable tool for 1D air-path modeling for control purposes. In [69], a first approach to a 1D control-oriented modeling platform has been considered by formulating alternative solutions of the non-homentropic (change of entropy level) inflow and outflow boundary problem.

Indeed, the boundary problem resolution is one of the most difficult subjects to address when building a control-oriented model of a Diesel engine air-path. The classical restriction boundary problem resolution methods found in the literature are generally based on an isentropic flow assumption, which significantly simplifies the boundary problem [10] [101]. However, this hypothesis is not verified experimentally as higher flow rates are systematically obtained through the restrictions. Therefore, experimental discharge coefficients are generally introduced to deal with this issue artificially [32] [33] [91]. The drawback of this strategy is that experimental measurements must be performed, which increases the costs of the model calibration. Additionally, when no experimental data are available to determine the discharge coefficients, simulation results can be in total disagreement with bench measurements. Another technique consists in using a computational fluid dynamics code as a numerical test bench [31]. However, this technique is time consuming and experimental results are necessary to validate the numerical bench. This motivates the search for restriction models and non-homentropic restriction boundary resolution methods capable of offering a greater predictability and more flexibility in terms of modeling capabilities.

In this chapter, we focus on the non-homentropic outflow and intra-pipe problem. More precisely, we develop two innovative non-homentropic boundary resolution methods which are independent of the physical boundary restriction model. In other words, these boundary resolution methods permit introducing more predictable physical boundary models into the boundary resolution schemes without the need of adding artificial discharge coefficients. Moreover, the boundary resolution methods given in this chapter allow creating the interaction between the physical model of the boundary and the in-pipe numerical scheme while always being physically consistent with the non-homentropic formulation. The principal benefits obtained by the proposed boundary resolution methods are:

- increase of the flexibility and predictability of the 1D modeling platforms;
- reduction of model calibration (avoidance of artificial correction coefficients);
- reduction of CPU calculation load.

which are specially interesting characteristics for the control-oriented modeling platforms.

Chapter Structure This chapter begins with a review on: the fundamental equations to model a 1D compressible flow in a pipe, the basic equations and hypotheses associated with the boundary conditions and some of the most representative boundary resolution methods. In Section 5.2, we provide some alternative non-homentropic outflow and intra-pipe restriction quasi-steady (QS) models that allow improving the predictability of the 1D unsteady flow modeling. Also, we detail the methodologies to store the solution of these QS models into data-maps and we perform a comparison between the different physical boundary formulations.

In Section 5.3, we propose outflow and intra-pipe boundary resolution methods that do not take into account the classical isentropic contraction assumption. More precisely, we develop two methods capable of solving the non-homentropic boundary problem independently of the QS approaches considered to model the restriction at the boundaries. Additionally, other improvements are brought to the resolutions methods, such as more efficient numerical schemes and reference-free entropy correction. Finally, in Section 5.4, the performance of the outflow and intra-pipe non-homentropic resolution methods is experimentally evaluated by means of an apparatus specially designed for the validation of unsteady flow modeling strategies. We illustrate the benefits that arise from the proposed non-homentropic boundary resolution methods.

Publications

The main contributions presented in this chapter are the principal subject of the following publications:

- F. Castillo, E. Witrant, V. Talon, L. Dugard. Restriction Model Independent Method for Non-Isentropic Outflow Valve Boundary Problem Resolution, SAE Technical Paper, 2012, doi:10.4271/2012-01-0676;
- F. Castillo, E. Witrant, L. Dugard, V. Talon, David Chalet, Pascal Chesse. Intra-Pipe Restriction Non-Homentropic Boundary Resolution Method, SAE Technical Paper 2013-01-0582, doi:10.4271/2013-01-0582, 2013.

5.1 Literature Review

5.1.1 Pipe Flow Governing Equations and Discretization Schemes

The fundamental equations of fluids mechanics that describe the evolution of a compressible flow are derived using three fundamental principles: the mass conservation, the energy conservation and the momentum conservation. These conservation laws define the rate

of change of a conserved property in a fixed volume as a result of the net effect of the flux of the property across the boundaries and the changes due to internal and external sources. According to this, we consider Figure 5.1 to represent the flow of a compressible fluid through an infinitesimal section of pipe.

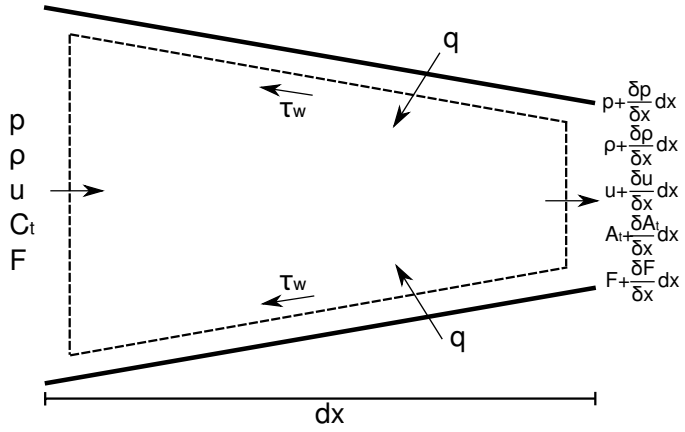

Figure 5.1: Schematic diagram of control volume in general duct

As depicted in Figure 5.1, we consider an ideal compressible fluid with pressure p, density ρ, particle speed u and air fraction F that runs through a pipe of infinitesimal length dx and cross-sectional area C_t. The pipe is subject to cross-sectional area variation, heat exchanges q and wall shear stress τ_w and each property of the fluid undergoes a variation along the infinitesimal length of the pipe.

To keep the mathematical developments of this thesis as simple as possible, let us consider the following hypotheses for the formulation of the fundamental equations that characterize the evolution of a 1D compressible flow in a pipe:

Hypothesis 5.1.1.

- *continuous medium satisfying the compressible ideal gas*
- *fluid properties approximately uniform across any cross-section*
- *flow considered to be quasi-one-dimensional*
- *flow with no viscosity (inviscid flow)*

According to Hypotheses 5.1.1, the variations on the fluid properties along a pipe are governed by the following three fundamental PDE:

The conservation of mass equation

$$\frac{\partial(\rho C_t)}{\partial t} + \frac{\partial(\rho u C_t)}{\partial x} = 0 \tag{5.1.1}$$

The momentum equation

$$\frac{\partial(\rho u C_t)}{\partial t} + \frac{\partial(\rho u^2 + p)C_t}{\partial x} - p\frac{\partial C_t}{\partial x} + \frac{1}{2}\rho u^2 f \pi D = 0 \tag{5.1.2}$$

The energy equation

$$\frac{\partial(\rho e_0 C_t)}{\partial t} + \frac{\partial u h_0 C_t}{\partial x} - q\rho C_t = 0 \tag{5.1.3}$$

where f is the friction factor, D an equivalent diameter of the duct, e_0 the specific internal energy, h_0 the specific enthalpy and q the heat transfer per unit of mass. As in this thesis we are also interested in modeling the dynamics of the air fraction, consider the change in air fraction (a non-reacting chemical species) across a control volume of length dx as follows [101]:

$$\frac{\partial(\rho C_t F)}{\partial t} + \frac{\partial(\rho u C_t F)}{\partial x} = 0 \tag{5.1.4}$$

Assuming that there are no diffusion and chemical reactions, the fundamental equations (5.1.1), (5.1.2), (5.1.3) and (5.1.4), which are also known as the one-dimensional Euler equations, can be rewritten in conservational and vectorial form as follows:

$$\frac{\partial \mathbf{W}}{\partial t} + \frac{\partial \mathbf{F}(\mathbf{W})}{\partial x} + \mathbf{C}(\mathbf{W}) = 0 \tag{5.1.5}$$

where

$$\mathbf{W} = \begin{bmatrix} \rho C_t \\ \rho u C_t \\ \rho e_0 C_t \\ \rho F C_t \end{bmatrix}; \mathbf{F}(\mathbf{W}) = \begin{bmatrix} \rho u C_t \\ (\rho u^2 + p) C_t \\ \rho u h_0 C_t \\ \rho u F C_t \end{bmatrix}; \mathbf{C}(\mathbf{W}) = \begin{bmatrix} 0 \\ -p\frac{dC_t}{dx} \\ 0 \\ 0 \end{bmatrix} + \begin{bmatrix} 0 \\ \rho G C_t \\ -\rho q C_t \\ -\rho F C_t \end{bmatrix} \tag{5.1.6}$$

and $G = \frac{4}{2D} u \mid u \mid f$.

In general, it is not possible to obtain analytical solutions for the first-order hyperbolic PDE given in (5.1.5). Therefore, numerical techniques are typically used to discretize (5.1.5), allowing to form a set of algebraic relationships that can be solved by means of a digital computer. There are several discretization strategies available in the literature to approximate the solution of the in-pipe flow evolution [37] [89] [101] (by in-pipe, we mean that the solution at the boundaries is not considered, the solution of the boundary conditions is the main concern of the next sections). Indeed, this subject has been exhaustively investigated and many numerical schemes that can be considered as suitable for control purposes, have been proposed. In this thesis, we consider the MacCormack conservative explicit method along with a post-processing routine based on Total Variation Diminishing (TVD) to solve (5.1.5). This numerical technique has been chosen because of its good compromise between accuracy, robustness and computational load [101]. For more details on this method, refer to Appendix A.3.

5.1.2 Engine Air-Path Boundary Conditions

The boundary conditions play a major role in the simulation of the internal combustion engine air-path as they provide the amount of mass and energy that flows through the system. Thus, it is essential to accurately represent and solve the boundary problem of (5.1.5) in order to develop an effective 1D simulation platform for control purposes. In this section, we provide a literature review on some of the boundary problem resolution strategies classically used in engine air-path modeling. More precisely, we present the method of characteristics (MOC) for non-homentropic flow, which is a key tool for the boundary problem resolution. Then, we introduce the quasi-steady (QS) physical models of some of the most representative boundary conditions found in the engine air-path. Finally, we illustrate how the MOC along with a QS boundary formulation allows solving the boundary problem by presenting some classical works on boundary problem resolution by means of the MOC.

5.1.2.1 Method of Characteristics for Non-Homentropic Flow

The Method of Characteristics (MOC) is a finite difference, first-order accurate in space and in time technique based on a special formulation of the equations that characterize the flow of a compressible fluid (namely (5.1.5)). It was the dominant numerical technique for simulation of gas dynamics in engines air-paths until the 1980's, when it was replaced by modern finite differences schemes due to their greater accuracy and robustness (e.g. MacCormack method). However, nowadays the MOC still plays a very important role in the solution of the boundary conditions because of its versatility to incorporate the boundaries in the wave action numerical schemes [101]. Indeed, the MOC is a crucial tool for the resolution of the boundary conditions as it creates the interaction between the in-pipe numerical method (e.g. MacCormack scheme) and the physical model of the boundary. We do not detail the theory behind the MOC as it is not the main concern of this work, nevertheless if further details are required, refer to [10] and [101].

The notion of the Riemann invariants is the base of the MOC. Riemann invariants are mathematical transformations made on a system of quasi-linear first-order partial differential equations (such as (5.1.5)) to make them easier to solve. The Riemann invariants are constant along the characteristic curves of the hyperbolic PDE, which justifies the origin of the term "invariant". To better illustrate this concept, we depict in Figure 5.2 the notion of the characteristic curves and their respective Riemann invariants in time and space.

According to Figure 5.2, three characteristic curves are defined for (5.1.5): $dx/dt = u+a$, $dx/dt = u$ and $dx/dt = u-a$, where a is the speed of sound. For each of these three trajectories, there is a Riemann invariant associated, namely λ_L, s_S and β_R, respectively.

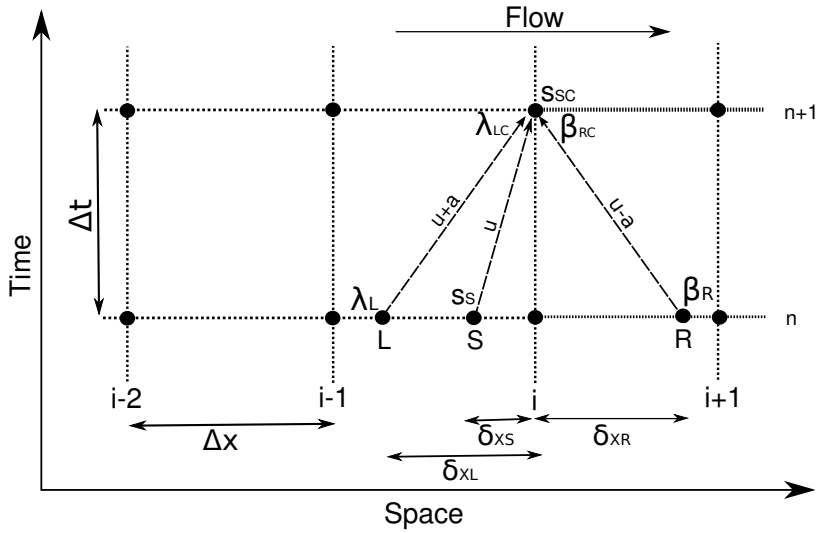

Figure 5.2: Method of characteristics schematic in time and space

As depicted in Figure 5.2, δ_{XL}, δ_{XS} and δ_{XR} are the distances from the finite element i and the respective Riemann invariant trajectory at time n. The Riemann invariants only remain constant under homentropic flow assumption; in other words, when there is no entropy creation or change of entropy level in the flow. Thus, an homentropic flow implies that $\lambda_L^n = \lambda_{LC}^{n+1}$, $s_S^n = s_{SC}^{n+1}$ and $\beta_R^n = \beta_{RC}^{n+1}$. For an homentropic flow, the Riemann invariants for (5.1.5) are defined as [101]:

$$\lambda_L^n = a_i^{n+1} + \frac{\gamma - 1}{2} u_i^{n+1} = a_L^n + \frac{\gamma - 1}{2} u_L^n \tag{5.1.7}$$

$$s_S^n = s_i^{n+1} \tag{5.1.8}$$

$$\beta_R^n = a_i^{n+1} - \frac{\gamma - 1}{2} u_i^{n+1} = a_R^n - \frac{\gamma - 1}{2} u_R^n \tag{5.1.9}$$

where s is the entropy. The Riemman invariants at L, S and R can be defined by means of a linear interpolation using the two closest finite elements as follows:

$$\lambda_L = \lambda_i + \frac{\delta_{XL}}{\Delta_X}(\lambda_i - \lambda_{i-1}) \tag{5.1.10}$$

$$S_R = S_i + \frac{\delta_{XS}}{\Delta_X}(S_i - S_{i-1}) \tag{5.1.11}$$

$$\beta_R = \beta_i + \frac{\delta_{XR}}{\Delta_X}(\beta_{i+1} - \beta_i) \tag{5.1.12}$$

The distances δ_{XR}, δ_{XS} and δ_{XL} can be calculated as follows (for further details, see [101]):

$$\frac{\delta_{XL}}{\Delta x} = \frac{\Psi_L \lambda_i - \Theta_L \beta_i}{\frac{\Delta x}{\Delta t} + \Psi_L(\lambda_i - \lambda_{i-1}) - \Theta_L(\beta_{i+1} - \beta_i)} \tag{5.1.13}$$

$$\frac{\delta_{XS}}{\Delta x} = \frac{\lambda_i - \beta_i}{\frac{\Delta x}{\Delta t}(\gamma - 1) + (\lambda_2 - \lambda_1) - (\beta_2 - \beta_1)} \tag{5.1.14}$$

$$\frac{\delta_{XR}}{\Delta x} = -\frac{\Psi_R \lambda_i - \Theta_R \beta_i}{\frac{\Delta x}{\Delta t} - \Psi_R(\lambda_i - \lambda_{i-1}) + \Theta_R(\beta_{i+1} - \beta_i)} \tag{5.1.15}$$

where

$$\Psi_R = \frac{3-\gamma}{2(\gamma-1)}, \quad \Theta_R = \frac{\gamma+1}{2(\gamma-1)}, \quad \Psi_L = \frac{\gamma+1}{2(\gamma-1)}, \quad \Theta_L = \frac{3-\gamma}{2(\gamma-1)} \tag{5.1.16}$$

Equations (5.1.7) - (5.1.16) imply that if the solution of (5.1.5) is known at time n, then the solution at time $n+1$ can be approximated by means of the MOC.

However, homentropic conditions are almost never obtained in a real flow due to the change of flow entropy level, friction, heat exchanges and pipe cross-sectional variations. Therefore, the Riemann invariants λ_L, s_S and β_R stop being constant along the trajectories $u+a$, $u-a$ and u, respectively. For this reason, the Riemann invariants have to be corrected in order to take these changes into account. As we are interested in using the MOC only at the boundaries, the changes of entropy due to the friction, pipe cross-sectional variations and thermal exchanges are neglected as the creation of entropy over one finite element is small in comparison with the entropy change along the whole pipe. On the other hand, the variation of entropy level has a significant effect at the boundaries, thus the MOC for non-homentropic flow is only formulated taking into account the variation of the Riemann invariants with respect to the flow entropy level [10] [69].

To formulate the MOC for non-homentropic flow, let us define the following non-dimensional speed of sound:

$$A = \frac{a}{a_{ref}} \tag{5.1.17}$$

and the entropy level as:

$$A_A = A\left(\frac{p_{ref}}{p}\right)^{\frac{\gamma-1}{2\gamma}} \tag{5.1.18}$$

where a_{ref} and p_{ref} are some speed of sound and pressure references. It has been shown in [10] that the variation of the Riemann invariants with respect to the change of entropy level is given by:

$$\delta\lambda = A_i^{n+1}\frac{dA_A}{A_{Ai}} \approx A_i^{n+1}\frac{A_{Ai}^{n+1} - A_{AL}^{n}}{A_{Ai}^{n+1}} \tag{5.1.19}$$

$$\delta\beta = A_i^{n+1}\frac{dA_A}{A_{Ai}} \approx A_i^{n+1}\frac{A_{Ai}^{n+1} - A_{AR}^{n}}{A_{Ai}^{n+1}} \tag{5.1.20}$$

Then, the corrected Riemann invariants at $n+1$ are given by:

$$\lambda_{LC}^{n+1} = \lambda_L^n + \delta\lambda, \quad \beta_{RC}^{n+1} = \beta_R^n + \delta\beta \tag{5.1.21}$$

Note that the values of the Riemann invariants (5.1.21) depend on the conditions at the point i at time $n+1$; more precisely, they depend on the non-dimensional speed of sound A_i^{n+1} and on the entropy level A_{Ai}^{n+1}, which are unknown. For the non-homentropic flow, the MOC does not provide an explicit expression of the Riemann invariants and therefore numerical methods have to be used to solve the boundary problem.

5.1.2.2 Classical Boundary Conditions Quasi-Steady Equations

In this section, we consider three of the main air-path boundary conditions: the inflow, outflow and intra-pipe restrictions. Other boundary conditions such as an inflow open end, outflow open end and sudden pipe area change are particular cases of the first three boundary conditions. We provide the traditional restriction boundary problem formulation for each of the considered cases with the purpose of illustrating how the boundary problem is established.

Inflow Restriction : Figure 5.3 presents the schematic of a pipe inflow restriction boundary.

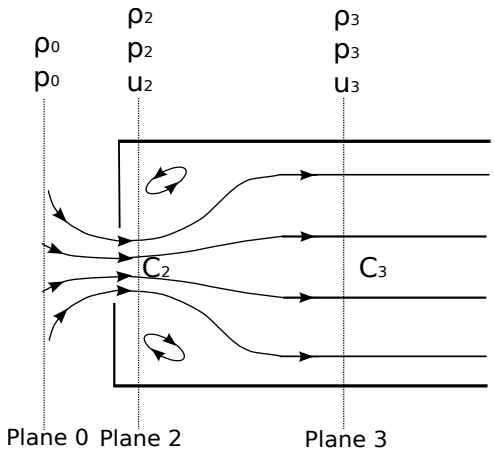

Figure 5.3: Inflow Restriction Schematic

As depicted in Figure 5.3, three quasi-stationary planes are defined in the inflow restriction boundary: the plane "0" represents the stagnation state ($u_0 = 0$) where a pressure p_0 and density ρ_0 are defined, plane "2" is located at the restriction throat and plane "3" is located just downstream of the restriction after the gas expansion. From the stagnation state, the

gas enters the pipe as a jet of cross-sectional area C_2, which then expands to occupy the full bore of cross-sectional area C_3 at plane "3". There are six unknown quantities, namely the pressure, particle velocity and density at planes "2" and "3", therefore six equations have to be defined to solve the inflow boundary problem. Typically, two formulations are considered: a first one for subsonic flow and a second one for sonic flow.

Consider the following hypotheses to formulate a momentum-based QS model for the inflow restriction boundary for subsonic flow [46]:

Hypothesis 5.1.2.

- *the flow is quasi-steady over the three planes;*
- *the energy is conserved over the three planes;*
- *the momentum between planes "2" and "3" is conserved;*
- *the contraction is isentropic between planes "0" and "2";*

Other hypotheses can be stated to formulate alternative inflow restriction quasi-steady models. However, for sake of simplicity, we develop only one. For more inflow boundary models, refer to [46]. To state the basic equations for the inflow QS model, we consider three conservational laws according to the Hypotheses 5.1.2: the energy conservation, the mass conservation and the momentum conservation. As the heat exchange and wall friction terms are removed (implicit in Hypotheses 5.1.2), the energy conservation between the three planes can be formulated as [101]:

$$a_0^2 = a_2^2 + \frac{\gamma - 1}{2} u_2^2 = a_3^2 + \frac{\gamma - 1}{2} u_3^2 \tag{5.1.22}$$

where γ is the specific heat ratio. The variable indexes are associated with the planes defined according to Figure 5.3. The mass conservation between the planes 2 and 3 is defined as [69]:

$$\frac{C_2 p_2 u_2}{a_2^2} = \frac{C_3 p_3 u_3}{a_3^2} \tag{5.1.23}$$

and the momentum equation between planes "2" and "3" is given by:

$$(p_2 + \rho_2 u_2^2) C_2 = (p_3 + \rho_3 u_3^2) C_3 \tag{5.1.24}$$

Additionally, the isentropic contraction between planes "0" and "2" is represented by the following equation:

$$\frac{p_0}{p_2} = \left(\frac{a_0}{a_2} \right)^{\frac{2\gamma}{\gamma - 1}} \tag{5.1.25}$$

Equations (5.1.22) - (5.1.25) provide five of the six equations required for the boundary problem resolution. The five equations are: the energy conservation between planes 0 and 2 and planes "2" and "3", the mass conservation between planes "2" and "3", the momentum conservation between 2 and 3 and the isentropic contraction between planes "0" and "2". However, note that none of these equations relates the boundary conditions with the in-pipe conditions. To address this issue, a sixth equation is formulated using the MOC. Indeed, the MOC enables to create the interaction between the in-pipe conditions and the boundaries. To illustrate this interaction, consider the representation of the MOC at the inflow boundary depicted in Figure 5.4:

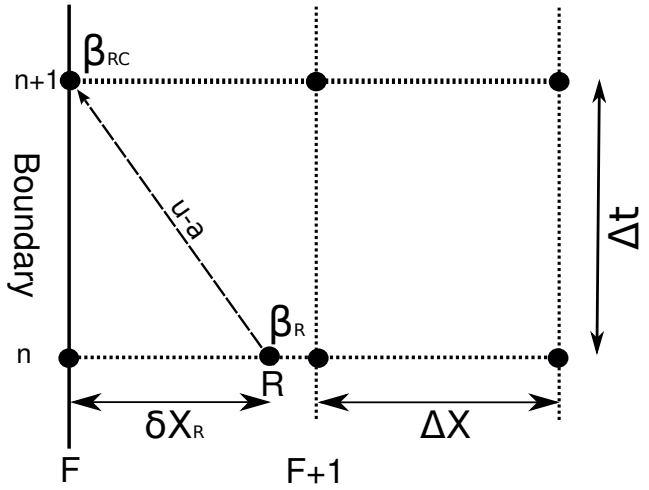

Figure 5.4: Inflow MOC Diagram

For sake of simplicity, we consider the MOC for homentropic flow. Using (5.1.9), the sixth equation for the solution of the boundary problem can be formulated, according to Figure 5.4, as:

$$\beta_R = a_F^{n+1} - \frac{\gamma - 1}{2} u_F^{n+1} = a_R^n - \frac{\gamma - 1}{2} u_R^n \tag{5.1.26}$$

where $a_F = a_3$ and $u_F = u_3$. Equation (5.1.26) completes the system of equations (5.1.22) - (5.1.26) required to solve the boundary problem. However, the solution of this system cannot be found analytically and therefore numerical methods have to be used to solve the boundary problem. The numerical methods applied to solve the boundary is what is known as the boundary resolution methods. In this thesis, we do not focus on the non-homentropic inflow boundary resolution methods as they have been already considered in details in [46]. Nonetheless, this introduction is crucial to establish the intra-pipe boundary problem.

As the pressure ratio across the partially open-end increases, sonic flow can occur at the restriction throat. Under these conditions, the behavior of the gas changes and therefore different considerations have to be taken into account to solve the boundary problem.

More precisely, in the case of sonic flow, the momentum equation (5.1.24) is replaced by the definition of sonic flow at the throat, which is given by:

$$u_2 = a_2 \tag{5.1.27}$$

With (5.1.27), six equations are obtained, allowing to formulate the inflow boundary problem for sonic flow.

As previously mentioned, it is systematically found that there is a significant deviation between the experimental results and the numerical boundary problem solution. Hence, many works focus on the development of discharge coefficients in order to artificially correct the modeling inaccuracies. These corrections are typically applied on the mass flow rate equation by calculating the ratio between the experimental and the model mass flow rates as follows:

$$(C_3 u_3 \rho_3)_{expe} = C_d (C_3 u_3 \rho_3)_{model} \tag{5.1.28}$$

Equation (5.1.28) implies that the boundary modeling inaccuracies are hidden behind the discharge coefficients C_d. This approach is widely used as it allows getting fairly accurate results. However, this technique requires experimental measurements in order to determine the artificial coefficient C_d, which increases significantly the costs of the model calibration.

Remark 5.1.1. Note that when $C_2 = C_3$, the inflow open-end boundary problem is obtained.

Outflow Restriction : Figure 5.5 presents the schematic of a pipe outflow restriction boundary.

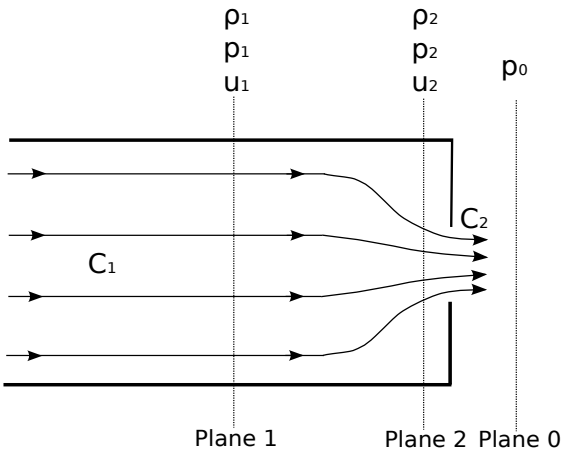

Figure 5.5: Outflow Restriction Schematic

For the outflow restriction boundary, also three quasi-steady planes are considered. The plane "0" represents the stagnation state where a pressure p_0 is defined, the plane 1 is

located upstream of the restriction and the plane "2" is located at the restriction throat. The gas exits the pipe of cross-sectional area C_1 by the outflow restriction throat as a jet of cross-sectional area C_2. As in the inflow boundary case, there are also six unknown quantities that have to be found to solve the boundary problem. These unknowns are: the pressure p, the particle speed u and the density ρ at planes"1" and "2". To illustrate how a outflow boundary problem is formulated, we consider the classical isentropic contraction based approach. Let define the following hypotheses in order to formulate the outflow boundary problem for subsonic flow:

Hypothesis 5.1.3.

- *the flow is quasi-steady over the three planes;*
- *the energy is conserved over planes"1" and "2";*
- *the contraction is isentropic between planes"1" and "2";*
- *no allowance is made for pressure recovery between planes "2" and "0".*

Taking in account Hypotheses 5.1.3 allows defining the following energy and mass conservation equations, respectively:

$$a_1^2 + \frac{\gamma - 1}{2} u_1^2 = a_2^2 + \frac{\gamma - 1}{2} u_2^2 \tag{5.1.29}$$

$$\frac{C_1 p_1 u_1}{a_1^2} = \frac{C_2 p_2 u_2}{a_2^2} \tag{5.1.30}$$

The isentropic contraction between planes"1" and "2" is defined as:

$$\frac{p_1}{p_2} = \left(\frac{a_1}{a_2} \right)^{\frac{2\gamma}{\gamma - 1}} \tag{5.1.31}$$

and the pressure at the throat in terms of the stagnation pressure is given by:

$$p_2 = p_0 \tag{5.1.32}$$

Equations (5.1.29) - (5.1.32) provide four of the six equations required to formulate the outflow boundary problem. A fifth is obtained from the definition of the speed of sound as follows [10]:

$$a_2 = \frac{\gamma p_2}{\rho_2} \tag{5.1.33}$$

Finally, the sixth equation is given by the MOC, which allows creating the interaction between the boundary model and the in-pipe flow conditions. Consider for the outflow boundary the following diagram of the MOC:

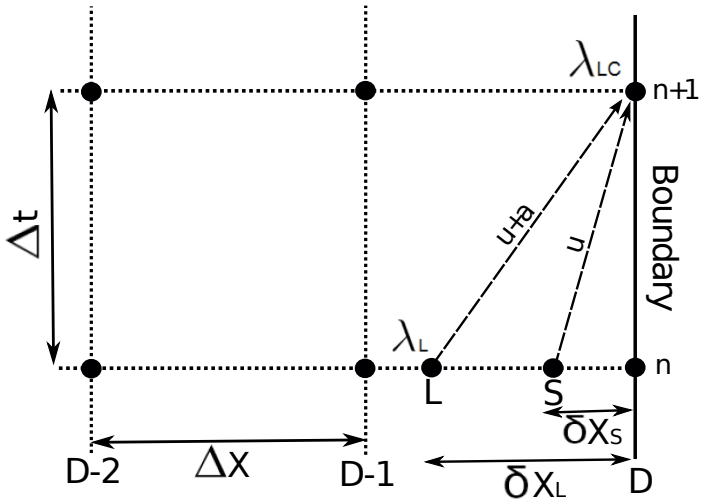

Figure 5.6: Outflow MOC Diagram

For illustration purposes, we consider once again the MOC for homentropic flow. Using (5.1.7) gives the following:

$$\lambda_L = a_D^{n+1} + \frac{\gamma - 1}{2} u_D^{n+1} = a_L^n + \frac{\gamma - 1}{2} u_L^n \tag{5.1.34}$$

where $a_D = a_1$ and $u_D = u_1$. To solve the boundary problem given by the system of equations (5.1.29) - (5.1.34), a boundary resolution method has to be used as an analytical solution cannot be found. The classical boundary resolution method to solve this system is described in Section 5.1.3. In Section 5.3, we proposed an alternative completely non-homentropic boundary resolution scheme to solve the outflow boundary problem independently of the QS formulation (namely equations (5.1.29)-(5.1.33)).

When the pressure ratio across the partially open-end is large enough to have sonic flow, the boundary problem is reformulated by replacing (5.1.32) with the sonic flow equation given in (5.1.27). As done in the inflow case, the boundary problem (5.1.29) - (5.1.33) is typically complemented by adding discharge coefficients to correct the model inaccuracies.

Remark 5.1.2. Note that when $C_1 = C_2$, the outflow open-end boundary problem is obtained.

Intra-Pipe Restriction : Figure 5.7 presents the schematic of an intra-pipe restriction boundary.

As shown in Figure 5.7, three quasi-steady planes are defined. Plane 1 is located upstream of the restriction just before the gas contraction, plane "2" is located at the restriction throat and plane "3" is placed downstream of the restriction after the gas expansion. The gas comes from the pipe of cross-sectional area C_1 and passes through the restriction throat as a jet of cross-sectional area C_2. Then, the gas expands in

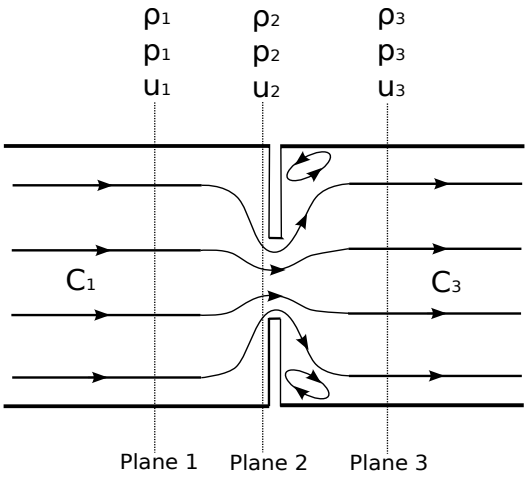

Figure 5.7: Intra-pipe Restriction Schematic

a pipe of cross-sectional area C_3. For the intra-pipe boundary problem, there are nine unknowns: the pressure, particle speed and density in all three planes. The intra-pipe restriction can be considered as a combination of an inflow and outflow boundary. Nevertheless, different considerations inherent of the intra-pipe boundary problem have to be taken into account. Consider the following hypotheses in order to set the basic QS equations for the intra-pipe boundary problem by using the traditional momentum-based inflow and the isentropic-based outflow boundary formulations:

Hypothesis 5.1.4.

- *the flow is quasi-steady over the three planes;*
- *the energy is conserved over the three planes;*
- *the contraction is isentropic between planes"1" and "2";*
- *the momentum between planes "2" and "3" is conserved.*

Based on the previous hypotheses, the intra-pipe restriction energy and mass conservation equations can be defined as:

$$a_1^2 + \frac{\gamma - 1}{2} u_1^2 = a_2^2 + \frac{\gamma - 1}{2} u_2^2 = a_3^2 + \frac{\gamma - 1}{2} u_3^2 \tag{5.1.35}$$

and

$$\frac{C_1 p_1 u_1}{a_1^2} = \frac{C_2 p_2 u_2}{a_2^2} = \frac{C_3 p_3 u_3}{a_3^2} \tag{5.1.36}$$

Equations (5.1.35) and (5.1.36) provide four of the required equations equations. The fifth is given by the isentropic contraction (5.1.31), the sixth by the inflow momentum

conservation (5.1.23) and the seventh by the speed of sound (5.1.33). The other two equations left to formulate the boundary problem are obtained from MOC according to Figure (5.8).

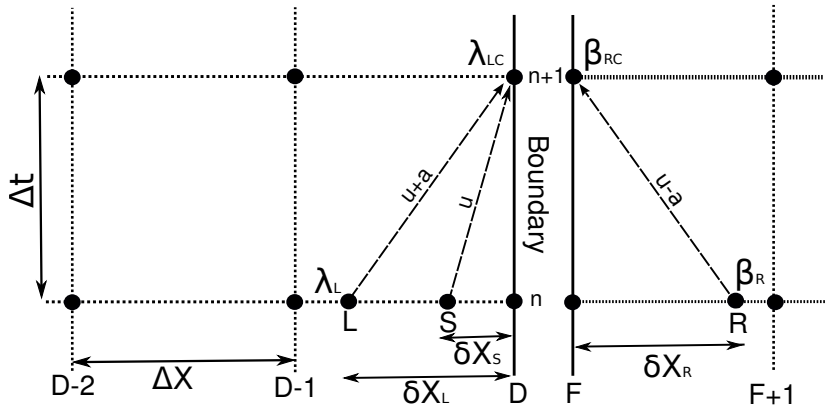

Figure 5.8: Intra-pipe MOC diagram

We also consider a homentropic flow for illustration purposes. The MOC equations for the intra-pipe boundary problem are given by (5.1.26) and (5.1.34). To define the boundary problem for sonic flow, the momentum conservation (5.1.24) is replaced by (5.1.27). As done for the other two boundary conditions, it is usual to define discharge coefficients to artificially correct the mass flow rate. An alternative non-homentropic boundary resolution method for the system of equations associated with the intra-pipe boundary problem is addressed in Section 5.3.

Remark 5.1.3. Note that when $C_1 = C_2$ and $C_2 = C_3$, a sudden pipe enlargement and a sudden pipe contraction boundaries are obtained, respectively .

To summarize, we have presented the traditional QS equations and hypotheses that allow describing the boundary problem for an inflow, outflow and intra-pipe restriction boundary conditions. In the next section, we present some of the most representative MOC-based boundary resolution methods found in the literature.

5.1.3 Boundary Resolution Methods Review

In this section we provide a review on some of the most representative boundary resolution methods used in 1D engine air-path simulation. Specifically, we focus on the outflow boundary resolution schemes. We describe the classical method introduced in the work of Benson [10] and later extended in the work of Winterbone and Pearson [101]. Then, we present the developments on non-homentropic outflow boundary resolution introduced in the work of Martin [46]. The intra-pipe boundary resolution methods are not detailed in this review as a significant part of these is based on the outflow boundary resolution.

5.1.3.1 Outflow boundary resolution method proposed by Benson, Winterbone and Pearson

Benson introduced a strategy to solve the homentropic outflow boundary problem based on the outflow boundary model provided in Section (5.1.2.2). This method can be modified to solve for non-homentropic flow by the introduction of the "starred Riemann variables" (for further details, refer to [10] and [101]). However, even in the non-homentropic formulation, the isentropic contraction is systematically assumed for the boundary resolution method.

To introduce the work of Benson, let us define the speed of sound a and the particle speed u in the non-dimensional form given in (5.1.17). We develop the system of equations (5.1.29) - (5.1.34) (subsonic flow) in order to write an implicit formulation of the boundary problem in terms of the non-dimensional speed of sound at the boundary A_1 as follows:

$$f\left(A_1\right) = \left(A_1^{\frac{4}{\gamma-1}} - \Phi_1^2\right)\left(\tilde{\lambda}_L - A_1\right)^2 - \frac{\gamma-1}{2}\left(A_1^2 - 1\right)\Phi_1^2 = 0 \tag{5.1.37}$$

where $\Phi_1 = C_2/C_1$ and $\tilde{\lambda}_L$ is the non-dimensional Riemann invariant λ_L. Note that (5.1.37) cannot be solved explicitly and therefore a numerical procedure has to be performed at every simulation time step. Benson proposed the following numerical scheme to solve the outflow boundary problem:

1. the algorithm is initialized at $A_{it} = \frac{\tilde{\lambda}_L+1}{2}$ as the solution of (5.1.37) is in the range $[1, \tilde{\lambda}_L]$;
2. the initial step is defined as $\Delta A_{it} = \frac{\tilde{\lambda}_L-1}{4}$;
3. equation (5.1.37) is evaluated using A_{it}. If $f\left(A_{it}\right) < 0$ then set $A_{it+1} = A_{it} - \Delta A_{it}$; else set $A_{it+1} = A_{it} + \Delta A_{it}$;
4. if $f\left(A_{it}\right) < \epsilon$ (where ϵ is a small scalar that sets the accuracy of the solution of (5.1.37)) then return $A_{it} = A_1$, else set $\Delta A_{it+1} = \frac{\Delta A_{it}}{2}$ and $A_{it} = A_{it+1}$ and go back to step 3.

The remaining quantities at the boundary u_1 and p_1 are then found using the MOC equation

$$U_1 = \frac{2}{\gamma-1}\left(\tilde{\lambda}_L - A_1\right) \tag{5.1.38}$$

and the isentropic contraction

$$A_1 = \left(\frac{p_1}{p_{ref}}\right)^{\frac{\gamma-1}{2\gamma}} \tag{5.1.39}$$

When the flow in the throat is sonic, the outflow boundary model changes and therefore the boundary problem has be to modified. Benson proposed the following equation to address the boundary problem under sonic flow conditions:

$$f\left(A_{1cr}\right) = \Phi_1^2 - \left[\frac{\gamma+1}{\gamma-1} - \left(\frac{2}{\gamma-1}\right)\left(A_{1cr}\right)^2\right]\left(A_{1cr}\right)^{\frac{4}{\gamma-1}} = 0 \tag{5.1.40}$$

where A_{1cr} is the critical non-dimensional speed of sound at the boundary. Note that for a given value of Φ_1 there is only one corresponding A_{1cr}. It is crucial to highlight that the boundary resolution method proposed by Benson (5.1.37) is completely dependent on the QS formulation of the outflow boundary. Therefore, if an alternative approach is used for the outflow modeling (different from the classical model shown in Section 5.1.2.2), then (5.1.37) is not valid anymore and the boundary resolution method has to be reformulated.

5.1.3.2 Outflow boundary resolution method proposed by Martin

Most of the developed outflow restriction models found in the literature rely on the isentropic contraction assumption between planes"1" and "2" of Figure 5.5. As mentioned previously, this hypothesis is in disagreement with respect to experimental results and hence discharge coefficients C_d have to be introduced to correct the modeling inaccuracies. Martin developed in his work a non-isentropic outflow boundary model in an attempt to reduce the need of such artificial corrections. He proposed a polytopic contraction formulation instead of the traditional isentropic contraction with the purpose of being consistent with the non-homentropic formulation. He used the same equation as the one found by Benson to state the boundary problem, with the difference that he replaced the heat ratio γ in (5.1.37) by a polytopic coefficient denoted as κ. This polytopic coefficient is computed by means of a data-map, which depends on the Riemann invariant λ_L and the area ratio Φ_1 (for further detail refer to [69]).

Additionally, Martin proposed a Newton-Raphson (NR) algorithm to solve (5.1.37), as an alternative for the numerical method proposed by Benson. The choice of the NR scheme was based on the improvement (in terms of calculation efficiency) that this approach had brought to the inflow boundary resolution method [46]. However, for the outflow boundary resolution, the method proposed by Martin did not improve significantly the calculation performance. The following steps describe the boundary resolution method proposed by Martin:

1. the algorithm is initialized at $A_{it} = \frac{\tilde{\lambda}_L+1}{2}$;
2. the non-dimensional particle speed U_{it} is calculated using the energy equation $1 = A_{it}^2 + \frac{\gamma-1}{2}U_{it}^2$;
3. the polytropic coefficient is found using the data-map $\kappa = datamap_\kappa(\tilde{\lambda_L}, \Phi_1)$;

4. evaluate (5.1.37) (since κ, A_{it} and λ_L are defined). If $f(A_{it}) < \epsilon$ then $A_1 = A_{it}$; else, compute the NR algorithm to update A_{it} and go back to step 2.

With the introduction of the works of Benson, Winterbone, Pearson and Martin, we conclude the review on some of the outflow boundary resolution methods classically used for 1D engine air-path modeling. One of the objectives of this thesis is to propose alternative boundary resolution methods that allow obtaining 1D engine air-path models more suitable for control purposes. In this sense, and based on the same concerns of Martin with respect to the implications of the isentropic assumption on the outflow boundary models, in this thesis we formulate alternative methods to solve the boundary problem without assuming an isentropic contraction. The main benefits obtained from the approach considered in this chapter are:

- reduction of the need of discharge coefficient, which is a consequence of the increase on predictability;
- quasi-steady model independent resolution method, which gives flexibility to the simulation platform;
- better numerical performance, therefore less computational load and better accuracy.

In Section 5.2, we present some alternative QS models for the inflow, outflow and intra-pipe boundaries as well as how to put their solution into data-maps, which is essential for the development of the proposed boundary resolution methods. In Section 5.3, we provide a detailed description of the novel non-homentropic boundary resolution methods for outflow and intra-pipe restrictions. Finally, in Section 5.4, an experimental evaluation of the proposed boundary resolution methods is given.

5.2 Quasi-Steady Boundary Models and Data-map Generation

In the boundary problem formulation seen in Section 5.1.2.2, there is a set of equations associated with the boundary QS physical model and others related with the interaction between the in-pipe conditions and the boundary (namely the MOC equations). Traditionally, the boundary resolution methods have considered the whole set of boundary equations to formulate a numerical procedure to solve the boundary problem, thus, obtaining boundary resolution methods that depend on the physical QS models. In other words, if a physical equation is changed, the whole boundary resolution method has to

be reformulated. In this thesis we propose to slit these two types of equations to formulate the boundary physical model apart from the MOC equations. More precisely, in this section we focus on the alternative physical QS boundary equations while in Section 5.3, we focus on a non-homentropic method to create the interaction between the in-pipe conditions and boundary QS models resolution method and the numerical procedure to solve the boundary problem.

5.2.1 Quasi-Steady Boundary Outflow Models

Before describing the alternative QS boundary models, it is important to state the following hypothesis:

Hypothesis 5.2.1.

- *no change of the gas heat ratio with respect to the temperature and EGR percentage (gas composition) is considered.*

Hypothesis 5.2.1 is reasonable for an engine air-path operated with EGR because the effect of the heat ratio variation on the QS model is much smaller than the effect of the QS model formulation itself, as illustrated in Appendix A.2. Thus, the variation of the heat ratio is not critical for control and estimation purposes. Nevertheless, if the impact of this variation is required, it can be considered by adding a supplementary input to the QS model data-maps.

To model the outflow boundary, we develop two different approaches: the traditional model with isentropic contraction (for illustration purposes) and the a novel momentum-based method. However, many other outflow models can be proposed such as the ones given in [69]. The aim in this section is to put the boundary physical models in the form of two algebraic expressions that relate the non-dimensional particles speeds and pressures between the planes“1” and “2” of Figure 5.5.

5.2.1.1 Outflow model using the isentropic contraction equation

The basic equations and hypotheses for the classical outflow restriction model have been given in (5.1.29) - (5.1.33) and Hypotheses 5.1.3, respectively. To build the algebraic expressions, let us start with the energy conservation equation in the following form:

$$a_{tot}^2 = a_1^2 + \frac{\gamma - 1}{2} u_1^2 = a_2^2 + \frac{\gamma - 1}{2} u_2^2 \tag{5.2.1}$$

where

$$a_{tot} = \sqrt{a_1^2 + \frac{\gamma - 1}{2} u_1^2} \tag{5.2.2}$$

is the total speed of sound. The energy equation (5.2.1) can be rewritten as follows:

$$\left(\frac{a_1}{a_2}\right)^2 = \left(\frac{a_{tot}}{a_2}\right)^2 - \frac{\gamma-1}{2}\left(\frac{u_1}{a_2}\right)^2 \tag{5.2.3}$$

Combining the mass conservation and the isentropic contraction equations ((5.1.30) and (5.1.31), respectively) gives:

$$\left[\left(\frac{a_1}{a_2}\right)^2\right]^{\frac{\gamma}{\gamma-1}} = \Phi_1 \frac{u_2}{u_1}\left(\frac{a_1}{a_2}\right)^2 \tag{5.2.4}$$

Define the non-dimensional speeds as $A = a/a_{tot}$ and $U = u/a_{tot}$, which implies that the energy conservation (5.2.1) can be written as:

$$1 = A_1^2 + \frac{\gamma-1}{2}U_1^2 = A_2^2 + \frac{\gamma-1}{2}U_2^2 \tag{5.2.5}$$

By plugging (5.2.3) into (5.2.4) and defining all the speeds in their non-dimensional form, the following algebraic equation is obtained:

$$U_1 = \Phi_1 U_2 \left[\left(\frac{1}{A_2}\right)^2 - \frac{\gamma-1}{2}\left(\frac{U_1}{A_2}\right)^2\right]^{\frac{-1}{\gamma-1}} \tag{5.2.6}$$

Equation (5.2.6) provides an implicit algebraic expression between the speed at the throat U_2 and the speed at the boundary U_1. Note that A_2 can be written in terms of U_2 by using (5.2.5). From the isentropic contraction assumption, the following relationship between the non-dimensional speeds of the sound and the pressure ratio p_1/p_2 is established:

$$\frac{p_1}{p_2} = \left(\frac{A_1}{A_2}\right)^{\frac{2\gamma}{\gamma-1}} \tag{5.2.7}$$

Equations (5.2.6) and (5.2.7) constitute the algebraic expressions that represent the QS model of the traditional outflow boundary condition under subsonic flow. To analyze the model under sonic flow, consider the energy conservation (5.2.5) and the fact that $u_2 = a_2$. This implies that the non-dimensional speeds at the throat are given by $U_2 = A_2 = \sqrt{\frac{2}{\gamma+1}}$. Applying this result in (5.2.7), the critical non-dimensional particle speed U_{1cr} is found using:

$$U_{1cr} = \Phi_1 \sqrt{\frac{2}{\gamma+1}} \left[\left(\frac{\gamma+1}{2}\right) - \frac{\gamma^2-1}{4}\left(U_{1cr}\right)^2\right]^{\frac{-1}{\gamma-1}} \tag{5.2.8}$$

5.2.1.2 Outflow model using a momentum-based equation

To develop an alternative outflow model formulation, we propose a new outflow modeling strategy that does not assume the isentropic contraction between planes“1” and “2”. We

replace this hypothesis by a momentum conservation based equation, which allows being consistent with a non-homentropic formulation. The remaining hypotheses given in Hypotheses 5.1.3 are considered for this modeling strategy.

Figure 5.9 presents the control volume approach to formulate the momentum-based equation.

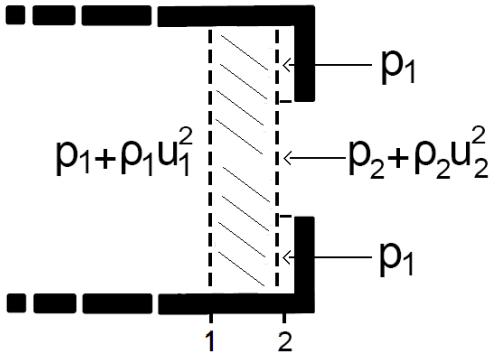

Figure 5.9: Proposed pressure distribution for the momentum approach

Figure 5.9 shows the pressure distribution at the boundary that allows stating the momentum conservation according to the defined control volume (volume between plane 1 and 2). There are three sections defined over plane "2": two sections right in front of the restriction walls and one facing the restriction throat. Consider the following hypotheses in order to develop the momentum-based model:

Hypothesis 5.2.2.

- *u_2 normal to the restriction wall at plane "2" is zero;*
- *the pressure and speed on plane "2" right next to the throat are defined as p_2 and u_2, respectively;*
- *the pressures right next to the restriction over plane "2" are considered to be equal to p_1.*

According to Hypotheses 5.2.2, the momentum conservation over the virtual control volume shown in Figure 5.9 can be formulated as follows:

$$p_1 C_1 - p_2 C_2 - p_1(C_1 - C_2) = \rho_2 u_2^2 C_2 - \rho_1 u_1^2 C_1 \tag{5.2.9}$$

Combining the speed of sound equation $a = \sqrt{\gamma p/\rho}$ and (5.2.9) gives the following:

$$\frac{p_1}{p_2} = \left(\frac{1 + \gamma \left(\frac{u_2}{a_2}\right)^2}{1 + \frac{\gamma}{\Phi_1}\left(\frac{u_1}{a_1}\right)^2} \right) \tag{5.2.10}$$

As proposed in Section 5.2.1.1, it is crucial to find an algebraic expression that relates the non-dimensional particle speed U_1 with U_2 (this with the purpose of generating the model data-maps). Therefore, we consider (5.1.30) along with (5.2.10) to obtain:

$$\Phi_1 \frac{u_2}{u_1}\frac{a_1^2}{a_2^2} + \gamma \frac{u_2}{a_2^2} u_1 = 1 + \gamma \left(\frac{u_2}{a_2}\right)^2 \tag{5.2.11}$$

By developing (5.2.11) and using the energy conservation (5.2.5) to write A_1 in terms of U_1, the following quadratic function of U_1 is obtained:

$$\left(\gamma - \Phi_1 \frac{\gamma - 1}{2}\right) U_1^2 - \left(\frac{A_2^2}{U_2} + \gamma U_2\right) U_1 + \Phi_1 = 0 \tag{5.2.12}$$

Equations (5.2.10) and (5.2.12) provide the algebraic equations for the momentum-based outflow restriction model under subsonic flow. The expression for sonic flow is given as follows:

$$\left(\gamma - \Phi_1 \frac{\gamma - 1}{2}\right) U_{1cr}^2 - \sqrt{2(\gamma + 1)} U_{1cr} + \Phi_1 = 0 \tag{5.2.13}$$

With this we conclude the algebraic equations required to represent the two proposed outflow QS models. In the next section, we provide the procedure that allows storing the solution of these models into data-maps.

5.2.1.3 Outflow Data-map Generation

At the time when the QS models were developed, desktop computers memory did not allow pre-calculating the solutions into data-maps. Indeed, numerical algorithms were used to solve the boundary problem introducing an iterative procedure at each simulation time step. The main issues with this approach is that greater calculation loads were required for the boundary resolution and that the numerical scheme had to be modified for each specific model, reducing significantly the flexibility of 1D simulation platforms. On the other hand, modern computers allow storing the solution of the QS boundary models into data-maps, which can then be easily reconstructed using highly efficient linear interpolation procedures (look-up table techniques). Therefore, for a control-oriented modeling platform it is advantageous to use pre-processed data-maps at the interface between the QS model and the in-pipe 1D numerical scheme.

Equations (5.2.6) and (5.2.7) or (5.2.12) and (5.2.10) provide for every U_2, a respective U_1 and p_1/p_2. Hence, by defining a set of U_2, the corresponding set of U_1 and p_1/p_2 can be determined and then stored into a data-map. These data-maps can be configured then to solve p_1/p_2 in terms of U_1 and the area ratio Φ_1, which we represent as follows:

$$\frac{p_1}{p_2} = Datamap_{OR}(U_1, \Phi_1) \tag{5.2.14}$$

To better illustrate how to perform this configuration and generate the data-maps in the form (5.2.14), consider the following procedure:

1. set a range of U_2 equal to $\left[0, \sqrt{\frac{2}{\gamma+1}}\right]$ (Subsonic range), A_2 is found using (5.2.5);
2. with U_2 and A_2, the QS model ((5.2.6) and (5.2.12) for instance) is solved numerically (or analytically depending on the model) to get the corresponding U_1. To find A_1 use (5.2.5) once again;
3. using U_1 in the pressure ratio equation (for example (5.2.7) or (5.2.10)), the values of p_1/p_2 can be found;
4. to include the sonic solution in the data-map, solve the model equations with $U_2 = A_2 = \sqrt{\frac{2}{\gamma+1}}$

5.2.1.4 Outflow models comparison

In Figure 5.10 we perform a comparison between the data-maps of the outflow boundary models developed in the previous sections.

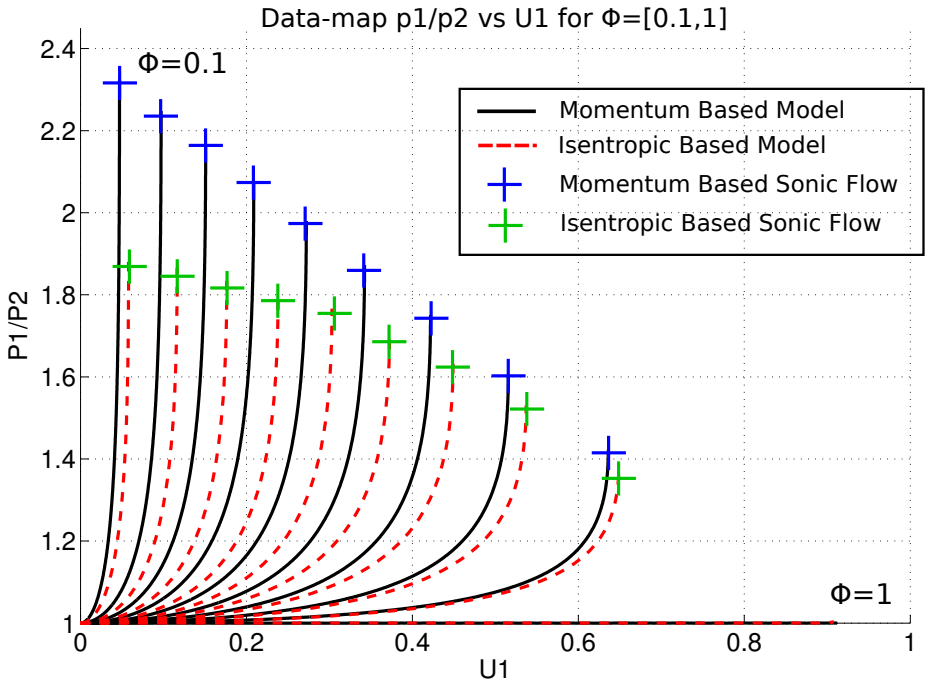

Figure 5.10: Outflow restriction data-map for isentropic and momentum-based models

As depicted, the non-dimensional flow velocities are systematically higher in the isentropic contraction-based model than in the momentum-based one. This behavior occurs

because the isentropic contraction approach does not take into account the increase of entropy through the restriction, which allows obtaining greater flow speeds. When comparing these results with 3D CFD simulations of the outflow restriction, it has been found that both models overestimate the non-dimensional particle speed U_1. This result is not surprising as friction (among other phenomena) has been neglected in both boundary problem formulations. Nevertheless, the momentum-based model is significantly more predictive than the isentropic model (this is later verified experimentally in Section 5.4). To illustrate this, Table 5.1 shows the artificial correction (discharge coefficients) required for each approach to fit the 3D CFD results.

Φ_1	Momentum Model	Isentropic Model
0.2	0.9798	0.7841
0.4	0.9414	0.7803
0.6	0.9229	0.8189
0.8	0.9320	0.8871

Table 5.1: Discharge coefficients for both models with respect to the CFD results

As seen in Table 5.1, the necessary correction for the momentum-based model is significantly smaller in comparison with the traditional isentropic-based outflow model. This implies that the momentum-based approach is more predictive, which motivates the development of a boundary resolution method capable of integrating this alternative formulation with the in-pipe numerical scheme. Indeed, the traditional resolution method presented in Section 5.1.3, is only valid under the isentropic contraction assumption. Therefore, to solve the non-homentropic boundary problem with the momentum-based approach, an alternative boundary resolution method has to be developed. This problem is addressed in Section 5.3.

5.2.2 Quasi-Steady Intra-Pipe Restriction Models

In this section we develop some alternative QS intra-pipe restriction models and we describe a procedure to store them into data-maps. We use a combination of various inflow and outflow models to state the algebraic equations that relate the non-dimensional particle speeds and the pressure ratio between planes “1” and “3” of Figure 5.7.

To start with the formulation of the intra-pipe boundary models, let us introduce the two inflow restriction models considered in this section.

5.2.2.1 Inflow Models

In [46], the inflow boundary problem has been considered in detail and different inflow QS models have been proposed. For sake of simplicity, we only consider two of the proposed inflow models: a momentum-based and a constant pressure model.

Based on the Hypotheses 5.1.2 and the QS equations (5.1.22) - (5.1.25) given in Section 5.1.2.2, the following algebraic equations are obtained to model the inflow boundary:

$$U_3^2 + \left(\frac{2}{\gamma+1}\right)\left(\frac{A_2^2}{\Phi_3 U_2} + \gamma U_2\right) U_3 + \frac{2}{\gamma+1} = 0 \tag{5.2.15}$$

$$\frac{p_3}{p_2} = \frac{1 + \gamma\Phi_3\left(\frac{U_2}{A_2}\right)^2}{1 + \gamma\left(\frac{U_3}{A_3}\right)^2} \tag{5.2.16}$$

where $\Phi_3 = C_2/C_3$. Equations (5.2.15) and (5.2.16) constitute what we call the momentum-based inflow model (this is due to the momentum conservation formulation 5.1.24).

The second inflow model is formulated by replacing the momentum conservation hypothesis (5.1.24) by the assumption of having the same pressure between planes "2" and "3" (namely $p_2 = p_3$). By developing this hypothesis along with the QS equations (5.1.22), (5.1.23) and (5.1.25), the following algebraic inflow model is obtained:

$$U_3^2 + \left(\frac{2A_2^2}{\Phi_3(\gamma-1)U_2}\right) U_3 - \frac{2}{\gamma-1} = 0 \tag{5.2.17}$$

$$\frac{p_3}{p_2} = 1 \tag{5.2.18}$$

Equations (5.2.17) - (5.2.18) constitute the pressure constant inflow model. Note that both of the proposed inflow models allow establishing a quadratic relationship between the non-dimensional particle speeds U_2 and U_3 and the pressure ratio p_3/p_2. In [46], it has been shown that the momentum-based model (5.2.15) - (5.2.16) systematically presents higher flow speeds than the constant pressure inflow model (5.2.17) - (5.2.18). This behavior is explained by the pressure recovery allowed by the momentum-based formulation. In [69], both models were compared with respect to 3D CFD simulation results and it was found that the constant pressure inflow model (5.2.17) - (5.2.18) had a better predictability than the momentum-based model (5.2.15) - (5.2.16).

5.2.2.2 Intra-pipe Restriction Models

For the intra-pipe restriction model formulation, we consider the outflow models given in (5.2.6) and (5.2.12) and the two inflow models (5.2.15) and (5.2.17). From these four

QS restriction models, we can be formulate four intra-pipe models, which result from the permutation between the two outflow with the two inflow models.

We present two of the four models to illustrate how the algebraic equations for the intra-pipe boundary models are obtained. The other two can be established using the same philosophy. First, let us formulate the intra-pipe model using both momentum-based approaches (namely (5.2.12) and (5.2.15)). To integrate the outflow and the inflow models, the non-dimensional speeds U_2 and A_2 and the pressure p_2 are considered as common for both QS approaches. Taking this into account along with Hypotheses 5.1.4 and the momentum-based models discussed in the previous sections, the following algebraic model is obtained:

$$\begin{aligned} &\left(\gamma - \Phi_1 \frac{\gamma-1}{2}\right) U_1^2 + \left(\frac{A_2^2}{U_2} + \gamma U_2\right) U_1 + \Phi_1 = 0 \\ &U_3^2 + \left(\frac{2}{\gamma+1}\right)\left(\frac{A_2^2}{\Phi_3 U_2} + \gamma U_2\right) U_3 + \frac{2}{\gamma+1} = 0 \end{aligned} \tag{5.2.19}$$

$$\frac{p_3}{p_1} = \frac{1+\gamma\Phi_3\left(\frac{U_2}{A_2}\right)^2}{1+\gamma\left(\frac{U_3}{A_3}\right)^2} \frac{1+\frac{\gamma}{\Phi_1}\left(\frac{U_1}{A_1}\right)^2}{1+\gamma\left(\frac{U_2}{A_2}\right)^2} \tag{5.2.20}$$

Note that (5.2.19) and (5.2.20) are the momentum-based inflow and outflow models put together. This model gives for every U_2, the respective values for U_1, U_3 and pressure ratio p_3/p_1, which is suitable to later store the solution in data-maps.

The second intra-pipe model that we consider is the combination between traditional isentropic contraction outflow and the constant pressure inflow model. The following algebraic equations are obtained:

$$\begin{aligned} &U_1 = \Phi U_2 \left[\left(\frac{1}{A_2}\right)^2 - \frac{\gamma-1}{2}\left(\frac{U_1}{A_2}\right)^2\right]^{\frac{-1}{\gamma-1}} \\ &U_3^2 + \left(\frac{2A_2^2}{\Phi_3(\gamma-1)U_2}\right) U_3 - \frac{2}{\gamma-1} = 0 \end{aligned} \tag{5.2.21}$$

$$\frac{p_3}{p_1} = \left(\frac{A_1}{A_2}\right)^{\frac{-2\gamma}{\gamma-1}} \tag{5.2.22}$$

Note that the are significant differences between the models given in (5.2.19) - (5.2.20) and (5.2.21) - (5.2.22). These differences are discussed in the next section and their performance is experimentally evaluated in 5.4. To obtain the intra-pipe models for sonic flow, replace $U_2 = A_2 = \sqrt{2/(\gamma+1)}$ in (5.2.19), (5.2.20), (5.2.21) and (5.2.22).

5.2.2.3 Intra-pipe Data-map Generation

As done in Section 5.2.1.3, the solution of the intra-pipe models (for instance (5.2.19) - (5.2.20) and (5.2.21) - (5.2.22)) can be easily stored into data-maps, which allows re-calculating later the solution using look-up table techniques along with a trilinear interpolation. These data-maps can be configured to solve p_3/p_1 and U_3 in terms of $U1$, Φ_1 and Φ_3 as follows:

$$\frac{p_3}{p_1} = Datamap_{IRP}(U1, \Phi_1, \Phi_3) \tag{5.2.23}$$

and

$$U_3 = Datamap_{IRU}(U1, \Phi_1, \Phi_3) \tag{5.2.24}$$

The data-maps (5.2.23) and (5.2.24) imply that the non-dimensional particle speed U_3 and the pressure ratio p_3/p_1 can be calculated directly from the non-dimensional particle speed upstream of the intra-pipe restriction. This property is particularly useful for the intra-pipe boundary resolution as it is shown later in Section 5.3.2.

We propose the following procedure to obtain the intra-pipe data-maps in the form of (5.2.23) and (5.2.24):

1. set a range of U_2 equal to $\left[0, \sqrt{\frac{2}{\gamma+1}}\right]$ (Subsonic range): A_2 is found using the energy conservation;
2. with U_2 and A_2, the algebraic particle speed equations (for instance (5.2.19)) are solved to get U_1 and U_3. To find A_1 and A_3, use the energy equation once again;
3. using U_1 and U_3 and the pressure ratio equation (for example (5.2.20)), the values of p_3/p_1 can be found;
4. to include the sonic solution in the data-map, solve the QS algebraic model equations with $U_2 = A_2 = \sqrt{\frac{2}{\gamma+1}}$

In Figure 5.11 we depict the corresponding data-maps of the intra-pipe models considered in Section 5.2.2.2.

As depicted in Figure 5.11, there are important differences between both approaches. The intra-pipe model obtained from the combination of the outflow isentropic contraction model and the constant-pressure inflow model (denoted in Figure 5.11 as Isen-CP) systematically presents greater particle speeds than the momentum-based strategy (Mom-Mom). This is consistent with the results obtained for the outflow boundary in Section 5.2.1.4, where it was seen that this behavior resulted from not taking into account the increase of

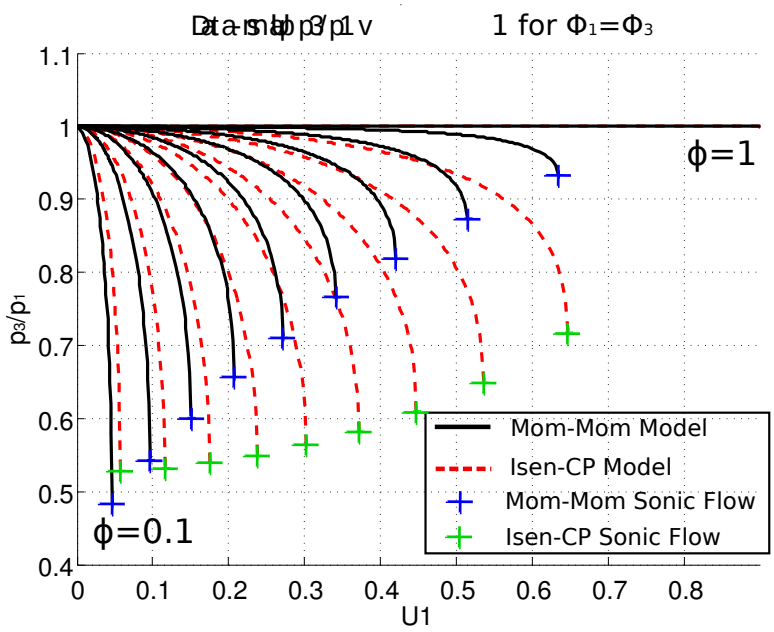

Figure 5.11: Intra-pipe restriction data-map for $\Phi_1 = \Phi_3$

entropy level at the boundary. In Section 5.4, we compare the four intra-pipe restriction models with experimental measurements in order to evaluate their performance in terms of predictability.

With this, we conclude the QS outflow and intra-pipe models considered in this thesis. In the next section, we describe the proposed non-homentropic boundary resolution methods for the outflow and intra-pipe boundaries conditions.

5.3 Outflow and Intra-pipe Boundary Resolution Methods

As previously mentioned, most boundary resolution methods found in the literature are systematically based on the isentropic contraction assumption, implying that if an alternative formulation is considered (such as the non-homentropic model developed in Section 5.2.1.2), then the whole boundary resolution method has to be modified or artificially corrected by means of discharge coefficients. This motivates the search for novel boundary resolution schemes capable of integrating various non-homentropic boundary models with the in-pipe wave action method. Indeed, this would allow increasing the efficiency, flexibility and predictability of the 1D air-path simulation platforms, which is of significant importance for control-oriented applications.

In this sense, the main concern of this section is to propose two boundary resolution meth-

ods (for the outflow and intra-pipe boundaries) capable of integrating any QS model in the form of (5.2.14), (5.2.23) and (5.2.24) into the wave action methods while being completely consistent with an non-homentropic formulation. Additionally, other improvements are obtained with the proposed boundary resolution methods such as a more efficient numerical scheme and a reference-free entropy correction.

5.3.1 Outflow Boundary Resolution Methods

Let consider the MOC schematic for the outflow boundary given in Figure 5.12.

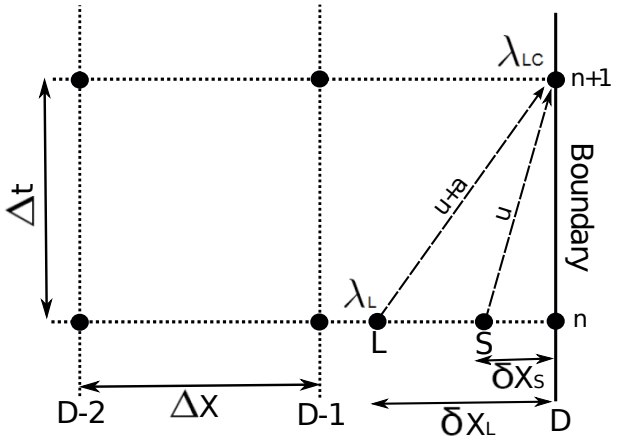

Figure 5.12: Characteristics Outflow Restriction Boundary

The index D represents the value of a variable at the boundary and the index L represents the interpolated point between D and $D-1$, where the trajectory $u+a$ crosses at time n. The index S is associated to the trajectory u at time n. To solve the outflow boundary problem (namely, finding the values of u_D, a_D and p_D), three equations have to be formulated.

As seen is Section 5.1.3, traditional outflow boundary resolution methods use the isentropic contraction as one of these equations. However, in our approach, we replace this assumption by the information provided by the Riemann invariant associated with the trajectory u. More precisely, we propose to use the following three equations to solve the outflow boundary problem:

- the MOC equation associated with the trajectory $u+a$;
- the MOC equation associated with the trajectory u;
- the physical outflow boundary model given by the data-maps (5.2.14).

Two of the three equations are related with the in-pipe conditions (MOC equations) and one to the physical model of the boundary. The main idea of the proposed resolution scheme is to formulate a method independent of the physical model contained in the outflow data-map. In so doing, if a different outflow model formulation is considered, the boundary resolution method does not have to be modified.

5.3.1.1 Outflow Resolution Scheme

As previously presented in Section 5.1.2.1, a modification of the MOC has to be performed in order to take into account the variation of entropy level at the boundary. Typically, to carry out the entropy correction, a pressure and a speed of sound references have to be defined. Nevertheless, we have found that a much simpler representation for the entropy level correction can be formulated, allowing to remove the pressure and speed of sound references and to provide an explicit relation between the pressure and particle speed at the boundary.

According to the definition of the Riemann invariants given in Section 5.1.2.1, consider the particle speed at the boundary at time $n+1$, defined in terms of the corrected Riemann invariant λ_{LC} as follows:

$$u_D^{n+1} = \frac{2}{\gamma - 1}\left(\lambda_{LC} - a_D^{n+1}\right) \tag{5.3.1}$$

The corrected Riemann invariant λ_{LC} can be replaced in (5.3.1) by its definition given in (5.1.21), allowing to express (5.3.1) as follows:

$$u_D^{n+1} = \frac{2}{\gamma - 1}\left(\lambda_L^n + a_D^{n+1}\left(1 - \frac{A_{AL}^n}{A_{AD}^{n+1}}\right) - a_D^{n+1}\right) \tag{5.3.2}$$

Using the definition of the entropy levels given in (5.1.18) and developing (5.3.2) gives:

$$u_D^{n+1} = \frac{2}{\gamma - 1}\left(\lambda_L^n + a_D^{n+1}\left(1 - \frac{a_L}{a_D^{n+1}}\frac{p_D^{n+1}}{p_L^n}\right)^{\frac{\gamma-1}{2\gamma}} - a_D^{n+1}\right) \tag{5.3.3}$$

Note that the speeds of sound at the boundary a_D^{n+1} cancel out in (5.3.3), yielding the following expression:

$$u_D^{n+1} = \frac{2}{\gamma - 1}\left(\lambda_L^n - a_L^n\left(\frac{p_D^{n+1}}{p_L^n}\right)^{\frac{\gamma-1}{2\gamma}}\right) \tag{5.3.4}$$

Note that (5.3.4) gives a direct and explicit relationship between the pressure and particle speed at the boundary (p_D^{n+1} and u_D^{n+1}, respectively) since λ_L, a_L and p_L are known at time n from the linear interpolations given in Section 5.1.2.1. Moreover, no pressure or sound speed reference have to be defined, simplifying significantly (in comparison with (5.1.21))

the formulation of the MOC associated with the trajectory $u + a$. Therefore, (5.3.4) constitutes the first of the MOC equations used for the boundary resolution method.

The second equation is derived from the MOC equation associated with the trajectory u. In other words, we consider the constant entropy along this trajectory, which can be written according to Figure 5.12 as follows:

$$s_D^{n+1} = s_S^n \tag{5.3.5}$$

Equation (5.3.5) implies that:

$$\frac{p_D^{n+1}}{\left(\rho_D^{n+1}\right)^\gamma} = \frac{p_S^n}{(\rho_S^n)^\gamma} \tag{5.3.6}$$

The following is obtained by replacing the density ρ in terms of pressure and speed of sound and developing (5.3.6):

$$a_D^{n+1} = \sqrt{\gamma s_S^{n\,\frac{1}{\gamma}}}\left(p_D^{n+1}\right)^{\frac{\gamma-1}{2\gamma}} \tag{5.3.7}$$

Similar to (5.3.4), (5.3.7) gives an explicit expression to relate the pressure and the speed of sound at the boundary (namely, p_D^{n+1} and a_D^{n+1}). Hence, (5.3.7) is considered as the second equation required to solve the boundary problem. Note that (5.3.4) and (5.3.7) imply that if the pressure at the boundary is known, then the boundary problem can be solved explicitly.

The third equation is obtained from the QS outflow models given in the form of (5.2.14), which provide the pressure at the boundary in terms of the particle speed and the area ratio Φ_1. Indeed, the outflow models are essential to create the interaction between the boundary and the in-pipe numerical scheme. However, these data-maps introduce an algebraic loop in the system of equations (5.3.4), (5.3.7) and (5.2.14) since the pressure is required to calculate u_D and vice-versa. This implies that the solution of the boundary problem cannot be found analytically and therefore a numerical procedure is necessary.

To solve (5.3.4), (5.3.7) and (5.2.14), we propose a Newton-Raphson (NR) numerical scheme that uses the pressure at the boundary as the convergence variable instead of the non-dimensional speed of sound typically used in [10] [69]. This choice is made, based on the good results that have been obtained for the inflow boundary resolution by using the pressure as the convergence variable [46] (in comparison with the numerical method proposed by Benson). Moreover, from the boundary problem formulation (namely, (5.3.4), (5.3.7) and (5.2.14)), the pressure seems to be a good convergence variable as it enables to explicitly obtain the particle speed and the speed of sound at the boundary.

To start with the numerical solution of the boundary problem, it is necessary to set an adequate initial pressure to initialize the NR method. Indeed, the choice of this initial value is crucial as the convergence speed of the numerical algorithm strongly depends on it.

Therefore in this method, the solution of the in-pipe numerical scheme is used to initialize the pressure as close as possible to the actual boundary problem solution, minimizing the amount of iterations and hence improving the boundary resolution performance.

Consider the following initialization for the boundary resolution method:

$$p_D^0 = 2p_{D-1}^{n+1} - p_{D-2}^{n+1} \tag{5.3.8}$$

where p_D^0 is the initial pressure of the NR algorithm. Equation (5.3.8) is the linear extrapolation using the pressure of the two closest finite elements in the tube (obtained from the in-pipe numerical scheme). This extrapolation can be very close to the solution, specially during the steady-state stages, avoiding the use of the iterative algorithm and therefore allowing to decrease the boundary resolution calculation load.

With p_D^{it} available (it stands for the current iteration), is it possible to calculate explicitly u_D^{it} and a_D^{it} with (5.3.4) and (5.3.7), respectively. The total speed of sound a_{tot}^{it} is calculated with (5.2.2) in order to find the non-dimensional particle speed at the boundary U_D^{it}. This particle speed along with the data-map (5.2.14) allows verifying whether the pressure at the boundary p_D^{it} is consistent with the boundary model or not. In other words, the consistency of the solution can be evaluated using the following function:

$$f_{out} = \left| \left(\frac{p_D^{it}}{p_0} \right) - datamap_{OR}(U_D^{it}, \Phi_1) \right| < \epsilon \tag{5.3.9}$$

where p_0 is the back-pressure and $\epsilon > 0$ is a scalar that sets the convergence accuracy. However, nothing guaranties that (5.3.8) satisfies the criterion (5.3.9) and hence the pressure at the boundary p_D^{it} has to be updated using in this case, the NR method. In order to avoid the calculation of the derivative of f_{out} with respect to p_D, the following approximation of NR method is considered (as done in Section 4.4.2):

$$p_D^{it+1} = p_D^{it} - \frac{f\left(p_D^{it}\right)}{\frac{f\left(p_D^{it}+\Delta p\right) - f\left(p_D^{it}\right)}{\Delta p}} \tag{5.3.10}$$

where Δp is a small pressure differential to approximate the derivative numerically. This approach is usually more efficient than calculating $f_{out}^{'}$. This is due to the avoidance of the derivative calculation and to the save in linear algebra work and matrix storage. The price of such an approximation is that the method converges more slowly. However, the overall resolution cost is significantly reduced [59]. The boundary problem is then solved by evaluating (5.3.10) until the condition (5.3.9) is satisfied. A similar algorithm has to be considered for the sonic flow, with the difference that the data-maps are built in this case considering $U_2 = A_2 = \sqrt{\frac{2}{\gamma+1}}$.

To implement the proposed outflow boundary resolution method, perform the following steps:

1. calculate λ_L^n and s_s^n: use equations (5.1.10) and (5.3.6), respectively;
2. initialize $p_D^{it} = 2p_{D-1}^{n+1} - p_{D-2}^{n+1}$. This is the linear extrapolation using the two closest nodes inside the pipe where p_{D-1}^{n+1} and p_{D-2}^{n+1} are obtained by the in-pipe numerical scheme;
3. use (5.3.7) to calculate a_D^{it} and (5.3.4) to compute u_D^{it};
4. calculate the total speed of sound a_{tot}^{it} and compute the non-dimensional speeds U_D^{it} and A_D^{it};
5. compute $\frac{p_D}{p_b} = datamap_{OR}(U_D^{it}, \Phi)$ using any of the outflow models;
6. evaluate (5.3.9). If $f < \epsilon$ then return $p_D^{n+1} = p_D^{it}$, $a_D^{n+1} = a_D^{it}$ and $u_D^{n+1} = u_D^{it}$. Otherwise, use (5.3.10) to update p_D^{it} and return to the step 3.

Note that the boundary resolution procedure is independent of the QS boundary physical model as the proposed scheme itself does not depend on the formulation considered for the generation of the outflow boundary data-map.

5.3.1.2 Intake valve unsteady flow simulation

To evaluate the behavior of the proposed outflow boundary resolution method under engine air-path unsteady flow conditions along with its numerical performance, a simple engine cylinder setup is analyzed for illustration purposes. Figure 5.13 presents the proposed setup using GT-Power®, which is composed by two pipes, intake and exhaust valves and a cylinder.

The simulation of the system is performed using the outflow boundary resolution method proposed in this section (implemented in Matlab/Simulink®) along with GT-Power® as a reference.

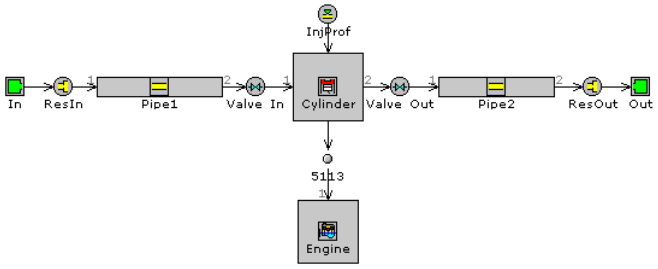

Figure 5.13: Engine cylinder scheme for the proposed method unsteady validation.

A simple cylinder model (no wall losses or combustion model) has been developed in Simulink® according to [82]. For the exhaust valve we consider the inflow boundary resolution method proposed in [46], already validated for this setup. To compare objectively

the proposed method with the solution generated by GT-Power®, the isentropic-based outflow model is used since GT-Power considers this formulation for the boundary resolution. For both simulations, the actual data-maps of the intake and exhaust valves of a Diesel engine are used. The intake and exhaust valves data-maps include already discharge coefficients. Table 5.2 presents the parameters used in the simulations and Figure (5.14) depicts the simulation results.

Parameter	Value	Units
Input Restriction Area Ratio	1	.
Input Pressure	1.4×10^5	Pa
Input Temperature	300	K
Output Restriction Area Ratio	1	.
Output Pressure	1.0×10^5	Pa
Pipes Lengths	1	m
Pipes Diameters	0.03	m
Pipes Discretization Length	0.02	m
Proposed Method Time Step	3×10^{-5}	s
GT-Power Time Step	$< 10 \times 10^{-5}$	s
Engine Speed	3000	rpm
Cylinder Diameter	80×10^{-3}	m
Stroke	79.5	m
Length Connecting Rods	142.6×10^{-3}	m
Compression Ratio	15.5	.

Table 5.2: Cylinder setup simulation parameters

For the analysis of the simulation results, the pressure, particle speed and temperature at the middle of the intake pipe are captured along with the cylinder pressure. The measurements in the pipe are taken at the middle in order to present a more feasible experiment for future validation as installing sensors at the boundaries is hardly achievable in practice. This does not degrade the evaluation process as the form of the waves inside the tube strongly depends on the boundary conditions.

The results presented in Figure 5.14 reveal that the developed boundary resolution method shows a good agreement with respect to the results obtained with GT-Power®. This demonstrates that the proposed boundary resolution method is able to represent the unsteady flow even under strong transient conditions, such as the ones found in an engine air-path. To test the predictability of the proposed boundary resolution method, an experimental evaluation is developed in Section 5.4.

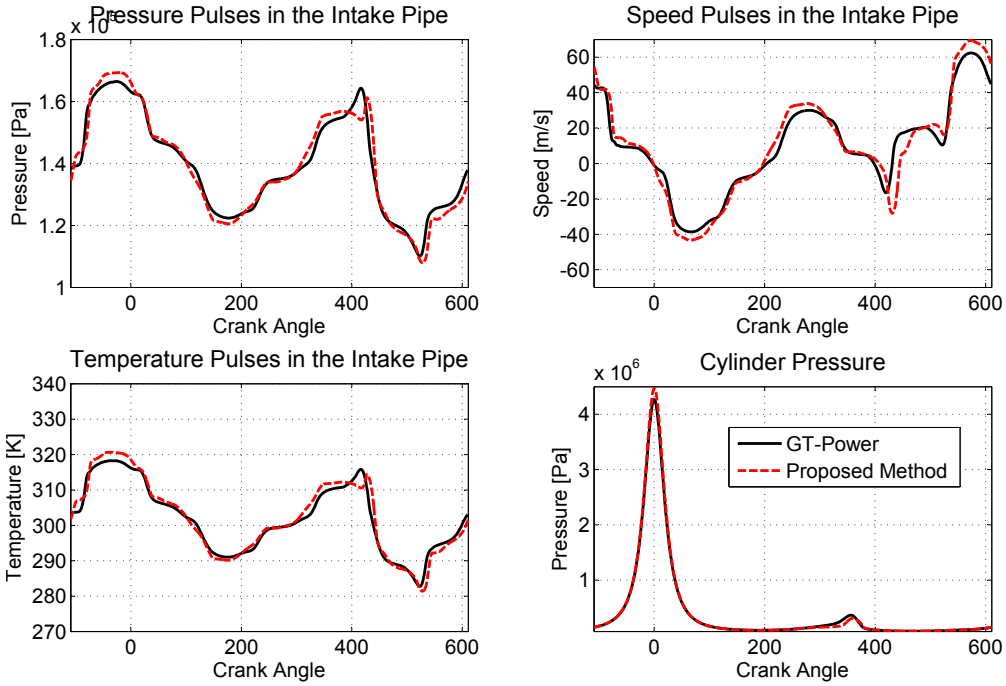

Figure 5.14: Results of unsteady simulation

5.3.1.3 Convergence performance

To study the convergence performance of the outflow boundary resolution scheme presented in this chapter, we provide a comparison with respect to the numerical method proposed by Benson, given in Section 5.1.3. We evaluate the numerical performance using the same unsteady flow simulation setup described in Section 5.3.1.2. As the criterion of convergence of Benson's method is different from the criterion proposed in this work, a more general criterion is used to perform an objective comparison. The parameter tolerance defined by $TolP = \Delta p_D^{it}/p_D^{it}$ and $TolA = \Delta A_D^{it}/A_D^{it}$ (for our method and Benson's, respectively) is used as a convergence criterion. This tolerance is set to $TolP = TolA = 1 \times 10^{-5}$ for the numerical performance evaluation.

Figures 5.15 and 5.16 show the numerical results (number of iterations and accuracy, respectively) obtained for a complete opening and closure of an intake valve. As depicted in Figure 5.15, the proposed resolution scheme provides a more efficient behavior in terms of necessary number of iterations for a given accuracy (approximately 5 times less iterations for a tolerance of 1×10^{-5}) than the numerical method proposed by Benson. For more constraining tolerances, the iteration ratio between the schemes can increase significantly: for example for $TolP = 1 \times 10^{-6}$, the proposed scheme performs 8 times less iterations than what Benson's method does. Figure 5.16 shows the final $TolP$ and $TolA$ of the solution obtained for each scheme. It is logical that all the values are under 1×10^{-5} as it is the convergence criterion. Nonetheless, the proposed method presents a better accuracy since smaller tolerances are systematically obtained when compared with respect

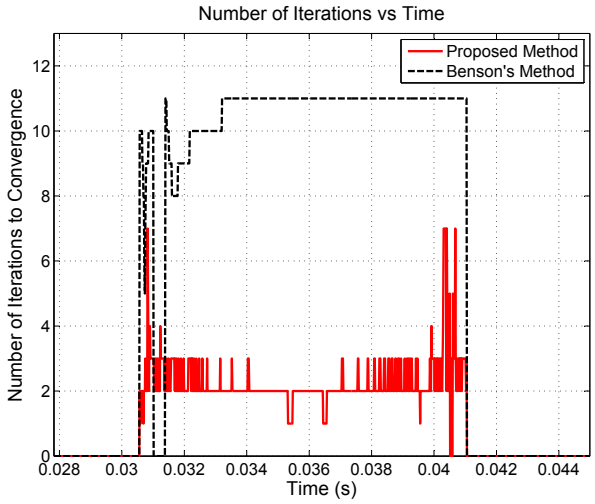

Figure 5.15: Comparison of the number of iterations required by the literature scheme and the proposed scheme. Convergence criterion: $TolP = 1 \times 10^{-5}$.

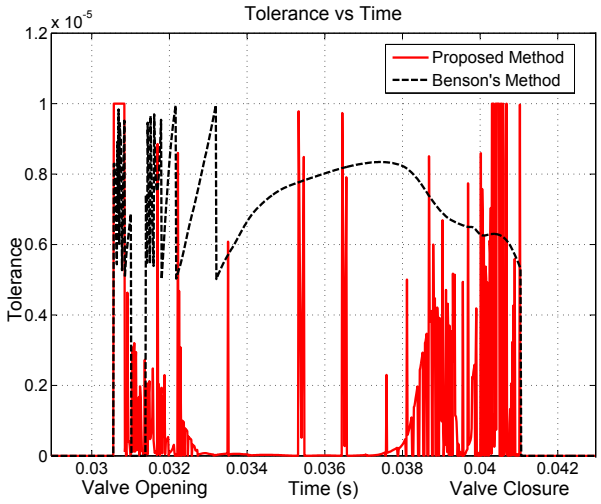

Figure 5.16: Accuracy obtained by the schemes

to Benson's method. This behavior is the result of quadratic convergence associated with the NR method together with the pressure initialization using the extrapolation technique presented in (5.3.8).

5.3.2 Intra-Pipe Restriction Boundary Problem Resolution

In this section, we extend the boundary resolution method considered in Section 5.3.1 to the intra-pipe boundary problem. Let start by introducing the schematic of the MOC for the intra-pipe boundary shown in Figure 5.17.

The index D represents the value of a variable upstream of the boundary, the index F

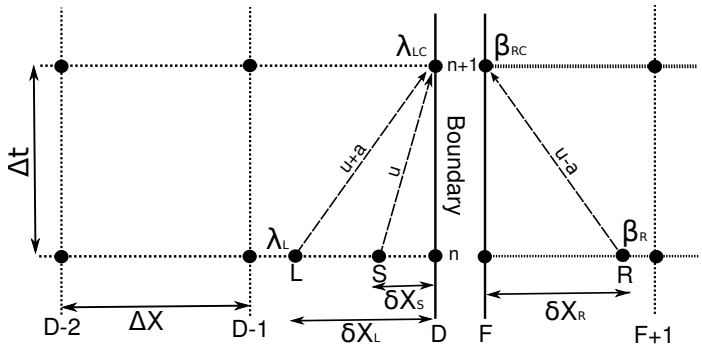

Figure 5.17: Intra-pipe MOC diagram

represents the value of a variable downstream of the boundary, the index L represents the interpolated point between D and $D-1$ where the trajectory $u+a$ crosses at time n and the index R represents the interpolated point between F and $F+1$ where the trajectory $a-u$ crosses at time n. The index S is associated to the trajectory u at time n. For the solution of the boundary problem, six unknowns have to be found (u_D^{n+1}, a_D^{n+1}, p_D^{n+1}, u_F^{n+1}, a_F^{n+1} and p_F^{n+1}), thus six equations are required.

Besides the two MOC equations associated with the trajectories $u+a$ and u described in the previous section ((5.3.4) and (5.3.7), respectively), a third equation, associated with the trajectory $a-u$ has to be formulated for the intra-pipe restriction boundary resolution. As introduced in (5.1.21), this MOC equation also has to be modified to take into account the change of entropy level at the boundary. Following a similar procedure as the one performed for (5.3.4), the following reference-free equation is obtained:

$$u_F^{n+1} = \frac{2}{\gamma - 1}\left(\beta_R^n - a_R^n \left(\frac{p_F^{n+1}}{p_R^n}\right)^{\frac{\gamma-1}{2\gamma}}\right) \tag{5.3.11}$$

Note that (5.3.11) gives an explicit relation between the downstream pressure p_F^{n+1} and particle speed u_F^{n+1}. The MOC-based equations (5.3.4), (5.3.7) and (5.3.11) provide three of the required equations for the boundary resolution. The fourth and fifth ones are obtained from the intra-pipe restriction model data-maps (5.2.23) and (5.2.24) and the sixth is given by the energy conservation. As in the outflow boundary resolution method, this system of equations cannot be solved analytically, therefore, a numerical scheme has to be considered once again. Due to the good results obtained for the outflow boundary problem, we also consider the NR method along with the numerical scheme initialization (5.3.8) for the intra-pipe boundary resolution. Although both methods are based on in the same numerical procedure, significant differences appear due to the inherent differences between both boundary problems (e.g. different choice for the convergence criterion).

Let us describe the procedure to solve the intra-pipe boundary problem. From the scheme initialization given in (5.3.8), a p_D^{it} is obtained. The particle speed and speed of sound upstream of the restriction u_D^{it} and a_D^{it} are calculated with (5.3.4) and (5.3.7), respectively.

The total speed of sound a_{tot}^{it} is calculated with (5.2.2) to find U_D^{it}. The pressure downstream of the restriction is computed using (5.2.23) and then, the particle speed U_F^{it} is explicitly calculated with (5.3.11). The energy conservation allows obtaining the speed of sound a_F^{n+1}. As nothing guaranties that the initialization (5.3.8) gives a consistent solution, the consistency of the system of equation is verified using the following convergence criterion:

$$f_{intra} =\mid p_F^{it}/p_D^{it} - datamap_{IRP}(U_D^{it}, \Phi_1, \Phi_3) \mid < \epsilon \tag{5.3.12}$$

If (5.3.12) is not satisfied, then the iterative NR method (5.3.10) is used to upgrade the pressure until the solution is consistent.

To implement the proposed method, consider the following steps:

1. calculate λ_L^n, s_S^n and β_R^n: use (5.1.10), (5.3.6) and (5.1.12), respectively;
2. initialize $p_D^{it} = 2p_{D-1}^{n+1} - p_{D-2}^{n+1}$ (this is the linear extrapolation using the two closest nodes inside the pipe where p_{D-1}^{n+1} and p_{D-2}^{n+1} are obtained by the in-pipe numerical scheme);
3. use (5.3.7) to calculate a_D^{it} and (5.3.4) to compute u_D^{it};
4. calculate the total sound speed with (5.2.2) and compute the non-dimensional speeds U_D^{it} and A_D^{it};
5. compute $U_F^{it} = datamap_{IRP}(U_D^{it}, \Phi_1, \Phi_3)$ using any of the restriction models;
6. use the total sound speed to calculate u_F^{it};
7. calculate p_F^{it} using (5.3.11). Use the energy conservation to find a_F^{it};
8. evaluate (5.3.12). If $f_{intra} < \epsilon$, then return $p_D^{n+1} = p_D^{it}$, $a_D^{n+1} = a_D^{it}$, $u_D^{n+1} = u_D^{it}$, $p_F^{n+1} = p_F^{it}$, $a_F^{n+1} = a_F^{it}$ and $u_F^{n+1} = u_F^{it}$. Otherwise, use (5.3.10) to update p_D^{it} and return to the step 3.

With this, we complete the presentation of the proposed outflow and intra-pipe boundary resolution methods. In the next Section, the performances of the non-homentropic boundary resolution methods are evaluated experimentally.

5.4 Experimental Evaluation of the Proposed Boundary Resolution Methods

In this chapter, we evaluate the performance of the proposed boundary resolution methods in terms of predictability and flexibility. The evaluation is carried out using experimental

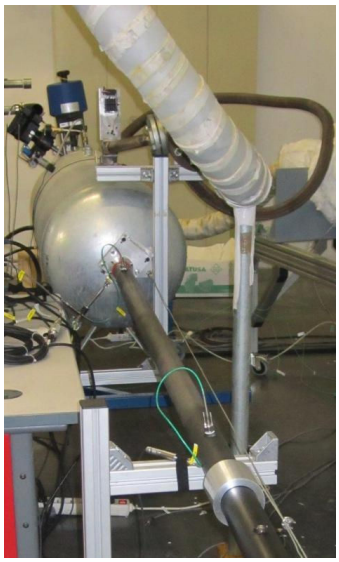

Figure 5.18: Experimental setup for the evaluation of the boundary resolution methods

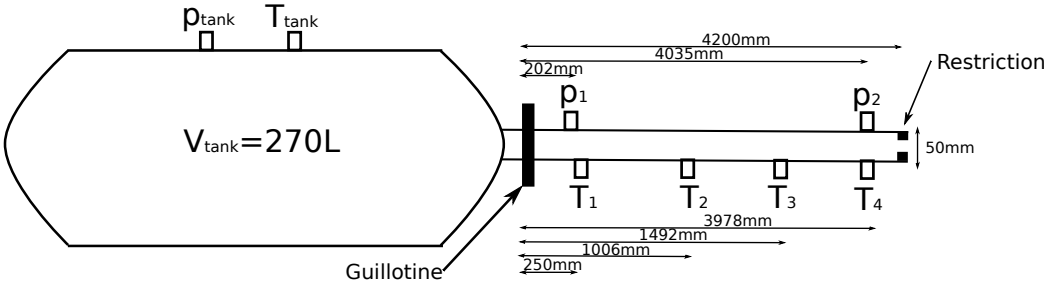

Figure 5.19: Schematic of the outflow restriction experimental setup

results obtained from an experimental setup specially designed for the validation of 1D unsteady flow models. Various alternative QS models are used to test effectiveness of the proposed boundary resolution schemes to integrate non-homentropic formulations into the wave action methods. The improvement in terms of predictability obtained from the complete non-homentropic formulations is demonstrated.

5.4.1 Experimental Setup

Figure 5.18 depicts a photo of the experimental apparatus designed for the evaluation of the boundary resolution methods developed in this thesis.

Two different assemblies of the apparatus are considered to evaluate separately the outflow and intra-pipe restriction boundary resolution methods. The schematics of each of the setups are presented in Figures 5.19 and 5.20, respectively.

The experimental setup consists of a thermally isolated reservoir of volume V_{tank}, a guil-

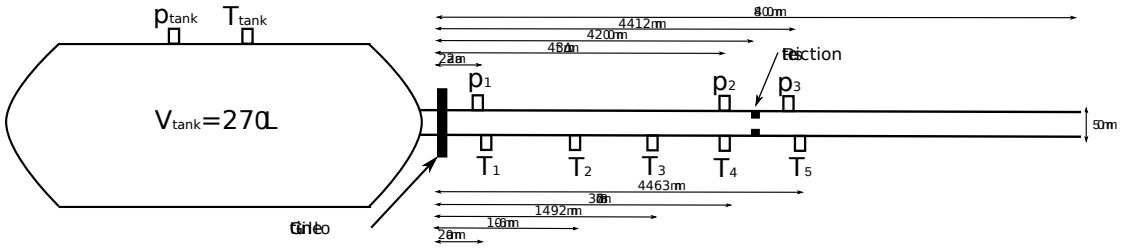

Figure 5.20: Schematic of the intra-pipe restriction experimental setup

lotine at the entrance of the tube and a pipe with an outflow restriction (or two pipes connected by a restriction for the intra-pipe restriction). The guillotine is designed to open very quickly allowing to introduce a shock wave in the tubes and therefore generating strong unsteady flow conditions. The gas inside the tank is heated up to introduce a change of the entropy level at the boundaries. Prior to the guillotine opening, the desired initial gas temperature is set by operating an inlet and an outlet valve connected to the reservoir. These valves are installed in a parallel air heating system not detailed in this work. After the warm-up phase, the valves are closed and remain in this position during the tests. The guillotine position is measured in order to approximate the area ratio of the input restriction during its unsteady conditions. The instantaneous pressures and temperatures are measured, as shown in Figures 5.19 and 5.20, to capture the behavior of the unsteady flow at different places of the setup. The instantaneous pressures are measured with Kistler 4049A10SP22 piezoresistive sensors and the temperatures are measured with thermosensors of type K with a diameter of 0.075 mm.

5.4.2 Outflow Boundary Resolution Method Evaluation

To illustrate the gain in terms of predictability and flexibility of the proposed non-homentropic outflow boundary resolution method described in Section 5.3.1, we evaluate its performance by comparing different QS outflow models with respect to experimental results. More precisely, we compare the performance of the isentropic-based outflow boundary formulation of Section 5.2.1.1 to that of the non-homentropic momentum-based approach given in Section 5.2.1.2.

Based on the setup depicted in Figure 5.19, three experiments are carried out with three different restriction areas ratios and three different initial values of p_{tank}. The dynamics of the reservoir pressure and temperature are modeled using the classical 0D thermodynamical model given in Section 3.2. This 0D model is initialized with the measurements $p_{tank}(t=0)$ and $T_{tank}(t=0)$. As the reservoir is thermally isolated, no heat wall transfers are considered. The in-pipe numerical scheme is the MacCormack method with Time Varying Diminishing post-processing given in Appendix A.3. The pipes friction and thermal exchange coefficients have been identified with the setup operating without

any restriction. To model the flow through the guillotine, the inflow boundary resolution method developed in [46] is implemented along with the constant pressure QS model (5.2.17) - (5.2.18). Taking these considerations into account, the setup given in Figure 5.19 has been built in a 1D platform developed in Matlab Simulink®. Table 5.3 shows the parameters chosen for the experiments:

Experiment/Parameter	Φ_1	p_{tank}
Experiment 1	0.1	1.1×10^5 [Pa]
Experiment 2	0.2	1.2×10^5 [Pa]
Experiment 3	0.5	1.4×10^5 [Pa]

Table 5.3: Outflow boundary experiment parameters

Figures 5.21, 5.22 and 5.23 depict the unsteady flow evolution obtained for the three different experimental conditions. Figures 5.21, 5.22 and 5.23 correspond to the experiments 1, 2 and 3, respectively. The initial reservoir temperature for all the experiments is $T_{tank}(t = 0) \approx 500K$ in order to introduce a significant change of entropy level. The pipe initial conditions are the atmospheric conditions, namely a pressure of $1.0 \times 10^5\ Pa$ and a temperature of $300K$. Two pressure and two temperature measurements are considered for the boundary resolution evaluation (according to Figure 5.19: p_1, p_2, T_1 and T_2).

The pressure decrease of the reservoir depends directly on the mass flow rate going through the guillotine, which is a good indicator for identifying the accuracy of the modeling strategies (see the pressure evolution at 202mm presented in Figures 5.21, 5.22 and 5.23). It is important to notice that the time responses of the sensors have to be taken into account for the results analysis, specially the temperature measurements. Table 5.4 presents a summary of the results using the root-mean-square deviation (RMSD) with respect to the measurements for each case. The pressures p_1 and p_2 have been chosen to illustrate the results.

Model/Variable	Model	p_1	p_2
$\Phi = 0.1$	Momentum-Based	2.9 %	4.9 %
	Isentopic-Based	9.0 %	11.0 %
$\Phi = 0.2$	Momentum-Based	6.2 %	7.3 %
	Isentopic-Based	18.7 %	20.4 %
$\Phi = 0.5$	Momentum-Based	18.9 %	20.2%
	Isentopic-Based	29.4 %	33.8 %

Table 5.4: RMSD for the outflow momentum-based and isentropic-based models.

The results of Figures 5.21, 5.22 and 5.23 and Table 5.4 indicate that the momentum-

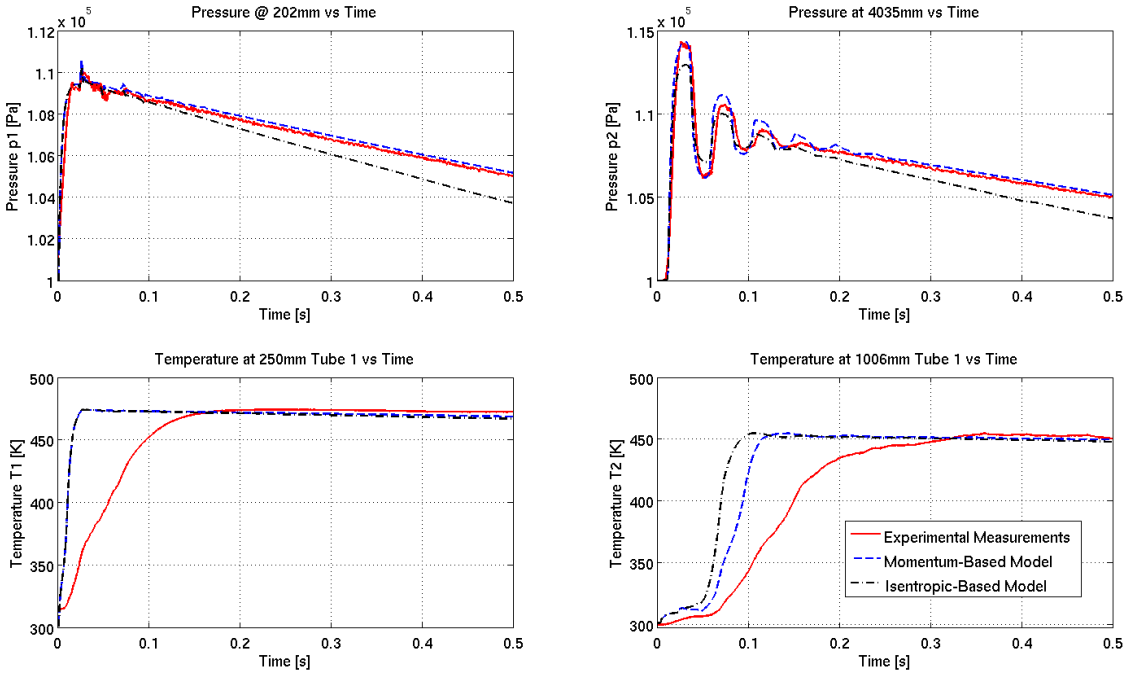

Figure 5.21: Evaluation results for $\Phi = 0.1$ and an initial reservoir pressure of 1.1×10^5 [Pa] (Experiment 1)

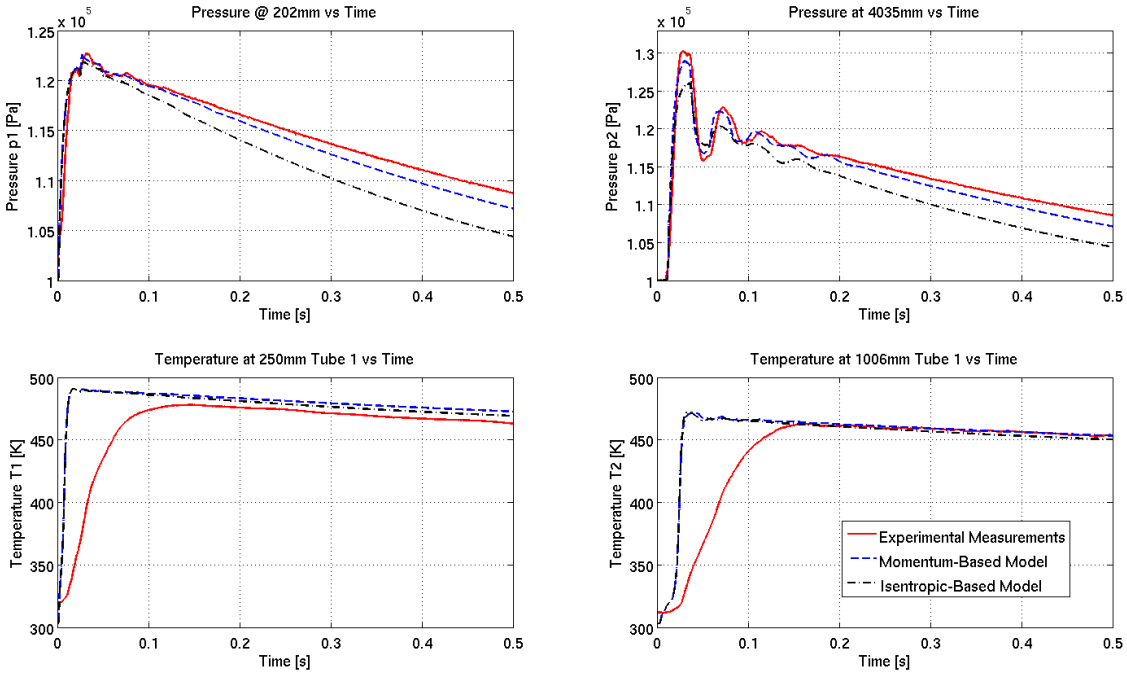

Figure 5.22: Evaluation results for $\Phi = 0.2$ and an initial reservoir pressure of 1.2×10^5 [Pa] (Experiment 2)

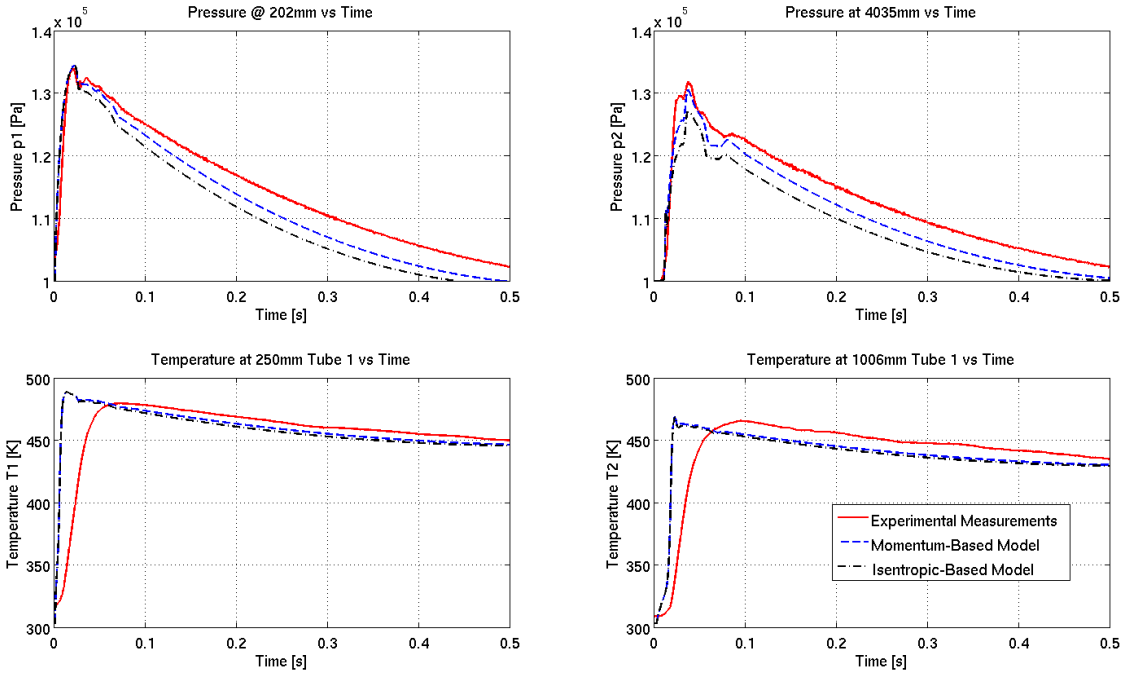

Figure 5.23: Evaluation results for $\Phi = 0.5$ and an initial reservoir pressure of 1.4×10^5 [Pa] (Experiment 3)

based outflow restriction model has a better predictability compared to the traditional isentropic-based approach. This result is consistent with the previous results in Section 5.2.1.4, where the momentum-based model exhibited a more predictable behavior than the isentropic-based approach. Moreover, these results show the effectiveness of the proposed non-homentropic boundary resolution method as the momentum-based model (which is a non-homentropic strategy) has been successfully integrated into the wave action numerical scheme. Also, both simulations were carried out using the proposed boundary resolution method, which shows the flexibility of the boundary resolution formulation since different QS models can be used without changing the boundary resolution method.

The unsteady flow behavior presented in Figures 5.21, 5.22 and 5.23 shows the impact that the outflow boundary formulation has on the performance of 1D simulation platforms. This confirms the significant importance of formulating better strategies for the boundary problem resolution.

5.4.2.1 Intra-Pipe Boundary Resolution Method Evaluation

To evaluate the performance of the intra-pipe boundary resolution method, we propose a comparison of four different QS restriction models with respect to the experimental results obtained in the setup of Figure 5.20. This allows illustrating the gain in predictability and

flexibility of the non-homentropic formulation developed in Section 5.3.2. The following QS intra-pipe models are considered:

- Isentropic outflow and constant pressure inflow model (denoted as Isen-CP Model);
- Isentropic outflow and momentum inflow model (denoted as Isen-Mom Model);
- Momentum outflow and constant pressure inflow model (denoted as Mom-CP Model);
- Momentum outflow and momentum inflow model (denoted as Mom-Mom Model).

As previously done for the outflow boundary resolution evaluation, three different experiments are carried out on the setup depicted in Figure 5.20 using the parameters presented in Table 5.5.

Experiment/Parameter	$\Phi_1 = \Phi_3$	p_{tank}
Experiment 1	0.1	1.1×10^5 [Pa]
Experiment 2	0.2	1.2×10^5 [Pa]
Experiment 3	0.5	1.4×10^5 [Pa]

Table 5.5: Intra-pipe restriction boundary experiment parameters

Figures 5.24, 5.25 and 5.26 show the results obtained for the experiments 1, 2 and 3, respectively. The initial reservoir temperature for all the experiments is set to $T_{tank}(t = 0) \approx 500K$. Three pressures and one temperature measurements are considered for the intra-pipe restriction boundary resolution method evaluation (according to Figure 5.20, p_1, p_2, p_3 and T_4, respectively). Table 5.6 summarizes the results using the RMSD for each case. The pressures p_1 and p_2 have been chosen to illustrate the results.

As shown in Figures 5.24, 5.25 and 5.26 and Table 5.6, the choice of the QS intra-pipe restriction model has a significant impact on the 1D unsteady flow simulation. The completely non-homentropic restriction model with momentum outflow and constant pressure inflow exhibits the best predictability according to the results of Table 5.6. It is curious that the traditionally used QS model of the intra-pipe restriction (Isen-Mom model) presents the lowest predictability, which confirms the importance of non-homentropic model independent boundary resolution methods. All four simulations were carried out using the same boundary resolution method, which, as seen in the results, has effectively solved the non-homentropic boundary problem independently of the QS model formulation. The method has successfully introduced a completely non-homentropic intra-pipe boundary resolution that performs much better in terms of predictability than traditional boundary resolution methods (see Table 5.6).

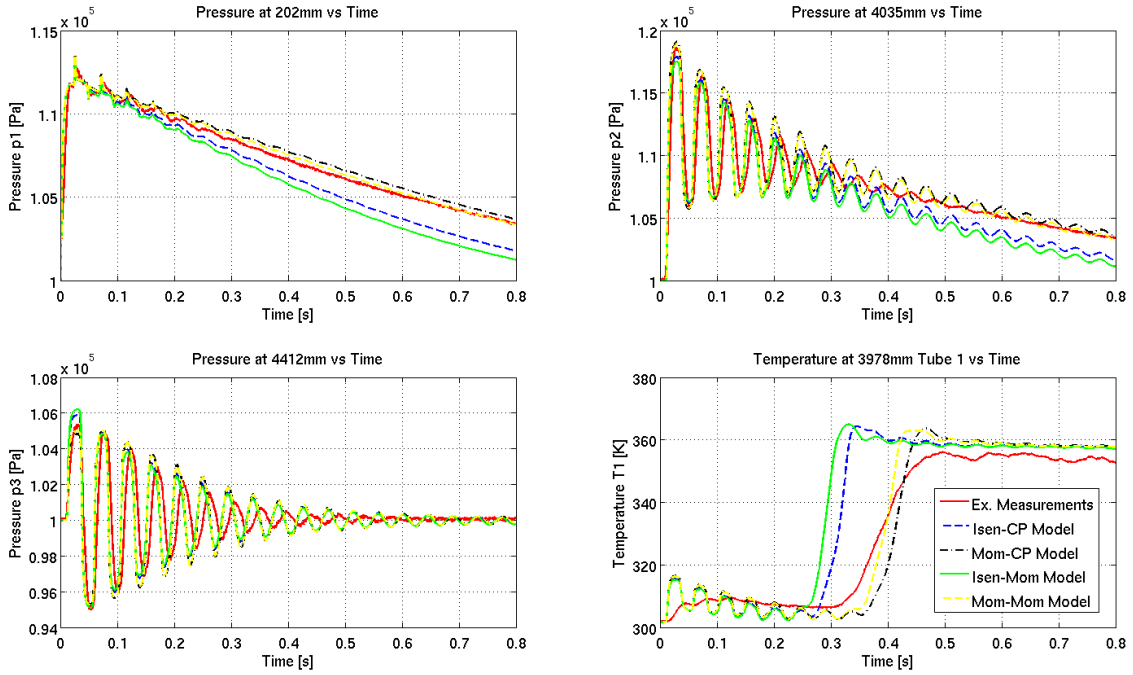

Figure 5.24: Evaluation results for $\Phi_1 = \Phi_3 = 0.1$ and an initial reservoir pressure of 1.1×10^5 [Pa] (Experiment 1)

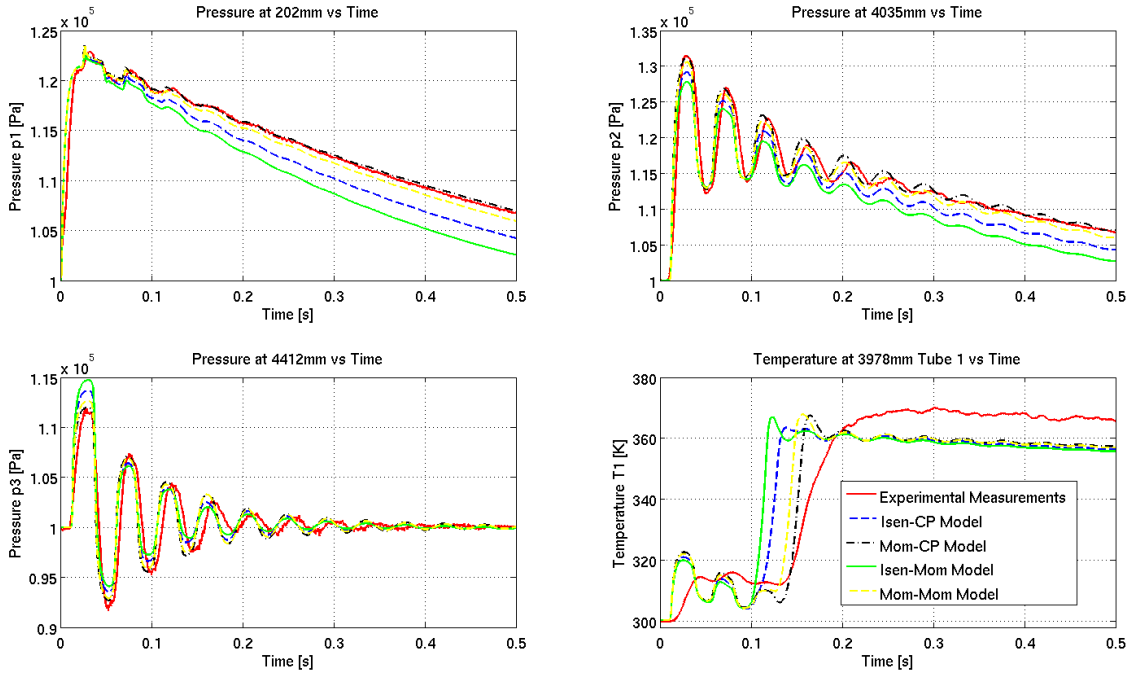

Figure 5.25: Evaluation results for $\Phi_1 = \Phi_3 = 0.2$ and an initial reservoir pressure of 1.2×10^5 [Pa] (Experiment 2)

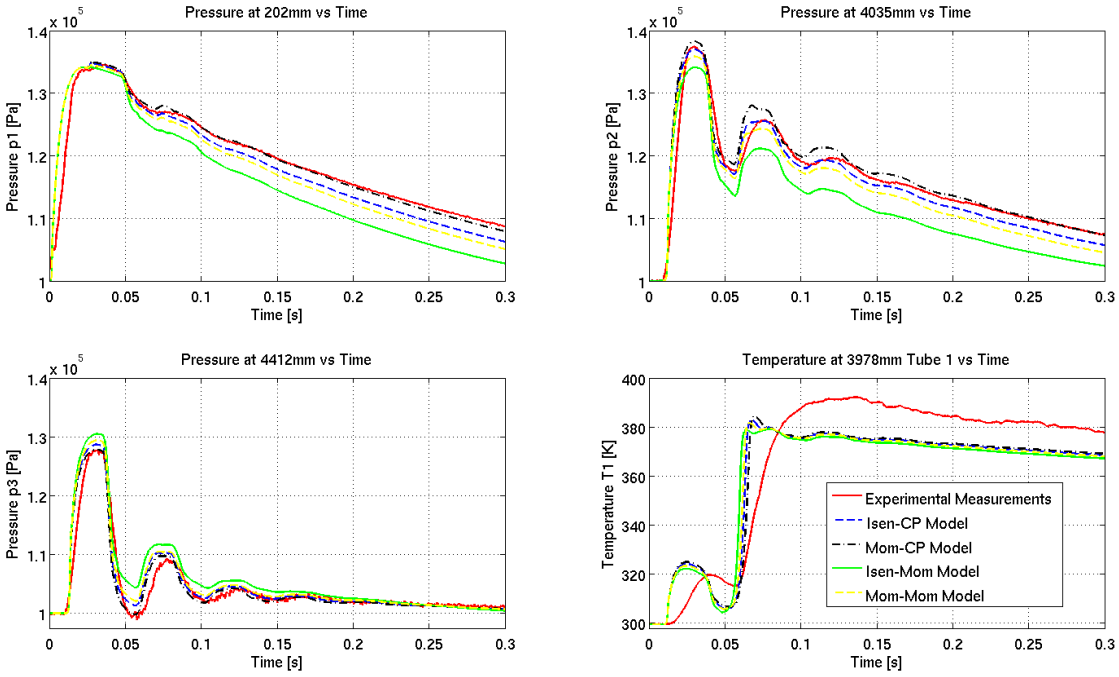

Figure 5.26: Evaluation results for $\Phi_1 = \Phi_3 = 0.5$ and an initial reservoir pressure of 1.4×10^5 [Pa] (Experiment 3)

Model/Variable	Model	p_1	p_2
$\Phi_1 = \Phi_3 = 0.1$	Isen-CP	13.1 %	20.2 %
	Mom-CP	5.6 %	15.3 %
	Isen-Mom	18.5 %	24.6 %
	Mom-Mom	3.1 %	14.0 %
$\Phi_1 = \Phi_3 = 0.2$	Isen-CP	13.2 %	15.5 %
	Mom-CP	2.5 %	8.3 %
	Isen-Mom	21.5%	23.7 %
	Mom-Mom	4.9 %	8.7 %
$\Phi_1 = \Phi_3 = 0.5$	Isen-CP	11.6 %	9.7%
	Mom-CP	5.2 %	6.4 %
	Isen-Mom	25.7 %	30.6 %
	Mom-Mom	15.7 %	15.5%

Table 5.6: RMS percentage error for the intra-pipe restriction boundary resolution methods

To summarize, in this section we have shown that by means of the non-homentropic boundary resolution methods developed in this chapter, the predictability, flexibility and numerical performance of 1D unsteady flow simulators can be significantly improved al-

lowing to obtain 1D engine air-path models better suited for control purposes.

5.5 Chapter Summary

In this chapter, alternative non-homentropic methods have been proposed for the outflow and intra-pipe boundary problem resolution. The main difference with respect to other boundary resolution formulations is that the assumption of the isentropic contraction at the boundary is removed, allowing to formulate completely non-homentropic methods. Moreover, the proposed methods allow incorporating various QS restriction models without having to modify the boundary resolution schemes. Additionally, other improvements are brought to the methods such as better numerical performance and reference-free entropy level correction.

Some alternative QS models for outflow as well as intra-pipe restrictions have been considered to illustrate the interest of non-homentropic boundary formulations. Two different QS outflow restriction models (isentropic-based and momentum-based strategies) have been introduced and then compared using 3D CFD simulation results. The momentum-based model has presented more predictability than the traditional QS model based on the isentropic contraction assumption, which evidences the importance of addressing the non-homentropic boundary resolution problem. A methodology to build intra-pipe QS models from a combination of an outflow and inflow formulation has also been discussed. Significant differences have been found between restriction models based on the isentropic contraction and non-homentropic formulations. To reduce the CPU calculation load, it is advantageous to store the solutions of the physical boundary models into data-maps. The procedures to perform these tasks have been described in details.

Based on a MOC approach modified to take into account the effects of the variation of entropy level at the boundaries, complete non-homentropic outflow and intra-pipe boundary resolution methods have been proposed. The traditional assumption of isentropic contraction at the outflow boundary has been removed to be consistent with a non-homentropic formulation. The proposed methods are more flexible than the traditional methods since different QS models can be considered without changing the boundary resolution schemes or adding artificial discharge coefficients. A NR method along with a linear extrapolation for the initialization of the numerical scheme has been considered to solve the boundary problem. A significant improvement in terms of calculation efficiency and accuracy has been obtained.

An experimental evaluation has been done using different QS restriction models in order to illustrate the effectiveness and the gain in terms of predictability and flexibility of the proposed non-homentropic boundary resolution method. It has been shown that the proposed boundary resolution method successfully integrated the non-homentropic

outflow and intra-pipe restriction models into the wave action method, allowing to obtain significant improvements in terms of predictability with respect to traditional isentropic approaches.

Chapter 6

Boundary Control and Observation of First-Order Hyperbolic Systems

As discussed in the previous chapters, it is of significant importance to effectively control and estimate the fresh air mass fraction in the intake manifold of dual-loop EGR Diesel engine air-paths. Indeed, a good control of the gas composition allows implementing alternative combustion modes, which are the key enabler to improve the engine emission performance. Most of the current engine control and estimation approaches are based on 0D modeling strategies, which have been successfully used during the recent years. However, as the complexity of the engine air-path increases and the engine emission regulations become more restrictive, the intrinsic limitations of 0D modeling have begun to constrain the performance of modern engine control strategies. For example, the mass transport in the engine air-path is a phenomenon that cannot be represented by means of 0D modeling, which currently generates a systematic degradation of the engine emission performance. Therefore, it is crucial to propose alternative control strategies (such as 1D model based control strategies) in order to comply with the future engine emission regulations.

The use of 1D air-path engine models for control purposes seems to be a natural approach to address many of the current limitations, such as the representation of the mass transport phenomenon. As seen in Chapter 5, these infinite dimensional models are described by a first-order quasi-linear hyperbolic partial differential equation (PDE) of the form (5.1.5), along with the boundary conditions that vary depending on the actuator associated with the boundary (i.e. EGR valves). It is common for most of the industrial processes to have the sensors and actuators only available at the boundaries. Indeed, this is particularly true for the engine air-path as no spacially distributed control or measurements are available in production engines. Thus, the use of boundary control strategies for hyperbolic systems appears as a good strategy to address the problem of the air fraction regulation in Diesel engines.

The boundary control of hyperbolic systems has been exhaustively investigated in the literature. However, most results consider that the boundary control can react fast enough when compared to the travel time of waves. More precisely, no time response limitation is taken into account at the boundary conditions. For many applications the wave travel can be considered much slower than the actuator time response, e.g for the boundary stabilization of open channels [9] [41] . Hence, a static relationship can be established between the control input and the boundary condition. Nevertheless, there are applications where the dynamics associated with the boundary control cannot be neglected (e.g. the air fraction control in an engine air-path) and thus alternative regulation strategies have to be proposed. The stability problem of hyperbolic systems in presence of dynamic behavior at the boundary conditions is a significantly less explored subject.

In this Chapter we address the problem of the dynamic boundary stabilization and the boundary observation of linear, quasi-linear and LPV first-order hyperbolic systems. We give sufficient conditions for the exponential stability for this class of infinite dimensional systems by means of Lyapunov based techniques and matrix inequalities. An air fraction boundary control for a Diesel engine operated with LP-EGR is proposed using some of the main results developed in this chapter. Although in this thesis we focus on the air fraction control and estimation in Diesel engines, the main results of this chapter extend to a large amount of industrial applications of significant importance such as hydraulic networks [85], multiphase flow [70], road traffic networks [51], gas flow in pipelines [8] and flow regulation in deep pits [102].

Chapter Structure This chapter starts with a description of the class of first-order hyperbolic systems considered in this thesis, followed by a review on the most representative boundary control strategies found in the literature. In Section 6.2 we use Lyapunov based techniques to find sufficient conditions for exponential stability of linear, LPV and quasi-linear hyperbolic systems with dynamics associated with their boundary conditions. A polytopic approach is developed for the LPV and quasi-linear hyperbolic systems to guarantee the exponential stability inside a prescribed non-empty convex set. The main results are presented using a matrix inequality framework.

In Section 6.3 we address the problem of the boundary observer design for one-dimensional first-order linear and quasi-linear strict hyperbolic systems with n rightward convecting transport PDEs. By means of Lyapunov based techniques, we derive some sufficient conditions for observer design using only the information from the boundary control and the boundary conditions. Both static and dynamic boundary controls are considered. In Section 6.4 we model the air fraction transport phenomenon using a cascade of first-order LPV hyperbolic systems with dynamics associated with the boundary conditions. Then, based of the theoretical developments of this chapter, we propose a new solution for the air fraction control in a Diesel engine operated with LP-EGR. Finally, the air-path boundary control is evaluated in simulation using a 1D model of the engine admission air-path.

Publications

The main contributions presented in this chapter are mostly described in the following publications:

- F. Castillo, E. Witrant, C. Prieur, and L. Dugard. Boundary Observers for Linear and Quasi-Linear Hyperbolic Systems with Application to Flow Control. *Automatica, 10.1016/j.automatica.2013.07.027*
- F. Castillo, E. Witrant, C. Prieur, V. Talon and L. Dugard. Engine Fresh Air Mass Fraction Control Using Dynamic Boundary Stabilization of Linear Parameter Varying Hyperbolic Systems. *Submitted to IEEE Transactions on Control Systems Technology*;
- F. Castillo, E. Witrant, C. Prieur, and L. Dugard. Dynamic boundary stabilization of linear and quasi-linear hyperbolic systems. Proceedings of the 51st IEEE Control and Decision Conference, Maui, Hawai, 2012;
- F. Castillo, E. Witrant, L. Dugard. Dynamic Boundary Stabilization of Linear Parameter Varying Hyperbolic Systems: Application to a Poiseuille Flow. Proceedings of the 11th IFAC Workshop on Time-Delay Systems, Grenoble, France. 2013;
- F. Castillo, E. Witrant, L. Dugard. Contrôle de température dans un flux de Poiseuille. Proceedings of the IEEE Conférence Internationale Francophone d'Automatique, Grenoble, France. 2012.

6.1 Linear and Quasi-Linear Hyperbolic Systems: Boundary Control Review

Let n be a positive integer and Θ be an open non-empty convex set of $\mathbb{R}^n$. Consider the following class of quasi-linear hyperbolic systems of order n:

$$\partial_t \xi(x,t) + \Lambda(\xi)\partial_x \xi(x,t) = 0 \quad \forall\, x \in [0,1], t \geq 0 \tag{6.1.1}$$

where $\xi : [0,1] \times [0,\infty) \to \mathbb{R}^n$ and Λ is a continuously differentiable diagonal matrix function $\Lambda : \Theta \to \mathbb{R}^{n\times n}$ such that $\Lambda(\xi) = diag(\lambda_1(\xi), \lambda_2(\xi), ..., \lambda_n(\xi))$. Assume the following.

Assumptions 6.1.1. *The following inequalities hold for all $\xi \in \Theta$:*

$$0 < \lambda_1(\xi) < \lambda_2(\xi) < ... < \lambda_n(\xi) \tag{6.1.2}$$

If $\Lambda(\xi) = \Lambda$, then (6.1.1) is a linear hyperbolic system given by:

$$\partial_t \xi(x,t) + \Lambda\partial_x \xi(x,t) = 0 \quad \forall\, x \in [0,1], t \geq 0 \tag{6.1.3}$$

Remark 6.1.1. *Define the open non-empty convex set of* $\mathbb{R}^n$ Ω *and consider the general class of quasi-linear hyperbolic systems of order* n *defined as follows [90]:*

$$\partial_t s(x,t) + F(s(x,t))\partial_x s(x,t) = 0 \tag{6.1.4}$$

where $s(x,t) \in \Omega$*, and* $F : \Omega \to \mathbb{R}^{n\times n}$ *is a continuously differentiable function. If* (6.1.4) *is strictly hyperbolic (all eigenvalues of* $F(s)$ *are different from zero and different between each other), then a bijection* $\xi(s) \in \Theta \subset \mathbb{R}^n$ *may exist, such that* (6.1.4) *can be transformed into the following system of coupled transport equations (it has been proved that for* $n \leq 2$*, this bijection always exists [38]):*

$$\partial_t \xi_i(x,t) + \lambda_i(\xi(x,t))\partial_x \xi_i(x,t) = 0, \quad i \in [1,...,n] \tag{6.1.5}$$

where $\xi_i(x,t)$ *are called the Riemann coordinates of* (6.1.4)*, which are constant along the characteristic curves described by:*

$$\frac{dx}{dt} = \lambda_i(\xi(x,t)) \tag{6.1.6}$$

where $\xi = [\xi_1, \xi_2, ..., \xi_n]^T$*. Using the transformation with Riemann coordinates, the system* (6.1.4) *can be expressed in the form of* (6.1.1)*.*

We consider two types of boundary controls for the quasi-linear hyperbolic system (6.1.1). The first one is a static boundary control given by:

$$\xi(0,t) = u_c(t) \tag{6.1.7}$$

and the second one is the dynamic boundary control:

$$\begin{aligned} \dot{X}_c &= A_c X_c(t) + B_c u_c(t) \\ Y_c(t) &= C_c X_c(t) + D_c u_c(t) \end{aligned} \tag{6.1.8}$$

with

$$Y_c(t) = \xi(0,t), \quad u_c = K\xi(1,t) \tag{6.1.9}$$

where $X_c \in \mathbb{R}^{n_x}$, $A_c \in \mathbb{R}^{n_x\times n_x}$, $B_c \in \mathbb{R}^{n_x\times n}$, $C_c \in \mathbb{R}^{n\times n_x}$, $D_c \in \mathbb{R}^{n\times n}$, $K \in \mathbb{R}^{n\times n}$, $u \in \mathbb{R}^n$ and $n_x \geq 1$. Define the initial condition for (6.1.1) and (6.1.8) as:

$$\begin{cases} \xi(x,0) = \xi^0(x), \quad \forall\, x \in [0,1] \\ X_c(0) = X_c^0 \end{cases} \tag{6.1.10}$$

where $\xi^0(x) \in L^2((0,1);\mathbb{R}^n)$ and $X_c^0 \in \mathbb{R}^{n_x}$. It has been proved that there exists a $\delta_0 > 0$ and a $T > 0$ such that for every $\xi^0 \in H^2((0,1),\mathbb{R}^n)$ satisfying $|\xi^0|_{H^2((0,1),\mathbb{R}^n)} < \delta_0$ and the zero-order and one-order compatibility conditions, the Cauchy problems ((6.1.1), (6.1.7)

and (6.1.10)) and ((6.1.1), (6.1.8) and (6.1.10)) have a unique maximal classical solution satisfying (see e.g. [39] and [58], among other references):

$$|\xi(.,t)|_{H^2} < \delta_0 \quad \forall t \in [0,T) \tag{6.1.11}$$

Moreover, for linear hyperbolic systems (6.1.3), it holds for $T = +\infty$. For the quasi-linear hyperbolic system (6.1.1), the following assumption is necessary for some of the results of this thesis.

Assumptions 6.1.2. *Given a sufficiently small initial condition (6.1.10), the solutions for (6.1.1), with boundary condition (6.1.7) or (6.1.8) and initial condition (6.1.10) are assumed to be defined for all $t > 0$.*

Remark 6.1.2. *Under Assumption 6.1.1 and the boundary conditions (6.1.7), there is no coupling between the states and thus a controller and an observer can be designed for each state separately. However, this is not true for the dynamic boundary conditions (6.1.8) as it induces a coupling between the states and motivates further analysis for the control and observer design.*

Several results are available in the literature for the control of first-order hyperbolic systems. For instance, sufficient conditions for controllability and observability of quasilinear hyperbolic systems have been obtained in [66]. The works of Krstic and co-workers (e.g. [63], [62], [72] and [92]) on boundary control using backstepping designs, and the works of Coron and co-workers (e.g. [39], [40], [9] and [42]) on dissipative boundary conditions, are some of the most representative references for the boundary control of first-order hyperbolic systems. Hence, these strategies are reviewed in details in this section. In [67], the boundary control problem is investigated using a frequency domain approach while [1] focuses in the disturbance rejection problem. In [80], a strict time-varying Lyapunov function that allows establishing the asymptotic stability of time-varying hyperbolic systems is formulated for time-invariant boundary conditions and in [79] the boundary control of switched linear hyperbolic systems is considered. Other important references on boundary control are found in [41], [65], [75] and [84].

The following two sections summarize two of the main approaches for the boundary stabilization for first-order hyperbolic systems.

6.1.1 Backstepping boundary control for first-order hyperbolic PDEs (M. Krstic, A. Smyshlyaev, F. Di Meglio and R. Vazquez.)

This boundary control strategy for first-order hyperbolic systems is based on the backstepping method initially developed by Krstic and co-workers for parabolic PDEs and

later for second-order hyperbolic systems [63]. The underlying idea of the backstepping method is to use an invertible Volterra integral transformation together with a specific boundary feedback to convert the hyperbolic PDE into a target system that is known to converge to zero in finite time. It turns out that for first-order hyperbolic systems, the kernel of this transformation is also a class of hyperbolic PDEs, which can be solved numerically, or, in certain cases, even in closed form. Some of the most representative works using this boundary control strategy are found in [62], [71] and [92].

To illustrate the basis of the backstepping boundary control method, define the following general first-order hyperbolic system:

$$\begin{aligned} \partial_t \xi &= \partial_x \xi + g(x)\xi(0) + \int_0^x (f(x,y)\xi(y))\, dy \\ \xi(1) &= \text{control input} \end{aligned} \tag{6.1.12}$$

where $\xi(1) = \xi(1,t)$. Consider the Volterra integral transformation given by:

$$w(x) = \xi(x) - \int_0^x k(x,y)\xi(y)dy \tag{6.1.13}$$

along with the full-state feedback control:

$$\xi(1) = \int_0^1 k(1,y)\xi(y)dy \tag{6.1.14}$$

where $k(x,y)$ is the gain kernel. The transformation (6.1.13) along with the control input (6.1.14) allows converting (6.1.12) into the following target system:

$$\begin{aligned} \partial_t w &= \partial_x w \\ w(1) &= 0 \end{aligned} \tag{6.1.15}$$

which is exponentially stable [63]. The main goal of this boundary control strategy is to find the kernel gain $k(x,y)$ such that the system (6.1.12) with the control (6.1.14) behaves like the target system (6.1.15). In [62], it has been found that from (6.1.12)-(6.1.15), one can derive the following PDE to generate the kernel gain:

$$\begin{aligned} \partial_x k(x,y) + \partial_y k(x,y) &= \int_y^x k(x,\upsilon) f(\upsilon,y) d\upsilon - f(x,y) \\ k(x,0) &= \int_0^x k(x,y) g(y) dy - g(x) \end{aligned} \tag{6.1.16}$$

System (6.1.16) has to be solved in order to generate the boundary control (6.1.14). Note that this requires the knowledge of the full-state ξ.

Despite the efficiency of this boundary control strategy, the required knowledge of the full-state to set the control input implies performing a state observation, leading to relatively heavy computations (e.g. infinite dimensional calculations and online solution of PDEs), which does not match the Specifications 4.0.1.

6.1.2 Dissisative boundary conditions for one-dimensional hyperbolic systems (J-M. Coron, G. Bastin, B. d'Andréa-Novel, C. Prieur, V. Dos Santos.)

This boundary control strategy relies on the construction of an explicit strict Lyapunov function. Sufficient conditions on the boundary conditions are given for the exponential stability of one-dimensional linear and non-linear hyperbolic systems. The boundary control is set using only the information available at the boundaries, along with a boundary control gain that can be easily calculated using matrix inequalities. This boundary control strategy has been extensively used, e.g. see [9],[39], [42], [81] and [85], among others.

Consider the linear hyperbolic system given in (6.1.3) with the static boundary control:

$$\xi(0,t) = K\xi(1,t) \tag{6.1.17}$$

where K is the gain of the boundary control. The main goal of the dissipative boundary control approach is to find the set of K such that (6.1.3) together with (6.1.17) is exponentially stable. In [40], the following Lyapunov function candidate was proposed:

$$V(\xi) = \int_0^1 \xi^T \xi e^{-\mu x} dx \tag{6.1.18}$$

where μ is a positive scalar. Computing the time derivative $\dot{V}$ of V along the classical L^2-solutions of (6.1.3) with boundary conditions (6.1.18), yields the following:

$$\dot{V} = -\xi^T(1,t)\left[e^{-\mu}\Lambda - K^T\Lambda K\right]\xi(1,t) - \mu\int_0^1 \xi^T\Lambda\xi e^{-\mu x}dx \tag{6.1.19}$$

By considering that μ is small enough, Coron and co-workers showed that the sufficient condition for the exponential stability of (6.1.3) and (6.1.17) is the following [39]:

$$\rho_1(K) := \mathrm{Inf}\{\parallel \Delta K\Delta^{-1} \parallel; \Delta \in \mathbb{D}_{n,+}\} < 1 \tag{6.1.20}$$

where $\mathbb{D}_{n,+}$ denotes the set on $n \times n$ real strictly positive diagonal matrices. Based on the explicit strict Lyapunov function (6.1.18) and the static boundary control (6.1.17) (both modified depending on the case), a large amount of extensions to more complex hyperbolic systems have been developed: e.g. in [39], sufficient conditions for the exponential stability of quasi-linear hyperbolic systems have been found, in [79] for switched linear hyperbolic systems and in [42], the boundary dissipative conditions for linear hyperbolic systems of balances laws have been given.

The main advantage of this approach is that only the information at the boundaries is required for the implementation of the control law, which makes it suitable to answer the Specifications 4.0.1.

The boundary control of hyperbolic systems is currently a very active research area, with many issues that still need to be addressed. The dynamic boundary stabilization of hyperbolic systems and the boundary observer design for quasi-linear hyperbolic systems are considered in this thesis. Specifically, we develop sufficient conditions for:

- boundary stabilization of linear and quasi-linear hyperbolic systems with dynamic boundary conditions given by (6.1.8);
- boundary stabilization of LPV hyperbolic systems with LPV dynamic boundary conditions;
- boundary observation of linear hyperbolic systems with dynamic boundary conditions;
- boundary observation of quasi-linear hyperbolic systems with static and dynamic boundary conditions.

In Section 6.2, we develop our main results on dynamic boundary stabilization of hyperbolic systems. In Section 6.3, we establish sufficient conditions for the boundary observer design of linear and quasi-linear hyperbolic systems. Finally in Section 6.4, we proposed a new strategy to control the air fraction in the intake manifold of Diesel engines operated with LP-EGR using some of the theoretical results of this chapter.

6.2 Dynamic Boundary Stabilization of Hyperbolic Systems

In this section, we give sufficient conditions for the dynamic boundary stabilization of linear, LPV and quasilinear hyperbolic systems (Sections 6.2.1, 6.2.2 and 6.2.3, respectively). More precisely, we address the problem of finding the boundary control gain K (according to (6.1.8) - (6.2.19)) such that (6.1.1) is exponentially stable.

6.2.1 Stability of Linear Hyperbolic Systems with Dynamic Boundary Conditions

Sufficient conditions for the exponential stability of (6.1.3) with boundary conditions (6.1.8) and initial condition (6.1.10) are obtained with the following theorem:

Theorem 6.2.1. *[Stability analysis] Along with Assumption 6.1.1, assume that there exist two diagonal positive definite matrices* $P_1 \in \mathbb{R}^{n_x \times n_x}$ *and* $P_2 \in \mathbb{R}^{n \times n}$ *and a scalar* $\mu > 0$

such that the following matrix inequality is satisfied,

$$M = \left[\begin{array}{c|c} \begin{array}{c} A_c^T P_1 + P_1 A_c + C_c^T \Lambda P_2 C_c \\ + K D_c^T \Lambda P_2 D_c K + \mu \Lambda P_1 \end{array} & P_1 B_c K + C_c^T \Lambda P_2 D_c K \\ \hline K^T B_c^T P_1 + K^T D_c^T \Lambda P_2 C_c & -e^{-\mu} \Lambda P_2 \end{array}\right] \preceq 0 \tag{6.2.1}$$

Then, there exist two constant scalars $a > 0$ and $b > 0$ such that, for all $\xi^0 \in L^2((0,1);\mathbb{R}^n)$ and $X_c^0 \in \mathbb{R}^{n_x}$, the solution of (6.1.3), (6.1.8) and (6.1.10) satisfies, for all $t \geq 0$

$$||X_c(t)||^2 + ||\xi(t)||_{L^2(0,1)} \leq b e^{-at} \left(||X_c^0||^2 + ||\xi^0||_{L^2(0,1)} \right) \tag{6.2.2}$$

Proof: Given the diagonal positive definite matrices P_1 and P_2, consider (as an extension of the Lyapunov function proposed in [40]) the quadratic strict Lyapunov function candidate defined for all continuously differentiable functions $\xi : [0,1] \to \Theta$ as:

$$V(\xi, X_c) = X_c^T P_1 X_c + \int_0^1 \left(\xi^T P_2 \xi \right) e^{-\mu x} dx \tag{6.2.3}$$

where μ is a positive scalar. Note that (6.2.3) has some similarities with respect to the Lyapunov function proposed in [84] for boundary control with integral action. Computing the time derivative $\dot{V}$ of V along the classical C^1-solutions of (6.1.3) with boundary conditions (6.1.8) and initial condition (6.1.10), yields to the following:

$$\dot{V} = \dot{X}_c^T P_1 X_c + X_c^T P_1 \dot{X}_c + \int_0^1 \left(\dot{\xi}^T P_2 \xi + \xi^T P_2 \dot{\xi} \right) e^{-\mu x} dx \tag{6.2.4}$$

After integration by parts, the following is obtained:

$$\begin{aligned} \dot{V} = & \left(X_c^T \left(A_c^T P_1 + P_1 A_c \right) X_c \right) + \left(\xi(1)^T K^T B_c^T P_1 X_c + X_c^T P_1 B_c K \xi(1) \right) \\ & - \left[e^{-\mu x} \xi^T \Lambda P_2 \xi \right] \Big|_0^1 - \mu \int_0^1 \left(\xi^T \Lambda P_2 \xi \right) e^{-\mu x} dx \end{aligned} \tag{6.2.5}$$

where $\xi(1) = \xi(1,t)$. The previous equation can be written using the boundary conditions (6.1.8) as follows:

$$\begin{aligned} \dot{V} = & \left(X_c^T \left(A_c^T P_1 + P_1 A_c \right) X_c \right) + \left(\xi(1)^T K^T B_c^T P_1 X_c + X_c^T P_1 B_c K \xi(1) \right) \\ & - e^{-\mu} \xi(1)^T \Lambda P_2 \xi(1) + X_c^T C_c^T \Lambda P_2 C_c X_c + X_c^T C_c^T \Lambda P_2 D_c K \xi(1) \\ & + \xi(1)^T K^T D_c^T \Lambda P_2 C_c X_c + \xi(1)^T K^T D_c^T \Lambda P_2 D_c K \xi(1) - \mu \int_0^1 \left(\xi^T \Lambda P_2 \xi \right) e^{-\mu x} dx \\ = & -\mu X_c^T \Lambda P_1 X_c - \mu \int_0^1 \left(\xi^T \Lambda P_2 \xi \right) e^{-\mu x} dx + \begin{bmatrix} X_c \\ \xi(1) \end{bmatrix}^T M \begin{bmatrix} X_c \\ \xi(1) \end{bmatrix} \end{aligned} \tag{6.2.6}$$

where the matrix M is defined as in (6.2.1). The matrix inequality $M \preceq 0$ implies that the last term of (6.2.6) is always negative or zero. This gives the following inequality:

$$\dot{V} \leq -\mu X_c^T \Lambda P_1 X_c - \mu \int_0^1 \left(\xi^T \Lambda P_2 \xi\right) e^{-\mu x} dx \tag{6.2.7}$$

From (6.1.2) it can be proved that there always exists a $\varrho > 0$ such that $\Lambda - \varrho I^{n\times n} \succ 0$ (e.g. ϱ could be the smallest eigenvalue of Λ. Moreover, the diagonality of P_1, P_2 and Λ implies that:

$$\dot{V} \leq -\mu\varrho V(\xi, X_c) \tag{6.2.8}$$

Therefore, the function (6.2.3) is a Lyapunov function for the hyperbolic system (6.1.3) with boundary conditions (6.1.8).

Integrating the inequality (6.2.8) from 0 to t gives the following:

$$V(t) \leq V(0) e^{-\mu\varrho t} \tag{6.2.9}$$

To obtain the final result (6.2.2), we bound the Lyapunov function as follows:

$$\begin{aligned} &\min\{\lambda_{min}(P_1), \lambda_{min}(P_2)\}(||X_c(t)||^2 + ||\xi(t)||_{L^2(0,1)}) \leq \\ &V(t) \leq \max\{\lambda_{max}(P_1), \lambda_{max}(P_2)\}(||X_c(t)||^2 + ||\xi(t)||_{L^2(0,1)}) \end{aligned} \tag{6.2.10}$$

where λ_{min} and λ_{max} are the minimum and maximum eigenvalues of the considered matrices, respectively. Then, using (6.2.9) together with (6.2.10) gives:

$$||X_c(t)||^2 + ||\xi(t)||_{L^2(0,1)} \leq \frac{\min\{\lambda_{min}(P_1), \lambda_{min}(P_2)\}}{\max\{\lambda_{max}(P_1), \lambda_{max}(P_2)\}} \left(||X_c^0||^2 + ||\xi^0||_{L^2(0,1)}\right) e^{-\mu\varrho t} \tag{6.2.11}$$

which implies that $a = \mu\varrho$ and $b = \min\{\lambda_{min}(P_1), \lambda_{min}(P_2)\}/\max\{\lambda_{max}(P_1), \lambda_{max}(P_2)\}$ in (6.2.2). ■

Note that the matrix inequality (6.2.1) considers, through the Lyapunov matrices P_1 and P_2 , the dynamic coupling between the system and its boundary conditions. Inequality (6.2.1) along with (6.2.8) implies that μ is a tuning parameter of the controller design as it explicitly enables to set the convergence speed of the Lyapunov function. Another interesting convergence feature can be deduced from (6.2.8): a faster convergence is obtained for larger values of ϱ. This implies that hyperbolic systems with high convective velocities converge faster, which is physically consistent.

The following corollary gives a sufficient condition for the design of a stabilizing controller for the particular case where C_c is a diagonal matrix, $D_c = 0$ and $n = n_x$.

Corollary 6.2.2. *[Design of a stabilizing controller] Along with Assumption 6.1.1, if C_c is diagonal and $D_c = 0$ and if there exists a diagonal positive definite matrix $Q \in \mathbb{R}^{n\times n}$ and a scalar $\mu > 0$ such that the following linear matrix inequality is satisfied,*

$$\begin{bmatrix} QA_c^T + A_cQ + C_c\Lambda QC_c + \mu\Lambda Q & B_c(w_i)Y \\ Y^TB_c^T & -e^{-\mu}\Lambda Q \end{bmatrix} \preceq 0 \tag{6.2.12}$$

where $Y = KQ$, then there exist two constants $\alpha > 0$ and $M > 0$ such that, for all $\xi^0(x) \in L^2((0,1);\mathbb{R}^n)$ and $X_c^0 \in \mathbb{R}^n$, the solution of (6.1.3) with boundary conditions (6.1.8) and initial condition (6.1.10) satisfies (6.2.2) for all $t \geq 0$.

Proof: Given a diagonal positive definite matrix P, consider the quadratic strict Lyapunov function candidate defined for all continuously differentiable functions $\xi : [0,1] \to \Theta$ as:

$$V(\xi, X_c) = X_c^TPX_c + \int_0^1 \left(\xi^TP\xi\right) e^{-\mu x}dx \tag{6.2.13}$$

where μ is a positive scalar. Performing the same procedure as the one presented in the proof of Theorem 6.2.1 and considering $D_c = 0$, the following equality is obtained

$$\dot{V} = -\mu X_c^T\Lambda PX_c - \mu\int_0^1 \left(\xi^T\Lambda P\xi\right) e^{-\mu x}dx + \begin{bmatrix} X_c \\ \xi(1) \end{bmatrix}^T H \begin{bmatrix} X_c \\ \xi(1) \end{bmatrix} \tag{6.2.14}$$

where

$$H = \begin{bmatrix} A_c^TP + PA_c + C_c\Lambda PC_c + \mu\Lambda P & PB_cK \\ K^TB_c^TP & -e^{-\mu}\Lambda P \end{bmatrix} \tag{6.2.15}$$

Note that (6.2.12) is equivalent to $H \preceq 0$. This is obtained by multiplying both sides of (6.2.32) by $diag\,(P^{-1}, P^{-1})$, commuting P^{-1} with C_c (both matrices being diagonal) and performing the variable transformations $Q = P^{-1}$ and $Y = KQ$. Therefore, as $H \preceq 0$ and $\Lambda - \varrho I^{n\times n} \succ 0$, the function (6.2.13) is a Lyapunov function for the hyperbolic system (6.1.3) with boundary conditions (6.1.8). ■

This corollary is interesting because, for systems where C_C is diagonal and $D_c = 0$, it provides a constructive approach to obtain the boundary control gain K using convex optimization algorithms after determining a suitable value of $\mu > 0$ (e.g. chosen to obtain a good performance versus robustness trade-off for the system considered).

Remark 6.2.1. The previous results (namely Theorem 6.2.1 and Corollary 6.2.2) extend to first-order hyperbolic systems with both negative and positive convective speeds ($\lambda_1 <$

$... < \lambda_m < 0 < \lambda_{m+1} < ... < \lambda_n$) by defining the state description $\xi = \begin{bmatrix} \xi_- \\ \xi_+ \end{bmatrix}$, where $\xi_- \in \mathbb{R}^m$ and $\xi_+ \in \mathbb{R}^{n-m}$, and the variable transformation $\tilde{\xi}(x,t) = \begin{pmatrix} \xi_-(1-x,t) \\ \xi_+(x,t) \end{pmatrix}$.

6.2.2 Stability of Parameter-Varying Linear Hyperbolic Systems with Dynamic Boundary Conditions

Let Z_φ be a non empty convex set of $\mathbb{R}^l$. Consider the general class of first-order LPV hyperbolic systems of order n defined as follows:

$$\partial_t \xi(x,t) + \Lambda(\varphi)\partial_x \xi(x,t) = 0 \quad \forall\, x \in [0,1], t \geq 0 \tag{6.2.16}$$

where $\xi : [0,1] \times [0,+\infty) \to \Theta$, φ is a varying parameter vector that takes values in the parameter space Z_φ, $\Lambda(\varphi) : Z_\varphi \to \mathbb{R}^{n\times n}$ is a diagonal and invertible matrix function (called the characteristic matrix) such that $\Lambda(\varphi) = diag(\lambda_1(\varphi), \lambda_2(\varphi), ..., \lambda_n(\varphi))$.

Assumptions 6.2.3. *Assume that the following inequalities hold for all $\varphi \in Z_\varphi$:*

$$0 < \lambda_1(\varphi) < ... < \lambda_n(\varphi) \tag{6.2.17}$$

Consider the following dynamic boundary conditions for (6.2.16):

$$\begin{aligned} \dot{X}_c &= A_c(\varphi)X_c + B_c(\varphi)u \\ Y_c &= C_c X_c + D_c u \end{aligned} \tag{6.2.18}$$

with

$$Y_c = \xi(0,t), \quad u = K\xi(1,t) \tag{6.2.19}$$

where $X_c \in \mathbb{R}^{n_x}$, $A_c : Z_\varphi \to \mathbb{R}^{n_x \times n_x}$, $B_c : Z_\varphi \to \mathbb{R}^{n_x \times n}$, $C_c \in \mathbb{R}^{n\times n_x}$, $D_c \in \mathbb{R}^{n\times n}$, $K \in \mathbb{R}^{n\times n}$, $u \in \mathbb{R}^n$ and $n_x \geq 1$. Define the initial condition for (6.2.16) as done in (6.1.10).

Let the polytope Z_φ be defined as follows:

$$Z_\varphi := \{[\varphi_1, ..., \varphi_l]^T \in \mathbb{R}^l \mid \varphi_i \in [\overline{\varphi}_i, \underline{\varphi}_i], \forall\, i = 1, ..., l\} \tag{6.2.20}$$

for given $\overline{\varphi}_i$, $\underline{\varphi}_i$ and $l \in \mathbb{N}^+$. We thus consider that all the admissible values of the vector φ are constrained in a hyperrectangle in the parameter space Z_φ. Consider the polytopic linear representation of the parameter varying characteristic matrix for all $\varphi \in Z_\varphi$ [7]:

$$\Lambda(\varphi) = \sum_{i=1}^{N_\varphi} \alpha_i(\varphi)\Lambda(w_i) \tag{6.2.21}$$

where $w_i \in Z_\varphi$ are the $N_\varphi = 2^l$ vertices of the polytope formed by all extremities ($\overline{\varphi}_i$ and $\underline{\varphi}_i$) of each varying parameter $\varphi \in Z_\varphi$, $\sum_{i=1}^{2^l} \alpha_i(\varphi)\Lambda(w_i) : Z_\varphi \to \mathbb{R}^{n\times n}$ and $\alpha_i(\varphi)$ is a scheduling function $\alpha_i : Z_\varphi \to [0,1]$ previously defined in (4.2.25) - (4.2.27).

The polytopic representation (6.2.21) can also be considered for the matrices $A_c(\varphi)$ and $B_c(\varphi)$ of the boundary conditions (6.2.18) using the same scheduling function (4.2.25). Define the polytopic linear representation (PLR) of the parameter varying hyperbolic system (6.2.16) with boundary conditions (6.2.18) as follows:

$$\begin{aligned} &\partial_t \xi(x,t) + \sum_{i=1}^{N_\varphi} \alpha_i(\varphi)\Lambda(w_i)\partial_x \xi(x,t) = 0 \\ &\forall\, \varphi \in Z_\varphi, \quad \forall\, x \in [0,1], \quad t \geq 0 \end{aligned} \tag{6.2.22}$$

with boundary conditions

$$\begin{aligned} \dot{X}_c &= \sum_{i=1}^{N_\varphi} \alpha_i(\varphi) A_c(w_i) X_c + \sum_{i=1}^{N_\varphi} \alpha_i(\varphi) B_c(w_i) u \\ Y_c &= C_c X_c + D_c u \end{aligned} \tag{6.2.23}$$

Based on the PLR (6.2.22) - (6.2.23), the following theorem states a sufficient condition to ensure the exponential stability for system (6.2.16) with boundary conditions (6.2.18) and initial condition (6.1.10) for all $\varphi \in Z_\varphi$.

Theorem 6.2.4. *[Stability analysis] Along with Assumption 6.2.3, assume that there exists two diagonal positive definite matrices $P_1 \in \mathbb{R}^{n_x \times n_x}$ and $P_2 \in \mathbb{R}^{n\times n}$ and a scalar $\mu > 0$ such that the following matrix inequality is satisfied, for all $i = 1, ..., N_\varphi$,*

$$M_i = \left[\begin{array}{c|c} \begin{array}{c} A_c(w_i)^T P_1 + P_1 A_c(w_i) + C_c^T \Lambda(w_i) P_2 C_c \\ + K D_c^T \Lambda(w_i) P_2 D_c K + \mu \Lambda(w_i) P_1 \end{array} & P_1 B_c(w_i) K + C_c^T \Lambda(w_i) P_2 D_c K \\ \hline K^T B_c(w_i)^T P_1 + K^T D_c^T \Lambda(w_i) P_2 C_c & -e^{-\mu} \Lambda(w_i) P_2 \end{array}\right] \preceq 0 \tag{6.2.24}$$

Then there exist two constant scalars $a > 0$ and $b > 0$ such that, for all $\xi^0 \in L^2((0,1);\mathbb{R}^n)$ and $X_c^0 \in \mathbb{R}^{n_x}$, the solution of (6.2.16), (6.2.18) and (6.1.10) satisfies (6.2.2), for all $t \geq 0$.

Proof: Consider once again the Lyapunov function candidate (6.2.3). Computing the time derivative $\dot{V}$ of V along the classical C^1-solutions of (6.2.16) with boundary conditions (6.2.18) and initial conditions (6.1.10), gives the following:

$$\dot{V} = \dot{X}_c^T P_1 X_c + X_c^T P_1 \dot{X}_c + \int_0^1 \left(\dot{\xi}^T P_2 \xi + \xi^T P_2 \dot{\xi}\right) e^{-\mu x} dx \tag{6.2.25}$$

After integration by parts and taking into account the PLR (6.2.16) and (6.2.18), the following is obtained:

$$\begin{aligned}\dot{V} = \sum_{i=1}^{2^l} \alpha_i(\varphi) \Big[\left(X_c^T \left(A_c(w_i)^T P_1 + P_1 A_c(w_i)\right) X_c\right) + \left(\xi(1)^T K^T B_c(w_i)^T P_1 X_c \right. \\ \left. + X_c^T P_1 B_c(w_i) K \xi(1)\right) - \left[e^{-\mu x} \xi^T \Lambda(w_i) P_2 \xi\right] \Big|_0^1 - \mu \int_0^1 \left(\xi^T \Lambda(w_i) P_2 \xi\right) e^{-\mu x} dx \Big]\end{aligned} \tag{6.2.26}$$

The previous equation can be written using the boundary conditions (6.2.18) as follows:

$$\begin{aligned}\dot{V} &= \sum_{i=1}^{2^l} \alpha_i(\varphi) \Big[\left(X_c^T \left(A_c(w_i)^T P_1 + P_1 A_c(w_i)\right) X_c\right) + \left(\xi(1)^T K^T B_c(w_i)^T P_1 X_c \right. \\ &\quad \left. + X_c^T P_1 B_c(w_i) K \xi(1)\right) - e^{-\mu} \xi(1)^T \Lambda(w_i) P_2 \xi(1) + X_c^T C_c^T \Lambda(w_i) P_2 C_c X_c \\ &\quad + X_c^T C_c^T \Lambda(w_i) P_2 D_c K \xi(1) + \xi(1)^T K^T D_c^T \Lambda(w_i) P_2 C_c X_c \\ &\quad + \xi(1)^T K^T D_c^T \Lambda(w_i) P_2 D_c K \xi(1) - \mu \int_0^1 \left(\xi^T \Lambda(w_i) P_2 \xi\right) e^{-\mu x} dx \Big] \\ &= \sum_{i=1}^{2^l} \alpha_i(\varphi) \Bigg[- \mu X_c^T \Lambda(w_i) P_1 X_c - \mu \int_0^1 \left(\xi^T \Lambda(w_i) P_2 \xi\right) e^{-\mu x} dx \\ &\quad + \begin{bmatrix} X_c \\ \xi(1) \end{bmatrix}^T M_i \begin{bmatrix} X_c \\ \xi(1) \end{bmatrix} \Bigg]\end{aligned} \tag{6.2.27}$$

where the matrix M_i is defined as in (6.2.24). The definition $\alpha_i \geq 0$ and the matrix inequality $M_i \preceq 0$ from (6.2.24) imply that the last term of (6.2.27) is always negative or zero. This gives the following inequality:

$$\dot{V} \leq \sum_{i=1}^{2^l} \alpha_i(\varphi) \left[-\mu X_c^T \Lambda(w_i) P_1 X_c - \mu \int_0^1 \left(\xi^T \Lambda(w_i) P_2 \xi\right) e^{-\mu x} dx \right] \tag{6.2.28}$$

From (6.2.17), it can be proved that there always exists a $\varrho > 0$ such that $\Lambda(\varphi) - \varrho I^{n \times n} \succ 0$ (e.g. ϱ could be the smallest eigenvalue of $\Lambda(\varphi)$ over Z_φ). Moreover, the diagonality of P_1, P_2 and Λ implies that:

$$\dot{V} \leq -\mu \varrho V(\xi, X_c) \tag{6.2.29}$$

Therefore, the function (6.2.3) is a Lyapunov function for the hyperbolic system (6.2.16) with boundary conditions (6.2.18). ■

Note that Theorem 6.2.4 allows verifying whether the boundary control gain K stabilizes the hyperbolic system (6.2.16) with boundary conditions (6.2.18) for all the varying parameters that belong to the convex set Z_φ.

As done for linear hyperbolic system, the following corollary gives sufficient conditions for the design of a stabilizing controller for the particular case where C_c is a diagonal matrix, $D_c = 0$ and $n = n_x$.

Corollary 6.2.5. *[Design of a stabilizing controller] Along with Assumption 6.2.3, if C_c is diagonal and $D_c = 0$ and if there exists a diagonal positive definite matrix $Q \in \mathbb{R}^{n\times n}$ and a scalar $\mu > 0$ such that the following linear matrix inequality is satisfied, for all $i \in 1, ..., N_\varphi$,*

$$\begin{bmatrix} QA_c(w_i)^T + A_c(w_i)Q + C_c\Lambda(w_i)QC_c + \mu\Lambda(w_i)Q & B_c(w_i)Y \\ Y^T B_c(w_i)^T & -e^{-\mu}\Lambda(w_i)Q \end{bmatrix} \preceq 0 \tag{6.2.30}$$

where $Y = KQ$, then there exist two constants $\alpha > 0$ and $M > 0$ such that, for all $\xi^0(x) \in L^2((0,1);\mathbb{R}^n)$ and $X_c^0 \in \mathbb{R}^n$, the solution of (6.2.16) with boundary conditions (6.2.18) and initial condition (6.1.10) satisfies (6.2.2) for all $t \geq 0$.

Proof: Consider once again the Lyapunov function candidate (6.2.13). Performing the same procedure as the one presented in the proof of Theorem 6.2.4 and considering $D_c = 0$, the following equality is obtained

$$\dot{V} = \sum_{i=1}^{2^l} \alpha_i(\varphi) \left[-\mu X_c^T \Lambda(w_i) P X_c - \mu \int_0^1 \left(\xi^T \Lambda(w_i) P \xi\right) e^{-\mu x} dx + \begin{bmatrix} X_c \\ \xi(1) \end{bmatrix}^T H_i \begin{bmatrix} X_c \\ \xi(1) \end{bmatrix} \right] \tag{6.2.31}$$

where

$$H_i = \begin{bmatrix} A_c(w_i)^T P + P A_c(w_i) + C_c\Lambda(w_i)PC_c + \mu\Lambda(w_i)P & PB_c(w_i)K \\ K^T B_c(w_i)^T P & -e^{-\mu}\Lambda(w_i)P \end{bmatrix} \tag{6.2.32}$$

Note that (6.2.12) is equivalent to $H_i \preceq 0$. This is obtained by multiplying both sides of (6.2.32) by $diag\,(P^{-1}, P^{-1})$, commuting P^{-1} with C_c (both matrices being diagonal) and performing the variable transformations $Q = P^{-1}$ and $Y = KQ$. Therefore, as $H_i \preceq 0$ and $\Lambda(\varphi) - \varrho I^{n\times n} \succ 0$, the function (6.2.13) is a Lyapunov function for the hyperbolic system (6.2.16) with boundary conditions (6.2.18). ■

Remark 6.2.2. The previous results (namely Theorem 6.2.4 and Corollary 6.2.5) extend to first-order hyperbolic systems with both negative and positive convective speeds $(\lambda_1(\varphi) < ... < \lambda_m(\varphi) < 0 < \lambda_{m+1}(\varphi) < ... < \lambda_n(\varphi))$ by defining the state description $\xi = \begin{bmatrix} \xi_- \\ \xi_+ \end{bmatrix}$, where $\xi_- \in \mathbb{R}^m$ and $\xi_+ \in \mathbb{R}^{n-m}$, and the variable transformation $\tilde{\xi}(x,t) = \begin{pmatrix} \xi_-(1-x,t) \\ \xi_+(x,t) \end{pmatrix}$.

6.2.3 Stability of Quasi-Linear Hyperbolic Systems with Dynamic Boundary Conditions

The local exponential stability of (6.1.1) with the static boundary conditions (6.1.17) and initial condition (6.1.10) has been studied in [39] using the following candidate Lyapunov function:

$$V(\xi) = V_1(\xi) + V_2(\xi, \xi_x) + V_3(\xi, \xi_x, \xi_{xx}) \tag{6.2.33}$$

where

$$\begin{gathered} V_1(\xi) = \int_0^1 \left(\xi^T Q(\xi)\xi\right) e^{-\mu x} dx, \quad V_2(\xi, \xi_x) = \int_0^1 \left(\xi_x^T R(\xi)\xi_x\right) e^{-\mu x} dx, \\ V_3(\xi, \xi_x, \xi_{xx}) = \int_0^1 \left(\xi_{xx}^T S(\xi)\xi_{xx}\right) e^{-\mu x} dx \end{gathered} \tag{6.2.34}$$

and $Q(\xi)$, $R(\xi)$ and $S(\xi)$ are symmetric positive definite matrices. Coron and co-workers have found that a boundary control (6.1.17) that satisfies the inequality (6.1.20), is a sufficient condition for the exponential stability of one-dimensional quasi-linear hyperbolic systems on a bounded interval. In this section, we study the stability of system (6.1.1) with dynamic boundary conditions (6.1.8) in a different way. We represent the nonlinear characteristic matrix $\Lambda(\xi)$ in a uncertain linear form described by a linear PDE that contains state variations, which are only known to belong to a prescribed bounded domain around the equilibrium. This allows using the results given in Section 6.2.2 for the study of the local stability of quasi-linear hyperbolic systems.

To represent the variation of the characteristic matrix with respect to the state, let us define the convex set Z_ξ as follows:

$$Z_\xi := \{[\xi_1, ..., \xi_n]^T \in \mathbb{R}^n \mid \xi_i \in [\underline{\xi}_i, \overline{\xi}_i], \forall\, i = 1, ..., n\} \tag{6.2.35}$$

where $\overline{\xi}_i$ and $\underline{\xi}_i$ are some maximal and minimal allowable values for ξ_i, respectively. In other words, the matrix $\Lambda(\xi)$ belongs to the matrix variation domain [11]:

$$D_\xi = \left\{ \Lambda : \Lambda = \sum_{i=1}^{2^n} \beta_i \Lambda(v_i), \beta_i \geq 0, \sum_{i=1}^{2^n} \beta_i = 1 \right\} \tag{6.2.36}$$

where $v_i \in Z_\xi$ are the $N_\xi = 2^n$ vertices of the polytope formed by all the state extremities $\overline{\xi}_i$ and $\underline{\xi}_i$. From this formulation we propose the following theorem, which gives sufficient conditions for the exponential stability of (6.1.1) with boundary conditions (6.1.8) and initial conditions (6.1.10) over the characteristic matrix variation domain D_ξ.

Theorem 6.2.6. *[Stability analysis] Along with Assumption 6.1.1, assume that there exists two diagonal positive definite matrices $P_1 \in \mathbb{R}^{n_x \times n_x}$ and $P_2 \in \mathbb{R}^{n \times n}$ and a scalar*

$\mu > 0$ such that the following matrix inequality is satisfied, for all $i = 1, ..., N_\xi$,

$$\left[\begin{array}{c|c} \begin{array}{c} A_c^T P_1 + P_1 A_c + C_c^T \Lambda(v_i) P_2 C_c \\ + K D_c^T \Lambda(v_i) P_2 D_c K + \mu \Lambda(v_i) P_1 \end{array} & P_1 B_c K + C_c^T \Lambda(v_i) P_2 D_c K \\ \hline K^T B_c^T P_1 + K^T D_c^T \Lambda(v_i) P_2 C_c & -e^{-\mu} \Lambda(v_i) P_2 \end{array}\right] \preceq 0 \tag{6.2.37}$$

Then there exist two constant scalars $a > 0$ and $b > 0$ such that, for all $\xi^0 \in Z_\xi$ and $X_c^0 \in \mathbb{R}^{n_x}$, the solution of (6.1.1), (6.1.8) and (6.1.10) satisfies (6.2.2), for all $t \geq 0$.

Proof: The proof of this theorem is very similar to the one developed for Theorem 6.2.4. The main difference is that in this case, the stability is proved over the convex set of the state variation Z_ξ instead of the parameter space Z_φ. ■

Similarly to the Corollaries 6.2.2 and 6.2.5, the following corollary can be formulated for quasilinear hyperbolic systems:

Corollary 6.2.7. *[Design of a stabilizing controller] Along with Assumption 6.1.1, if C_c is diagonal and $D_c = 0$ and if there exists a diagonal positive definite matrix $Q \in \mathbb{R}^{n \times n}$ and a scalar $\mu > 0$ such that the following linear matrix inequality is satisfied, for all $i \in 1, ..., N_\xi$,*

$$\left[\begin{array}{cc} Q A_c^T + A_c Q + C_c \Lambda(v_i) Q C_c + \mu \Lambda(v_i) Q & B_c Y \\ Y^T B_c^T & -e^{-\mu} \Lambda(v_i) Q \end{array}\right] \preceq 0 \tag{6.2.38}$$

where $Y = KQ$, then there exist two constants $\alpha > 0$ and $M > 0$ such that, for all $\xi^0(x) \in Z_\xi$ and $X_c^0 \in \mathbb{R}^n$, the solution of (6.1.1) with boundary conditions (6.1.8) and initial condition (6.1.10) satisfies (6.2.2), for all $t \geq 0$.

This corollary completes our results on dynamic boundary stabilization of hyperbolic systems. In the next section, we find some sufficient conditions for boundary observer design of linear and quasilinear hyperbolic systems.

6.3 Boundary Observers for Hyperbolic Systems

In this section, we consider the problem of boundary observer design for one-dimensional first-order linear and quasi-linear strict hyperbolic systems with n rightward convecting transport PDEs (Assumption 6.1.1). Inspired by the Lyapunov based techniques developed in the work of Coron and co-workers (Section 6.1.2), we derive some sufficient conditions for exponential boundary observer design using only the information from the boundary control and the boundary conditions. We consider static as well as dynamic

boundary controls for the boundary observer design.

Problem Formulation:
We consider the problem of establishing a Lyapunov approach to solve the problem of finding a state estimate $\hat{\xi}$ of ξ from the knowledge of the boundary control $u_c(t)$ and the boundary $\xi(1,t)$. Specifically, we focus on the design of exponential boundary observers defined as follows:

Definition 6.3.1. *Consider, for all $x \in [0,1]$ and $t \geq 0$ the quasi-linear hyperbolic system (6.1.1) with boundary conditions (6.1.7) (or (6.1.8)) and initial conditions (6.1.10) and the boundary observer given by the following system:*

$$\partial_t \hat{\xi}(x,t) + \Lambda(\hat{\xi})\partial_x \hat{\xi}(x,t) = 0 \tag{6.3.1}$$

with the boundary conditions:

$$\begin{aligned} \dot{X}_o(t) &= f(X_o(t), u_c(t), v(t)) \\ \hat{\xi}(0,t) &= h(X_o(t), u_c(t), v(t)) \end{aligned} \tag{6.3.2}$$

where $v(t)$ is the observer input, $X_o(t) \in \mathbb{R}^{n_x}$, $f : \mathbb{R}^n \times \mathbb{R}^n \times \mathbb{R}^{n_x} \to \mathbb{R}^{n_x}$ and $h : \mathbb{R}^n \times \mathbb{R}^n \times \mathbb{R}^{n_x} \to \mathbb{R}^n$. The initial condition is:

$$\hat{\xi}(x,0) = \hat{\xi}^0(x), \quad X_o(0) = X_o^0 \tag{6.3.3}$$

If there exist $a > 0$ and $b > 0$ such that for all ξ (solution of (6.1.1), (6.1.7) and (6.1.10) or (6.1.1), (6.1.8) and (6.1.10)) and $\hat{\xi}$ (solution of (6.3.1), (6.3.2) and (6.3.3)) the inequality

$$|X_c(t) - X_o(t)| + \|\hat{\xi}(.,t) - \xi(.,t)\|_{L^2} \leq M_0 e^{-\alpha_0 t}(|X_c^0 - X_o^0| + \|\hat{\xi}^0 - \xi^0\|_{L^2}), \forall\, t \geq 0 \tag{6.3.4}$$

holds, then (6.3.1) with boundary conditions (6.3.2) and initial condition (6.3.3) is called an exponential boundary observer.

We dedicate the following two sections to find sufficient conditions for the exponential boundary observer design for linear (Section 6.3.1) and quasi-linear (Section 6.3.2) hyperbolic systems with static boundary control (6.1.7) and dynamic boundary control (6.1.8).

6.3.1 Boundary Observer for Linear Hyperbolic Systems

The first problem we address is the boundary observer design for the system (6.1.3) and (6.1.10) with static boundary conditions (6.1.7). The following proposition presents some sufficient conditions for this boundary observer design.

Proposition 6.3.1. *Along with Assumption 6.1.1, consider the system (6.1.3) with static boundary conditions (6.1.7) and initial condition (6.1.10). Let $P \in \mathbb{R}^{n\times n}$ be a diagonal positive definite matrix, $\mu > 0$ be a constant and $L \in \mathbb{R}^{n\times n}$ be an observer gain such that:*

$$e^{-\mu}\Lambda P - L^T\Lambda P L \succeq 0 \tag{6.3.5}$$

then:

$$\partial_t\hat{\xi}(x,t) + \Lambda\partial_x\hat{\xi}(x,t) = 0 \tag{6.3.6}$$

$$\hat{\xi}(0,t) = u_c(t) + L(\xi(1,t) - \hat{\xi}(1,t)) \tag{6.3.7}$$

is an exponential boundary observer for all twice continuously differentiable functions $\hat{\xi}^0 : [0,1] \to \Theta$ satisfying the zero-order and one-order compatibility conditions.

Proof Define the estimation error $\varepsilon = \xi - \hat{\xi}$ with dynamics given by:

$$\partial_t\varepsilon(x,t) + \Lambda\partial_x\varepsilon(x,t) = 0 \tag{6.3.8}$$

$$\varepsilon(0,t) = -L(\xi(1,t) - \hat{\xi}(1,t)) = -L\varepsilon(1,t) \tag{6.3.9}$$

The problem of the exponential convergence of (6.3.8) with boundary conditions (6.3.9) has been already considered in [39]. However, we develop the proof for illustrating purposes, the sake of completeness and to allow discussing the speed of convergence. Given a diagonal positive definite matrix P, consider the quadratic Lyapunov function candidate proposed by [40] and defined for all continuously differentiable functions $\varepsilon : [0,1] \to \Theta$ as:

$$V(\varepsilon) = \int_0^1 \left(\varepsilon^T P\varepsilon\right) e^{-\mu x} dx \tag{6.3.10}$$

where μ is a positive scalar. Computing the time derivative $\dot{V}$ of V along the classical C^1-solutions of (6.3.8) with boundary conditions (6.3.9) yields to the following (after integrating by parts):

$$\dot{V} = -\left[e^{-\mu x}\varepsilon^T\Lambda P\varepsilon\right]\Big|_0^1 - \mu\int_0^1 \left(\varepsilon^T\Lambda P\varepsilon\right) e^{-\mu x} dx \tag{6.3.11}$$

The boundary conditions (6.3.9) imply that:

$$\dot{V} = -\varepsilon^T(1)\left[e^{-\mu}\Lambda P - L^T\Lambda P L\right]\varepsilon(1) - \mu\int_0^1 \left(\varepsilon^T\Lambda P\varepsilon\right) e^{-\mu x} dx \tag{6.3.12}$$

where $\varepsilon(1) = \varepsilon(1,t)$. From (6.3.5), the first term of (6.3.12) is always negative or zero. From (6.1.2) it can be proved that there always exists a $\varrho > 0$ such that $\Lambda > \varrho I^{n\times n}$ (e.g.

ϱ could be the smallest eigenvalue of Λ). Moreover, the diagonality of P and Λ implies that:

$$\dot{V} \leq -\mu\varrho V(\varepsilon) \tag{6.3.13}$$

Therefore, the function (6.3.10) is a Lyapunov function for the hyperbolic system (6.3.8) with boundary conditions (6.3.9). ■

Note that (6.3.5) and (6.3.13) imply that μ is a part of the observer design as it explicitly enables to assign the convergence speed. As the value of μ increases, the observer gain L that is necessary to satisfy (6.3.5) has to decrease. Having an observer gain $L = 0$ gives a trivial solution for Proposition 6.3.1. However, the boundary observer parameters μ and L allow designing the observer response (e.g. performance versus robustness trade-off).

The second problem we consider is the boundary observer design for (6.1.3) and (6.1.10) with dynamic boundary conditions (6.1.8). This is solved with the following theorem.

Theorem 6.3.2. *Along with Assumption 6.1.1, consider the system (6.1.3) with dynamic boundary conditions (6.1.8) and initial condition (6.1.10). Assume that there exist two diagonal positive definite matrices $P_1 \in \mathbb{R}^{n_x \times n_x}$ and $P_2 \in \mathbb{R}^{n \times n}$, a constant $\mu > 0$ and an observer gain $L \in \mathbb{R}^{n_x \times n}$ such that:*

$$\begin{bmatrix} A_c^T P_1 + P_1 A_c + C_c^T \Lambda P_2 C_c + \mu \Lambda P_1 & -P_1 L \\ -L^T P_1 & -e^{-\mu} \Lambda P_2 \end{bmatrix} \preceq 0 \tag{6.3.14}$$

then the boundary observer:

$$\begin{aligned} &\partial_t \hat{\xi}(x,t) + \Lambda \partial_x \hat{\xi}(x,t) = 0 \\ &\dot{\hat{X}}_c = A_c \hat{X}_c + B_c u_c(t) + L(\xi(1,t) - \hat{\xi}(1,t)) \\ &\hat{\xi}(0,t) = C_c \hat{X}_c + D_c u_c(t) \end{aligned} \tag{6.3.15}$$

ensures the exponential convergence of the observation error for all twice continuously differentiable functions $\hat{\xi}^0 : [0,1] \to \Theta$ satisfying the zero-order and one-order compatibility conditions.

Proof Define the dynamics of the estimation error $\varepsilon = \xi - \hat{\xi}$ as follows:

$$\partial_t \varepsilon(x,t) + \Lambda \partial_x \varepsilon(x,t) = 0 \tag{6.3.16}$$

with the boundary conditions:

$$\dot{\varepsilon}_c = A_c \varepsilon_c - L\varepsilon(1,t) \tag{6.3.17}$$

$$\varepsilon(0,t) = C\varepsilon_c \tag{6.3.18}$$

where $\varepsilon_c = X_c - \hat{X}_c$. Given the diagonal positive definite matrices P_1 and P_2, consider, as an extension of the Lyapunov function proposed in [40], the quadratic Lyapunov function candidate defined for all continuously differentiable functions $\varepsilon : [0,1] \to \Theta$ as:

$$V(\varepsilon, \varepsilon_c) = \varepsilon_c^T P_1 \varepsilon_c + \int_0^1 \left(\varepsilon^T P_2 \varepsilon\right) e^{-\mu x} dx \tag{6.3.19}$$

Computing the time derivative $\dot{V}$ of V along the classical C^1-solutions of (6.3.16) with boundary conditions (6.3.17) yields to the following equation:

$$\begin{aligned} \dot{V} =& \varepsilon_c^T \left(A_c^T P_1 + P_1 A_c\right) \varepsilon_c - \varepsilon(1)^T L^T P_1 \varepsilon_c - \varepsilon_c^T P_1 L \varepsilon(1) \\ & - \left[e^{-\mu x} \varepsilon^T \Lambda P_2 \varepsilon\right] \Big|_0^1 - \mu \int_0^1 \left(\varepsilon^T \Lambda P_2 \varepsilon\right) e^{-\mu x} dx \end{aligned} \tag{6.3.20}$$

which can be written in terms of the boundary conditions as follows:

$$\begin{aligned} \dot{V} =& -\mu \varepsilon_c^T \Lambda P_1 \varepsilon_c - \mu \int_0^1 \left(\varepsilon^T \Lambda P_2 \varepsilon\right) e^{-\mu x} dx \\ & + \begin{bmatrix} \varepsilon_c \\ \varepsilon(1) \end{bmatrix}^T \begin{bmatrix} A_c^T P_1 + P_1 A_c + C_c^T \Lambda P_2 C_c + \mu \Lambda P_1 & -P_1 L \\ -L^T P_1 & -e^{-\mu} \Lambda P_2 \end{bmatrix} \begin{bmatrix} \varepsilon_c \\ \varepsilon(1) \end{bmatrix} \end{aligned} \tag{6.3.21}$$

Note that (6.3.14) implies that the third term of (6.3.21) is always negative or zero. Using the same procedure as in the proof of Proposition 6.3.1, it can be easily shown that there exists a $\varrho > 0$ such that:

$$\dot{V} \leq -\mu \varrho V(\varepsilon, \varepsilon_c) \tag{6.3.22}$$

Therefore, the function (6.2.3) is a Lyapunov function for the hyperbolic system (6.3.16) and (6.3.17). ■

Note that the matrix inequality (6.3.14) considers, through the Lyapunov matrices P_1 and P_2, the coupling between the system's dynamics and the boundary conditions dynamics. As in Proposition 6.3.1, the strictly positive constant μ allows assigning the convergence speed. Note that for a fixed μ, (6.3.14) becomes an LMI that can be solved using numerical procedures such as convex optimization algorithms.

Remark 6.3.1. The previous results (namely Proposition 6.3.1 and Theorem 6.3.2) extend to first-order hyperbolic systems with both negative and positive convecting speeds ($\lambda_1 < ... < \lambda_m < 0 < \lambda_{m+1} < ... < \lambda_n$) by defining the state description $\xi = \begin{bmatrix} \xi_- \\ \xi_+ \end{bmatrix}$, where $\xi_- \in \mathbb{R}^m$ and $\xi_+ \in \mathbb{R}^{n-m}$, and the variable transformation $\tilde{\xi}(x,t) = \begin{pmatrix} \xi_-(1-x,t) \\ \xi_+(x,t) \end{pmatrix}$.

6.3.2 Boundary Observer for Quasi-Linear Hyperbolic Systems

In this section, under Assumption 6.1.2 , we present sufficient conditions for exponential observer design for the quasi-linear hyperbolic system (6.1.1) and the boundary controls (6.1.7) and (6.1.8). From Assumption 6.1.2, there exist $\iota_i > 0, \forall\, i \in [1, ..., n]$ and a unique C^1 solution for (6.1.1) with boundary conditions (6.1.7) or (6.1.8) and initial condition (6.1.10) such that:

$$\|\xi_i(., t)\|_{H^1} < \iota_i, \quad \forall\, t > 0, \quad \forall\, i \in [1, ..., n] \tag{6.3.23}$$

where $\iota_i \in \mathbb{R}^+$. Moreover, from compact injection from $H^1(0,1)$ to $L^\infty(0,1)$, there exists C_ξ (which does not depend on the solution) such that:

$$\|\xi_i(., t)\|_{L^\infty} \leq C_\xi \|\xi_i(., t)\|_{H1} \leq C_\xi \iota_i =: \gamma_i, \quad \forall\, t > 0, \quad \forall\, i \in [1, ..., n] \tag{6.3.24}$$

Define $\Gamma_\xi = diag(\gamma_1, ..., \gamma_n)$ and the non empty subset:

$$\Upsilon := B(\gamma_1) \times ... \times B(\gamma_n) \subset \Theta \tag{6.3.25}$$

As previously mentioned, the characteristic matrix $\Lambda(\xi)$ is continuously differentiable, implying that there exists a Lipschitz constant $\gamma_\Lambda > 0$ such that:

$$\left\| \partial_\xi \Lambda(\xi) \right\| < \gamma_\Lambda, \quad \forall\, \xi \in \Upsilon \tag{6.3.26}$$

Also, from the continuity of Λ, the characteristic matrix can be bounded as follows:

$$[\Lambda(\xi) - \Lambda_{min}] \succeq 0 \quad \text{and} \quad [\Lambda_{max} - \Lambda(\xi)] \succeq 0 \quad \forall\, \xi \in \Upsilon \tag{6.3.27}$$

where $\Lambda_{min}, \Lambda_{max} \in \mathbb{R}^{n \times n}$ are diagonal positive definite matrices which can be chosen, for example, as:

$$\Lambda_{min} = diag\left(\min_{\xi \in \Upsilon}(\lambda_1), .., \min_{\xi \in \Upsilon}(\lambda_n) \right), \quad \Lambda_{max} = diag\left(\max_{\xi \in \Upsilon}(\lambda_1), ..., \max_{\xi \in \Upsilon}(\lambda_n) \right) \tag{6.3.28}$$

Using the previous definitions and assumptions, the following theorem presents the sufficient conditions for the boundary observer design for (6.1.1) with boundary control (6.1.7).

Theorem 6.3.3. *Along with Assumption 6.1.1, consider the system (6.1.1) with static boundary conditions (6.1.7) and initial condition (6.1.10). Let $P \in \mathbb{R}^{n \times n}$ be a diagonal positive definite matrix, $\mu > 0$ be a constant and $L \in \mathbb{R}^{n \times n}$ be an observer gain such that:*

$$\begin{aligned} e^{-\mu} \Lambda_{min} P - L^T \Lambda_{max} P L \succeq 0 \\ \Lambda_{min} - \frac{3}{\mu} \gamma_\Lambda \Gamma_\xi \succ 0 \end{aligned} \tag{6.3.29}$$

are satisfied, then:

$$\partial_t \hat{\xi}(x,t) + \Lambda(\hat{\xi}(x,t)) \partial_x \hat{\xi}(x,t) = 0 \tag{6.3.30}$$

$$\hat{\xi}(0,t) = u_c(t) + L(\xi(1,t) - \hat{\xi}(1,t)) \tag{6.3.31}$$

is an exponentially converging boundary observer for all twice continuously differentiable functions $\hat{\xi}^0 : [0,1] \to \Upsilon$ satisfying the zero-order and one-order compatibility conditions.

Proof Defining $\varepsilon = \xi - \hat{\xi}$, the dynamics of the estimation error is given by:

$$\partial_t \varepsilon(x,t) + \Lambda(\xi)\partial_x \varepsilon(x,t) + v_e = 0 \tag{6.3.32}$$

with boundary condition

$$\varepsilon(0,t) = -L\varepsilon(1,t) \tag{6.3.33}$$

where $v_e = (\Lambda(\xi) - \Lambda(\hat{\xi}))\hat{\xi}_x$. From (6.3.26), it is possible to consider the term v_e of (6.3.32) as a vanishing perturbation. This implies that as $\varepsilon \to 0$ in L^2, $(\Lambda(\xi) - \Lambda(\hat{\xi}))\hat{\xi}_x \to 0$ in L^2. From (6.3.23) and (6.3.26), this perturbation can be bounded for all $\xi : [0,1] \to \Upsilon$ as follows:

$$\|v_e\|_{L^\infty} = \|(\Lambda(\xi) - \Lambda(\hat{\xi}))\hat{\xi}_x\|_{L^\infty} \leq \gamma_\Lambda \|\Gamma_\xi \varepsilon\|_{L^\infty} \tag{6.3.34}$$

Given a diagonal positive definite matrix $P \in \mathbb{R}^{n\times n}$, consider (6.3.10) as a Lyapunov function candidate defined for all continuously differentiable functions $\varepsilon : [0,1] \to \Upsilon$. Computing the time derivative $\dot{V}$ of V along the classical C^1-solutions of (6.3.32) with boundary conditions (6.3.33) yields to the following:

$$\begin{aligned} \dot{V} = &- \int_0^1 \left(v_e^T P\varepsilon + \varepsilon^T P v_e\right) e^{-\mu x} dx - \mu \int_0^1 \left(\varepsilon^T \Lambda(\xi) P\varepsilon\right) e^{-\mu x} dx \\ &+ \int_0^1 \left(\varepsilon^T \partial_\xi \Lambda(\xi)\xi_x P\varepsilon\right) e^{-\mu x} dx - \left[e^{-\mu x}\varepsilon^T \Lambda(\xi) P\varepsilon\right]\Big|_0^1 \end{aligned} \tag{6.3.35}$$

Using (6.3.23), (6.3.26), (6.3.28) and (6.3.34), the time derivative of the Lyapunov function can be bounded as:

$$\dot{V} \leq -\varepsilon(1)^T \left[e^{-\mu}\Lambda_{min} P - L^T \Lambda_{max} P L\right] \varepsilon(1) - \mu \int_0^1 \left[\varepsilon^T (\Lambda_{min} P - \frac{3}{\mu}\gamma_\Lambda \Gamma_\xi P)\varepsilon\right] e^{-\mu x} dx \tag{6.3.36}$$

Conditions (6.3.29) imply that (6.3.36) is always negative. It can be easily shown from conditions (6.3.29) that there exists a $\gamma_\varepsilon > 0$ such that:

$$\dot{V} \leq -\mu\gamma_\varepsilon V(\varepsilon) \tag{6.3.37}$$

where γ_ε could be for example the smallest eigenvalue of $\Lambda_{min} - \frac{3}{\mu}\gamma_\Lambda\Gamma_\xi$. Therefore, the function (6.3.10) is a Lyapunov function for the hyperbolic system (6.3.16) with boundary conditions (6.3.17) for all $\xi : [0,1] \to \Upsilon$. ■

Note that, unlike the linear hyperbolic case, not any $\mu > 0$ ensures the stability of boundary observer for quasi-linear hyperbolic systems. There is a minimum $\mu > 0$ such that the condition (6.3.29) is satisfied. More precisely, Assumption 6.1.1 implies that $\Lambda_{min} P \succ 0$. Therefore, there exists a finite $\mu > \mu_{min}$ and a small enough L such that (6.3.29) holds and thus such that (6.3.30)-(6.3.31) is an exponential observer for the system (6.1.1) with boundary conditions (6.1.7). The μ_{min} can be determined for example as follows:

$$\mu_{min} = \lambda_{max}\{3\gamma_\Lambda \Lambda_{min}^{-1}\Gamma_\xi\} \tag{6.3.38}$$

where λ_{max} stands for the maximal eigenvalue. Equation (6.3.38) implies that smaller values of μ are admissible when having large convecting speeds, and therefore faster observer convergence can be obtained.

In Theorem 6.3.4, sufficient conditions for the observer design with dynamic boundary conditions (6.1.8) are presented.

Theorem 6.3.4. *Along with Assumption 6.1.1, consider the system (6.1.1) with dynamic boundary condition (6.1.8) and initial conditions (6.1.10). Assume that there exist two diagonal positive definite matrices $P_1, P_2 \in \mathbb{R}^{n\times n}$, a constant $\mu > 0$ and an observer gain $L \in \mathbb{R}^{n\times n}$ such that:*

$$\left[\begin{array}{c|c} A_c^T P_1 + P_1 A_c + C_c^T \Lambda_{max} P_2 C_c & -P_1 L \\ +\mu\Lambda_{min} P_1 - 3\gamma_\Lambda \Gamma_\xi P_1 & \\ \hline -L^T P_1 & -e^{-\mu}\Lambda_{min} P_2 \end{array}\right] \preceq 0 \qquad \Lambda_{min} - \frac{3}{\mu}\gamma_\Lambda \Gamma_\xi \succ 0 \tag{6.3.39}$$

are satisfied, then:

$$\partial_t \hat{\xi}(x,t) + \Lambda \partial_x \hat{\xi}(x,t) = 0 \tag{6.3.40}$$

$$\begin{aligned} \dot{\hat{X}}_c &= A_c \hat{X}_c + B_c u(t) + L(\xi(1,t) - \hat{\xi}(1,t)) \\ \hat{\xi}(0,t) &= C_c \hat{X}_c + D_c u(t) \end{aligned} \tag{6.3.41}$$

is an exponentially converging boundary observer for all continuously differentiable functions $\hat{\xi}^0 : [0,1] \to \Upsilon$ satisfying the zero-order and one-order compatibility conditions.

Proof. Define the dynamics of the estimation error as in (6.3.32) with boundary conditions (6.3.17). Using the same vanishing perturbation approach as in the proof of Theorem 6.3.3 and the Lyapunov function candidate (6.3.19) defined for all continuously differentiable functions $\varepsilon : [0,1] \to \Upsilon$ gives:

$$\begin{aligned} \dot{V} = {} & \varepsilon^T \left(A^T P_1 + P_1 A\right) \varepsilon - \varepsilon(1)^T L^T P_1 \varepsilon - \varepsilon^T P_1 L \varepsilon(1) - \left[e^{-\mu x} \varepsilon^T \Lambda(\xi) P_2 \varepsilon\right] \Big|_0^1 \\ & - \mu \int_0^1 \left(\varepsilon^T \Lambda(\xi) P_2 \varepsilon\right) e^{-\mu x} dx + \int_0^1 \left(\varepsilon^T \partial_\xi \Lambda(\xi) \xi_x P_2 \varepsilon\right) e^{-\mu x} dx \\ & - \int_0^1 \left(v_e^T P_2 \varepsilon + \varepsilon^T P_2 v_e\right) e^{-\mu x} dx \end{aligned} \tag{6.3.42}$$

After expanding (6.3.42), we obtain the following:

$$\begin{aligned} \dot{V} = {} & -\mu \int_0^1 \left(\varepsilon^T \Lambda(\xi) P_2 \varepsilon\right) e^{-\mu x} dx + \int_0^1 \left(\varepsilon^T \partial_\xi \Lambda(\xi) \xi_x P_2 \varepsilon\right) e^{-\mu x} dx - \int_0^1 \left(v_e^T P_2 \varepsilon + \varepsilon^T P_2 v_e\right) e^{-\mu x} dx \\ & + \begin{bmatrix} \varepsilon \\ \varepsilon(1) \end{bmatrix}^T \begin{bmatrix} A^T P_1 + P_1 A + C^T \Lambda(\xi(0)) P_2 C & -P_1 L \\ -L^T P_1 & -e^{-\mu} \Lambda(\xi(1)) P_2 \end{bmatrix} \begin{bmatrix} \varepsilon \\ \varepsilon(1) \end{bmatrix} \end{aligned} \tag{6.3.43}$$

With the Schur complement, it can be easily shown that for all $\xi : [0,1] \to \Upsilon$:

$$\left[\begin{array}{c|c} A^TP_1 + P_1A & -P_1L \\ +C^T\Lambda_{max}P_2C & \\ \hline -L^TP_1 & -e^{-\mu}\Lambda_{min}P_2 \end{array}\right] - \left[\begin{array}{c|c} A^TP_1 + P_1A & -P_1L \\ +C^T\Lambda(\xi(0))P_2C & \\ \hline -L^TP_1 & -e^{-\mu}\Lambda(\xi(1))P_2 \end{array}\right] \succ 0 \tag{6.3.44}$$

Using (6.3.23), (6.3.26), (6.3.28) and (6.3.34), we can bound the time derivative of the Lyapunov function as follows:

$$\begin{aligned} \dot{V} \leq & -\mu \int_0^1 \left[\left(\varepsilon^T(\Lambda_{min}P_2 - \frac{3}{\mu}\gamma_\Lambda\Gamma_\xi P_2)\varepsilon\right)\right] e^{-\mu x}dx - \mu\varepsilon^T\left[\Lambda_{min}P_1 - \frac{3}{\mu}\gamma_\Lambda\Gamma_\xi P_1\right]\varepsilon \\ & + \begin{bmatrix} \varepsilon \\ \varepsilon(1) \end{bmatrix}^T \left[\begin{array}{c|c} A^TP_1 + P_1A + C^T\Lambda_{max}P_2C & -P_1L \\ +\mu\Lambda_{min}P_1 - 3\gamma_\Lambda\Gamma_\xi P_1 & \\ \hline -L^TP_1 & -e^{-\mu}\Lambda_{min}P_2 \end{array}\right] \begin{bmatrix} \varepsilon \\ \varepsilon(1) \end{bmatrix} \end{aligned} \tag{6.3.45}$$

The matrix inequalities in (6.3.39) imply that the third term of (6.3.45) is always negative or zero. Thus, as detailed in the proof of Theorem 6.3.3, it can be easily shown that:

$$\dot{V} \leq -\mu\gamma_\varepsilon V(\varepsilon, \varepsilon_c) \tag{6.3.46}$$

Therefore, for a suitable $\gamma_\varepsilon > 0$, the function (6.3.19) is a Lyapunov function for the hyperbolic system (6.3.32) and (6.3.17) for all $\xi : [0,1] \to \Upsilon$. ■

Like in Theorem 6.3.3, the value of μ cannot be any positive constant as it has some restrictions given by the second line of (6.3.39). To perform the boundary observer design, a μ that satisfies the second line of (6.3.39) is first computed. Then, this value of μ is employed to compute L, P_1 and P_2 satisfying (6.3.39).

With this, we conclude our contributions on boundary observer design for hyperbolic systems. In the next section, we use some of these theoretical results to design a boundary control for the air fraction in the intake manifold of Diesel engines operated with LP-EGR.

6.4 Fresh Air Mass Fraction Control

Several air mass fraction/EGR rate control and estimation methods have been proposed in the literature (e.g. [36] [48] [94] [103]). However, most of the current air fraction control techniques are based on zero-dimensional (0D) engine models, which does not allow taking into account the air transport inside the engine admission air-path. Indeed, the mass transport causes a degradation of the overall engine emission performance during strong transient conditions. This is mostly due to the LP-EGR, as the distance that the gas travels in the engine air-path is much longer than the one associated with HP-EGR. Taking into account the mass transport time is thus of significant importance in the control of air fraction. Although some works have been done to address this problem (such as in [14], where a simple time-varying input delay model was used to design a predictor-based controller), to the best of our knowledge, this subject remains mostly unexplored.

The transport of mass is often modeled by first-order hyperbolic partial differential equations (PDEs), as discussed in the previous chapters. However, the mass transport in the admission air-path strongly depends on the engine operating conditions, which makes the modeling and control of the air fraction much more challenging. It has been shown in [30] and [96] that this dependence can be modeled by using a linear parameter varying (LPV) formulation; therefore, it seems appropriate to chose an LPV hyperbolic model to capture the dynamics of the air mass fraction, which enables us to solve the air fraction control problem by applying the results of Section 6.2.2.

In this section we address the boundary control problem of the air fraction in the intake manifold of Diesel engines operated with LP-EGR. The air fraction transport phenomenon is modeled using a cascade of first-order linear parameter varying (LPV) hyperbolic systems with dynamics associated with their boundary conditions. Using the results obtained in Theorem 6.2.4, we design a boundary control that guarantees the exponential stability of the air fraction in the intake manifold over a prescribed convex set including the varying parameters, while satisfying some convergence time criterion.

For the boundary control of the air fraction, consider the admission air-path of a Diesel engine with low pressure exhaust gas recirculation (LP-EGR) presented in Figure 6.1.

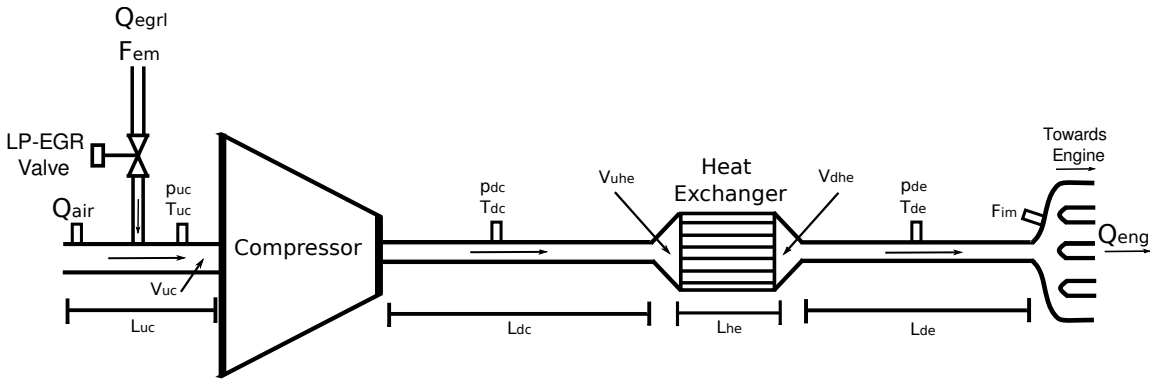

Figure 6.1: Schematic of a Diesel engine admission air-path

A fresh air mass flow rate Q_{air} enters the admission air-path where it is mixed upstream of the compressor with the LP-EGR (characterized by its mass flow rate Q_{egrl} and air fraction F_{em}). The exhaust gas recirculation mass flow rate is controlled by the position of the LP-EGR valve. F_{em} depends on the engine operating conditions and is considered here as a known exogenous input since this quantity is measured in production engines. The compressor increases the enthalpy of the gas which results in an increase of the compressor downstream gas pressure and temperature p_{dc} and T_{dc}, respectively (see Figure 6.1). To increase the gas mass in the engine cylinders and therefore the engine power, the gas coming from the compressor is cooled down by a heat exchanger, which increases the gas density and therefore the mass inside the cylinders. The pressure and temperature downstream of the heat exchanger are denoted as p_{de} and T_{de}, respectively. Finally, the gas travels from the heat exchanger to the intake manifold where the gas is delivered to the engine with a mass flow rate Q_{eng} and an air fraction F_{im}. In this section, we consider the problem of controlling the intake manifold air fraction F_{im} by

regulating the LP-EGR mass flow rate.

The admission air-path presented in Figure 6.1 can be considered as a series of tubes that are linked together by volumes, i.e. by the volumes upstream and downstream of the heat exchanger V_{uhe} and V_{dhe}, respectively. Using this formulation, we can define three tube sections and three control volumes. By control volume, we mean that only the volume-average dynamics are considered (no space variable is considered). The three tube sections are defined as: the tube downstream of the compressor (up to the heat exchanger), the heat exchanger with N_d tubes in parallel and the tube downstream of the heat exchanger. The control volumes are: the tube upstream of the compressor (denoted as V_{uc} where gas mixture occurs), the heat exchanger upstream volume V_{uhe} and downstream volume V_{dhe}.

As seen in Chapter 5, the one-dimensional modeling of the engine admission air-path is particularly complex as it involves solving the 1D Euler equations for a compressible gas, which is not feasible when designing real-time feedback strategies. Therefore, the following assumptions are made to simplify the complexity of the air fraction model, making it suitable for Diesel engine control.

Assumptions 6.4.1. *We assume the following:*

1. *the pressure and particle speed dynamics are much faster than the air fraction dynamics;*
2. *neither friction nor thermal losses are considered (except for the heat exchanger);*
3. *the speed density equation (3.3.26) is considered to model the engine intake mass flow rate. No pulsating flow is considered;*
4. *the cross-sectional area of each of the air-path sections (tube between two devices) is considered constant along the space variable x.*

Assumption 6.4.1-1 implies that $Q_{eng} = Q_{air} + Q_{egrl}$. Therefore, according to the air fraction 0D formulation given in (3.2.12), the following equations describe the air fraction dynamics in the tube upstream of the compressor and in both heat exchanger volumes:

$$\dot{F}_{uc} = \frac{RT_{uc}}{p_{uc}V_{uc}}(-(Q_{egrl} + Q_{air})F_{uc} + Q_{egrl}F_{em} + Q_{air}) \tag{6.4.1}$$

$$\dot{F}_{uhe} = \frac{RT_{dc}}{p_{dc}V_{uhe}}(-(Q_{egrl} + Q_{air})F_{uhe} + (Q_{egrl} + Q_{air})F_{dc}(L_{dc}, t)) \tag{6.4.2}$$

$$\dot{F}_{dhe} = \frac{RT_{de}}{p_{de}V_{dhe}}(-(Q_{egrl} + Q_{air})F_{dhe} + (Q_{egrl} + Q_{air})F_{he}(L_{he}, t)) \tag{6.4.3}$$

where F_{uc} and V_{uc} are the air fraction and volume upstream of the compressor and F_{uhe} and F_{dhe} are the air fractions upstream and downstream of the heat exchanger, respectively. F_{he} is the air fraction inside the heat exchanger and $F_{dc}(L_{dc}, t)$ and $F_{he}(L_{he}, t)$ are the output air fractions of the compressor downstream tube and the heat exchanger tubes, respectively.

For the 1D model of the air fraction dynamics in the tube sections, consider the change in mass fraction across a control volume of length ∂x, which can be expressed as:

$$\partial_t[\rho(x,t)C_t(x)F(x,t)] + \partial_x[\rho(x,t)u(x,t)C_t(x)F(x,t)] = 0, \quad \forall\, x \in [0,L],\, t \geq 0 \tag{6.4.4}$$

where L is the length of the pipe, C_t the tube cross section, ρ the gas density and u the speed of particles. Equation (6.4.4) can be expressed as (e.g. see [101] Chapter 4.2.5 for more details):

$$\partial_t[\rho(x,t)F(x,t)] + \partial_x[\rho(x,t)u(x,t)F(x,t)] + \rho(x,t)u(x,t)F(x,t)\partial_x[ln(C_t(x))] = 0 \tag{6.4.5}$$

Expanding (6.4.5) and dividing by $F(x,t)$ gives:

$$\begin{aligned} &\partial_t\rho(x,t) + u(x,t)\partial_x\rho(x,t) + \rho(x,t)\partial_x u(x,t) + \rho(x,t)u(x,t)\partial_x(ln(C_t(x))) \\ &+ \frac{\rho(x,t)}{F(x,t)}\partial_t F(x,t) + \frac{\rho(x,t)u(x,t)}{F(x,t)}\partial_x F(x,t) = 0 \end{aligned} \tag{6.4.6}$$

The first four terms of (6.4.6) constitute the global continuity of mass, implying that the sum of the four terms equals zero. Therefore, the air fraction continuity equation implies that:

$$\begin{aligned} \partial_t F(x,t) + u(x,t)\partial_x F(x,t) = 0 \\ F(0,t) = F_{in}(t) \quad F(x,0) = F_0(x), \quad \forall\, x \in [0,L],\, t \geq 0 \end{aligned} \tag{6.4.7}$$

where F_{in} is the air fraction at the input boundary condition, $F_0(x)$ is a continuous differentiable function describing the initial conditions and $u(t,x)$ is the air fraction propagation speed (independent of the air fraction).

The Assumptions 6.4.1-1, 2 and 4 imply that $u(x,t)$ is only time-varying (constant in space $u(x,t) \approx u(t)$), which significantly simplifies the solution of (6.4.7). For the heat exchanger, where Assumption 6.4.1-2 does not apply, an uniform space average pressure and temperature distribution are assumed inside the heat exchanger to obtain (6.4.8), which allows approximating a space average particle speed inside the heat exchanger as presented later in (6.4.12). The following temperature and pressure averages are defined:

$$T_{he} = \frac{T_{dc} + T_{de}}{2}, \quad p_{he} = \frac{p_{dc} + p_{de}}{2} \tag{6.4.8}$$

where T_{he} and p_{he} are the assumed heat exchanger temperature and pressure, respectively.

From (6.4.7) and (6.4.8), the dynamics of each tube section can be modeled with the following set of time-varying first-order hyperbolic partial differential equations:

$$\partial_t F_{dc} + u_{dc}(t)\partial_x F_{dc} = 0, \quad F_{dc}(0,t) = F_{uc}(t), \quad F_{dc}(x,0) = F_{apc0}(x) \tag{6.4.9}$$

$$\partial_t F_{he} + u_{he}(t)\partial_x F_{he} = 0, \quad F_{he}(0,t) = F_{uhe}(t), \quad F_{he}(x,0) = F_{he0}(x) \tag{6.4.10}$$

$$\partial_t F_{de} + u_{de}(t)\partial_x F_{de} = 0, \quad F_{de}(0,t) = F_{dhe}(t), \quad F_{de}(x,0) = F_{ape0}(x) \tag{6.4.11}$$

for all $x \in [0,1]$ and $t \geq 0$. The particle speeds for each air-path section u_{dc}, u_{he} and u_{de} can be normalized (implying that $x \in [0,1]$) and calculated using the ideal gas law as follows:

$$u_{dc} = \frac{RT_{dc}(Q_{air} + Q_{egrl})}{p_{dc}A_{dc}L_{dc}}, \quad u_{he} = \frac{RT_{he}(Q_{air} + Q_{egrl})}{p_{he}A_{he}L_{he}N_d}, \quad u_{de} = \frac{RT_{de}(Q_{air} + Q_{egrl})}{p_{de}A_{de}L_{de}} \tag{6.4.12}$$

where L_{dc}, L_{he} and L_{de} are the lengths and A_{dc}, A_{he}, A_{de} are the cross-sectional areas of each of the respective tube sections and N_d is the number of parallel tubes in the heat exchanger. To use the results of Theorem 6.2.4, the system has to be in the form of (6.2.16) with boundary conditions (6.2.18). System (6.4.9) - (6.4.11) is a cascade of hyperbolic systems connected by the dynamics defined by (6.4.1) - (6.4.3), which does not correspond to the system structure (6.2.16). Nevertheless, this problem is solved by following a similar approach as in [41], where n hyperbolic systems in cascade form are combined in one PDE of order n by re-defining the boundary control.

Note that the dynamics of (6.4.1) - (6.4.3) are defined in terms of the states with the exception of (6.4.1) that depends on the time-varying additive input $Q_{egrl}F_{em}+Q_{air}$. This issue is addressed in the sequel to obtain a system of dynamic boundary conditions that writes as (6.2.18). Consider the definition of the air fraction errors as:

$$\begin{aligned}\xi_{dc}(x,t)=F_{dc}(x,t)-F_{imSP},\quad \xi_{he}(x,t)=F_{he}(x,t)-F_{imSP},\\ \xi_{de}(x,t)=F_{de}(x,t)-F_{imSP}\end{aligned} \tag{6.4.13}$$

and

$$\xi_{uc}(t)=F_{uc}(t)-F_{imSP},\quad \xi_{uhe}(t)=F_{uhe}(t)-F_{imSP},\quad \xi_{dhe}(t)=F_{dhe}(t)-F_{imSP} \tag{6.4.14}$$

where F_{imSP} is a given scalar reference for the air fraction. According to (6.4.13) and (6.4.14), we can rewrite the dynamics of the simplified air fraction air-path model (6.4.1) - (6.4.3) and (6.4.9) - (6.4.11) as an LPV hyperbolic PDE of order 3 as follows:

$$\partial_t\begin{bmatrix}\xi_{dc}\\ \xi_{he}\\ \xi_{de}\end{bmatrix}+\begin{bmatrix}\frac{\varphi_2}{A_{dc}L_{dc}} & 0 & 0\\ 0 & \frac{\varphi_3}{A_{he}L_{he}N_d} & 0\\ 0 & 0 & \frac{\varphi_4}{A_{de}L_{de}}\end{bmatrix}\partial_x\begin{bmatrix}\xi_{dc}\\ \xi_{he}\\ \xi_{de}\end{bmatrix}=0 \tag{6.4.15}$$

with the boundary conditions:

$$\begin{bmatrix}\dot{\xi}_{uc}\\ \dot{\xi}_{uhe}\\ \dot{\xi}_{dhe}\end{bmatrix}=\begin{bmatrix}-\frac{\varphi_1}{V_{uc}} & 0 & 0\\ 0 & -\frac{\varphi_2}{V_{uhe}} & 0\\ 0 & 0 & -\frac{\varphi_4}{V_{dhe}}\end{bmatrix}\begin{bmatrix}\xi_{uc}\\ \xi_{uhe}\\ \xi_{dhe}\end{bmatrix}+\begin{bmatrix}\frac{\varphi_1}{V_{uc}} & 0 & 0\\ 0 & \frac{\varphi_2}{V_{uhe}} & 0\\ 0 & 0 & \frac{\varphi_4}{V_{dhe}}\end{bmatrix}\begin{bmatrix}\tilde{v}\\ \xi_{dc}(1)\\ \xi_{he}(1)\end{bmatrix} \tag{6.4.16}$$

The boundary control that allows writing the cascade of hyperbolic systems as a PDE of order 3 is:

$$\begin{bmatrix}\tilde{v}\\ \xi_{dc}(1)\\ \xi_{he}(1)\end{bmatrix}=\begin{bmatrix}0 & 0 & K\\ 1 & 0 & 0\\ 0 & 1 & 0\end{bmatrix}\begin{bmatrix}\xi_{dc}(1)\\ \xi_{he}(1)\\ \xi_{de}(1)\end{bmatrix} \tag{6.4.17}$$

where $\tilde{v}$ is a virtual control input that cancels the additive terms of (6.4.1) and is defined as:

$$\tilde{v}=\frac{F_{em}Q_{egrl}}{Q_{air}+Q_{egrl}}-F_{imSP}-\frac{Q_{air}}{Q_{air}+Q_{egrl}} \tag{6.4.18}$$

The time-varying parameters φ_i are given by:

$$\begin{aligned}\varphi_1=\frac{RT_{uc}(Q_{air}+Q_{egrl})}{p_{uc}},\quad \varphi_2=\frac{RT_{dc}(Q_{air}+Q_{egrl})}{p_{dc}},\\ \varphi_3=\frac{RT_{he}(Q_{air}+Q_{egrl})}{p_{he}},\quad \varphi_4=\frac{RT_{de}(Q_{air}+Q_{egrl})}{p_{de}}\end{aligned} \tag{6.4.19}$$

From (6.4.17) and (6.4.18), the LP-EGR mass flow rate is defined as:

$$Q_{egrl} = \frac{Q_{air}(F_{imSP} - 1 + K(\xi_{de}(1)))}{F_{em} - F_{imSP} - K(\xi_{de}(1))} \tag{6.4.20}$$

Equation (6.4.20) can be transformed into a valve position using (4.3.26)- (4.3.27) and therefore allowing us to control the air fraction in the admission path.

The system (6.4.15) - (6.4.19) with boundary control (6.4.17) is in the adequate form to apply the results of Theorem 6.2.4. However, with the definition of the varying parameters presented in (6.4.19), the polytope (convex set Z_φ) obtained by using the PLRs (6.2.22) and (6.2.23) is very large and therefore highly conservative. All the varying parameters in (6.4.19) are strongly dependent on $Q_{air} + Q_{egrl}$, which implies that a redefinition of the varying parameters may be a good strategy to reduce the size of the polytope and therefore to obtain less conservative results. Let us redefine the varying parameters as:

$$\tilde{\varphi}(t) = \left[Q_{air} + Q_{egrl},\ (Q_{air} + Q_{egrl})^2\right] \tag{6.4.21}$$

and the original varying parameters φ as a linear combination of $\tilde{\varphi}$ as follows:

$$\varphi_j(t) = \vartheta_j^T \psi(t), \quad j \in [1, ..., 4] \tag{6.4.22}$$

where $\vartheta_j \in \mathbb{R}^3$ is an unknown coefficient vector and $\psi(t) = [1, (Q_{air} + Q_{egrl}), (Q_{air} + Q_{egrl})^2]$. A classical least square method can be used to determine the optimal set of coefficients ϑ_j such that $|\varphi_j(t) - \vartheta_j^T \psi(t)|^2$ is minimized and the coefficient identification can be done using engine benchmark measurements over representative engine operating conditions. With this approach, the amount of varying parameters is decreased from four to two, which significantly reduces the conservatism of the control synthesis.

In Figure 6.2a, the polytope Z_φ formed by all the extremities of $\tilde{\varphi}_1$ and $\tilde{\varphi}_2$ is shown. As proposed in [78], the conservatism can be further reduced from the fact that $\tilde{\varphi}_2 = \tilde{\varphi}_1^2$, which allows considering only the polytope formed by three vertexes for the control synthesis, as shown in Figure 6.2b.

The bounds of the varying parameter vector $\tilde{\varphi}$ can also be found using experimental measurements over representative engine operating conditions. With this we complete the boundary control design for the air fraction control in the intake manifold on Diesel engine operated with LP-EGR. In the next section, we present some simulation results to illustrate the performance of the proposed air fraction control.

6.4.1 Simulation Results

To illustrate the effectiveness of the proposed LPV boundary control strategy, the air fraction control strategy(6.4.20) that satisfies Theorem 6.2.4 is simulated along with the setup shown in Figure 6.1. The simulation is performed using the 1D model developed in Chapter 5, computed on a 1D simulation platform developed in Matlab-Simulink®. Table 6.1 gives the physical parameters of a light-duty 1.6 liter Diesel engine considered for the simulation.

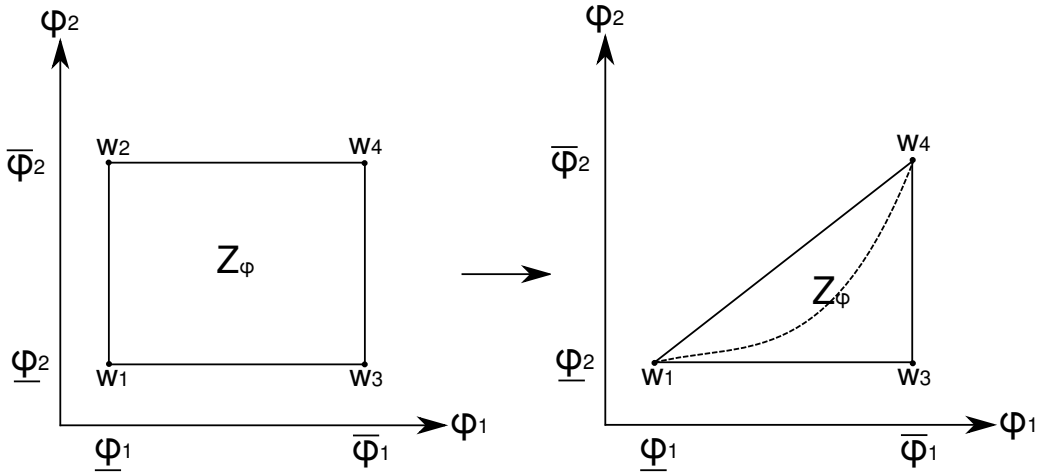

(a) Original parameter set (b) Reduced parameter set

Figure 6.2: Parameter set reduction

Variable	Value	Variable	Value
L_{dc}	$1.3\ m$	A_{he}	$6 \times 10^{-4}\ m^2$
A_{dc}	$0.002\ m^2$	V_{uhe}	$5 \times 10^{-4}\ m^3$
V_{uc}	$3 \times 10^{-4}\ m^3$	V_{dhe}	$5 \times 10^{-4}\ m^3$
N_d	8	L_{de}	$1.1\ m$
L_{he}	$0.58\ m$	A_{de}	$0.002\ m^2$

Table 6.1: Simulation parameters

The bounds on each parameter as well as the coefficients of (6.4.22) are found from measurements on an engine benchmark operated over a wide range of engine operating conditions. More precisely, we use the new motor vehicle emissions group (NMVEG) cycle along with two additional engine cycles. The bounds obtained for $\tilde{\varphi}$ are the following:

$$\tilde{\varphi_1} \in [0.009, 0.074], \quad \tilde{\varphi_2} \in [0.00009, 0.0054] \tag{6.4.23}$$

The identification of the coefficient vector ϑ_i is performed using a traditional least-squares-method and the Penrose-Moore pseudo-inverse. Table 6.2 presents the identified root-mean-square deviation (RMSD) of ϑ_i, where $RMSD_j = RMSD(\varphi_j(t) - \vartheta_j^T \psi(t))$.

As shown in Table 6.2, the parametrization (6.4.22) is representative of the engine varying parameters φ and is therefore adequate for the boundary control synthesis.

Consider, as a criterion for the boundary control design, a maximum air fraction convergence time of 1.2 s, (i.e. the time to reach 90% of the final asymptotic value). From (6.2.8) and the smallest eigenvalue of $\Lambda(\varphi)$, we find that $\mu > 0.6$ is required to achieve the desired convergence time. Solving (6.2.24) over the reduced polytope (presented in Figure 6.2b), leads to the following

Variable	Value
$RMSD_1$	0.1 %
$RMSD_2$	4.1 %
$RMSD_3$	2.9 %
$RMSD_4$	4.7 %

Table 6.2: The RMSD obtained after the solution of the least-squares method

control gain and Lyapunov matrices P_1 and P_2:

$$K = 0.25, \quad P_1 = \begin{bmatrix} 0.0422 & 0 & 0 \\ 0 & 0.0493 & 0 \\ 0 & 0 & 0.0353 \end{bmatrix}, \quad P_2 = \begin{bmatrix} 0.445 & 0 & 0 \\ 0 & 0.299 & 0 \\ 0 & 0 & 0.129 \end{bmatrix} \tag{6.4.24}$$

Figures 6.3 and 6.4 show the simulation results obtained from a change of air fraction reference (F_{imSP}) from 1 to 0.7 at time 0.1 s. Three different air-path operating conditions are simulated, in order to verify the robustness of the controller with respect to parameter variation.

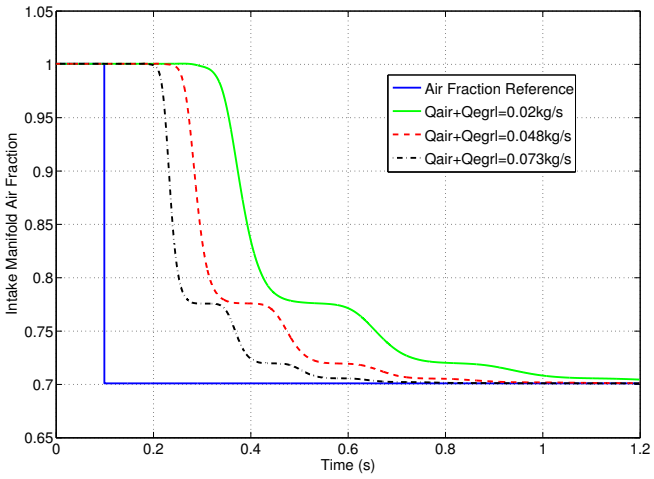

Figure 6.3: Intake manifold air fraction simulation results for a change of air fraction reference

As depicted in Figure 6.3, the intake manifold air fraction converges to the reference while respecting the convergence time criterion for the three operating conditions. The convergence time depends on the mass flow rate going through the air system (see Figure 6.3), which is due to the intrinsic time delays associated with transport in the system. In Figure 6.4 the LP-EGR mass flow rate is presented for the three engine operating conditions: when the mass flow rate increases in the system, Q_{egrl} also does to maintain the appropriate air fraction.

The convergence of the Lyapunov function (6.2.3) is illustrated on Figure 6.5, where it is shown that the actual system convergence is always faster than the exponential decrease predicted by (6.2.8).

Due to the low calculation load and low complexity of the boundary control (6.4.20), this approach is suitable for real-time implementation in a production engine. The current limitation to

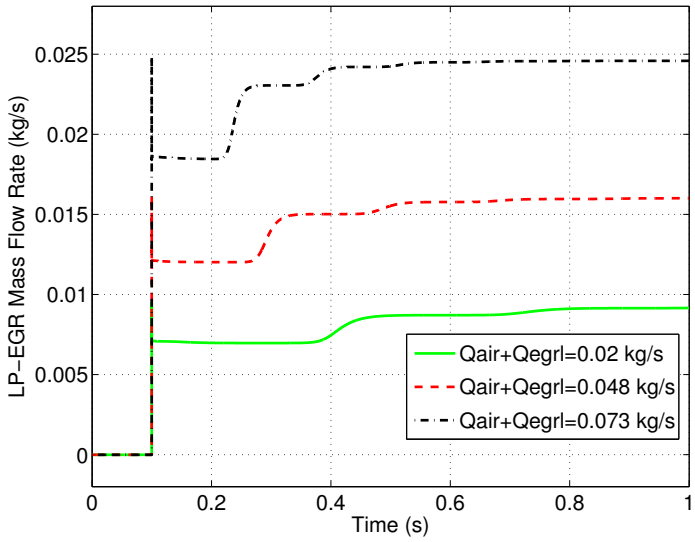

Figure 6.4: LP-EGR mass flow rate simulation results for a change of air fraction reference

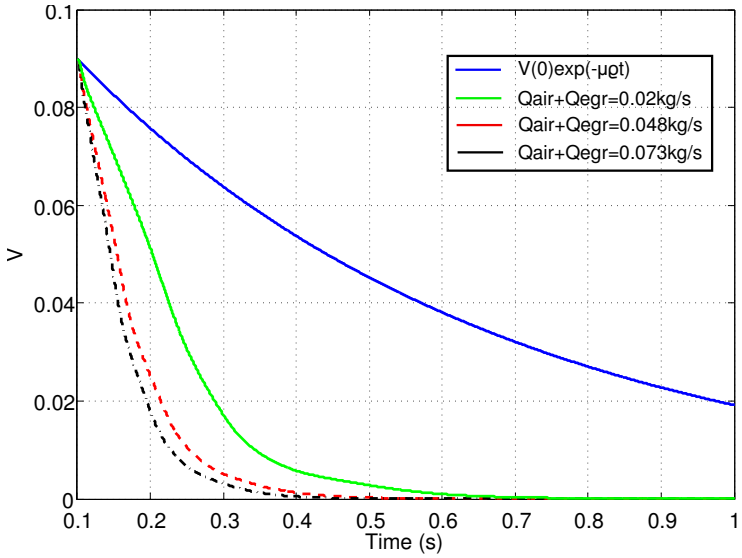

Figure 6.5: Convergence of the Lyapunov function

implement this strategy mainly comes from the lack of reliable measurements or estimations of the fresh air mass fraction in the intake manifold under strong transient conditions (e.g. lack of a reliable sensor to detect the mass transport). However, many efforts are being done to address this issue by using air fraction observers that take into account the mass transport phenomenon (e.g. Appendix A.4), which would enable the implementation of the proposed boundary control in production engines.

6.5 Chapter Summary

This chapter focused on the stabilization and observation of linear, LPV and quasi-linear first-order hyperbolic systems with dynamic boundary conditions and their application to air fraction control in Diesel engines. We found sufficient conditions for boundary control design for linear, LPV and quasi-linear strict hyperbolic systems with n rightward convecting PDEs with dynamic boundary conditions. An extension of the strict Lyapunov function proposed in [40] was used to demonstrate the exponential stability of this class of infinite dimensional systems. In Theorem 6.2.1, we presented the sufficient conditions for the boundary control design for linear hyperbolic systems with dynamic boundary control, for all $\xi^0 : [0,1] \to \Theta$. In Theorem 6.2.4, a polytopic formulation was considered to state sufficient conditions for boundary control design for LPV hyperbolic systems with LPV dynamics at the boundary conditions over a convex set Z_φ. Then, in Theorem 6.2.6, by representing the non-linear characteristic matrix $\Lambda(\xi)$ in an uncertain linear form, sufficient conditions for exponential stability were found for all $\xi^0 \in Z_\xi$.

We found sufficient conditions for the boundary observer design for linear and quasi-linear strict hyperbolic systems with n rightward convecting PDEs in presence of static (6.1.7) as well as dynamic boundary controls (6.1.8). The sufficient conditions were derived in terms of the system's and boundary conditions dynamics. In Proposition 6.3.1 and Theorem 6.3.2, we presented the sufficient conditions for the observer design for linear hyperbolic systems with static and dynamic boundary control for all $\xi^0 : [0,1] \to \Theta$, respectively. Then, in Theorems 6.3.3 and 6.3.4, sufficient conditions for boundary observer design for quasi-linear hyperbolic systems were determined for all $\xi^0 : [0,1] \to \Upsilon \subset \Theta$.

Based of the theoretical developments of this chapter, we proposed a new solution for the control of the fresh air mass fraction in a Diesel engine operated with low-pressure exhaust gas recirculation. To model the air fraction transport phenomenon, we considered a formulation using a cascade of first-order LPV hyperbolic systems with dynamics associated with the boundary conditions. By defining a minimal air fraction convergence time as the performance criterion, an air fraction regulation strategy was designed using the stability results given in Theorem 6.2.4. The conservatism of the boundary feedback control was significantly reduced by redefining the system varying parameters. The complexity of the obtained boundary control was very low, which made it suitable for real-time implementation. The effectiveness of the proposed boundary control was evaluated using a 1D simulation of the engine admission air-path.

Chapter 7

Conclusions and Perspectives

In this thesis, we proposed several developments to enhance the modeling and control of the Diesel engine air-path. These developments are an important contribution for the model-based control approach, which is one of the main directions of investigation by Renault to improve the engine performance and meet the current and future polluting emissions regulations. The main contributions of this thesis can be summarized as follows:

- An alternative industrial-oriented air-path control architecture was developed in order to regulate the pressure, air fraction and the EGR proportion in the engine intake manifold. The proposed approach was designed, taking into account Renault's needs in terms of: low time consuming and simple control calibration procedures, solutions relatively simple and easy to industrialize, the use of a similar air-path control architecture to the one currently used in Renault and the reduction of the number of sensors involved in the engine air-path control. The main differences obtained with respect to other existing air-path control architectures are: a closed-loop formulation to simultaneously estimate the LP-EGR mass flow rate and the air fraction in the intake manifold, an air fraction control that takes into account the EGR proportion, the estimation of the exhaust manifold pressure and a more effective way of positioning the VGT, which allows controlling the boost pressure without the need of a measurement of the exhaust manifold pressure. A detailed evaluation of each of the blocks associated with the air-path control architecture was performed using, as a reference, a 0D engine model validated with benchmark measurements in steady and transient conditions. The simulation results are promising and motivate future steps toward implementation.
- Alternative non-homentropic boundary resolution methods were proposed for the outflow and intra-pipe boundary problems. The main difference with respect to other boundary resolution formulations is that the assumption of the isentropic contraction at the boundary (which is systematically in disagreement with experimental results) is removed, allowing to formulate completely non-homentropic schemes. The proposed methods allow incorporating various QS restriction models without the need of modifying the boundary resolution schemes or adding discharge coefficients. Additionally, other improvements were brought

to the methods such as better numerical performance and reference-free entropy level correction. By means of an experimental setup, it was shown that the proposed boundary resolution methods successfully integrated the non-homentropic outflow and intra-pipe restriction models into the wave action method, allowing to obtain significant improvements in terms of predictability, numerical performance and flexibility, which is of significant importance for control-oriented applications.

- The stabilization and observation of linear, LPV and quasi-linear first-order hyperbolic systems with dynamic boundary conditions were addressed along with their application to the air fraction control in Diesel engines. We found sufficient conditions for boundary control and observer design for linear, LPV and quasi-linear strict hyperbolic systems with n rightward convecting PDEs with dynamic boundary conditions. An extension of the strict Lyapunov function proposed in [40] was used to demonstrate the exponential stability of this class of infinite dimensional systems. The sufficient conditions for exponential stability were given in the framework of matrix inequalities. We proposed a new solution for the control of the air fraction in a Diesel engine operated with low-pressure exhaust gas recirculation. To model the air fraction transport phenomenon, we considered a formulation using a cascade of first-order LPV hyperbolic systems with dynamics associated with the boundary conditions. The effectiveness of the proposed boundary control was evaluated using a 1D simulation of the engine admission air-path. The low complexity of the boundary control and the very promising results obtained in simulation show the potential of this control approach in the future air-path control strategies.

The following future work directions have been identified to improve and complement the methods developed in this thesis:

- A natural extension of the work presented in Chapter 4 is the benchmark evaluation of the proposed control and estimation strategies and the final implementation of the complete air-path control architecture given in Figure 4.4 in production engines. The implementation of the simultaneous LP-EGR mass flow rate and air fraction observer has been done in an much more evolved engine reference model, giving promising results and its benchmark and vehicle implementation is planned for November of 2013. By means of the proposed air fraction estimation, an observer of the polluting emission NOx is planned to be implemented in the first trimester of 2014. The decision to implement the air fraction and boost pressure controllers (given in Sections 4.3 and 4.5, respectively) in the engine version EURO 6c will be taken in the second trimester of 2014.

- Recent trends in automotive industry suggest that the dual-stage supercharging system is one of the key enablers to further improve the output power of Diesel engines. The advantage of dual-stage boosting over the single-stage systems is the simultaneous increase of the steady-state torque at low engine speeds along with the improvement of the supercharging system transient response (since it allows to rapidly build up the boost pressure). In this sense, dual-stage supercharging is a suitable method to significantly increase the boost level as well as a wider operating range due to its higher flexibility. Therefore, an

evolution of the air-path control architecture toward this class of supercharging strategy seems to be a natural evolution of this work.

- The next steps to follow in the construction of 1D control-oriented air-path models is the development of similar boundary resolution methods (with respect to the models developed in Chapter 5) for other intra-pipe boundary conditions such as after-treatment systems, compressors and turbines. The development of boundary resolution methods capable of taking into account the dynamics at the boundaries of these devices (avoidance of the quasi-steady formulation) seems to be a very challenging issue.

- The theoretical work given in Chapter 6 has many applications in various systems governed by hyperbolic PDE and thus the development of boundary controls and observers for other physical processes would substantially complement this work. For instance, we have developed the application to the boundary temperature control in a Poiseuille flow [22]. The boundary control and observer design of quasi-linear first-order hyperbolic systems with dynamics boundary conditions and with n rightward and $m > 2$ leftward convective transport PDEs is still an open problem, as well as the generalization of the observer and control design of systems with non-linear dynamic boundary conditions. Also, the analysis of the effect of perturbations in the hyperbolic systems and in their boundary conditions is also a natural extension of this work.

- Since an estimation of the air fraction in the intake manifold is required for the implementation of the air fraction boundary control described in Section 6.4, an evaluation of this control strategy along with an air fraction estimator capable of describing the mass transport phenomenon (such as the observer given in Appendix A.4) would complement the results of this application.

The following future work directions have been identified in a long term:

- To allow the evolution toward the 1D model-based engine air-path control, 1D modeling strategies (such as the ones proposed in this thesis) will have to be adapted to be used in real-time applications. To accomplish this, it will be necessary to find the adequate trade-off between the engine modeling complexity and the computational resources demanded by the numerical schemes. Moreover, many efforts will have to be done to develop highly efficient numerical methods to solve in real-time, the partial differential equations inherently associated with a 1D approach. Different modeling and estimation techniques, different from the ones proposed in this study, will have to be tested in order to analyze possible improvements to obtain more suitable algorithms for real-time control purposes.

- Future emissions standards force the vehicle manufacturers to design engines with more advanced after-treatment systems. Indeed, many of the Diesel engines designed to meet the Euro 6 standard are equipped with NOx catalyst (NOx Trap) or selective catalytic reduction (SCR). For the adequate functioning of these after-treatment systems, it is crucial to know the NOx load in order to optimize the purge phases. An excess in purges leads to more fuel consumption in the case of NOx-trap and in the case of SCR, an excess

in urea consumption. Therefore, vehicle manufacturers install a NOx upstream of the after-treatment systems to measure the NOx rate, allowing thus to adequately optimize the purge phases. However, alternative methods to estimate the NOx have been developed to avoid the additional cost of installing the NOx sensor in engines, such as the NOx estimation from the measurement of the in-cylinder pressure. This solution has shown to be very effective, but with the drawback of requiring special engine instrumentation such as a cylinder pressure sensor and a more powerful CPU than the average found in production engines. Thus, it is of significant importance to propose alternative NOx estimators that only use the resources usually available in production engines. Looking for closed-loop polluting emission estimation techniques (evidently for NOx and other emissions such as Diesel particulate matter and CO) could be one of the long term directions of the future works in the engine control community.

Bibliography

[1] O. Aamo. Disturbance rejection in 2x2 linear hyperbolic systems. *IEEE transactions on automatic control*, 58:1095–1106, 2006.

[2] M. Adams, S. Cryan, and A. Mourelatou. Air emission inventory data in Europe: new perspectives. *European Union emission inventory report 1990-2009 under the UNECE Convention on Long-range Transboundary Air Pollution (LRTAP)*, 2009.

[3] K. Akihama, Y. Takatory, K. Inagaki, S. Sasaki, and A. Dean. Mechanism of the smokeless rich Diesel combustion by reducing temperature. *SAE Technical Paper 2001-01-0655, doi:10.4271/2001-01-0655*, 2001.

[4] M. Alriksson and I. Denbrantt. Low temperature combustion in a heavy duty Diesel engine using high levels of EGR. *SAE Technical Paper 2006-01-0075, doi:10.4271/2006-01-0075*, 2006.

[5] M. Ammann, N. Fekete, L. Guzzella, and A. Glattfelder. Model-based control of the VGT and EGR in a turbocharged common-rail Diesel engine: theory and passenger car implementation. *SAE World Congress, Detroit, USA, Paper 2003-01-0357*, 2003.

[6] B. Anderson and J. Moore. *Linear Optimal Control.* Prentice Hall, Englewood Cliffs, N.J., 1971.

[7] G. Angelis. *System Analysis, Modelling and Control with Polytopic Linear Models. PhD Thesis.* Technische Universiteit Eindhoven, Eindhoven, 2001.

[8] G. Bastin, J-M. Coron, and B. d'Andréa Novel. Using hyperbolic systems of balance laws for modelling, control and stability analysis of physical networks. *Lecture notes for the Pre-Congress Workshop on Complex Embedded and Networked Control Systems, 17th IFAC World Congress, Seoul, Korea*, 2008.

[9] G. Bastin, J-M. Coron, and B. d'Andréa Novel. On Lyapunov stability of linearized Saint-Venant equations for a sloping channel. *Networks and Heterogeneous Media.*, 4(2):177–187, 2009.

[10] R. Benson. *The Themodynamics and Gas Dynamics of Internal-Combustion Engines*, volume 1. Clarenton Press, 1982.

[11] J. Bernussou, P.L.D. Peres, and J.C. Geromel. A linear programming oriented procedure for quadratic stabilization of uncertain systems. *Systems and Control Letters*, 13:65–72, 1989.

[12] N. Bordet. *Modélisation 0D/1D de la Combustion Diesel: du Mode Conventionnel au Mode Homogène*. PhD thesis, Université d'Orléans, France, 2011.

[13] R. Brecha. Emission scenarios in the face of fossil-fuel peaking. *Energy Policy*, (36):3492–3504.

[14] D. Bresch-Pietri, T. Leroy, J. Chauvin, and N. Petit. Prediction-based trajectory tracking of external gas recirculation for turbocharged SI engines. *Proceedings of the American Control Conference, Montréal, Canada*, pages 5718–5724, 2012.

[15] G. Bression, P. Pacaud, D. Soleri, J. Cessou, D. Azoulay, N. Lawrence, L. Doradaux, and N. Guerrassi. Comparative study in LTC combustion between a short HP-EGR loop without cooler and a variable lift a duration system. *Proceedings of the 17th Aachen Colloquium on Automobile and Engine Technology*, 2008.

[16] F. Castillo, V. Talon, and G. Mauviot. Estimation des émissions de NOx pour moteur diesel sans utilisation de capteur de pression cylindre. (Submitted).

[17] F. Castillo, V. Talon, and E. Witrant. Estimation de la pression avant turbine en vue d'un contrôle de la suralimentation des moteurs à combustion interne. (INPI No FR 1251468).

[18] F. Castillo, V. Talon, and E. Witrant. Procédé d'acquisition de la composition des gaz d'admission dans un repartieur d'air d'un moteur a combustion interne. (INPI No FR 2973441).

[19] F. Castillo, V. Talon, E. Witrant, and L. Dugard. Procédé de regulation d'un turbocompreseur a geometrie variable. (INPI No FR 1260352).

[20] F. Castillo, V. Talon, E. Witrant, and L. Dugard. Système et procédé de détermination de la masse de gaz frais dans le collecteur d'admission d'un moteur à combustion interne de véhicule automobile. (INPI No FR 1355045).

[21] F. Castillo, E. Witrant, and L. Dugard. Contrôle de température dans un flux de Poiseuille. *Proceedings of the IEEE Conférence Internationale Francophone d'Automatique, Grenoble, France*, 2012.

[22] F. Castillo, E. Witrant, and L. Dugard. Dynamic boundary stabilization of linear parameter varying hyperbolic systems: Application to a Poiseuille flow. *Proceedings of the 11th IFAC Workshop on Time-Delay Systems, Grenoble, France*, 2013.

[23] F. Castillo, E. Witrant, L. Dugard, Vincent Talon, David Chalet, and Pascal Chesse. Intra-pipe restriction non-homentropic boundary resolution method. *SAE Technical Paper 2013-01-0582*, 2013.

[24] F. Castillo, E. Witrant, C. Prieur, and L. Dugard. Dynamic boundary stabilization of linear and quasi-linear hyperbolic systems. *Proceedings of the 51st IEEE Conference on Decision and Control, Maui, Hawai*, pages 2952–2957, 2012.

[25] F. Castillo, E. Witrant, C. Prieur, and L. Dugard. Boundary observers for linear and quasi-linear hyperbolic systems with application to flow control. *Automatica, to appear*, 2013.

[26] F. Castillo, E. Witrant, C. Prieur, V. Talon, and L. Dugard. Engine fresh air mass fraction control using dynamic boundary stabilization of linear parameter varying hyperbolic systems. *Submitted to IEEE Transactions on Control Systems Technology*, 2013.

[27] F. Castillo, E. Witrant, V. Talon, and L. Dugard. Restriction model independent method for non-isentropic outflow valve boundary problem resolution. *SAE Technical Paper 2012-01-0676, doi:10.4271/2012-01-0676*, 2012.

[28] F. Castillo, E. Witrant, V. Talon, and L. Dugard. Air fraction estimation taking into account the mass transport time in diesel engines. *Submitted to Control Engineering and Practice*, 2013.

[29] F. Castillo, E. Witrant, V. Talon, and L. Dugard. Exhaust manifold pressure estimation Diesel equipped with a vgt turbocharger. *SAE Technical Paper 2013-01-1752, doi:10.4271/2013-01-1752*, 2013.

[30] F. Castillo, E. Witrant, V. Talon, and L. Dugard. Simultaneous air fraction and low-pressure EGR mass flow rate estimation for Diesel engines. *Proceedings of the 5th IFAC Symposium on System Structure and Control, Grenoble, France*, 2013.

[31] D. Chalet and P. Chesse. Fluid dynamic modelling of junctions in internal combustion engine inlet and exhaust systems. *Journal of Thermal Science*, 19(5):410–418, 2010.

[32] D. Chalet, P. Chesse, and J-F. Hetet. Boundary conditions modelling of one-dimensional gas dynamics flows in an internal combustion engine. *International Journal of Engine Research*, 9(4):267–282, 2008.

[33] D. Chalet, P. Chesse, and X. Tauzia J-F. Hetet. Inflow boundary condition for one-dimensional gas dynamics simulation code of internal combustion engine manifolds. *Proceedings of the Institution of Mechanical Engineers, Part D, Journal of Automobile Engineering*, 223(7):953–965, 2009.

[34] J. Chauvin, G. Corde, C.Vigild, N. Petit, and P. Rouchon. Air path estimation on Diesel HCCI engine. *SAE Technical Paper 2006-01-1085, 2006, doi:10.4271/2006-01-1085*, 2006.

[35] J. Chauvin, G. Corde, and N. Petit. Constrained motion planning for the airpath of a Diesel HCCI engine. *Proceedings of the 45th IEEE Conference on Decision and Control*, pages 3589–3596, 2006.

[36] J. Chauvin, G. Corde, N. Petit, and P. Rouchon. Motion planning for experimental airpath control of a Diesel homogeneous charge-compression ignition engine. *Control Engineering Practice*, 16:1081–1091, 2008.

[37] T.J. Chung. *Computational Fluid Dynamics*. Cambridge University Press, United Kingdom, 2002.

[38] J-M. Coron. *Control and Nonlinearity*. American Mathematical Society, USA, 2007.

[39] J-M. Coron, G. Bastin, and B. d'Andréa Novel. Dissipative boundary conditions for one-dimensional nonlinear hyperbolic systems. *SIAM J. Control Optim*, 47:1460–1498, 2008.

[40] J-M. Coron, B. d'Andréa Novel, and G. Bastin. A strict Lyapunov function for boundary control of hyperbolic systems of conservation laws. *IEEE Transactions on Automatic control*, 52:2–11, 2007.

[41] J. de Halleux. *Boundary Control of Quasi-Linear Hyperbolic Initial Boundary-Value Problems. PhD Thesis*. Presses universitaires de Louvain, Louvain la Neuve, Belgium, 2004.

[42] A. Diagne, G. Bastin, and J-M. Coron. Lyapunov exponential stability of 1-D linear hyperbolic systems of balance laws. *Automatica*, 48:109–114, 2012.

[43] L. Eriksson, J. Wahlström, and M. Klein. Physical modeling of turbocharged engines and parameter identification. *Automotive Model Predictive Control, Lecture Notes in Control and Information Sciences*, 402:53–71, 2010.

[44] E. Feron, S. Boyd, and L. El Ghaoui. Numerical methods for H2 related problems. *Proceedings of the American Control Conference*, pages 2921–2922, 1992.

[45] J. Fredriksson and B. Egardt. Estimating exhaust manifold pressure in a turbocharged Diesel engine. *Proceedings of the IEEE International Conference on Control Applications, Glasgow, Scotland*, 2002.

[46] G.Martin, P. Brejaud, P. Higelin, and A. Charlet. Pressure ratio based method for non-isentropic inflow valve boundary condition resolution. *SAE Technical Paper 2010-01-1052, doi:10.4271/2010-01-1052*, 2010.

[47] G.Martin, V. Talon, P. Higelin, A. Charlet, and C. Caillol. Implementing turbomachinery physics into map-based turbocharger models. *SAE World Congress, Detroit, USA, Paper 2009-01-0310*, 2009.

[48] O. Grondin, P. Moulin, and J. Chauvin. Control of a turbocharged Diesel engine fitted with high pressure and low pressure exhaust gas recirculation systems. *48th IEEE Conference on Decision and Control, Shanghai, China*, pages 6582–6589, 2009.

[49] L. Guzzella and C.H. Onder. *Introduction to modeling and control of internal combustion engine systems*. Springer Verlag; 2nd ed, 2010.

[50] J. El Hadef. Physical-based algorithms for interpolation and extrapolation of turbocharger data maps. *Proceedings of the SAE World Congress, Detroit, USA, Paper 2012-01-0434*, 2012.

[51] F.M. Haut, G. Leugering, and T.I. Seidman. Modeling and analysis of modal switching in networked transport systems. *Applied Mathematics and Optimization*, 59(2):275–292, 2009.

[52] M. Herceg, T. Raff, R. Findeisen, and F. Allgower. Nonlinear model predictive control of a turbocharged Diesel engine. *Proceedings of the 2006 IEEE International Conference on Control Applications. Munich, Germany*, 2006.

[53] A. Hribernik. The potential of the high and low-pressure exhaust gas recirculation. *Proceedings of the SAE conference, Paper 2002-04-0029*, 2002.

[54] International Energy Agency. *CO2 Emissions from fuel combustion highligths.* IEA, 2011.

[55] Mrdjan Jankovic, Miroslava Jankovic, and Ilya Kolmanovsky. Constructive Lyapunov control design for turbocharged Diesel engines. *IEEE Transactions on Control Systems Technology*, 8(2):288–299, 2000.

[56] M. Jung and K. Glover. Calibratable linear parameter-varying control of a turbocharged Diesel engine. *IEEE Transactions on Control systems Technology*, 14(1):45–62.

[57] J.Wang. Smooth in-cylinder lean-rich combustion, swithching control for diesel engine exhaust-treatment system regenerations. *SAE Int. J. Passeng. Cars - Electron. Electr. Syst. doi:10.4271/2008-01-0979*, (1):340–348, 2008.

[58] V. Kato. The Cauchy problem for quasi-linear symmetric hyperbolic systems. *Arch. Rational Mech. Anal.*, 58:181–205, 1985.

[59] T. Kelley. *Solving non-linear equations with Newton's method.* Society of Industrial and Applied Mathematics, USA, 2003.

[60] U. Kiencke and L. Eriksson. *Automotive Control Systems.* Springer, 2005.

[61] I. Kolmanovski, J. Sun, and M. Druzhinina. Charge control for direct injection spark ignition engines with EGR. *Proceedings of the 45th IEEE Conference on Decision and Control*, pages 34–38, 2000.

[62] M. Krstic and A. Smyshlyaev. Backstepping boundary control for first-order hyperbolic PDEs and application to systems with actuator and sensor delays. *Systems and Control Letters*, 57(9):750–758, 2008.

[63] M. Krstic and A. Smyshlyaev. *Boundary Control of PDEs: A Course on Backstepping Designs.* Society for Industrial and Applied Mathematics, Philadelphia, USA, 2008.

[64] M. Krzyzanowski, B. Kuna-Dibbert, and J. Schneider. *Health effects of transport-related air pollution.* World Health Organization, 2005.

[65] T.T. Li. Global classical solutions for quasilinear hyperbolic systems. *RAM Res. Appl. Math. 32, Masson, Paris*, 1994.

[66] T.T. Li. Controllability and observability for quasilinear hyperbolic systems. *High Education Press, Beijing*, 3, 2012.

[67] X. Litrico and V. Fromion. Boundary control of hyperbolic conservation laws using a frequency domain approach. *Automatica*, 45:647–659, 2009.

[68] G. Malaczynski, M. Mueller, J. Pfeiffer, D. Cabush, and K. Hoyer. Replacing volumetric efficiency calibration look-up tables with artificial neural network-based algorithm for variable valve actuation. *SAE Technical Paper 2010-01-0158, doi:10.4271/2010-01-0158*, 2010.

[69] G. Martin. *0-D -1-D Modeling of the air path of ICE Engines for control purposes.* PhD thesis, Université d'Orléans, France, 2010.

[70] F. Di Meglio, G.O. Kaasa, N. Petit, and V. Alstad. Slugging in multiphase flow as a mixed initial-boundary value problem for a quasilinear hyperbolic system. *Proceedings of the American Control Conference, San Francisco, USA*, pages 3589–3596, 2011.

[71] F. Di Meglio, R. Vazquez, and M. Krstic. Stabilization of a system of n+1 coupled first-order hyperbolic linear PDEs with single boundary input. *IEEE Transactions on Automatic Control, to appear*, 2013.

[72] F. Di Meglio, R. Vazquez, M. Krstic, and N. Petit. Backstepping stabilization of an underactuated 3x3 linear hyperbolic system of fluid flow transport equations. *Proceedings of the American Control Conference, Montréal, Canada*, pages 3365–3370, 2012.

[73] C. Olalla, R. Leyva, A. El Aroudi, and I. Queinnec. Robust lqr control for pwm converters: An lmi approach. *IEEE Transactions on Industrial Electronics*, 56(7), 2009.

[74] P.M. Olin. A mean-value model for estimating exhaust manifold pressure in production engine applications. *Proceedings of the SAE World Congress, Detroit, USA, Paper 2008-01-1004*, 2007.

[75] L. Pavel and L. Chang. Lyapunov-based boundary control for a class of hyperbolic lotka-volterra systems. *IEEE Transactions on automatic control*, 57(3):701–714, 2012.

[76] W. Perruquetti and J.P Barbot. *Sliding Mode in Engineering.* Marcel Dekker, 2002.

[77] A. Plianos, R. Stobart, and A. Achir. Real-time adaptive predicitve control of the Diesel engine air-path based on fuzzy parameter estimation. *Proceedings of the SAE World Congress, Detroit, USA, Paper 2007-01-0971*, 2007.

[78] C. Poussot. *Commande robuste LPV multivariable de chassis automobile (available in english).* PhD thesis, Grenoble INP, France, 2008.

[79] C. Prieur, A. Girard, and E. Witrant. Lyapunov functions for switched linear hyperbolic systems. In *Proceedings of the 4th IFAC Conference on Analysis and Design of Hybrid Systems (ADHS'12)*, Eindhoven, The Netherlands, 2012.

[80] C. Prieur and F. Mazenc. ISS-Lyapunov functions for time-varying hyperbolic systems of balance laws. *Mathematics of Control, Signals and Systems*, 24(1):111–134, 2012.

[81] C. Prieur, J. Winkin, and G. Bastin. Robust boundary control of systems of conservation laws. *Mathematics of Control, Signals, and Systems*, 20(2):173–197, 2008.

[82] M. Rivas. *Modeling and control of a SI engine for euro VI European normative.* PhD thesis, Université de Grenoble, France, 2012.

[83] T. Ryan and A. Matheaus. Fuel requirements for HCCI engine operation. *SAE transactions-Journal of Fuels Lubricants*, 112:1143–1152, 2003.

[84] V. Dos Santos, G. Bastin, J-M. Coron, and B. d'Andréa Novel. Boundary control with integral action for hyperbolic systems of conservation laws: stability and experiments. *Automatica*, 44(1):1310–1318, 2008.

[85] V. Dos Santos and C. Prieur. Boundary control of open channels with numerical and experimental validations. *IEEE Transactions on Control Systems Technology*, 16(6):1252–1264, 2008.

[86] L. A. Smith, T. Fickenscher, and R. P. Osborne. Engine breathing - steady speed volumetric efficiency and its validity under transient engine operation. *SAE Technical Paper 1999-01-0212, doi:10.4271/1999-01-0212*, 1999.

[87] Summaries of EU legislation. Regulation of the european parliament and of the council of 23 april 2009 setting emission performance standards for new passenger cars as part of the community's integrated approach to reduce CO2 emissions from light-duty vehicles. *140 of 5.6.2009*, (443), 2009.

[88] V. Talon. *Modélisation 0-1D des moteurs à allumage commandé.* PhD thesis, Universite d'Orleans, France, 2004.

[89] J. Tannehill, D. Anderson, and R. Pletcher. *Computational Fluid Mechanics and Heat Transfer.* Taylor and Francis, Washington DC, USA, 1997.

[90] L. Tatsien and W. Libin. *Global propagation of regular nonlinear hyperbolic waves.* Springer, Boston, USA, 2009.

[91] Gamma Technologies. *A GT-SUITE Application for Engine Performance, Acoustics, and Control Simulation.* Gamma Technologies, 2004.

[92] F. Vazquez, M. Krstic, and J-M. Coron. Backstepping boundary stabilization and state estimation of a 2x2 linear hyperbolic system. *Proceedings of the 50th IEEE Conference on Decision and Control and European Control Conference, Orlando, FL, USA*, pages 4937–4942, 2011.

[93] J. Wahlström and L. Eriksson. Nonlinear input transformation for EGR] and VGT Control in Diesel Engines, year = 2010,. *SAE Int. J. Engines, 3(2):288-305, doi:10.4271/2010-01-2203.*

[94] J. Wang. Hybrid robust control for engines running low temperature combustion and conventional Diesel combustion modes. *IEEE Transactions on Control Systems Technology*, 16(6):1138–1151, 2007.

[95] J. Wang. Robust nonlinear control with singularity avoidance for Diesel engines having multiple combustion modes. *Proceedings of the American Control Conference, New York city, USA*, 2007.

[96] J. Wang. Air fraction estimation for multiple combustion mode Diesel engines with dual-loop EGR systems. *Control Engineering and Practice 16, 1479-1468*, 16, 2008.

[97] J. Wang and C.J. Chadwell. On the advanced air-path control and estimation for multiple and alternative combustion mode engines. *Proceedings of the SAE conference, Paper 2008-01-1730*, 2008.

[98] Y. Wang and I. Haskara. Exhaust pressure estimation and its application to variable geometry turbine and wastegate diagnostics. *Proceedings of the American Control Conference*, 2010.

[99] N. Watson and M.S. Janota. *Turbocharging the internal combustion engine.* Macmillan Publishers Limited, 1982.

[100] M. Weiss, P. Bonnel, R. Hummel, U. Manfredi, R. Colombo, G. Lanappe, P. Le Lijour, and M. Sculati. Analyzing on-road emissions of light-duty vehicles with portable emission measurement systems (PEMS). *JRC-IE Scientific and Technical Reports*, 2011.

[101] D.E. Winterbone and R.J. Pearson. *Theory of Engine Manifold Design: Wave Action Methods for IC Engines.* Society of Automotive Engineers. Inc, 2000.

[102] E. Witrant, A. D'Innocenzo, G. Sandou, F. Santucci, M. D. Di Benedetto, A. J. Isaksson, K. H. Johansson, S.-I. Niculescu, S. Olaru, E. Serra, S. Tennina, and U. Tiberi. Wireless ventilation control for large-scale systems: the mining industrial case. *International Journal of Robust and Nonlinear Control*, 20:226–251, Jan. 2010.

[103] F. Yan and J. Wang. Control of a dual loop EGR air-path systems for advanced combustion Diesel engines by singular perturbation methodology. *Proceedings of the American Control Conference, San Francisco, USA*, pages 1561–1566, 2011.

[104] B. Youssef, P. Moulin, and O. Grondin. Model based control of turbochargers: Application to a Diesel engine. *Proceedings of the 16th IEEE International Conference on Control Applications, Singapore*, 2007.

[105] K. Zhou, J. Doyle, and K. Glover. *Robust and Optimal Control.* Prentice Hall, New Jersey, 1995.

Appendix A

Appendix

A.1 Motivation for 1D modeling for control purposes

A simple example illustrates the current problem of the air mass fraction control in the intake manifold when a sudden change of the LP-EGR rate occurs. The system shown in Figure A.1 consists in a tube with restriction at both ends. At the left end, there is a known pressure p_{in}, a known temperature T_{in} and a known air mass fraction F_{in}. Assume that the system is at steady state at time 0. Then, a sudden change of F_{in} (from 0 to 1) is introduced at time 0 at the left end and the response is simulated using a 0D and a 1D model. The results obtained are presented in Figure A.2.

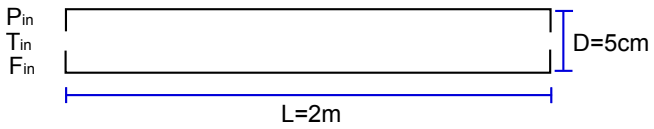

Figure A.1: System used to carry out the 0D and 1D approaches comparison

As depicted in Figure A.2, there is an important difference between the response obtained with the 0D model and the one with the 1D model. For example, the 0D model over-estimates the air mass fraction between 0 and 0.1 seconds (transient phase), which would compromise the engine NOx emission performance in that time interval. The 1D model response presents a more realistic behavior of the air mass fraction during the transient response, as it takes into account the mass transport time. This example illustrates the interest of using 1D models to synthesize control laws and observers that are efficient during the transients.

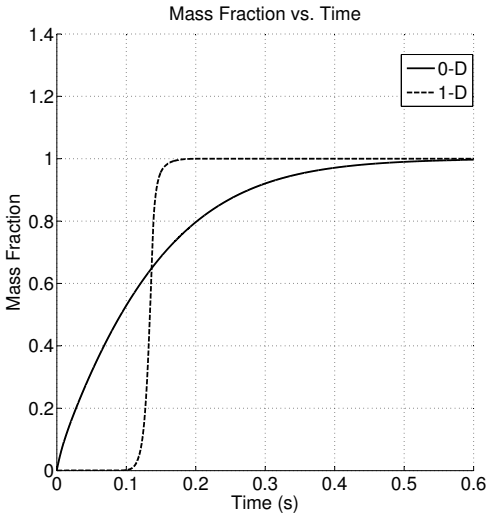

Figure A.2: Right tube end air mass fraction of the 0D and 1D models in response to an input air mass fraction unit step.

A.2 Effect of the variation of the heat ratio on the intra-pipe restriction models

In order to illustrate the effect of the variation of the heat ratio on the intra-pipe restriction quasi-steady models, a comparison between the data-maps generated with different heat ratios is performed. As presented in Figure 5.11, two of the quasi-steady restriction models are used to illustrate the impact of the heat ratio variation. As this work is focused on the modeling of the EGR and admission throttles, the variation of the heat ratio is considered between 1.4 and 1.32 (heat ratios of fresh air at $300K$ and EGR gas at $770K$ and with fresh mass fraction of 40%, respectively).

As depicted in Figure A.3, the effect of the variation of the heat ratio on the quasi-steady model is much smaller than the effect of the change of modeling formulation. This implies that the impact of the variation of the heat ratio on the quasi-steady models is not significant when compared with the impact of the modeling formulation (for the application considered in this work). The model variation with respect to the heat ratio is thus not considered for control and estimation purposes.

However, if the variation of the heat ratio is required, the data-map presented in (5.2.23) can be extended to take into account this variation as follows:

$$\frac{p_1}{p_3} = Datamap_p(U_3, \Phi_1, \Phi_3, \gamma) \tag{A.2.1}$$

This increases the usage of memory as well as the calculation load to solve the boundary problem, which is undesirable for control and estimation purposes.

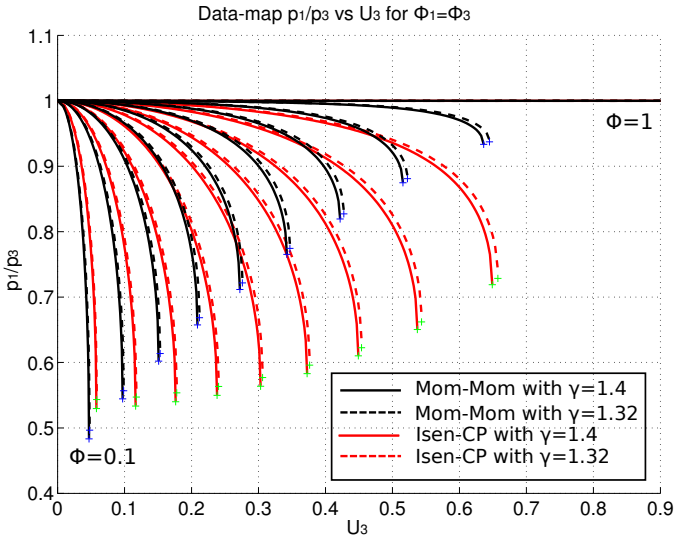

Figure A.3: Intra-pipe restriction model data-map comparison for different heat ratios

A.3 Conservative Discretizations

Shock waves can occur in the engine air-path and contact surfaces are produced in flows in reciprocating engines during every cycle of operation due to the interface between hot and cold gases. Explicit procedures for tracking the locations of discontinuities have to be implemented in order to capture the shock waves. There exists many shock capturing techniques which behave well under discontinuities and under smooth regions of the flow such as conservative explicit methods. These methods can be divided in two groups, symmetrical (the method does not depend on the direction of the characteristics) and upwind (Riemann solvers) techniques. In this review, we only consider symmetrical Lax-Wendroff based techniques because they present a good compromise between accuracy, robustness and computational load.

As their name suggests, conservative explicit methods are based on the differential form of the conservation laws. They use Taylor series expansion to provide discretizations which explicitly preserve the transport of mass, momentum and energy. For example, the well-known Lax-Wendroff method is a second order approximation of (5.1.5) that allows calculating $\mathbf{W}_i^{n+1}$ as follows:

$$\mathbf{W}_i^{n+1} = \mathbf{W}_i^n - \frac{\Delta t}{2\Delta x} A \left(\mathbf{W}_{i+1}^n - \mathbf{W}_{i-1}^n\right) + \frac{1}{2}\frac{\Delta t}{\Delta x}^2 A^2 \left(\mathbf{W}_{i+1}^n - 2\mathbf{W}_i^n + \mathbf{W}_{i-1}^n\right) \tag{A.3.1}$$

where $A = \frac{\delta \mathbf{F}}{\delta \mathbf{W}}$ which is the Jacobian matrix. This scheme is shock capturing, second order accuracy and stable as long as the Courant-Friedrichs-Lewy stability criterion $\Delta t < \frac{\Delta x}{c_{max}^n}$ is satisfied [101]. c_{max}^n is the maximum eigenvalue of the matrix A. One of the inconvenients of this approach is the need for calculating the Jacobian matrix at every time step. That is why Richtmyer and MacCormack proposed two different approaches which removed the need for calculating the Jacobian while retaining second-order accuracy. These approaches are known as

the two step Lax-Wendroff scheme and the MacCormack scheme, respectively. The widely used MacCormack method with discretization source terms $\mathbf{C(W)}$, which is considered in this thesis, is given as follows:

$$\mathbf{W}_i^* = \mathbf{W}_i^n - \frac{\Delta t}{\Delta x}\left(\mathbf{F}_{i+1}^n - \mathbf{F}_i^n\right) - \Delta t \mathbf{C}_i^n \tag{A.3.2}$$

$$\mathbf{W}_i^{n+1} = \frac{1}{2}\left[\mathbf{W}_i^n + \mathbf{W}_i^* - \frac{\Delta t}{\Delta x}\left(\mathbf{F}_i^* - \mathbf{C}_{i-1}^*\right) - \mathbf{C}_i^*\right] \tag{A.3.3}$$

where $\mathbf{F}_i^* = \mathbf{F}(\mathbf{W}_i^*)$. The main inconvenient with the second or higher order conservative explicit methods is that they tend to create spurious oscillations around discontinuities due to the Gibbs phenomena [101]. Therefore, various strategies have been developed with the purpose of avoiding the appearance of such oscillation by modifying the explicit method. The following strategies are some of the most currently used:

- Explicit artificial viscosity (EAV)
- Flux corrected transport (FTC)
- Symmetric total variation diminishing (TVD) scheme

Although all these strategies successfully eliminate the spurious oscillations, only the TVD scheme is considered in this thesis. The first two techniques, namely EAV and FTC, are not considered because they give non-physical solutions such as excessive dispersion and wave distortion.

Symmetric TVD scheme :

The total variation diminishing or TVD is a data criterion which ensures that a numerical scheme that generates data will not produce spurious oscillations at discontinuities. The TVD criterion also implies that the local maximum and monotonicity preservation criteria are satisfied. To understand this criterion, define the Total Variation (TV) quantity as:

$$TV(\mathbf{W}^n) = \Sigma \mid \mathbf{W}_{i+1}^n - \mathbf{W}_i^n \mid \tag{A.3.4}$$

If the TV of the solution $\mathbf{W}$ does not increase from one time step to the next, meaning that:

$$TV(\mathbf{W}^{n+1}) \leq TV(\mathbf{W}^n) \tag{A.3.5}$$

then, the data is said to be Total Variation Diminishing. The TVD property can be easily verified for a given numerical scheme allowing for the construction of methods having the TVD property. Consider the following general representation of an explicit numerical method:

$$\mathbf{W}^{n+1} = \mathbf{W}^n - C^n_{i-\frac{1}{2}}\Delta\mathbf{W}^n_{i-\frac{1}{2}} + D^n_{i+\frac{1}{2}}\Delta\mathbf{W}^n_{i+\frac{1}{2}} \tag{A.3.6}$$

where $\Delta\mathbf{W}^n_{i+\frac{1}{2}} = \mathbf{W}^n_{i+1} - \mathbf{W}^n_i$, $\Delta\mathbf{W}^n_{i-\frac{1}{2}} = \mathbf{W}^n_i - \mathbf{W}^n_{i-1}$ and the coefficients C and D that can depend on $\mathbf{W}^n$. The sufficient conditions for the scheme (A.3.6) to be TVD are the following:

$$0 \leq C^n_{i-\frac{1}{2}}; 0 \leq D^n_{i+\frac{1}{2}}; 0 \leq C^n_{i-\frac{1}{2}} + D^n_{i+\frac{1}{2}} \leq 1 \tag{A.3.7}$$

Inspired in the TVD concept, Davis introduced a post-processing routine that converts the results of a Lax-Wendroff based method and its derivatives into TVD scheme. We only give the main result as a detail development of the algorithm as it is outside the reach of this thesis. Consider the following definitions:

$$v = max_k \mid \lambda_k \mid \frac{\Delta t}{\Delta x}, \quad r^+ = \frac{\Delta\mathbf{W}^n_{i-1/2}}{\Delta\mathbf{W}^n_{i+1/2}}, \quad r^- = \frac{\Delta\mathbf{W}^n_{i+1/2}}{\Delta\mathbf{W}^n_{i-1/2}}, \tag{A.3.8}$$

$$C(v) = v(1-v) \quad \text{if} \quad v \leq 0.5 \quad \text{and} \quad C(v) = 0.25 \quad \text{if} \quad v \geq 0.5 \tag{A.3.9}$$

where λ_k are the eigenvalues of the Jacobian matrix A. Also define the flux limiter Φ as:

$$\Phi(r) = min(2r, 1) \quad \text{if} \quad r > 0 \quad \text{and} \quad \Phi(r) = 0 \quad \text{if} \quad r \leq 0 \tag{A.3.10}$$

Davis removed the local Courant number dependence of the scheme by defining:

$$\mathbf{G}^+(r^+) = \frac{1}{2}C(v)[1 - \Phi(r^+)] \tag{A.3.11}$$

Using the definitions (A.3.8) - (A.3.11), the final post-processing routine proposed by Davis is written as:

$$\mathbf{W}^{n+1}_i = \bar{\mathbf{W}}^{n+1}_i + \left[\mathbf{G}^+_{i+\frac{1}{2}}(r^+_i) + \mathbf{G}^-_{i+\frac{1}{2}}(r^-_{i+1})\right]\Delta\mathbf{W}^n_{i+\frac{1}{2}} - \left[\mathbf{G}^+_{i-\frac{1}{2}}(r^+_{i-1}) + \mathbf{G}^-_{i-\frac{1}{2}}(r^-_i)\right]\Delta\mathbf{W}^n_{i-\frac{1}{2}} \tag{A.3.12}$$

where $\bar{\mathbf{W}}_i^{n+1}$ is the result of a second order explicit method (i.e. MacCormack scheme) and $\mathbf{W}_i^{n+1}$ is the TVD solution.

The are other high-resolution schemes based on Godunov-types schemes (Riemman solvers) that have a superior performance in terms of accuracy than symmetric schemes. However, these methods are over three times slower than Lax-Wendroff schemes which makes them less suitable for engine air-path control purposes. This is why symmetric TVD methods are widely used in pipe flow simulation and also why we are considering them in this thesis.

Summarizing, (5.1.5) is partially solved in three steps by the calculation of (A.3.2), (A.3.2) and the TVD post-processing (A.3.12). Nevertheless, to obtain the complete solution of (5.1.5), the boundary conditions have to be solved as (A.3.2), (A.3.2) and (A.3.12) can only give the in-pipe solution.

A.4 Air Fraction Estimation Taking into Account the Mass Transport Time for Diesel Engines

Air Fraction Estimation Taking into Account the Mass Transport Time in Diesel Engines

Felipe Castillo[a,b], Emmanuel Witrant[a], Vincent Talon[b], Luc Dugard[a]

[a]UJF-Grenoble 1/CNRS, GIPSA Lab, 11 rue des mathématiques, BP 46, 38402 Saint Martin d'Hères Cedex, France
[b] Renault SAS, 1 allée Cournuel, 91510 Lardy, France

Abstract

In this paper we present a novel air fraction modeling and estimation strategy capable of representing the mass transport phenomenon, using the measurements typically available in production dual-loop EGR Diesel engines. A time-varying delay strategy is proposed to represent the air fraction transport phenomenon. This approach has a low calculation load, making it particularly suitable for control-oriented applications. Based on a discretization and reduction of the proposed air fraction model, an air fraction estimation method capable of taking into account the mass transport phenomenon is developed. The convergence of the observer is guaranteed over a prescribed convex parameter set using an LPV model formulation along with linear matrix inequalities (LMI). The performance of the air fraction observer is evaluated using as a reference, a validated engine model together with the time-varying delay air fraction modeling approach (sensors for air fraction transport are not yet available in the market).

Keywords: Air fraction estimation, Diesel engine control, time-varying delay

1. Introduction

Regulations of Diesel engine emissions have become stricter, and satisfying simultaneously the emissions legislations and the desired engine drivability objectives is a particularly challenging issue. Although significant improvements were made over the past years, there are still many technical issues that need to be addressed in order to meet the future regulation laws on emissions. The introduction of sophisticated alternative combustion modes such as homogeneous charge compression ignition (HCCI), low temperature combustion (LTC) and premixed controlled compression ignition (PCCI) offers a great potential to reduce the engine emissions levels [1] [2] [17]. However, these new modes require specific fueling strategies and in-cylinder conditions, thus creating the need for more complex, reliable and precise control systems and technologies.

Dual-loop exhaust gas recirculation (EGR) with both high (HP) and low-pressure (LP) recirculation is one of the new strategies that can provide the appropriate conditions for multiple combustion modes [14]. Indeed, the total in-cylinder EGR amount as well as the ratio between the high-pressure EGR (HP-EGR) and the low-pressure EGR (LP-EGR) allow controlling efficiently the in-cylinder combustion and the engine-out emissions. The air fraction regulation in the intake manifold is an effective way to control the in-cylinder EGR conditions [3] [13]. More precisely, for engines with dual EGR systems, the air fraction upstream of the compressor provides the LP-EGR rate while the air fraction in the intake manifold provides the total EGR rate. Therefore, if the air fractions in each section are well regulated, then the HP and LP-EGR can also be efficiently controlled.

However, controlling the air fraction is a difficult task because direct measurement of the air fraction is not available in production engines. Even in engine benchmarks, having a reliable air fraction measurement under strong transients is hardly obtained. Therefore, several air fraction/EGR rate estimation methods have been proposed in the literature to address this issue. In [13] [15], estimators of burned gas fraction in the intake manifold have been designed for single loop EGR. In [18], a method to estimate the air fraction in each section of the engine has been proposed for dual-loop EGR systems. In [11], the

problem of estimating the air fraction simultaneously with the LP-EGR mass flow rate is considered for a dual-loop EGR engine. Nonetheless, to the best of our knowledge, most of the air fraction estimation techniques are based on 0D engine modeling, which does not allow taking into account many physical phenomena such as the mass transport time.

One of the current issues with 0D model-based air fraction observers is their inability to represent the mass transport. Indeed, this phenomenon causes a degradation of the overall engine emission performance, specially for engines operated with LP-EGR as the distance that the gas has to travel is much longer than the one associated with HP-EGR. Therefore, alternative control-oriented modeling strategies to represent the air fraction dynamics have to be investigated. One-dimensional (1D) modeling allows the mass transport time to be estimated in the air-path of the engine, but it leads to more complex problems such as the wave action numerical methods and boundary conditions resolution schemes (see for instance [19]) that are not well suited for control and estimation purposes.

In this paper, a time-varying delay model is proposed to represent the mass transport phenomenon in the engine air-path by means of the information usually available in 0D simulation platforms. This approach results in an easier way to control and estimate the air fraction since the mass transport is accurately described while having a calculation load significantly less than the one obtain with traditional 1D modeling. Based on this model, a novel air fraction observer is proposed by using a first-order backward space discretization to approximate the air fraction transport phenomenon. By means of an LPV representation of the air fraction model, the convergence of the observer is guaranteed over a prescribed convex parameter set using a polytopic approach. In this sense, the main contributions of this work are:

- an air fraction modeling strategy capable of representing the mass transport while being compatible with the current 0D air-path models;
- an air fraction observer suitable for short term real-time implementation that takes into account the air fraction transport time.

This paper is organized as follows. In Section 2, we provide a description of the engine air-path considered in this work, its main components and its basic philosophy of operation. In Section 3, we introduce the time-varying delay to model the air fraction transport in a tube section. The effectiveness of the method is illustrated using, as a reference, a 1D model validated in a benchmark. In Section 4, the time-varying delay modeling strategy is applied to represent the air fraction dynamics in an engine admission air-path. A reduction of the resulting model is proposed to simplify its formulation for control purposes. Both approaches are evaluated using a 1D model. In Section 5, we develop an air fraction observer capable of taking into account the mass transport time. By means of an finite dimensional LPV representation of the air fraction dynamics, the convergence of the observers is guaranteed over a prescribed parameter convex set. Due to the lack of reliable air fraction measurements under strong transients, the performance of the proposed modeling strategy as well as the effectiveness of the air fraction observer are evaluated using as a reference, an experimentally validated engine model. The improvement obtained in the air fraction dynamics using the time-varying delay modeling approach is illustrated. The benchmark validation of the engine air-path model is presented in order to demonstrate that the simulations are representative of the engine (Appendix A).

2. Dual-Loop EGR Diesel Engine Air-Path

The engine air-path architecture considered in this work is based on a modern light-duty four-cylinder Diesel 1.6 liter engine with dual-loop exhaust gas recirculation (EGR) and a variable geometry turbine (VGT). Its schematic is depicted in Figure 1.

The engine shown in Figure 1 is equipped with a dual-loop EGR system (high-pressure and low-pressure EGR valves), a variable geometry turbocharger and exhaust-treatment systems such as a Diesel Particle Filter (DPF) and Diesel Oxidation Catalyst (DOC). With the high pressure EGR (HP-EGR), the burnt

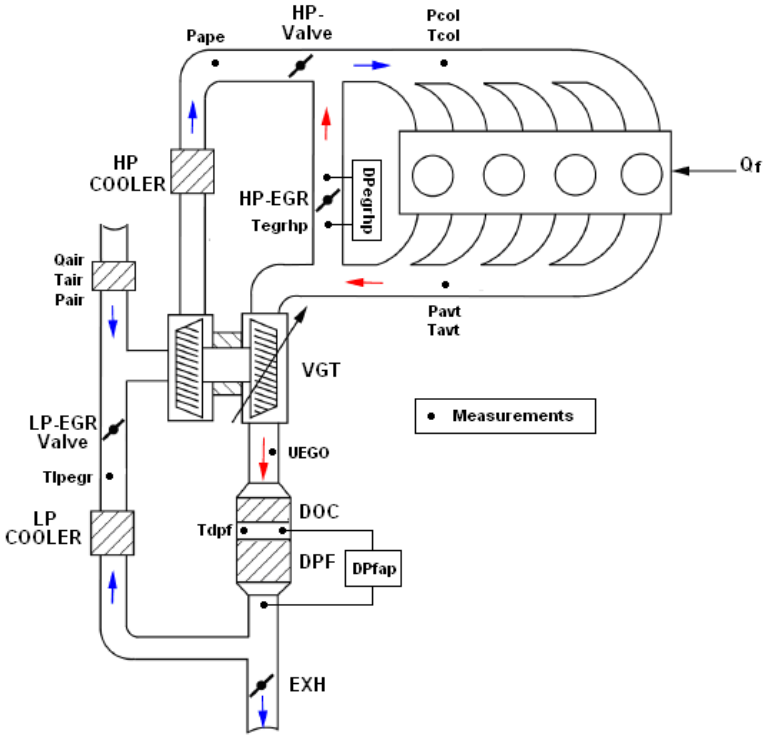

Figure 1: Schematic of the Dual-Loop EGR with VGT

gases from the exhaust manifold are recycled into the intake manifold. This configuration reduces the turbine flow and thus its power. However, the HP-EGR has a faster settling time and gives better HC and CO emission reduction than the low pressure EGR (LP-EGR) [8]. With the LP-EGR, the burnt gases are taken downstream of the exhaust post-treatment systems and reintroduced upstream of the compressor. With the LP-EGR all the exhaust gases go through the turbine allowing the supercharging system to operate optimally. Nevertheless, with the LP-EGR, the settling time of the intake manifold air fraction is longer in comparison with the HP-EGR. The dual-loop EGR configuration combines the advantages of the HP-EGR and the LP-EGR. With this EGR architecture, the mixing of hot HP-EGR gas and cold LP-EGR gas can be set to reach the optimal temperature regarding the HC-CO emission reduction. A prioritization of HP-EGR can be performed when a short settling time in the intake manifold air fraction is required while the LP-EGR can be prioritized when supercharging performance is needed.

The turbocharger with variable geometry turbine (VGT) provides two main benefits: first, it enables to extend the alternative combustion domain at high EGR levels and second it increases the engine power by increasing the quantity of the air mass in the cylinders at high engine loads. VGTs are of particular interest for advanced Diesel powertrains since they have the potential to provide accurate control of the pressure difference across the engine, as well as very quick response during engine transients. The high-pressure valve depicted in Figure 1, denoted as HP-valve, allows increasing the HP-EGR rate at light load, reduces the air mass flow rate during the DPF regeneration phases and blocks the air flow when operating the start-stop system. The high pressure cooler (HP-Cooler) increases the gas density, which allows obtaining more stable combustions and more mass inside the cylinders. The universal exhaust gas oxygen (UEGO) sensor is installed downstream of the VGT to avoid high pressure at the UEGO sensor. The LP-EGR includes an EGR valve, an EGR cooler and the exhaust valve. (denoted as EXH, which is necessary to create the necessary pressure drop in the LP-EGR system to ensure EGR flow).

3. Air Fraction Time-Varying Delay as a Model

In this section, we develop an air fraction time-varying delay approach to model the air fraction transport time inside a tube. A comparison between a 1D model, a 0D model and the proposed time-varying delay approach is done to illustrate the performance of each strategy.

3.1. Time-Varying Delay Model Formulation

Consider the problem of modeling the air fraction dynamics in a tube of length L and cross sectional area A_t (as shown in Figure 2). The change in fresh air mass fraction (referred to from now on as air fraction) across a control volume of length dx can be expressed by the following partial differential equation (PDE)[19]:

$$\partial_t[\rho(x,t)A_t(x)F(x,t)] + \partial_x[\rho(x,t)u(x,t)A_t(x)F(x,t)] = 0, \quad \forall\, x \in [0,L],\, t \geq 0 \tag{1}$$

where ∂_t and ∂_x are the partial derivative with respect to time and space, respectively, ρ is the gas density, u the speed of particles and F is the air fraction. Equation (1) can be expressed as follows (e.g. see [19] Chapter 4.2.5 for more details):

$$\partial_t[\rho(x,t)F(x,t)] + \partial_x[\rho(x,t)u(x,t)F(x,t)] + \rho(x,t)u(x,t)F(x,t)\partial_x[ln(A_t(x))] = 0 \tag{2}$$

Expanding (2) and dividing by $F(x,t)$ gives:

$$\begin{aligned} &\partial_t\rho(x,t) + u(x,t)\partial_x\rho(x,t) + \rho(x,t)\partial_x u(x,t) + \rho(x,t)u(x,t)\partial_x(ln(A_t(x))) \\ &+ \frac{\rho(x,t)}{F(x,t)}\partial_t F(x,t) + \frac{\rho(x,t)u(x,t)}{F(x,t)}\partial_x F(x,t) = 0 \end{aligned} \tag{3}$$

The first four terms of (3) constitute the global continuity of mass, implying that the sum of these four terms equals zero. Therefore, the air fraction continuity equation can be written as follows:

$$\begin{aligned} \partial_t F(x,t) + u(x,t)\partial_x F(x,t) = 0 \\ F(0,t) = F_{in}(t) \quad F(x,0) = F_0(x), \quad \forall\, x \in [0,L],\, t \geq 0 \end{aligned} \tag{4}$$

where F_{in} is the air fraction at the input boundary condition, $F_0(x)$ is a continuous differentiable function describing the initial condition and $u(t,x)$ is the air fraction propagation speed (independent of the air fraction). To simplify the solution of (4), consider the following hypotheses:

Hypotheses 1:

H-11: the pressure and particle speed dynamics are much faster than the air fraction dynamics;

H-12: neither friction nor thermal losses are considered;

H-13: the particles speed and temperature change slowly with respect to the mass transport time.

With H-11 and H-12, we remove the dependence of the air fraction propagation speed $u(t,x)$ with respect to x (u is average over the volume of the tube), which considerably simplifies the solution of (4) without a significant loss of model predictability for Diesel engines. The impact of assuming H-11 and H-12 is illustrated in Section 3.2. H-13 is a reasonable assumption since the change in the engine operating conditions is constrained by the system's inertia.

In [20], it was shown that the solution of (4) for $u(t,x) = u(t)$ at $x = L$ is given by:

$$F(t, L) = F(t - \tau_f) \quad \forall\, t > \tau_f(0) \tag{5}$$

where τ_f is the time delay associated with the air fraction transport, which is implicitly defined as:

$$L = \int_{t-\tau_f}^{t} u(\xi) d\xi \tag{6}$$

Assumption H-13 allows considering $u(t)$ constant for the time interval $[t - \tau_f, t]$, which simplifies (6) as:

$$\tau_f \approx \frac{L}{u(t)} \tag{7}$$

As the particle speed is typically not available in production engines, we need to represent the varying-time delay in terms of the gas mass flow rate, temperature and pressure by using the ideal gas law as follows:

$$u(t) = \frac{Q(t)}{A_t \rho(t)} = \frac{Q(t) R T(t)}{A_t p(t)} \tag{8}$$

From (7) and (8), the time delay can be approximated as:

$$\tau_f \approx \frac{p(t) V_{tube}}{R T(t) Q(t)} \tag{9}$$

where $V_{tube} = L A_t$ is the tube volume. The result obtained in (9) is very interesting because the mass transport time can be easily estimated using the measurements usually available in production engines. Moreover, to estimate the mass transport time, only the volume of the tube section has to be known (in other words, the estimation is independently on the pipe's length and cross section area), which is of significant relevance because this strategy can be applied on traditional 0D air-path models, where no dimensional information is available. This significantly simplifies the mass transport phenomenon modeling, making it suitable for implementation in 0D control-oriented models.

3.2. Accuracy of the Time-Varying Delay Model

To evaluate the effectiveness of the time-varying delay model (5) and (9) to describe the air fraction with transport time, the behavior of the air fraction inside the setup shown in Figure 2 is simulated using the proposed time-varying delay strategy, a 1D model and a traditional 0D approach.

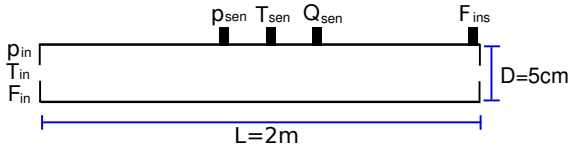

Figure 2: Schematic of the test setup

p_{in}, T_{in} and F_{in} are the tube's input pressure, temperature and air fraction, respectively. F_{ins} is the instantaneous tube's output air fraction. p_{sen}, T_{sen} and Q_{sen} are the tube's operating pressure, temperature and mass flow rate, which are obtained at the center of the tube after being filtered with a first-order model of the sensors. The filtering is done to reproduce the conditions of the instruments typically available in production engines. The time responses of the sensors have been chosen according to the following specifications:

- pressure sensor time response: 5 ms (Bosch pressure sensor part number: 0 281 002 257)
- mass flow rate sensor time response: 20 ms (Bosch air-mass meter part number: 0 280 217 102)
- temperature sensor time response: 5 s (Bosch temperature meter part number: 0 280 130 085)

A sudden change in the tube's input conditions (change of pressure and air fraction) is introduced to evaluate the behavior of the proposed method under unsteady flow conditions. The experiment is initialized with the following conditions for the tube flow:

$$p(x,0) = 1 \times 10^5\, Pa, \quad T(x,0) = 320\, K, \quad Q(x,0) = 0\, kg/s, \quad F(x,0) = 0 \tag{10}$$

Then, a sudden change of input pressure and air fraction is introduced at $t = 0.2\, s$ as follows:

$$p_{in} = 1.2 \times 10^5\, Pa, \quad F_{in} = 1, \quad \forall t > 0.2s \tag{11}$$

The experiment described in (10) - (11) is simulated using the time-delay model, a traditional 0D model and a 1D model, which is used as a reference since it has been previously validated for this setup [9] [10]. For the 1D simulation, it is assumed that the effect of diffusion is negligible. Figure 3 presents the simulation results.

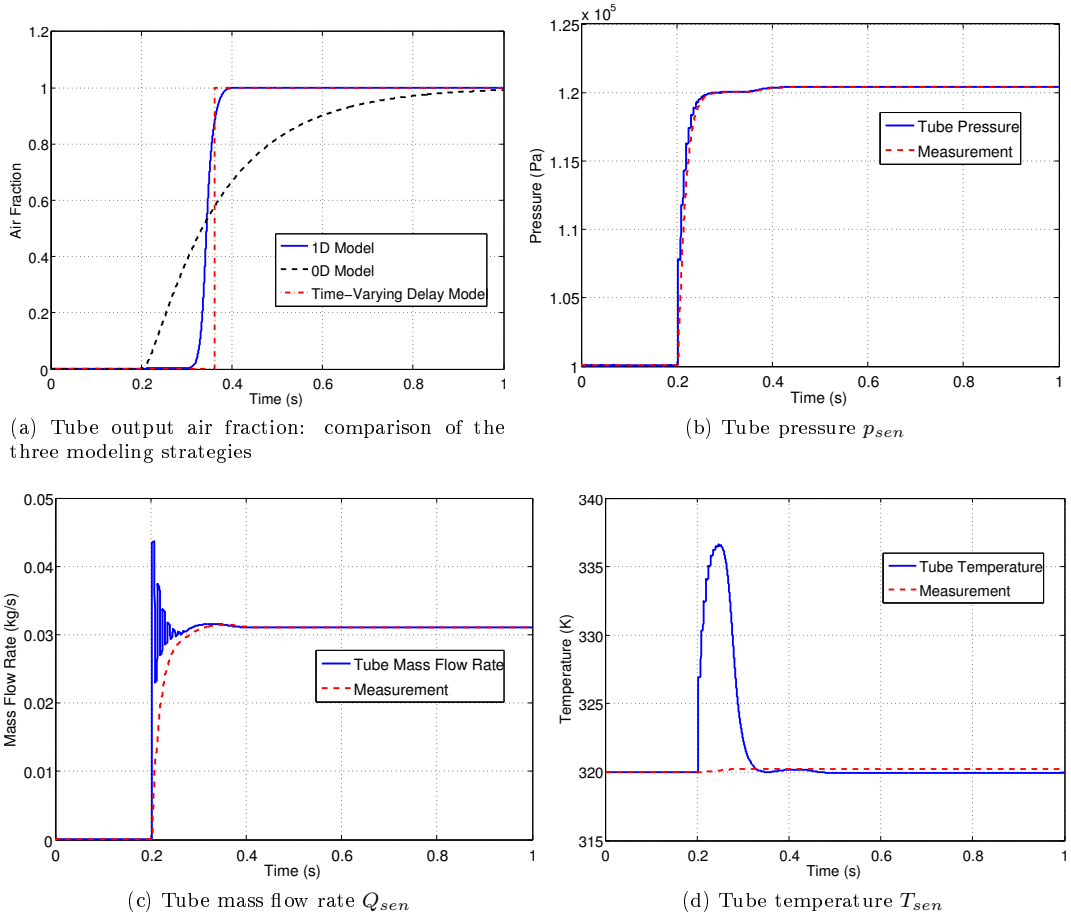

(a) Tube output air fraction: comparison of the three modeling strategies

(b) Tube pressure p_{sen}

(c) Tube mass flow rate Q_{sen}

(d) Tube temperature T_{sen}

Figure 3: Air fraction estimates and the 1D simulation results

Figure 3a depicts the comparison of the three modeling strategies (1D, 0D and time-varying delay), while Table 1 shows the calculation loads of each of the modeling strategies (normalized with respect to the

Model	Calculation Load
0D Model	1
Time-Varying Delay Model	1.4
1D Model	54

Table 1: Calculation load comparison using an Intel Xeon W3690 @ 3.47GHz CPU

calculation time of the 0D model). The 0D modeling approach over-estimates the air fraction during 130 ms and then under-estimates it for around 300 ms when compared with the 1D modeling strategy (Figure 3a). This phenomenon causes a degradation of the engine emission performance when used in supervision and control schemes. On the other hand, the proposed time-varying delay strategy presents a more physical behavior of the air fraction as it captures the mass transport time. This allows performing a more accurate air fraction estimation (even under strong transients) while significantly reducing the calculation load with respect to the 1D modeling (as illustrated in Table 1).

Figures 3b, 3c and 3d show the unsteady responses obtained at the center of the tube. A comparison between the 1D simulations (blue solid line) and the virtual measurement given by the sensors (dash red line) is given to illustrate the influence of the sensor on the construction of the time-varying delay model. The pressure sensor is very fast and gives a reliable pressure measurement. The mass flow rate measurement is slower, which causes the air fraction to be slightly delayed with respect to the 1D model. However, the impact of this delay on the air fraction model is not significant as shown in Figure 3a. The measurement of the temperature is typically the slowest (Figure 3d). Nevertheless, the entropy change in the engine admission path is also slow in comparison with the change of pressure and particles speed, which implies that the effect of the temperature measurement is not significant for the determination of the time-varying delay.

The Hypothesis H-13 is verified as the pressure and mass flow rate dynamics are much faster than the one associated with the air fraction (Figures 3b and 3c). These results show that the measurements of the pressure, temperature and mass flow rate in a tube (measurements available in production engines) can be used to estimate the mass transport time accurately, even under strong unsteady flow conditions.

4. Time-Varying Delay Approach for the Air-Path Air Fraction Model

In this section, we apply the air fraction time-varying delay approach (5) and (9) to model the dynamics of the gas composition in the air-path of a Diesel engine. To develop the model, the following hypotheses are made.

Hypotheses 2:

H-21: the air-path section, where gas mixture occurs, are modeled using a 0D model;

H-22: the volumes associated with the EGR are considered small;

H-23: the volume of the HP-Cooler is considered in the upstream and downstream tube sections;

H-24: Hypotheses 1 also apply.

The need for H-21 comes from the fact that the air-path sections where gas mixture occurs cannot be modeled with (5). However, these specific volumes (e.g. intake manifold and the compressor's suction) are small in comparison with the volume of the admission air-path (namely the volume between the compressor and the intake manifold). This implies that the transport time estimation of the air fraction is not significantly affected by the 0D modeling of theses sections. H-22 is usually considered since the volumes associated with the EGR are also small in comparison with the air system admission volumes. Finally, H-23 allows taking into account the mass transport time associated with HP-Cooler, which is

convenient because the gas conditions inside the heat exchanger cannot be easily defined.

After taking into account Hypotheses 2, using the traditional 0D models for the air fraction dynamics in the intake manifold and the compressor suction (see [11]) and applying the air fraction modeling approach (5) for the remaining of engine air-path, we obtain the following time-varying delay model for the dynamics of the air fraction in the engine air-path:

$$F_{em} = F_{eo}(t - \tau_{em}) \tag{12}$$

$$\dot{F}_{uc} = \frac{RT_{air}}{p_{air}V_{uc}}((F_{em} - 1)Q_{egrl} + (1 - F_{uc})(Q_{air} + Q_{egrl})) \tag{13}$$

$$F_{dc} = F_{uc}(t - \tau_{dc}) \tag{14}$$

$$F_{de} = F_{dc}(t - \tau_{de}) \tag{15}$$

$$\dot{F}_{im} = \frac{RT_{im}}{p_{im}V_{im}}((Q_{air} + Q_{egrl})(F_{de} - F_{im}) + Q_{egrh}(F_{em} - F_{im})) \tag{16}$$

where:

$$\tau_{em} = \frac{p_{em}V_{em}}{RT_{em}(Q_{air} + Q_{egrl} + Q_{egrh} + Q_f)}, \quad \tau_{dc} = \frac{p_{dc}(V_{dc} + 0.5V_{he})}{RT_{dc}(Q_{air} + Q_{egrl})}, \quad \tau_{de} = \frac{p_{de}(V_{de} + 0.5V_{he})}{RT_{de}(Q_{air} + Q_{egrl})} \tag{17}$$

The air fraction coming out of the cylinders, denoted as F_{eo}, can be estimated using the fueling rate Q_f and the stoichiometric air to fuel ratio PCO [18]. Note that the model (12) - (16) is rather simple to implement into a control-oriented 0D engine model since all the information required to estimate the air fraction transport time (namely (17)) is usually available in 0D air-path models. Indeed, in Section 6.1 we show the results obtained after implementing (12) - (16) in a experimentally validated 0D engine air-path model.

For control and observation purposes, a further reduction of system (12) - (16) can be performed, which allows simplifying the observation problem without affecting significantly the accuracy of the model for the air fraction transport. Consider the following hypotheses to simplify the system.

Hypotheses 3:

H-31: the HP-throttle is completely open during the LP-EGR operation;

H-32: the pressure and temperature conditions in the volumes V_{dc}, V_{he} and V_{de} are assumed to be equal during LP-EGR operation;

H-33: $V_{em} << V_{dc} + V_{he} + V_{de}$.

H-31 and H-32 allow considering V_{dc}, V_{he} and V_{de} as a single volume, which simplifies the amount of parameters to take into account for the mass transport time estimation. H-33 implies that the dynamics associated with the exhaust manifold is much faster than the dynamics of the admission path. Therefore, considering a 0D modeling for the exhaust manifold does not have a significant impact on the mass transport time estimation. After applying the hypotheses H-31 - H-33 on (12) - (16), the following reduced air fraction model is obtained:

$$\dot{F}_{em} = \frac{RT_{em}}{p_{em}V_{em}}((Q_{air} + Q_{egrl} + Q_{egrh})F_{im} - (Q_{air} + Q_{egrl} + Q_{egrh} + Q_f)F_{em} - PCOQ_f) \tag{18}$$

$$\dot{F}_{uc} = \frac{RT_{air}}{p_{air}V_{uc}}((F_{em} - 1)Q_{egrl} + (1 - F_{uc})(Q_{air} + Q_{egrl})) \tag{19}$$

$$F_{de} = F_{uc}(t - \tau_{adm}) \tag{20}$$

$$\dot{F}_{im} = \frac{RT_{im}}{p_{im}V_{im}}((Q_{air} + Q_{egrl})(F_{de} - F_{im}) + Q_{egrh}(F_{em} - F_{im})) \tag{21}$$

where

$$\tau_{adm} = \frac{p_{im}V_{adm}}{RT_{im}(Q_{air} + Q_{egrl})} \tag{22}$$

$V_{adm} = V_{dc} + V_{he} + V_{de}$ and F_{de} is the air fraction at the output of V_{adm}. System (18) - (21) contains only one time-varying delay, which is associated with the volume between the compressor and the intake manifold. This volume is the largest of the engine air-path and therefore, the one where most of the air fraction transport time comes from.

To evaluate the performance of the model (12) - (16) and the effect of the reduction considered in (18) - (21), a comparison with a 1D model and a 0D model is presented. This is performed to verify whether the proposed time-varying delay models are representative of the mass transport phenomenon in an engine air-path. To carry out the evaluation, consider the air-path schematic presented in Figure 4.

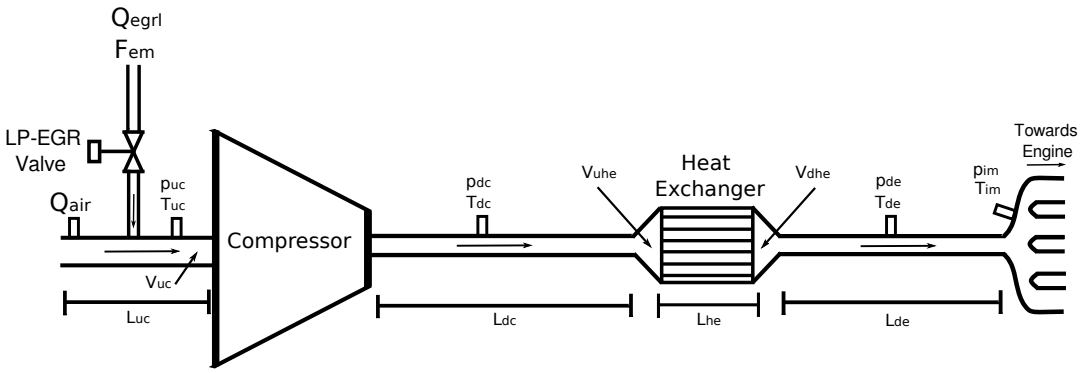

Figure 4: Schematic of the air Fraction air-path model for control purposes

The setup presented in Figure 4 is simulated for four different compressor speeds (denoted as N_{comp}) to evaluate the reduced time-varying delay model for different engine operating conditions. For the reduced model (18) - (21), only the measurements Q_{egrl}, Q_{air}, p_{de} and T_{im} (which are typically available production engines) are considered for the estimation of the time delay. For the complete time-varying delay model (12) - (16), the computation of the time delay is calculated using the required measurements for each of the air-path sections. Table 2 presents the air-path parameters considered in the simulation for a 1.6 liter Diesel engine. The simulation results are shown in Figure 5.

As depicted in Figure 5, both time-varying delay models show a good agreement with respect to the 1D reference model. The advantages obtained from the time-varying delay formulations over the 0D model

Variable	Value	Variable	Value
L_{dc}	$1.3\ m$	A_{he}	$6 \times 10^{-4}\ m^2$
A_{dc}	$0.002\ m^2$	V_{uhe}	$5 \times 10^{-4}\ m^3$
V_{uc}	$3 \times 10^{-4}\ m^3$	V_{dhe}	$5 \times 10^{-4}\ m^3$
N_{he}	8	L_{de}	$1.1\ m$
L_{he}	$0.58\ m$	A_{de}	$0.002\ m^2$

Table 2: Simulation parameters for the air-path of a 1.6 liter Diesel engine

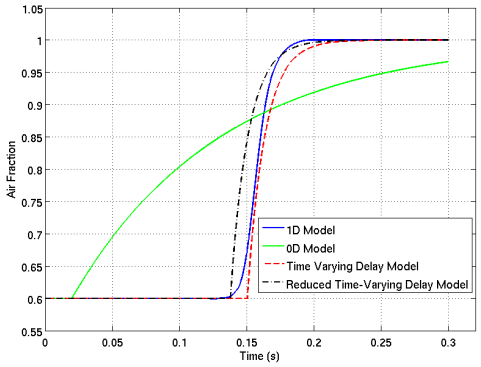

(a) Intake manifold air fraction comparison for $N_{comp} =$ 90000 rpm

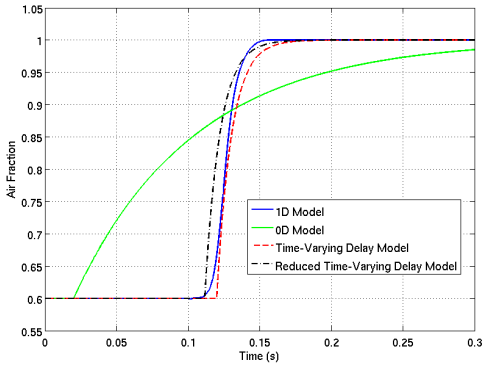

(b) Intake manifold air fraction comparison for $N_{comp} =$ 120000 rpm

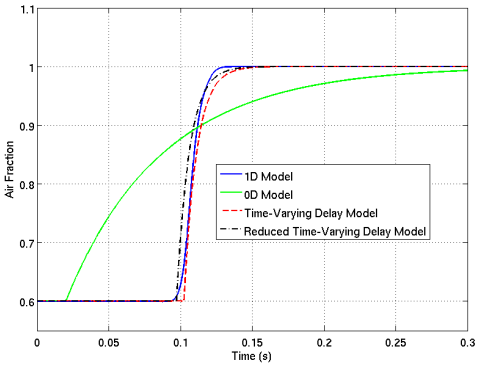

(c) Intake manifold air fraction comparison for $N_{comp} =$ 150000 rpm

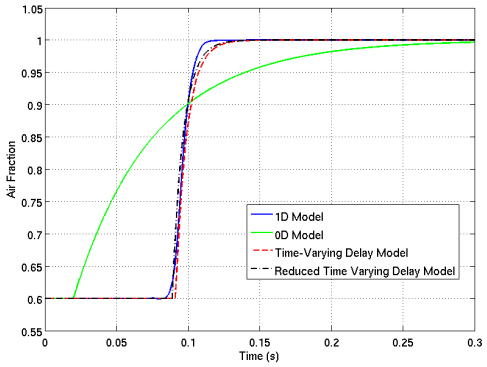

(d) Intake manifold air fraction comparison for $N_{comp} =$ 180000 rpm

Figure 5: Evaluation of the time-varying delay models for different compressor speeds in a 1.6 liter Diesel engine

can be clearly seen. The model (12) - (16) is more representative of the mass transport phenomenon than the reduced model (18) - (21). Indeed, the reduced model under-estimates the air-path mass, which translates into a smaller time delay. This originates from the hypothesis that the pressure upstream of the HP-Cooler is the same as the one downstream (no pressure drop across the heat exchanger in considered). Nonetheless, the difference between both time-varying delay models is negligible, allowing us to consider the reduced model as representative enough for the mass transport phenomenon.

5. Air Fraction Estimation with Mass Transport Time

In this section, we design an intake manifold air fraction observer capable of taking into account the mass transport in the admission air-path while being suitable for real-time implementation. The dynamics of

the air fraction (18) - (21) belongs to a class of systems denominated linear parameter varying (LPV) with time-delay, which are mathematically represented as follows:

$$\dot{x}(t) = A(\varphi)x(t) + A_h(\varphi)x(t - h(t)) \tag{23}$$
$$x(\theta) = \phi(\theta), \quad \theta \in [-h_m, 0] \tag{24}$$

where φ is a time varying parameter vector, $\phi(\theta)$ is a functional initial condition, $h(t)$ is the time-varying delay and h_m is the maximum time delay value. Even though there has been some works in the observation of (23) (e.g. [12]), it is very complicated to deal with this theoretical framework for engine control applications. This is due to the large amount of varying parameters associated with (18) - (21) as well as the difficulty of implementation in a production engine. Therefore, we simplify the observer formulation by discretizing the admission air-path into finite volumes by means of a first-order discretization technique. The main advantage obtained from this approach is the avoidance of infinite dimensional terms in the observer formulation.

Consider the following PDE representation of (20):

$$\begin{aligned} &\partial_t F_{adm}(x,t) + \frac{L_{adm} R T_{im}}{p_{im} V_{adm}}(Q_{air} + Q_{egrl})\partial_x F_{adm}(x,t) = 0 \\ &F_{de} = F_{adm}(L_{adm}, t), \quad F_{adm}(0,t) = F_{uc}, \quad \forall x \in [0, L_{adm}], \quad t > 0 \end{aligned} \tag{25}$$

where F_{adm} is the distribution of air fraction inside the engine admission air-path (namely V_{adm}). To approximate the space partial derivative, consider following the first-order backward space discretization:

$$\partial_x F_{adm} \approx \frac{F_{adm\_i} - F_{adm\_i-1}}{\Delta x}, \quad i \in [1, ..., N_d] \tag{26}$$

where $\Delta x = L_{adm}/N_d$ is the space differential and N_d is the discretization size (number of finite elements considered for the discretization). By applying (26) into (25), the following approximation of the dynamics of air fraction distribution in the admission path is obtained:

$$\dot{F}_{adm\_1} = N_d \frac{R T_{im}}{p_{im} V_{adm}}(Q_{air} + Q_{egrl})(F_{uc} - F_{adm\_1}) \tag{27}$$

$$\dot{F}_{adm\_i} = N_d \frac{R T_{im}}{p_{im} V_{adm}}(Q_{air} + Q_{egrl})(F_{adm\_i-1} - F_{adm\_i}) \tag{28}$$

$$\dot{F}_{adm\_N_d} = N_d \frac{R T_{im}}{p_{im} V_{adm}}(Q_{air} + Q_{egrl})(F_{adm\_N_d-1} - F_{adm\_N_d}) \tag{29}$$

This allows expressing (18) - (21) in a finite dimensional LPV form, where classical LPV control and observation techniques can be applied. Consider the following LPV representation of the discretized system (18) - (21):

$$\begin{aligned} \dot{X} &= A(\varphi)X + W(\varphi) + \xi_x \\ y &= CX + \xi_y \end{aligned} \tag{30}$$

where ξ_x and ξ_y are the mean zero noises associated with the process and the measurement, respectively, $X = [F_{em}\, F_{uc}\, F_{adm\_1} \ldots F_{adm\_N_d}\, F_{im}]^T$ and $C = [1\, 0 \ldots 0\, 0]$. The matrix $A(\varphi)$ and $W(\varphi)$ are defined for $N_d = 2$ (for example) as follows:

$$A(\varphi) = \begin{bmatrix} -\varphi_1 - \varphi_2 & 0 & 0 & 0 & \varphi_1 \\ \varphi_3 & -\varphi_3 - \rho_4 & 0 & 0 & 0 \\ 0 & \frac{2\varphi_5}{V_{adm}} & -\frac{2\varphi_5}{V_{adm}} & 0 & 0 \\ 0 & 0 & \frac{2\varphi_5}{V_{adm}} & -\frac{2\varphi_5}{V_{adm}} & 0 \\ \varphi_6 & 0 & 0 & \frac{\varphi_5}{V_{im}} & -\frac{\varphi_5}{V_{im}} - \frac{\varphi_6}{V_{im}} \end{bmatrix} \quad W(\varphi) = \begin{bmatrix} -PCO\varphi_2 \\ \varphi_4 \\ 0 \\ 0 \\ 0 \end{bmatrix} \tag{31}$$

and the vector that contains all the time varying parameters $\varphi = [\varphi_1\, \varphi_2 \ldots \varphi_5\, \varphi_6]$ is defined as:

$$\begin{aligned} \varphi_1 &= \frac{RT_{em}}{p_{em}V_{em}}(Q_{air} + Q_{egrl} + Q_{egrh}), \quad \varphi_2 = \frac{RT_{em}}{p_{em}V_{em}}Q_f \\ \varphi_3 &= \frac{RT_{air}}{p_{air}V_{uc}}Q_{egrl}, \quad \varphi_4 = \frac{RT_{air}}{p_{air}V_{uc}}Q_{air} \\ \varphi_5 &= \frac{RT_{im}}{p_{im}}(Q_{air} + Q_{egrl}), \quad \varphi_6 = \frac{RT_{im}}{p_{im}}Q_{egrh} \end{aligned} \tag{32}$$

In a general case, the vector φ consists of n_φ varying parameters $[\varphi_1\, \varphi_2 \ldots \varphi_{n_\varphi}]$ where each varying parameter φ_i is bounded by a minimum and maximum value $\underline{\varphi_i}$ and $\overline{\varphi_i}$. The admissible values of the vector φ are constrained in an hyperrectangle in the parameter subset $Z_\varphi \subset \mathbb{R}^{n_\varphi}$ with $N_\varphi = 2^{n_\varphi}$ vertexes $\{v_1, v_2, \ldots v_{N_\varphi}\}$. The images of the matrix $[A(\varphi), W(\varphi)]$ for each vertex v_i correspond to a set $\{\Omega_1, \ldots, \Omega_{N_\varphi}\}$. The components of the set $\{\Omega_1, \ldots, \Omega_{N_\varphi}\}$ are the extrema of a convex polytope which contains the images for all admissible values of φ if the matrix $[A(\varphi), W(\varphi)]$ depends linearly on φ [4].

More precisely, the polytope Z_φ is defined as follows:

$$Z_\varphi := \{[\varphi_1, \ldots, \varphi_{n_\varphi}]^T \in \mathbb{R}^{n_\varphi} \mid \varphi_i \in [\overline{\varphi}_i, \underline{\varphi}_i],\, \forall\, i = 1, \ldots, n_\varphi\} \tag{33}$$

and the equivalent linear polytopic representation of (30) is given by:

$$\begin{aligned} \dot{X} &= \sum_{i=1}^{N_\varphi} \alpha_i(\varphi) A(v_i) X + \sum_{i=1}^{N_\varphi} \alpha_i(\varphi) W(v_i) + \xi_x \\ y &= CX + \xi_y \end{aligned} \tag{34}$$

where the scheduling functions α_i have the following properties [4]:

$$\alpha_i(\varphi) \geq 0, \quad \sum_{i=1}^{N_\varphi} \alpha_i(\varphi) = 1 \tag{35}$$

For further details on polytopic models refer to [4], [5] and [7]. The bounds $\underline{\varphi_i}$ and $\overline{\varphi_i}$ can be established experimentally by calculating the maximum and minimum of the parameter vector φ over a representative operating range of the engine.

Consider the following LPV Luenberger-like observer form:

$$\dot{\hat{X}} = A(\varphi)\hat{X} + W(\varphi) + L(F_{em} - \hat{F}_{em}) \tag{36}$$

where L is a constant observer gain vector that ensures the asymptotic stability of the estimation error for all $\varphi \in Z_\varphi$. This approach may give relatively conservative results when compared with a φ dependent observer gain $L(\varphi)$ (obtained for example with an LTV Kalman filter [6]). However, its implementation simplicity, its low calculation load and the good results that are obtained (e.g. Section 6.1) suggest that (36) is an appropriate approach for this application. To calculate the observer gain L, we consider the dual of the LQR problem, which is given by the following theorem:

Theorem 1. *[16] Consider the system* (30)*. If there exist a symmetric positive definite matrix* $P > 0$*, a matrix* Y *and a symmetric matrix* X*, for a given diagonal process covariance matrix* $V > 0$ *and a diagonal measurement covariance matrix* $W_y > 0$*, such that the following linear matrix inequalities are satisfied for all* $i \in [1 \dots N_\varphi]$*:*

$$A(v_i)^T P + PA(v_i) + C^T Y + Y^T C + I \prec 0 \tag{37}$$

$$\begin{bmatrix} X & W_y^{\frac{1}{2}} Y \\ Y^T W_y^{\frac{1}{2}} & P \end{bmatrix} \succ 0 \quad L = YP^{-1} \tag{38}$$

subject to:

$$\arg \min_{P,X,Y} \{Tr(VP) + Tr(X)\} \tag{39}$$

then, (36) *is an observer of system* (30) *such that* $(A(\varphi) - LC)^T P + P(A(\varphi) - LC) < 0$ *for all* $\varphi \in Z_\varphi$*.*

With Theorem 1, an observer gain for (36) can be easily found using convex optimization tools. This observer guarantees the convergence of the estimation error over the prescribed polytope Z_φ. Moreover, the gain and phase margin inherently obtained from a LQR formulation provide robustness against model uncertainties, which is particularly interesting for this air fraction estimation since the determination of φ in (36) presents a unavoidable amount of dispersion (modeling uncertainty). The air fraction estimation results are presented in the next section.

6. Time-Varying Delay Model and Air Fraction Observer Results

In this section we add the air fraction time-varying delay model proposed in Section 4 into a 0D engine air-path reference model, which has been previously validated in a benchmark. The model validation results are presented in Appendix A to show that the reference model is representative of the engine considered in this work. To illustrate the improvement obtained from the implementation of (12) - (16), a comparison between the 0D model and the proposed approach is performed. The benefits of adding the time-varying delay are illustrated in details.

An evaluation of the air fraction observer (36) is carried out using various discretization sizes to show their effect on the quality of the estimation. Since no air fraction measurements capable of detecting the mass transport phenomenon are currently available, the estimated intake manifold air fraction is compared with the reference engine air-path model along with the time-varying delay approach (12) - (16).

6.1. Air Fraction Time-Varying Delay Model Results

Figure 6 depicts the comparison of the time-varying delay approach (12) - (16) and the 0D engine air-path model. The evaluation has been done using an engine cycle with strong transient conditions in the air fraction as well as in the engine operating conditions. As expected from the results shown in Figures 3a and 5, there are significant differences between both models. To better illustrate the results obtained, a zoom in Figure 6 is performed and the position of the LP-EGR valve is added. This is presented in Figure 7.

As depicted in Figure 7, when a sudden change of LP-EGR valve position is introduced, immediately a change of the intake manifold air fraction is obtained in the 0D air fraction model, which, as seen in Figure 3a, is not physically consistent. However, the time-varying delay model gives a more physical response as

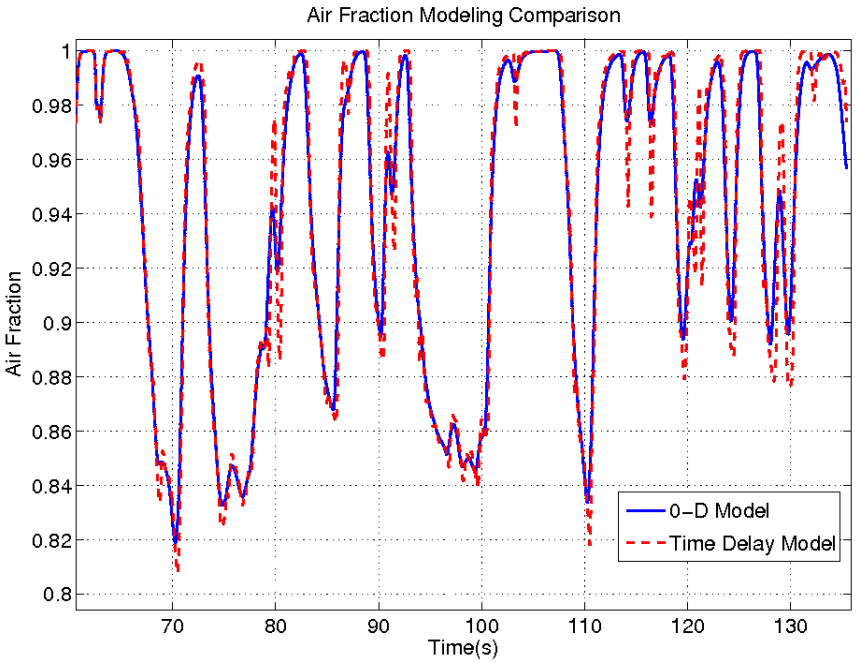

Figure 6: 0D and time delay air fraction model comparison

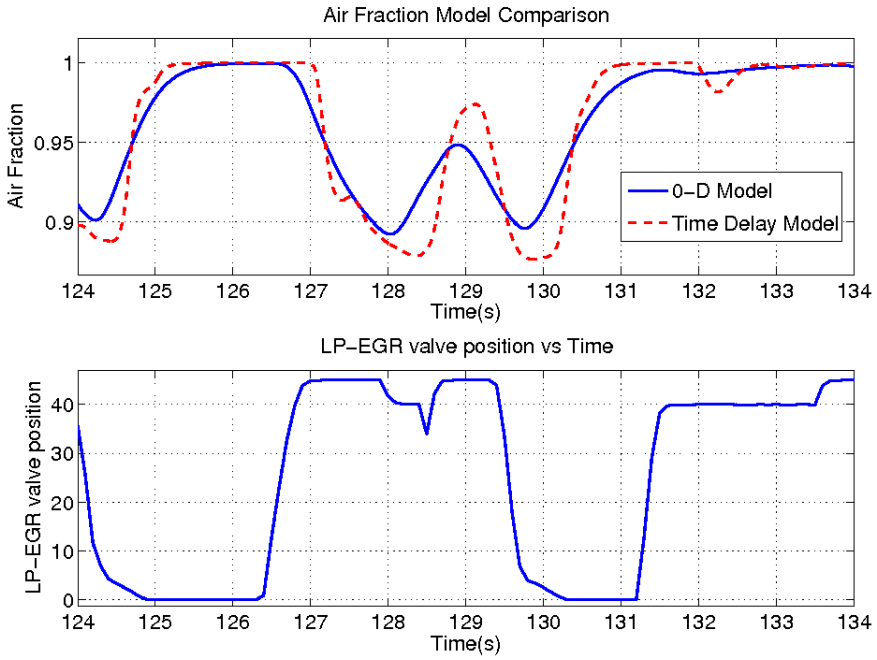

Figure 7: 0D and time delay air fraction model comparison

the intake manifold air fraction remains constant over a fraction of time while the air fraction travels along the engine admission path. These results show that the air fraction modeling under strong transient can be significantly improved using the time-varying delay air fraction model without increasing significantly the calculation load. Moreover, the results shown in Figure 7 illustrate how the representation of the air fraction dynamics can be significantly improved while keeping a 0D formulation for the rest of the variables associated with the engine air-path model (namely, pressure, temperature and mass flow rate).

6.2. Observer Results

Before evaluating the air fraction observer proposed in Section 5, the polytope Z_φ has to be defined in order to apply the results of Theorem 1. The bounds of the LPV parameter vector φ (required for the definition of Z_φ) are obtained using experimental measurements over representative engine operating conditions. The bounds are given in Table 3.

Parameter	ValueMin	ValueMax
φ_1	8.33	49.02
φ_2	0	2.17
φ_3	0	2.98
φ_4	0.98	9.38
φ_5	0.0051	0.033
φ_6	0	0.0073

Table 3: Bounds on the parameter vector φ

Defining $V = 0.001 \times I^{n\times n}$ and $W = 0.005$ (the respective process and measurements noise covariance matrices added in the model) and building the polytope according to Table 3 allow us to apply Theorem 1. By means of convex optimization algorithms, we calculate the observer gain L for three different discretization sizes obtaining the following:

Discretization size	Gain
$N = 1$	$L = [0.65 \quad 0.43 \quad 0.54 \quad 0.59]^T$
$N = 3$	$L = [0.98 \quad 0.47 \quad 0.59 \quad 0.80 \quad 1.09 \quad 0.98]^T$
$N = 6$	$L = [3.35 \quad 0.59 \quad 0.36 \quad 0.75 \quad 1.64 \quad 2.94 \quad 4.37 \quad 5.53 \quad 3.51]^T$

Table 4: Observer gains obtained

Figure 8 shows the result obtained with the observer using a discretization size of $N = 6$ (we use same engine cycle as the one used in Section 3.2) and Figure 9 presents a zoom in Figure 8 to better illustrate the estimation results for different discretization sizes.

As depicted in Figure 8, an accurate estimation of the air fraction is achieved over the engine cycle. As shown in Figure 9, as the discretization size increases, the accuracy of the estimation also does. Using a discretization size of $N = 1$ would be equivalent to use the traditional 0D model based approach. However, it is also important to note that as the discretization size increases, the calculation load also does. $N = 6$ seems to be a good choice for the discretization size as a good accuracy is obtained without increasing significantly the calculation load (this has been verified in simulation). It is important to highlight that the observer will never perfectly fit system (12) - (16) independently of the size of N, since the observer is built from the reduction and discretization this system. Nonetheless, the results obtained show that the proposed air fraction observer significantly improves the estimation of the air fraction in the intake manifold as the main effect of the mass transport is mostly represented. Additionally, the fact that the observer (36) is able to estimate the air fraction in Figures 8 and 9 suggests a good robustness of the proposed observer with respect to model uncertainties (the reference model is quite different from the model considered in the observer).

7. Conclusions

In this paper, an air fraction time-varying delay modeling strategy that takes into account the mass transport time has been developed for a dual-EGR Diesel engine. This modeling strategy has shown to be a good approach to model the mass transport phenomenon in the admission path since good accuracy is obtained while reducing the calculation load. Moreover, with this approach the air fraction dynamics

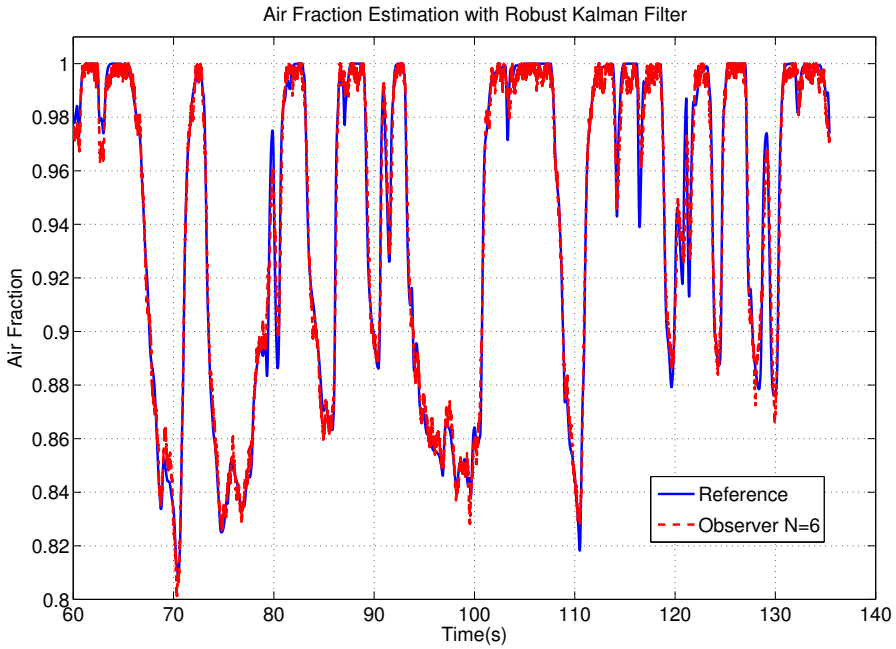

Figure 8: Robust observer response for N=6

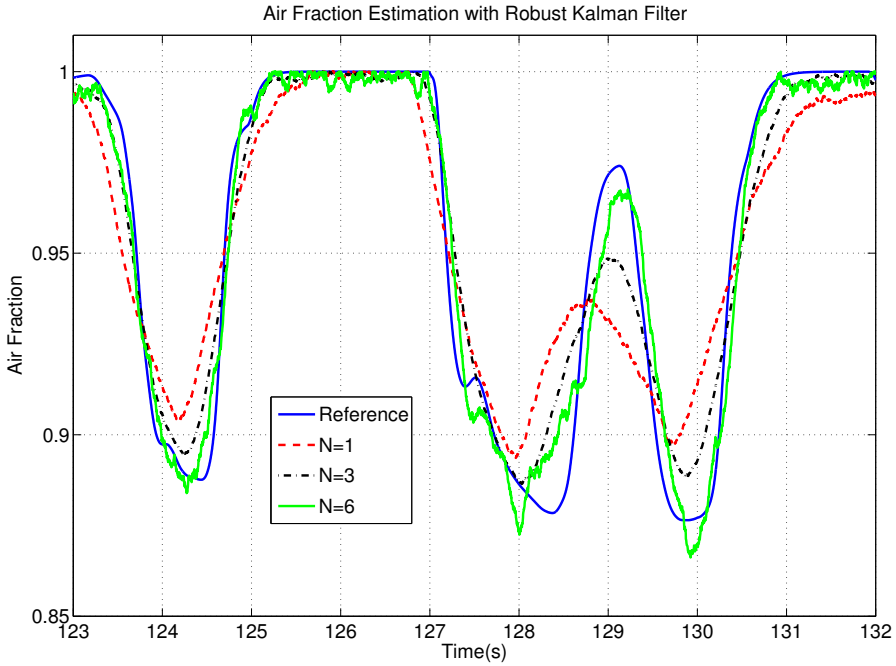

Figure 9: Robust observer response for N=1, N=3 and N=6

can be significantly improved while keeping a 0D formulation for the rest of the variables associated with the engine air-path model. A discretization of the admission path is performed to derive an intake manifold air fraction observer within the LPV framework. The convergence of the observer is guaranteed over a prescribed convex set using a synthesis based on linear matrix inequalities. The effectiveness of the time-varying delay air fraction modeling strategy and the estimator has been evaluated using an experimentally validated engine model as a reference. The simulation results are promising and motivate

future steps toward implementation.

References

[1] K. Akihama, Y. Takatory, K. Inagaki, S. Sasaki, and A. Dean. Mechanism of the smokeless rich Diesel combustion by reducing temperature. *SAE Technical Paper 2001-01-0655, doi:10.4271/2001-01-0655*, 2001.

[2] M. Alriksson and I. Denbrantt. Low temperature combustion in a heavy duty Diesel engine using high levels of EGR. *SAE Technical Paper 2006-01-0075, doi:10.4271/2006-01-0075*, 2006.

[3] M. Ammann, N. Fekete, L. Guzzella, and A. Glattfelder. Model-based control of the VGT and EGR in a turbocharged common-rail Diesel engine: theory and passenger car implementation. *SAE World Congress, Detroit, USA, Paper 2003-01-0357*, 2003.

[4] G. Angelis. *System Analysis, Modelling and Control with Polytopic Linear Models. PhD Thesis.* Technische Universiteit Eindhoven, Eindhoven, 2001.

[5] J. Bernussou, P.L.D. Peres, and J.C. Geromel. A linear programming oriented procedure for quadratic stabilization of uncertain systems. *Systems and Control Letters*, 13:65–72, 1989.

[6] G. Besançon. *Nonlinear Observers and Applications.* Springer, Berlin Heidelberg, 2007.

[7] S. Boyd, L. El Ghauoui, E. Feron, and V. Balakrishnan. Linear matrix inequalities in system and control theory. pages 7–8, 1994.

[8] G. Bression, P. Pacaud, D. Soleri, J. Cessou, D. Azoulay, N. Lawrence, L. Doradaux, and N. Guerrassi. Comparative study in LTC combustion between a short HP-EGR loop without cooler and a variable lift a duration system. *Proceedings of the 17th Aachen Colloquium Automobile and Engine Technology*, 2008.

[9] F. Castillo, E. Witrant, L. Dugard, Vincent Talon, David Chalet, and Pascal Chesse. Intra-pipe restriction non-homentropic boundary resolution method. *SAE Technical Paper 2013-01-0582*, 2013.

[10] F. Castillo, E. Witrant, V. Talon, and L. Dugard. Restriction model independent method for non-isentropic outflow valve boundary problem resolution. *SAE Technical Paper 2012-01-0676, doi:10.4271/2012-01-0676*, 2012.

[11] F. Castillo, E. Witrant, V. Talon, and L. Dugard. Simultaneous air fraction and low-pressure EGR mass flow rate estimation for Diesel engines. *Proceedings of the 5th IFAC Symposium on System Structure and Control, Grenoble, France*, 2013.

[12] C.Briat. *Commande et observation robustes des systémes LPV à retards.* PhD thesis, Grenoble INPG, 2009.

[13] J. Chauvin, G. Corde, and N. Petit. Constrained motion planning for the airpath of a Diesel HCCI engine. *Proceedings of the 45th IEEE conference on decision and control*, pages 3589–3596, 2006.

[14] A. Hribernik. The potential of the high and low-pressure exhaust gas recirculation. *Proceedings of the SAE conference, Paper 2002-04-0029*, 2002.

[15] I. Kolmanovski, J. Sun, and M. Druzhinina. Charge control for direct injection spark ignition engines with EGR. *Proceedings of the 45th IEEE Conference on Decision and Control*, pages 34–38, 2000.

[16] M. Rivas. *Modeling and control of a SI engine for euro VI European normative.* PhD thesis, Université de Grenoble, France, 2012.

[17] T. Ryan and A. Matheaus. Fuel requirements for HCCI engine operation. *SAE transactions-Journal of Fuels Lubricants*, 112:1143–1152, 2003.

[18] J. Wang. Air fraction estimation for multiple combustion mode Diesel engines with dual-loop EGR systems. *Control Engine Practice 16, 1479-1468*, 16, 2008.

[19] D.E. Winterbone and R.J. Pearson. *Theory of Engine Manifold Design: Wave Action Methods for IC Engines*. Society of Automotive Engineers. Inc, 2000.

[20] E. Witrant and S. I. Niculescu. Modeling and control of large convective flows with time-delays. *Mathematics in Engineering, Science and Aerospace*, 1(2):191–205, 2010.

Appendix A. Model Benchmark Validation

To show that the developed 0D model is representative of the engine, a benchmark model validation is proposed. Two validations are performed: one under engine steady state conditions and a second one in engine transient conditions. Each validation allows verifying different characteristics of the model. The steady state validation permits corroborating whether the statics of the engine air-path are well posed and whether the identified parameters, such as the volumetric and engine efficiencies, among others, have been described accurately for a wide range of engine operating conditions. The validation in transient allows verifying whether the dynamic formulation for the engine air-path is correct.

Appendix A.1. Steady State Validation

The steady state validation is performed using a wide range of the engine operating conditions at steady-state (147 different points). The validation has been done using the measurements of the intake manifold pressure p_{im}, the temperature after the turbine T_{apt}, the percentage of EGR at the intake manifold $\%EGR$, the exhaust manifold temperature T_{em}, the pressure after turbine p_{apt} and the fresh air mass flow Q_{air}. Figure A.10 depicts a comparison of the 147 benchmark engine operating points with respect the control-oriented model.

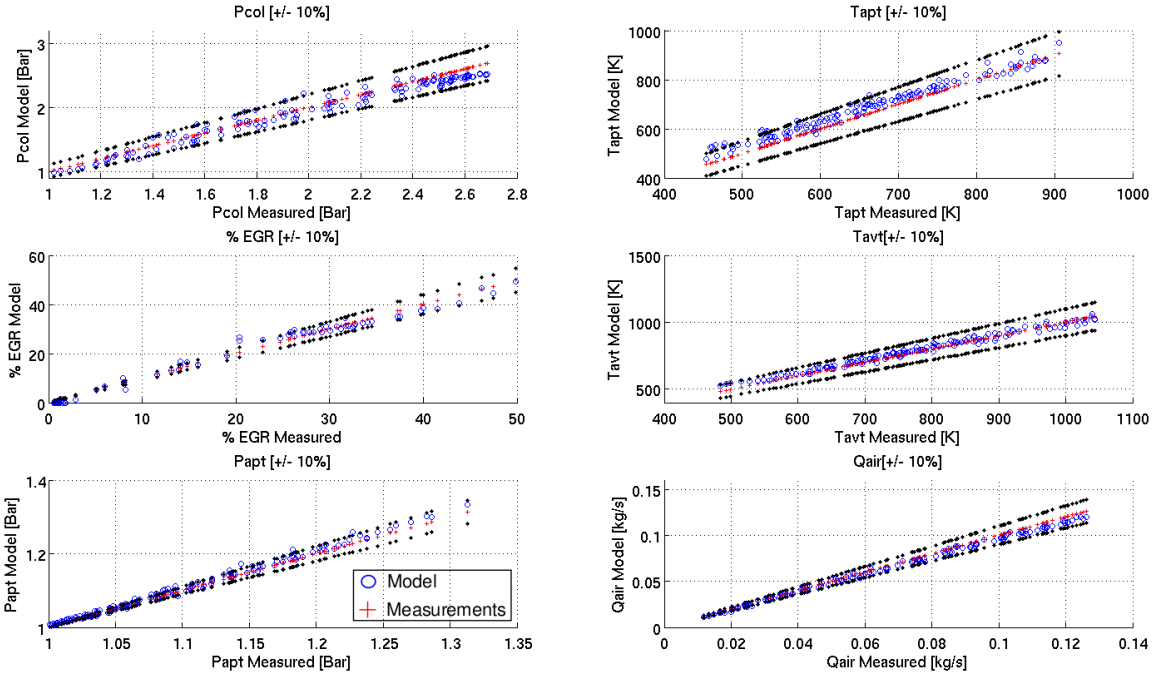

Figure A.10: Steady state validation with 147 operating points

As shown in Figure A.10, the model has a good agreement with the measurements taken on the engine. An accuracy better than 10% has been obtained for most of the 147 operating points over the six measurements considered. The dispersion obtained is intrinsic of the modeling process and can come from many different sources such an unmodeled phenomena, inaccuracies in the parametric identifications, measurement noise, etc. Table A.5 presents the root-mean-square deviation (RMSD) of the model with respect to the 147 engine operating conditions.

The results of Table A.5 show that the developed 0-D model has an overall accuracy better that 5%, which allows us to consider it as representative of the engine in steady-state conditions.

Variable	RMSD	Variable	RMSD
p_{im}	4.1 %	T_{apt}	4.4 %
$\%EGR$	2.5 %	T_{em}	2.5 %
p_{apt}	0.62 %	Q_{air}	4.2%

Table A.5: Model root-mean-square deviation percentage error in steady state for 147 engine operating points

Appendix A.2. Transient Validation

The validation under transient conditions is done using three different engine cycles: Cycle 1, is a cycle with HP-EGR and LP-EGR and not much supercharging, Cycle 2 is a well supercharged cycle with LP-EGR and Cycle 3 is the NMVEG engine cycle. Figures A.11, A.12 and A.13 present the results obtained for the transient validation using as a reference, the measurements of p_{im}, p_{em} and Q_{air}.

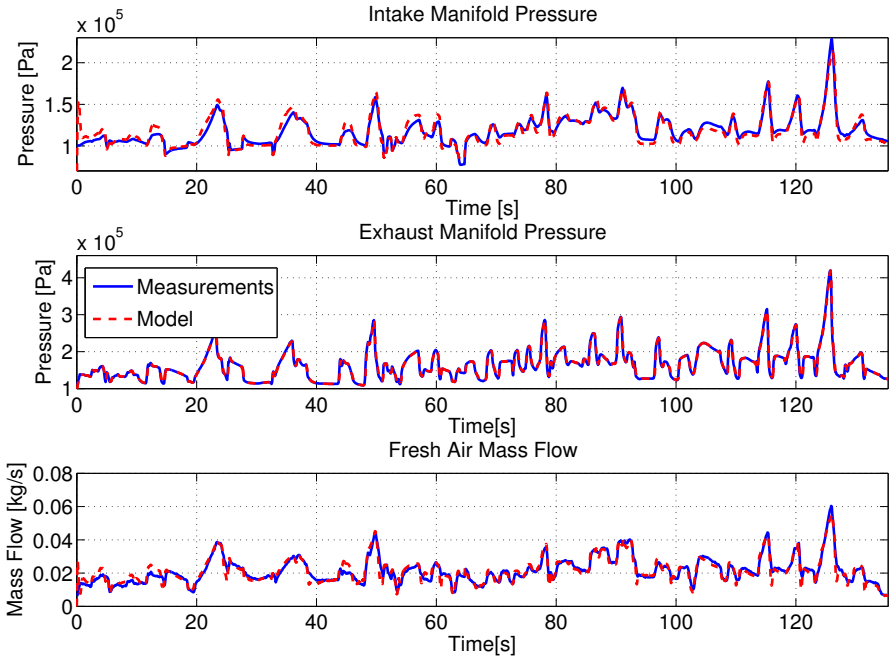

Figure A.11: Validation in transient with Cycle 1

As depicted in Figures A.11, A.12 and A.13, the model has a good agreement with the benchmark engine measurements. Some parts of the cycles are deviated from the reference, however, we can see that the overall dynamics are well represented by the model. Table A.6 shows the RMSD of each cycle wtih respect the benchmark measurements.

Variable/Cycle	Cycle 1	Cycle 2	NMVEG Cycle
p_{im}	3.7 %	4.6%	3.9%
p_{em}	1.8 %	1.2%	1.7 %
Q_{air}	8.6 %	6.0%	4.6%

Table A.6: Model root-mean-square deviation percentage error in transient for three different engine cycles

As illustrated in Table A.6, the accuracy obtained is better than 9%. We can see that the least represented variable of the three considered in this validation is the fresh mass flow rate Q_{air}. This can be due to the inaccuracies in the compressor model and the volumetric efficiency. Nonetheless, the results

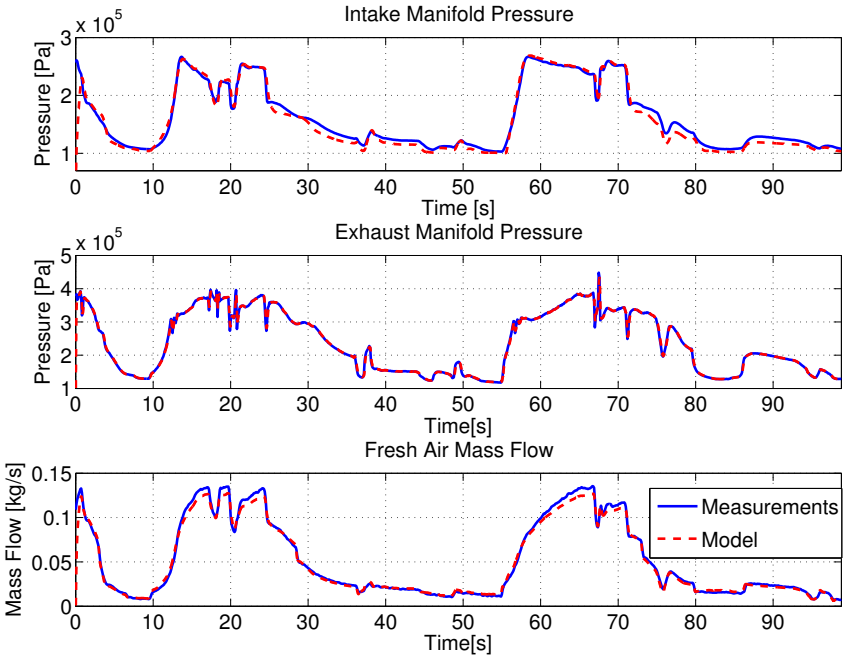

Figure A.12: Validation in transient with Cycle 2

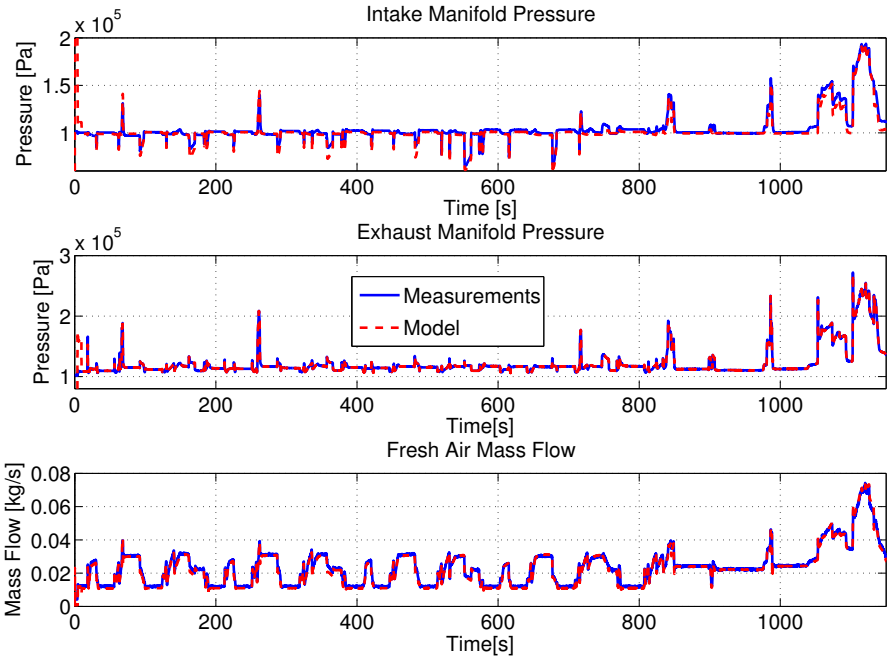

Figure A.13: Validation in transient with Cycle 3

obtained can be consider good enough for control purposes.

Summary

The engine air-path has become a crucial part in the development of modern engines. The control of the air-path has a direct impact on the engine performance as well as on its pollutant emission level. Indeed, air system strategies allow controlling the species that are introduced in the cylinder, which is a cost-effective way to reduce pollutant emissions. As a consequence, the automotive air systems have become increasingly complex in order to achieve pollutant reduction strategies and to allow fuel consumption reductions. In this context, this thesis focuses on the modeling and control of the air-path of Diesel engines. We address many of the current Renault's concerns regarding the control of the engine air-path. We provide industry-oriented solutions suitable for implementation, taking into account the resources currently available for production engines. We focus on the modeling, estimation and control of the mass transport phenomenon in the engine air-path. We contribute with the development of boundary resolution methods for 1D modeling control-oriented platforms of the engine air-path and we build a part of the theoretical framework to enable the control and estimation of the intake manifold air fraction within an infinite dimensional approach.

Keywords: Engine control, boundary control, infinite dimensional systems, one-dimensional modeling.

Resumé

La chaîne d'air du moteur est devenue un élément essentiel dans le développement des moteurs modernes. Le contrôle du système d'air a un impact direct sur les performances du moteur ainsi que sur son niveau d'émission de polluants. En effet, les stratégies qui agissent sur le système d'air permettent de contrôler les composants introduits dans le cylindre, ce qui est un moyen efficace et rentable de réduire les émissions polluantes. En conséquence, les chaînes d'air des moteurs modernes sont devenues de plus en plus complexes afin d'atteindre les stratégies de réduction de pollution et de permettre des réductions de consommation de carburant. Dans ce contexte, cette thèse se focalise sur la modélisation et le contrôle de la chaîne d'air des moteurs Diesel. Nous abordons plusieurs problématiques au niveau du contrôle de la chaîne d'air qui intéressent actuellement Renault. Nous fournissons des solutions orientées vers l'industrie, appropriées pour la mise en oeuvre, avec les ressources disponibles sur les moteurs actuellement produits. Nous nous concentrons sur la modélisation, l'estimation et le contrôle du phénomène de transport de masse dans la chaîne d'air des moteurs Diesel. Nous contribuons au développement de méthodes de résolution de conditions limites axées sur les plateformes de simulation 1D orientées contrôle et nous construisons une partie du cadre théorique (approche de dimension infinie) qui permet de contrôler et d'estimer la fraction d'air frais dans le collecteur d'admission en prenant en compte le temps de transport de masse.

Mots clés: Contrôle moteur, contrôle frontière, systèmes à dimension infinie, modélisation monodimensionnelle.